X-ray Insights into Massive Star Evolution: the X-ray Source Population of M33 as seen by *XMM-Newton*, *Chandra*, and the *Hubble Space Telescope*

Kristen Garofali

A dissertation
submitted in partial fulfillment of the
requirements for the degree of

Doctor of Philosophy

University of Washington

2018

Reading Committee:

Benjamin F. Williams, Chair

Emily Levesque

Scott F. Anderson

Program Authorized to Offer Degree:
Astronomy

University of Washington

Abstract

X-ray Insights into Massive Star Evolution: the X-ray Source Population of M33 as seen by *XMM-Newton*, *Chandra*, and the *Hubble Space Telescope*

Kristen Garofali

Chair of the Supervisory Committee:
Professor Benjamin F. Williams
Astronomy

Massive stars are key drivers in the cycle of star formation and overall galactic chemical evolution, but many aspects of the evolution of high-mass stars, in particular the end stages of their lifetimes, are difficult to constrain observationally. High-mass X-ray binaries (HMXBs) and supernova remnants (SNRs) are observable at a broad range of wavelengths and are unique probes into how massive stars evolve, die and subsequently interact with and enrich their environments. Previous studies of HMXB and SNR populations, both galactic and extragalactic, have demonstrated the wealth of knowledge to be gleaned from X-ray observations of these objects. However, these studies have been limited in the range of galactic host environments (metallicities and star formation rates) probed, as well as suffering from distance, extinction and X-ray positional uncertainties.

M33, a late-type Sc spiral, is ideal for X-ray studies of both HMXBs and SNRs. It's proximity to the Milky Way makes both HMXBs and SNRs resolvable for study, and its low foreground extinction and close to face-on inclination make it easier to study such objects as populations. Furthermore, it has deep, and wide coverage from *Chandra*, which affords high spatial resolution, and *XMM-Newton*, which offers high soft sensitivity, in conjunction with considerable archival *Hubble Space Telescope (HST)* coverage. In this thesis, I probe the X-ray source population of M33 with a particular emphasis on massive stars and their end products, which are well-characterized using the available multiwavelength coverage.

I characterize the large X-ray point source population of M33 from deep *XMM-Newton* observations, from which I identify a sizable number of new soft sources, and produce a deep X-ray luminosity function indicative of a substantial population of HMXBs. The source population from this catalog forms the backbone for studying M33's massive star population from the X-ray perspective. From this source population, I also identify a large number of SNRs newly detected in X-rays in M33. With this large sample of SNRs I examine the effect of host galaxy properties, such as metallicity and star formation rate, on SNR characteristics and detectability. I further study the massive star population of M33 through identification and characterization of a new sample of candidate HMXBs in M33 found using archival *HST* and *Chandra* imaging. I use the *HST* photometric data to model the color-magnitude diagrams in the vicinity of each candidate HMXB to measure a resolved recent star formation history, and thus a formation time-scale, or age for each source. For a subset of these HMXBs, I present an in-depth source classification on the basis of available X-ray and optical spectra and colors.

I discuss these results in the context of massive star, and massive binary evolution and their connection to host galaxy environment as seen through the lens of M33. Studying large samples of massive star end products in a nearby galaxy such as M33 paves the way towards understanding massive star and massive binary evolution, and the implications for formation of compact object binaries and gravitational wave sources.

Contents

List of Figures

List of Tables

Acknowledgments

The work presented in this thesis is culmination of nearly six years in graduate school, with incredible support from family, friends, fellow graduate students, and faculty advisors along the way.

I would like to thank the chair of my committee, and my advisor since day one, Ben Williams, for his unending enthusiasm, support, and mentorship. His guidance throughout my time in graduate school has been invaluable, and I will forever be grateful for his dedication as a mentor. I would also like to thank Emily Levesque, and Scott Anderson who, as my committee members, helped broaden my horizons.

The graduate students at UW were an integral part of my graduate career here, and I'm sure I would not be where I am without their support, camaraderie, and karaoke. I'd like to thank all my wonderful officemates over the years: Ferah Munshi, Michael Tremmel, Grace Telford, and Kathryn Neugent for endless discussions, both scientific and otherwise, and for being great colleagues and friends. I'd also like to give a special thanks to Nell Byler, Phoebe Upton Sanderbeck, and Diana Windemuth for their friendship, and for always being there when I needed to chat or take a night off for board games.

All my friends in Seattle, and back home in the Midwest have also lent me their unending support. In particular, I want to thank Andrew Kinnavy, Wonder Compton, and Wendy and Ward Groesbeck for being my family in Seattle, and allowing me to step away from grad school when needed for homemade dinners, hiking, and backpacking trips. Without them I would not have been able to call Seattle home.

I also have to thank my best friend and partner, Brad Olson, for his constant love and support, and for the following (non-exhaustive) list of things: for moving across the country (twice) for me, for always knowing how to make me laugh, for making dinners for me when I got home late, and for being the best dog dad to our PhDogs, Lando and Leia. I would not have made it so far and been so happy along the way without his companionship.

Most importantly, I would like to thank my family: my parents, Charlie and Cindy, and my sister, Leah, for their lifelong support. Without their love, confidence in me, and frequent trips to Seattle I would surely not be where I am today.

Finally, I would like to acknowledge the sources of funding that provided support for this work. Support for work in Chapter 2 and Chapter 3 was provided by NASA grants NNX12AD42G and NNX12AI52G. Support for work in Chapter 4 was provided by grant GO-14324 from the Space Telescope Science Institute, which is operated by the Association of Universities for Research in Astronomy, Incorporated, under NASA contract NAS5-26555. Support for work in Chapter 5 was provided by NASA through Chandra Award Number AR8-19006X issued by the Chandra X-ray Center, which is operated by the Smithsonian Astrophysical Observatory for and on behalf of the National Aeronautics Space Administration under contract NAS8-03060.

Dedication

To my family: Charlie, Cindy, and Leah for inspiring me to become an astronomer.

Chapter 1: Introduction

We are stardust. Billion year old carbon. We are golden. — Joni Mitchell

Carl Sagan famously noted "The nitrogen in our DNA, the calcium in our teeth, the iron in our blood, the carbon in our apple pies were made in the interiors of collapsing stars. We are made of star stuff." It's a testament to Carl Sagan as a science communicator that this statement has become ubiquitous, being incorporated into song lyrics, printed on t-shirts, and used in countless lessons to directly connect people with the cosmos.

Delving into the astrophysical meaning behind this quote, the picture is not so simple: we are indeed made of star stuff, but not all stars make the same stuff. Stars, very broadly, may be separated into low-mass (< 1 $M_\odot$), intermediate mass ($1 < M < 8$ $M_\odot$), and high-mass (> 8 $M_\odot$) stars. According to the empirically measured initial mass function for stars, there is an abundance of stars of mass lower than the Sun, while those stars with masses > 8 $M_\odot$ are relatively rare. Though rare, these high-mass stars are of vital importance astrophysically speaking, as well as to life. Many of the heavy elements present in the universe today are synthesized during the lives and energetic death throes of massive stars. Thus understanding how these stars evolve and end their lives is vital towards understanding their role in shaping the cosmos as we know it today.

The goal of this thesis is advancing our understanding of the lives and deaths of massive stars and their connection to their host galaxy environments towards a better understanding of the evolution of massive stars. This can be achieved, in part, by observations of various massive star products at different stages of evolution. Using large archival datasets I have probed massive stars as observed primarily in X-rays through the characterization of SNRs and HMXBs. This work cataloguing and characterizing massive star evolution products provides detailed observational constraints to massive star modeling efforts in the era of large time-domain surveys and multi-messenger astronomy, as massive stars are the progenitors of exotic astrophysical transients, and gravitational wave sources.

In this Chapter I introduce concepts that I will delve into throughout the rest of the thesis. I begin with an introduction to and overview of high-mass stars and their evolution. I next describe the massive star evolution products observable in X-rays as probed in this thesis, namely SNRs and HMXBs, and describe the history of observations of such objects in nearby galaxies. I next describe the telescopes and data products used in this thesis, and finally conclude with a brief outline for the remainder of the thesis.

1.1 Massive Star Evolution

Massive stars, stars > 8 $M_{\odot}$, ultimately end their lives as compact objects, either black holes (BHs) or neutron stars (NS). Empirical measurements of the initial mass function for stars reveal that high mass stars are relatively rare, compared to low-mass stars (Salpeter, 1955; Kroupa, 2001). Despite this rarity, massive stars are observable in great numbers both nearby (e.g. Massey et al., 2006) and even at cosmological distances (e.g. Kelly et al., 2018) owing to their extremely high luminosities. The substantial radiative output of hot, massive stars drives strong stellar winds (Pauldrach et al., 1986), which leads to mass loss (Vink et al., 2001), changes in luminosity and therefore evolution timescales, and chemical mixing (Kudritzki & Puls, 2000; Smith, 2014). In addition, the strong, line-driven winds of massive stars modify their surroundings via feedback and chemical enrichment (Abbott, 1982). Thus, the energetic lives and deaths of massive stars are integral to the cycle of star formation and overall galactic chemical evolution, both enriching their surroundings via nucleosynthetic products and seeding new generations of star formation, as well as suppressing star formation via feedback.

On its way to becoming a compact object a massive star will evolve rapidly through several evolutionary phases which are highly dependent on the star's initial mass, chemical composition, rotation rate, how much mass it loses via stellar winds during its lifetime, and possibly the effects of binarity (Maeder & Meynet, 2000; Ekström et al., 2012; Sana et al., 2012; de Mink et al., 2013). Generally speaking, OB stars (massive hydrogen-burning stars on the main sequence) will move off the main sequence in tens of Myr and evolve into subsequent phases, where they will be observable as red supergiants (RSGs), yellow supergiants (YSGs), blue supergiants (BSGs), luminous blue variables (LBVs), Wolf-Rayet (WR) stars, or Be stars, depending on their physical parameters as mentioned above. RSGs and YSGs fall into the class of "cool" evolved massive stars which most likely originate from the lower end of massive star progenitors, while BSGs, LBVs, WR stars and Be stars are all "hot" evolved massive stars, most likely evolving from very high-mass stars (> 25 $M_{\odot}$). LBVs are unique given their eruptive mass loss episodes, while WR stars, helium-burning massive stars, are identified via their broad stellar emission lines of helium, as well as carbon (WC stars), and nitrogen (WN stars), indicative of strong stellar winds and stripped hydrogen envelopes owing to previous episodes of mass loss or stripping. Be stars are rapidly rotating evolved B stars identifiable by their strong stellar emission lines, such as Hα, indicative of circumstellar disks.

Understanding the stages of evolution a massive star of a given initial stellar mass will undergo based on its mass loss history, and rotation rate has long been sought after both observationally, and theoretically (e.g. Humphreys & Davidson, 1979; Conti et al., 1983; Meynet et al., 1994; Langer et al., 1994; Heger et al., 2000; Massey, 2003; Crowther, 2007; Georgy et al., 2012; Levesque et al., 2012; Leitherer et al., 2014). However, regardless the evolutionary path followed, the ultimate fate for a star > 8 $M_{\odot}$ following exhaustion of sufficient radiation pressure to provide support against gravitational collapse is either a core-collapse (CC) supernova (SN) (Woosley et al., 2002), or direct collapse into a BH (Fryer, 1999). Much work has also been done in predicting and observationally constraining the stellar evolution phases that directly precede different subclasses of SNe (e.g. Heger et al., 2003; Eldridge & Tout, 2004; Smartt et al., 2009; Smartt, 2009, 2015), and modeling the end stages of massive stars to determine if there is a mass threshold for stars that end as SNe explosions or direct collapse into BHs (e.g. Woosley & Weaver, 1995; Sukhbold et al., 2016, 2017).

Another complicating factor in the evolution of massive stars is the role of multiplicity (Podsiadlowski et al., 1992). It has been shown that the majority of massive stars ($\sim 70\%$) are in close enough binaries for mass transfer or mergers to occur, which can dramatically alter the evolution of the stars (e.g. Sana et al., 2012; de Mink et al., 2013). The evolutionary paths taken depend strongly on often-unknown initial orbital parameters, and suffer from the same uncertainties that exist for single stars (e.g. mass-loss rates, rotation, metallicity effects, etc.), in addition to prescriptions for binary interactions including mass transfer efficiency, the common-envelope phase, and more. Understanding massive star evolution, and therefore the products of massive star death in a statistical sense is of the utmost importance in the era of multi-messenger astronomy, as such systems are the precursors to close compact object-compact object binaries.

The uncertainties in massive star evolution can be mitigated by studying massive stars and their end products at various stages in their evolution. In particular, the extremely energetic core-collapse SNe that mark the ends of massive star lives can be studied out to cosmological distances. Prompt observations of the SNe light curves on the order of weeks post-explosion reveal information about the structure of the outer layers of the stars themselves just prior to explosion (Filippenko, 1997), while observations on the order of years post-explosion can probe the nebular phase of the supernova and reveal information about the progenitor star itself (e.g. Jerkstrand et al., 2012). On timescales of thousands of years, the material and shockwave from the SNe explosion interacts

with the interstellar medium (ISM), making it visible in wavelengths that include optical, radio and X-ray (Chevalier, 1982). This last stage can be studied in far larger numbers than the explosion itself as the SNR that is left behind is much more long-lasting than the SNe. SNRs are thus a key observational touchstone for unlocking useful information about the progenitor star and its lasting effects on the surrounding interstellar medium (Reynolds, 2008).

With SNe and SNRs it is often difficult to constrain the effect of multiplicity as evidence of the progenitor(s) is destroyed, and the remaining compact object can be difficult to observe (Alp et al., 2018). For this reason, other observational touchtones are needed to probe the effect of multiplicity on massive star evolution. HMXBs, binary stars that contain a compact object (BH or NS) accreting mass from a high-mass ($> \sim 8$ $M_{\odot}$) companion, provide such an observational touchstone, as they are unique windows into the underlying processes of both binary as well as massive star evolution. The compact object properties provide insight into the circumstances of the death of the progenitor, while the interactions between the surviving companion and compact object provide clues regarding preferred binary evolution pathways, and the effects of mass transfer and stellar winds. HMXBs are also potential precursors to compact object-compact object binaries, making observations of HMXBs across a range of environments fundamental to understanding evolution of gravitational wave sources in the era of multi-messenger astronomy. In the remainder of this Chapter I will delve into each of these topics in more detail, and provide an outline for the rest of the thesis.

1.2 Supernovae and Their Remnants

SNe are the explosive deaths of stars. Broadly SNe are classified as either Type Ia, the thermonuclear detonation of a white dwarf that has reached is Chandresekhar limit, or CC, the explosive death of a massive star owing to the collapse of the stellar core, which may be either an Fe or O-Ne-Mg core at the time of death, depending on the mass of the star. For the purposes of this thesis, I will focus on CC SNe, as these are exclusively the products of massive star evolution.

Much work has been dedicated to modeling the mechanisms behind CC SNe (Janka, 2012). In the same vein, there are myriad observations of the many subclasses of CC SNe (Type II-P, Type II-L, Type IIb, Type Ib, Type Ic, Type IIn, etc.) aimed at better understanding the stage of massive star evolution that directly precedes explosion (e.g. Podsiadlowski et al., 1993; Smartt

et al., 2004; Maund & Smartt, 2005; Foley et al., 2007; Gal-Yam et al., 2007; Smartt, 2009, 2015; Kilpatrick et al., 2017). While observations of SNe are available out to cosmological distances, there are far fewer available to study nearby in detail owing to their short-lived nature, and there are only a handful of nearby SNe for which pre-collapse imaging is available (Van Dyk et al., 2003; Smartt et al., 2009). Thus, basic questions remain as to the link between the properties of a SNe and the characteristics of its progenitor, the mass threshold (if any) for BH versus NS formation, the properties of the the compact objects and remnants left behind, and the nucleosynthetic yields of SNe.

SNRs offer a different avenue for probing some outstanding questions related to massive star evolution and death. As the ejecta and blast wave from the SN explosion interact with the circumstellar medium and ISM the SN transitions into an SNR, visible across the electromagnetic spectrum. The SNR continues to deposit energy and metals into the ISM, driving galactic chemical evolution. Compared to the short-lived SNe events themselves, the SNRs left behind are much more numerous, and thus offer a more plentiful avenue for unlocking information about the progenitor and its lasting impacts on its surroundings (Chevalier, 2005). However, there is the basic but non-trivial question as to the nature of the SNR progenitor, i.e. CC or Type Ia, which is key to connecting the remnant to the evolution of its progenitor system. To this end, studies of SNRs that can characterize CC SNR populations and their connection to host galaxy environment are of paramount importance in understanding massive star evolution. Key but difficult to constrain in such studies is dissociating the SNR characteristics that come from interactions with the surroundings from the characteristics that arise due to the progenitor.

Most Galactic SNRs were first identified as non-thermal radio sources. By contrast, many of the numerous extragalactic SNRs (> 1000 in the Local Volume) were first identified via interference filter imaging. In particular, the [S II]/Hα ratio is typically used as a way to distinguish optical emission from shocked regions in SNRs from emission from H II regions, with a cutoff at > 0.4 for classification as an SNR candidate. This technique, suggested by Mathewson & Clarke (1973), is efficient at separating SNRs from H II regions as material in H II regions is typically too highly ionized for forbidden line transitions such as [S II], while such lines form in abundance via recombination in the cooling gas behind the SN shock. While many SNRs have been discovered via these optical line ratios, a much smaller number show optical emission that is directly indicative

of a core-collapse progenitor. These include so-called "oxygen-rich" SNRs that show strong [O III] emission (e.g. Dopita et al., 1981; Blair et al., 2000), indicative of core-collapse ejecta interacting with the surroundings, and pulsar wind nebulae, in which distinct emissions lines are visible from material photoionized by the synchrotron emission from a central pulsar.

Beyond SNR surveys using optical emission line ratios, X-ray measurements provide helpful confirmation of SNRs on the basis of soft, thermal X-ray spectra. This soft, thermal emissions arises from hot gas as the shock interacts with the ISM and ejecta. The detectability of an X-ray SNR thus depends on the density of the medium the SN explodes into, as well as the phase of evolution, with SNRs brightest in X-rays during the Sedov phase, and fainter both preceding and tailing this phase.

Significant effort has been put into X-ray detections of SNRs, as the thermal spectra of young, ejecta dominated SNRs can be indicative of the progenitor (e.g. Vink et al., 2003; Badenes et al., 2003; Gaetz et al., 2007; Badenes et al., 2007; Reynolds, 2008; Long et al., 2010; Vink, 2012; Yamaguchi et al., 2014; Pannuti et al., 2014; Long et al., 2014; Maggi et al., 2016). Progenitor classifications have been recorded for a number of SNRs on the basis of ejecta signatures, light echoes, X-ray morphologies, Fe Kα line measurements, and detection of central compact objects (Hughes et al., 1995; Rest et al., 2005; Borkowski et al., 2006; Lopez et al., 2009, 2011; Yamaguchi et al., 2014; Maggi et al., 2014). Much of this work in securing more precise progenitor classifications, however, has focused in detailed studies of individual objects, thus a large number of nearby SNRs lacking deep observations still remain without secure classification, hampering inferences as to the connection of progenitor type with environment on the basis of large population studies. To this end, in Chapter 3 I present the largest, multiwavelength catalog of SNRs in M33 to date. With this catalog SNR detectability across different wavelength regimes can be quantified in a statistical way to produce cleaner samples for large population studies, and SNR progenitor typing methods can be tested.

1.3 High-Mass X-ray Binaries

HMXBs offer a unique window into massive binary evolution. As observable remains of the post-collapse evolution of tightly bound binary stars, they can act as a fossil record of past binary interactions. In addition, HMXBs may be gamma-ray burst progenitors (Dominik et al., 2012),

precursors to close compact object binaries, and gravitational wave sources (Hainich et al., 2017; Tauris et al., 2017), and potentially play a role in heating the intergalactic medium at high redshift (Justham & Schawinski, 2012; Fragos et al., 2013; Madau & Fragos, 2017). Therefore, constraining the observed HMXB population across a variety of environments is of utmost importance to a broad range of astrophysics.

In resolved HMXB population studies it is instructive to delineate between the various HMXB subclasses, as typically defined by the spectral type of the donor star. The most observationally abundant subclass of HMXBs are Be/X-ray binaries (Be-XRBs), systems that consist of a compact object in a high eccentricity orbit that accretes material as it passes through the circumstellar disk of its companion, typically an early type B star (O9 V – B2 V) that exhibits Hα emission from its equatorial disk. The systems can be highly variable owing to their high eccentricity orbits, but are also very bright during outburst as the compact object passes through the equatorial disk of the companion star. The companion stars are also more easily characterized in this case by the strong Hα emission emanating from their equatorial disks (Porter & Rivinius, 2003). The fast rotation periods measured for Be stars, and subsequent formation of equatorial disks around the stars is postulated to be the result of binary evolution (Rappaport & van den Heuvel, 1982; McSwain & Gies, 2005). The distribution of spectral classifications for donor stars (peaking $\sim$ B2) is also indicative of preferred binary evolution scenarios (van Bever & Vanbeveren, 1997; Negueruela, 1998; Negueruela & Coe, 2002).

By contrast, there is a relative paucity of observed HMXBs with supergiant companions (SG-XRBs), which are typically wind-fed systems, though may also be fed via Roche Lobe overflow (RLOF). There is only one such SG-XRB known in the SMC (Coe et al., 2005), four systems in the LMC (Antoniou & Zezas, 2016), and a rising number in the Milky Way thanks to observations with *INTEGRAL* (e.g. Walter et al., 2015). These systems, as they are typically wind-fed, are persistent, but often lower luminosity than Be-XRBs. There may also be a large population of unobserved HMXBs with supergiant companions belonging to the more recently discovered class of systems known as supergiant fast X-ray transients (SFXTs). This subclass is generally harder to detect owing to the systems' extremely short outbursts (minutes to hours), and low luminosities in quiescence (Negueruela et al., 2006). Still more rarely observed are the subclass of HMXBs that contain a compact object accreting material from a WR star, with only five such systems

observed to date (van Kerkwijk et al., 1996; Prestwich et al., 2007; Crowther et al., 2010; Liu et al., 2013; Maccarone et al., 2014). Issues such as stellar crowding, and uncertainty in X-ray point source position hamper the classification of HMXBs by their donor star counterparts, which leads to relatively large numbers of inferred HMXB populations without secured system properties. Multiwavelength characterization (e.g. UV, IR and optical) of the donor stars is thus critical to fully understanding HMXBs as a population.

Beyond classifying the donor star, characterizing the nature of the compact object in terms of type (BH or NS), mass, and accretion state is crucial to understanding the systems. In general, X-ray observations provide the most accessible way to type the compact object. If the compact object is a pulsar pulsations can be detected, proving the compact object is a NS, and a spin period measured. Early on, Corbet (1984, 1986) demonstrated the relationship between pulse period and orbital period in what has now become known as the Corbet diagram. Notably, Be-XRBs occupy a locus in spin period versus orbital period space with a strong correlation between the two quantities (i.e. the longer the orbital period, the slower the spin period), while wind-fed systems show no such correlation, and the few known RLOF systems display an anticorrelation. The relationship between spin period and orbital period can be understood for Be-XRBs in that a wide orbit, as is typically the case for Be-XRBs, leads to lower wind densities, which in turn leads to smaller accretion pressures on the surface of the compact object, and thus a slower rotation period. Ultimately, the slower rotation period makes it easier for the pulsar to accrete more material, resulting in more easily observed (i.e. brighter) systems. The lack of correlation seen for wind fed systems implies that the wind accretion mechanism is not successful at transferring angular momentum between system components. The relationships derived from the Corbet diagram can be used to predict spin or orbital period if one system quantity is known, or otherwise predict HMXB accretion mechanism, and therefore subclass, if both spin and orbital period are measured.

In the absence of pulsations, the nature of the compact object is much more difficult to determine on the basis of X-ray data alone. With the recent launch of *NuSTAR*, however, X-ray photons at much harder energies (e.g. > 12 keV) are now accessible, which opens new avenues for probing accretion states and compact object types. Namely, X-ray color-color and color-intensity diagrams in the hard bands can be used to distinguish between different accretions states (e.g. Wik et al., 2014), i.e. between accreting pulsars and soft or hard state BHs. The ability to broadly

classify compact objects on the basis of X-ray data narrows the scope of point sources for which to pursue time-resolved spectroscopic follow-up, which has so far been used only for a handful of bright HMXBs to derive compact object mass estimates on the basis of time-intensive radial velocity measurements (e.g. Orosz et al., 2007; Silverman & Filippenko, 2008; Crowther et al., 2010).

Observationally constraining the number of systems present in the various subclasses, the distribution of donor star spectral classes, and compact object masses and accretion states as they relate to host environment properties is a fundamental link in understanding massive binary evolution. Understanding HMXBs better as a class of objects based on all available multiwavelength data is likewise key to expanding their role as observational touchstones when it comes to understanding formation and evolution of gravitational wave sources (Belczynski et al., 2002, 2007). In Chapter 4 I present work on the identification and measurement of the formation timescale for a large population of HMXBs in M33. In Chapter 5 I discuss the further characterization of these sources on the basis of their donor star counterpart spectra and *Hubble Space Telescope (HST)* colors, as well as their X-ray spectral characteristics. These chapters provide a framework for leveraging multiwavelength characterization of binary components to understand preferred evolution pathways for HMXBs.

1.4 X-ray Observations of Massive Star Products in the Local Group

Local Volume galaxies provide an unparalleled environment in which to study the products of massive star evolution. Such galaxies, and in particular, Local Group (LG) galaxies such as M31, M33, and the Magellanic Clouds (MCs), are near enough that individual sources such as HMXBs and SNRs can be resolved, while also probing different metallicity regimes as compared to the Galaxy. Within the Milky Way, it can be difficult to systematically compare SNR and HMXB properties with host environment because most detailed studies to date have focused on single objects. In addition, population studies in the Milky Way are difficult due to distance uncertainties and variable absorption to the individual objects (Woltjer, 1972; Milne, 1979; Raymond, 1984; Green, 2014). SNRs and HMXBs in LG galaxies, however, are in the unique position to be studied as a population in relation to the surrounding stellar population, because they are all at a common distance and have similar foreground extinction. In the following sections I will discuss previous

works that have explored SNRs and HMXBs as populations in the LG.

1.4.1 Supernova Remnants in the Local Group

The SNR populations in both the Small Magellanic Cloud (SMC) and Large Magellanic Cloud (LMC) have been studied in great detail, with the first extragalactic SNRs discovered in the LMC (Mathewson & Healey, 1963). The SMC and LMC, both irregular dwarf galaxies at $\sim$ 60 kpc from the Milky Way, represent significantly different star-forming environments than the Galaxy, at $\sim$ 0.3$\times$ and 0.5$\times$ solar metallicity, respectively. In the MCs, the progenitor types, spectral properties, X-ray morphologies, explosion types and size distribution of the SNR population have all been well characterized in optical, X-ray, and radio wavelengths, revealing a population of $>$ 70 SNRs, $>$ 20 in the SMC, and $>$ 50 in the LMC (Mathewson & Clarke, 1973; Long & Helfand, 1979; Long et al., 1981; Mathewson et al., 1983; Chu & Kennicutt, 1988; Hughes et al., 1998; Smith et al., 2000; Yokogawa et al., 2003; Filipović et al., 2005; Borkowski et al., 2006; Payne et al., 2007; Harris & Zaritsky, 2009a; Badenes et al., 2010; Lopez et al., 2011; Haberl et al., 2012; Maggi et al., 2014, 2016). Of these SNRs, however, $<$ 40% have secured progenitor classifications listed in the literature (Hughes et al., 1995; Rest et al., 2005; Borkowski et al., 2006; Lopez et al., 2009, 2011; Yamaguchi et al., 2014; Maggi et al., 2014, 2016). Thus, despite this breadth of analysis there are still a large number of SNRs that remain without secure classification, and tensions persist over classification of individual sources on the basis of different analysis techniques (e.g. Lee et al., 2011; Lopez et al., 2014; Roper et al., 2015; Maggi et al., 2016), and the extent to which metallicity and/or local star formation histories (SFHs) affect the resultant population (e.g. Maggi et al., 2016).

M31 hosts a population of $\sim$ 150 optically identified SNRs (Blair et al., 1981; Braun & Walterbos, 1993; Magnier et al., 1995; Lee & Lee, 2014a), a small subset ($\sim$ 20) of which are confirmed to be X-ray emitting SNRs from *XMM-Newton* (Sasaki et al., 2012). The extensive *HST* coverage of M31 (Dalcanton et al., 2009, 2012) has also allowed for progenitor masses to be estimated for a subset of CC SNRs on the basis of their surrounding stellar populations. Notably, for the $\sim$ 60 SNRs for which progenitor masses have been estimated in M31 a minimum mass of $\sim$ 7.3 $M_{\odot}$ for core-collapse was found, as well as some possible evidence for a maximum mass limit (Jennings et al., 2012, 2014; Díaz-Rodríguez et al., 2018).

Despite this extensive work, we are still lacking a full picture across all relevant wavelengths connecting SNR progenitors to their environments and the resultant SNRs. Unfortunately, it is still difficult to systematically infer SNR progenitor type due to uncertainty in the evolutionary state of SNRs, selection biases (Badenes et al., 2010), and the confounding effects of SNR ejecta mixing with circumstellar material. Without secured progenitor types for a large population, it is not possible to cleanly measure quantities like the delay-time distribution for SNe (Maoz & Badenes, 2010; Badenes et al., 2010) and disentangle the influence of the effects of binarity versus Type Ia SNe contamination.

1.4.2 High-Mass X-ray Binaries in the Local Group

Studies of resolved HMXB populations in the Milky Way and Local Group galaxies have accumulated hundreds of candidate sources: nearly 100 bright HMXBs of known type in the Milky Way, of which $\sim$ 40 are SG-XRBs, and 60 are Be-XRBs (Liu et al., 2000; Walter et al., 2015); the SMC which contains $\sim$ 120 sources, the vast majority of which are Be-XRBs hosting pulsars (Haberl & Sturm, 2016); and the LMC which contains $\sim$ 40 sources, of which the vast majority again are Be-XRBs (Antoniou & Zezas, 2016), with only a handful of SG-XRBs identified. These populations have been used to constrain and confirm many key evolutionary qualities, such as NS kick velocities, the formation rate of XRBs locally, the X-ray luminosity function (XLF) shape, correlations with host galaxy star formation rate (SFR), and the relation of HMXB formation to parent stellar population age (e.g. Liu et al., 2000; Grimm et al., 2003; Shtykovskiy & Gilfanov, 2005; Coe et al., 2005; Liu et al., 2006; Antoniou et al., 2010; Binder et al., 2012; Mineo et al., 2012; Sturm et al., 2013; Williams et al., 2013a; Walter et al., 2015; Antoniou & Zezas, 2016; Haberl & Sturm, 2016; Laycock et al., 2017).

While these results provide a promising number of HMXB candidates there is still uncertainty in the relative significance of host galaxy properties like SFH and metallicity on the number of systems that move through the various HMXB formation pathways, and how this affects their subsequent evolution into compact object binaries. Because of the aforementioned difficulty in definitively determining the compact object type in the absence of X-ray pulsations or dynamical mass measurements there is uncertainty in the nature of the compact object population, and thus poor constraints for modeling the binary evolution pathways that lead to their formation. To

date most known HMXBs are Be-XRBs and most of these contain accreting neutron stars (Liu et al., 2006; Lutovinov & Tsygankov, 2009). This makes Be-XRBs prime candidates for NS-NS binaries, which themselves are potential progenitors of short-duration gamma-ray bursts, as well as gravitational wave sources. The distinct lack of Be-XRBs known to host BHs is not altogether surprising as the lack of Be-BH XRBs itself can be seen as a consequence of binary evolution; such systems would most likely undergo a merger during a common-envelope phase, and are therefore predicted to be rare (Belczynski & Ziolkowski, 2009). However, the fraction can also be strongly affected by SFH (e.g. Antoniou et al., 2010), and prescriptions for mass loss, so the extent to which this evolutionary pathway is truly disfavored must be further constrained with populations of observed HMXBs in more environments with robust classifications.

Metallicity is also a confounding effect, with theory suggesting that low metallicity environments will effect binary evolution both through mass and angular momentum losses, possibly leading to more massive compact objects and tighter orbits in low metallicity environments (Dray, 2006; Linden et al., 2010). The lack of HMXBs with secured compact objects masses makes this difficult to constrain empirically. A promising avenue in this respect is the ability of *NuSTAR* to separate out compact object type and accretion state for more sources in the LG (e.g. Yukita et al., 2017; Lazzarini et al., 2018).

Thus, while there are hundreds of HMXB candidates that have been identified in the LG to date, there are still open questions as to the effect of SFH, SFR, and metallicity on the evolution pathways that determine the relative importance of each subclass of HMXBs. A more complete sample probing a range of environments will allow for these effects to be disentangled and to forward model to the inferred population of resultant compact object binaries, e.g. NS-NS binaries, NS-BH binaries, and BH-BH binaries.

1.5 The Importance of M33

M33, a late-type Sc spiral and the third most massive galaxy in the LG, is ideally suited to build on and augment these past works. At a distance of 817±58 kpc (Freedman et al., 2001), M33 is close enough that individual sources like SNRs and HMXBs are resolvable. With distance known, these sources can be studied as large populations, without the distance uncertainties that hinder Galactic samples. Further, M33 is close to face-on (angle of inclination, $i = 56° \pm 1°$, Zaritsky

et al., 1989), and has low foreground absorption ($N_H \approx 6 \times 10^{20} cm^{-2}$, Stark et al., 1992), allowing for sources to be resolved across the disk of the galaxy. In addition, the known metallicity gradient, which ranges from roughly solar in the interior to LMC-like at larger galactocentric radii with a break at 3 kpc (Magrini et al., 2007), allows different environments to be probed within the same galaxy by surveying across the disk. Beyond these favorable physical characteristics, M33 has extensive past multiwavelength coverage, making it a prime target for resolved source population studies.

The X-ray source population of M33 in particular has been studied with increasing depth and spatial resolution for nearly 40 years. The first detection of discrete X-ray sources in M33 were made by (Long et al., 1981) using the *Einstein* Observatory. These early observations revealed 11 bright point sources ($L_X > 10^{37}$ ergs s^{-1} at the distance of M33), of which the brightest was the nucleus, whose source of X-ray emission is still an active topic of research today (Merritt et al., 2001; Dubus & Rutledge, 2002; Long et al., 2002; Dubus et al., 2004; Foschini et al., 2004). Since this first survey with *Einstein*, M33's X-ray source population has been characterized by numerous X-ray telescopes with increasingly expansive survey areas, and higher spatial resolution, resulting in order of magnitude increases in detection limits and the number of discrete X-ray point sources known (Markert & Rallis, 1983; Schulman & Bregman, 1995; Long et al., 1996; Haberl & Pietsch, 2001; Pietsch et al., 2003, 2004a; Misanovic et al., 2006; Pietsch et al., 2006; Grimm et al., 2007; Plucinsky et al., 2008; Tüllmann et al., 2011; Williams et al., 2015).

Most recently, deep X-ray surveys by Tüllmann et al. (2011) and Williams et al. (2015) with *Chandra* and *XMM-Newton*, respectively, surveyed out to the D_{25} isophote of M33 with nearly 2 Ms of combined exposure time. Taken together, these surveys reveal well over 1000 discrete X-ray point sources, from the first pulsar observed in M33 (Trudolyubov, 2013; Williams et al., 2015), to unique XRBs (e.g. Pietsch et al., 2009), to a plethora of SNRs (e.g. Long et al., 2010). Furthermore, the decades-long baselines across all aforementioned surveys allow for source characterization on the basis of X-ray variability, both for short- and long-term variable sources (e.g. Williams et al., 2008).

Complementary to the detailed X-ray coverage that exists for M33, there is extensive coverage of the galaxy from ground-based broad-band and narrow-band imaging surveys (e.g. Massey et al., 2006; Neugent & Massey, 2011) to a plethora of archival *HST* observations useful for studying re-

solved stellar populations. These past multiwavelength surveys of M33 from the infrared (2MASS; *Spitzer*, Cutri et al., 2003; Khan et al., 2015), to the ultraviolet (GALEX, Mudd & Stanek, 2015) are useful not only for identifying X-ray point source types via their IR, optical, and UV characteristics, but also offer the unique opportunity for studying X-ray source populations as they relate to their surrounding stellar populations and the ISM.

Narrow-band imaging (e.g. Massey et al., 2006) in particular is useful to delineating H II regions from SNRs, and again allows for characterization of the interaction of the SNR with the surrounding ISM. Resolved stellar populations, both ground-based and from *HST*, offer a strong complement to HMXB studies, as they provide a catalog of potential massive, donor star counterparts to hard X-ray point sources. Resolved stellar populations from *HST* in the vicinities of sources like HMXBs and SNRs can be modeled to reproduced detailed SFHs, providing clues to the mass and energetics of the progenitor system.

To date, M33 boasts one of the largest populations of resolvable, multiwavelength detected SNRs ($\sim$ 220 sources) in any nearby galaxy (Gordon et al., 1998; Long et al., 2010; Lee & Lee, 2014b; Garofali et al., 2017; Long et al., 2018), and given its star formation rate and XLF, a large inferred HMXB population ($\sim$ 100 sources), which prior to this work has remained largely uncharacterized, with only three sources robustly characterized (Long et al., 2002; Pietsch et al., 2004c; Grimm et al., 2005; Pietsch et al., 2006, 2009). Thus, M33 presents a unique opportunity for the multiwavelength characterization of a population of massive star evolution products in a large, star-forming spiral galaxy.

This thesis focuses on the characterization of the X-ray source population in M33 as it relates to massive star evolution. To carry out this aim, I make extensive use of past multiwavelength coverage of M33, including *XMM-Newton*, *Chandra*, and *HST* archival data as described below, in addition to ground-based coverage (e.g. Hectospec, Chapter 5). The specific utility of each data set will be described in detail in the relevant chapters, and I broadly introduce these instruments and data sets as they relate to this thesis below.

1.6 Sources of M33 Observations

In this section I provide details of the instruments and survey data used in this thesis. In Chapter 2 I use a deep *XMM-Newton* survey to characterize the X-ray source population in M33 as a

whole, and in regards to its SNR population specifically in Chapter 3. In Chapters 4–5 I present work on identification and characterization of a population of candidate HMXBs in M33 using a combination of a deep *Chandra* survey of M33, publicly available archival *HST* data, and ground-based spectroscopic follow-up. This section serves as an overview of the survey data, both new and archival, used throughout this thesis, with more detailed discussions for each data set in subsequent chapters.

1.6.1 *XMM-Newton*

Launched in 1999, *XMM-Newton* is one of ESA's cornerstone missions (Jansen et al., 2001), and provides a natural complement to NASA's *Chandra X-ray Observatory*, also launched in 1999, described below. Unlike optical telescopes most X-ray telescopes, like *XMM-Newton* and *Chandra*, are constructed using nested cylindrical (parabolic or hyperbolic) mirrors in a "barrel" shape, giving the telescope a very long focal length. This set-up ensures that the high-energy photons, which are reflected only at large angles of incidence, will hit the mirrors at grazing angles and be effectively focused towards the detector. *XMM-Newton's* three telescopes, each with collecting areas of ~ 1500 cm^2, are "Wolter" telescopes, composed of 58 cylindrical mirrors nested together.

XMM-Newton contains two main X-ray instruments, the three European Photon Imaging Cameras (EPIC), and the Reflection Grating Spectrometers (RGS). For the purposes of this thesis, I will focus on the three imaging cameras: the EPIC pn, and the two EPIC MOS cameras, which are used for both imaging and spectroscopy. The EPIC MOS cameras are each composed of 7 charge-coupled devices (CCDs), while the EPIC pn camera is composed of 12 CCDs, with angular resolution of ~ 6", and a field-of-view of ~ 30' (Strüder et al., 2001; Turner et al., 2001). The EPIC MOS and pn cameras have several different read-out modes, but generally record for each "event" the arrival time, detector location, and photon energy to create event lists for each observation. They are sensitive to energies from 0.2–12 keV, with the EPIC MOS cameras most sensitive to soft X-rays, and the EPIC pn camera most sensitive to harder energies.

The *XMM-Newton* instrumental set-up, and telescopes' large collecting area allows for wide field-of-views to be surveyed with sensitivity to imaging and spectroscopy of both soft and hard X-ray sources. Beyond this, the EPIC pn camera has superior timing resolution: 73.4 μs in full frame mode, 0.3 μs in timing mode, and down to 7 μs in burst mode. This timing resolution makes

it possible for light-curves to be constructed for variable sources.

Over the course of nearly two decades of operation *XMM-Newton* has made astounding contributions to the field of high-energy astrophysics, from insights into galaxy cluster formation, to the accretion physics around distant active galactic nuclei, to the nature of relatively nearby accreting compact objects. Most recently, the third *XMM-Newton* serendipitous source catalog was released, with nearly 400,000 discrete X-ray point sources, and spectra and light curves for some 130,000 of the brightest sources.

In this thesis, the data I employ come from a relatively recent *XMM-Newton* survey of M33 (Williams et al., 2015). The catalog contains nearly 1300 discrete X-ray point sources, which are analyzed in more detail in Chapters 2–3. A deep *XMM-Newton* image of the survey area with at least 40 ks of exposure is reproduced from Williams et al. (2015) in Figure 1.1 below.

1.6.2 *Chandra*

The *Chandra X-ray Observatory*, one of NASA's flagship missions, is a space-based X-ray telescope that has probed the high-energy sky at unprecedented angular resolution (0.5") for nearly 20 years. Like *XMM-Newton*, *Chandra*, which launched in 1999, is a Wolter telescope, with an assembly of four nested mirrors for focusing X-ray photons, and a collecting area of 0.04 m^2.

Chandra has two main instruments, the Advanced CCD Imaging Spectrometer (ACIS), and the High Resolution Camera (HRC). For the purposes of this thesis, I will focus on the ACIS instrument, which consists of 10 CCDs and probes energies from 0.2-10 keV in both imaging and spectroscopy. *Chandra* provides a highly complementary telescope to *XMM-Newton* given its incredible angular resolution (0.5") for localizing X-ray point sources. Over the course of its nearly 20 year mission, *Chandra* has provided exquisitely resolved images and spectra of nearby supernova remnants, flares from the supermassive black hole at the center of the Milky Way, evidence for dark matter in galaxy cluster collisions, and more recently the X-ray afterglow of the first multi-messenger astrophysical source, GW170817.

In this thesis, I use *Chandra* data from a deep (1.4 Ms) *Chandra* survey of M33 (ChASeM33 Tüllmann et al., 2011), which contains ~ 660 sources. A three color image from the survey is shown below in Figure 1.2, depicting the richness of point sources present in the galaxy. In Chapters 4–5 I employ the ChASeM33 data for localizing X-ray point sources with high precision such that visible

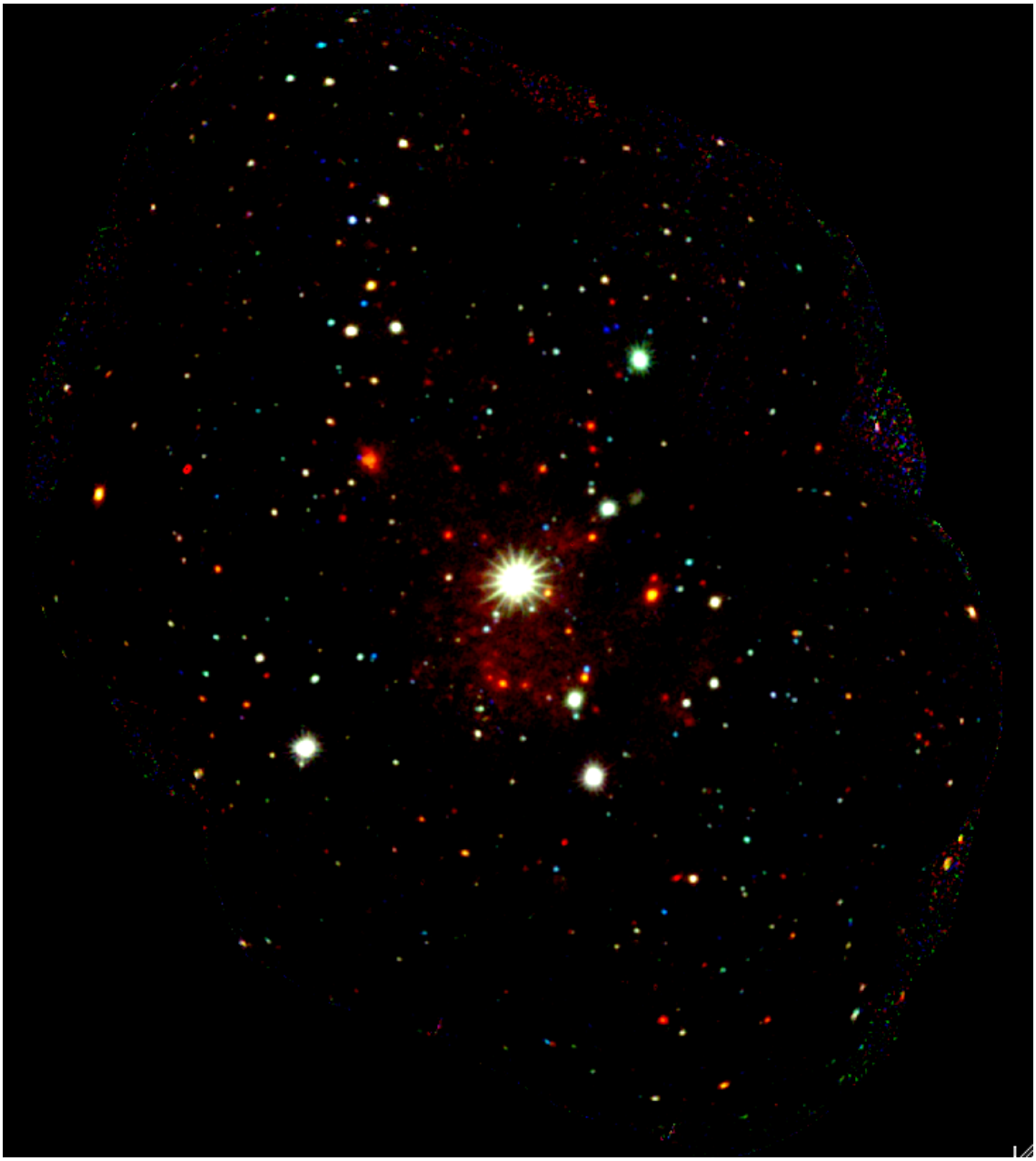

Figure 1.1: Three color image of all survey area with at least 40 ks of exposure time reproduced with permission from Williams et al. (2015). Red is 0.2-1.0 keV (soft), green is 1-2 keV (medium), and blue is 2-4.5 keV (hard).

counterparts can be identified from *HST*, in addition to analyzing the spectral characteristics of a select subset of bright sources. Of the $\sim$ 660 sources from Tüllmann et al. (2011), $\sim$ 40% have overlapping *HST* coverage, as shown in Figure 1.3.

1.6.3 *Hubble Space Telescope*

The *HST* launched in a low-Earth orbit in 1990 and has taken over a million observations to date. As one of NASA's great observatories, *HST* has continued to advance our understanding of the cosmos across a broad range of astronomical fields for nearly three decades, from studies of Pluto and its moons to measurements of the accelerating expansion of the universe. *HST's* currently operational instruments allow the telescope to observe targets in the near-UV, visible, and near-IR. Its location above the Earth's atmosphere and 2.4-m diameter mirror give it an unprecedented angular resolution of < 0.1", and coupled with its high pointing accuracy (0.007") *HST* is able to view some of the first galaxies 10 billion light-years away, as well as resolve crowded stellar regions in nearby galaxies in our Local Volume (e.g. Dalcanton et al., 2009, 2012).

HST's monumental contributions to a wide array of astronomical disciplines has been aided over the years by a suite of 12 instruments, all with complementary abilities and science goals. For the purposes of this thesis I will focus on two of the longest running optical cameras in use on *HST*, beginning with the Wide Field Planetary Camera 2 (WFPC2), which was installed in 1993. This instrument was composed of four CCDs arranged in a "bat-wing" configuration with three wide-field cameras (resolution $\sim$ 0.1", FOV: 80"x80") and one higher-resolution "planetary camera" (resolution $\sim$ 0.05", FOV: 36"x36"). The WFPC2 consisted of 48 filters covering from the near-UV to near-IR with highest sensitivity in the optical range, and was in use through 2009 (Holtzman et al., 1995b,a).

The Advanced Camera for Surveys (ACS) was installed in 2002 as a successor to some of *HST's* original instrumentation. The ACS Wide Field Camera (WFC) consists of two CCDs arranged as a rhombus. The total field of view is 202"x202", with an angular resolution of $\sim$ 0.05", allowing for large areas to be covered at high resolution. The ACS WFC consists of a set of 38 filters covering a wavelength range from the UV to the near-IR. We list all WFPC2 and ACS WFC filters used as part of this thesis along with their associated central wavelengths, bandwidths, and equivalent filters in other systems (if any) in Table 1.1.

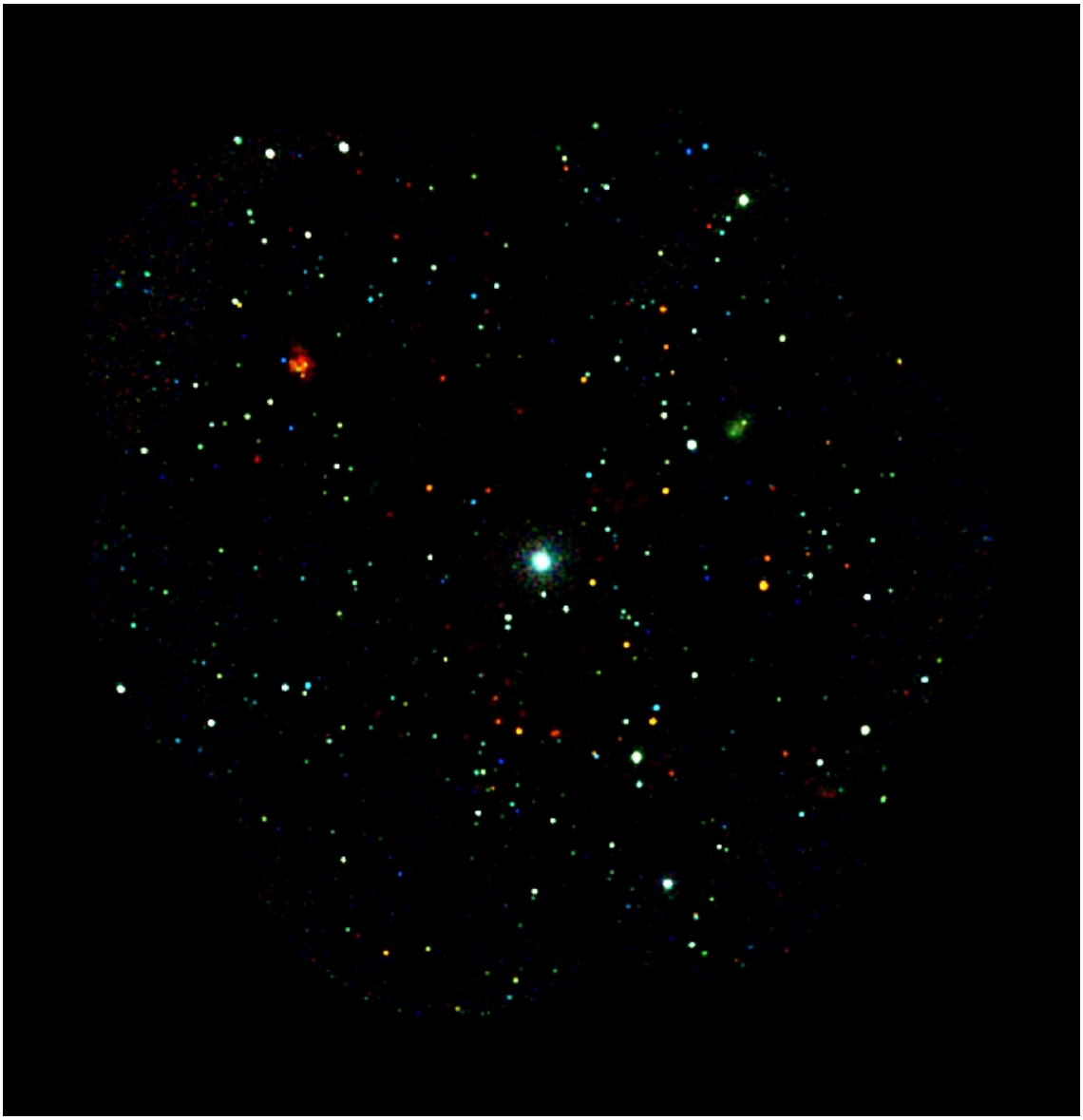

Figure 1.2: Three color mosaic image of the ChASeM33 survey (Tüllmann et al., 2011). Red is 0.35–1.0 keV (soft band), green is 1.0–2.0 keV (medium band), and blue is 2.0–8.0 keV (hard band).

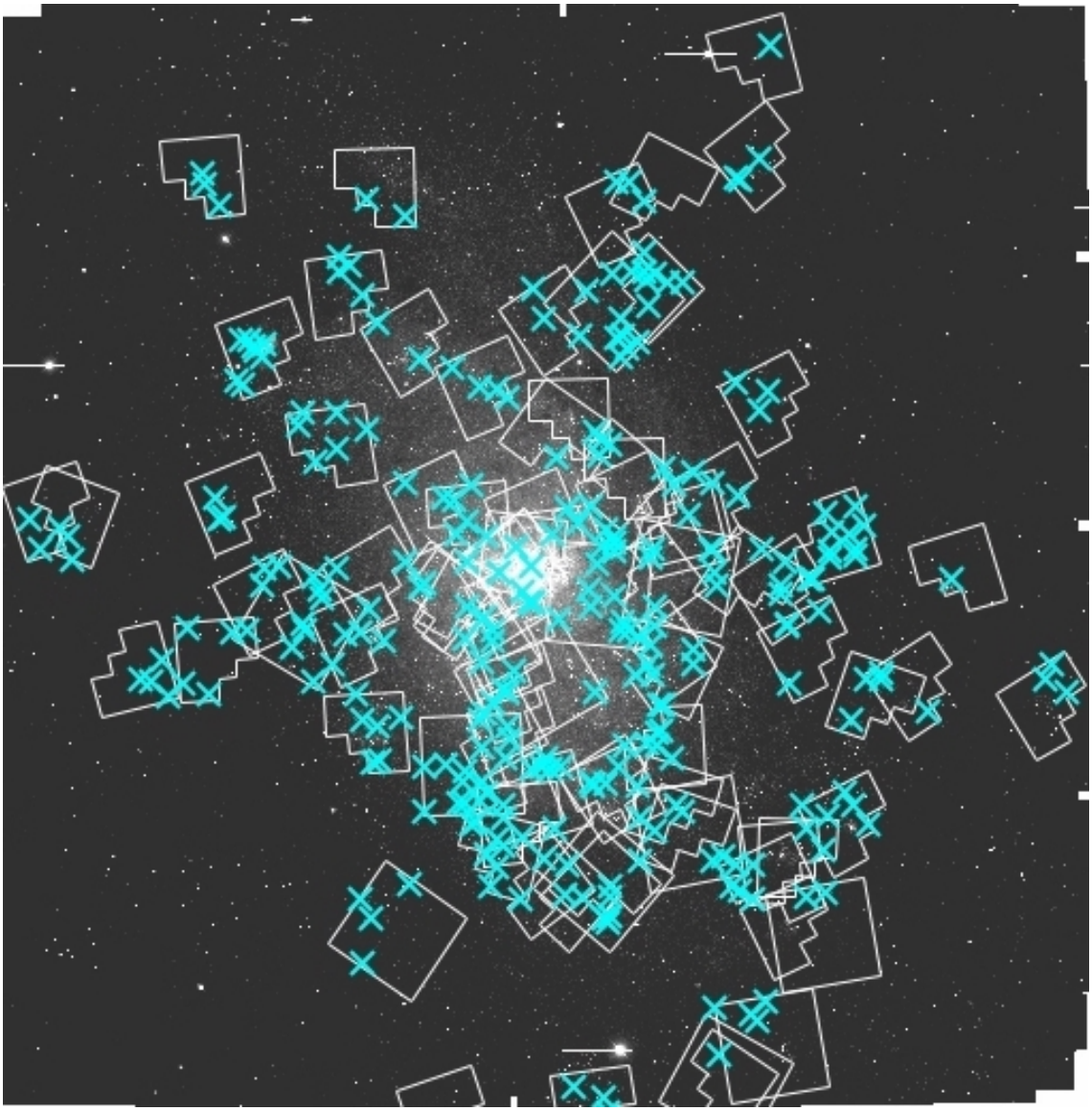

Figure 1.3: R band Local Group Galaxy Survey (Massey et al., 2006) image of M33 overlaid with all 89 archival *HST* fields (grey). Cyan crosses are X-ray sources from Tüllmann et al. (2011) that fall within the current archival *HST* coverage. There are 270 X-ray sources covered by 89 *HST* fields.

Table 1.1: *HST* filters with central wavelengths, bandwidth, and equivalent filters as used in this thesis.

Filter	Central Wavelength (nm)	Bandwidth (nm)	Equivalent Filter
F336W	334.4	37.4	Johnson-Cousins U
F439W	431.1	47.3	Johnson-Cousins B
F475W	476.0	145.8	SDSS g
$F555W_{wfpc2}$	543.9	122.8	Johnson-Cousins V
$F555W_{wfc}$	534.6	119.3	Johnson-Cousins V
$F606W_{wfpc2}$	599.7	150.2	Broad V
$F606W_{wfc}$	590.7	234.2	Broad V
$F814W_{wfpc2}$	801.2	153.9	Johnson-Cousins I
$F814W_{wfc}$	833.3	251.1	Johnson-Cousins I

The subset of *HST* data employed in this thesis includes all available archival *HST* data in M33 with coverage in at least two broad-band filters. This amounts to 89 fields, which overlaps $\sim$ 40% of deepest X-ray survey of M33 from *Chandra* (Tüllmann et al., 2011). The full archival *HST* coverage of M33 (white regions) and its overlap with the X-ray point source catalog (cyan crosses) used in Chapter 4 is shown in Figure 1.3. The use of this data, particularly for characterizing the stellar populations in the vicinities of candidate HMXBs is discussed extensively in Chapter 4.

Outline of Thesis

This dissertation focuses on the characterization of massive stars as probed via X-ray source populations, as described above. This Chapter has already delved into the nature of SNRs and HMXBs as they relate to massive star evolution, and discussed the utility of X-ray observations of these sources in the Local Group, and M33 in particular. Furthermore, it has introduced the multiwavelength data sets employed in this thesis to study the X-ray source population of M33.

In Chapter 2 I will discuss the characterization of the X-ray source population of M33 from a deep *XMM-Newton* survey on the basis of X-ray colors, variability, and luminosity function. This survey forms the basis for delving in the X-ray source population of M33 as it relates to massive stars.

Next, in Chapter 3 I describe the results of an *XMM-Newton* survey of the SNR population of M33. The soft sensitivity and large field of view of the survey provide the largest sample of multiwavelength confirmed SNRs in M33 to date for which we can compare global population characteristics to host galaxy environment.

In Chapters 4–5, I focus on the characterization of the HMXB population in M33 using a combination of *Chandra* and *HST*. In particular, the archival *HST* data is crucial for analyzing the stellar population surrounding each HMXB candidate such that we can determine preferred formation timescales for HMXBs in the environment of M33. I also detail the multiwavelength source properties for a subset of unusual HMXB candidates, on the basis of their optical, ultraviolet, and infrared colors, their X-ray and ground-based spectra, where available.

To close, I provide a brief discussion and summary of this thesis work in the context of future studies.

Chapter 2:

X-ray Source Populations as Tracers of Massive Stars

2 The X-ray Source Population of M33 as Seen by *XMM-Newton*

Material in this chapter was previously published in collaboration with Benjamin F. Williams, Brian Wold, Frank Haberl, William P. Blair, Terrance J. Gaetz, K.D. Kuntz, Knox S. Long, Thomas G. Pannuti, Wolfgang Pietsch, Paul P. Plucinsky, and Frank P. Winkler in the May 2015 edition of the Astrophysical Journal Supplement Series ((Williams et al., 2015); ©2015 American Astronomical Society), and is reproduced below with permission of the American Astronomical Society.

2.1 Introduction

In tracing the high-energy populations of galaxies, X-ray surveys reveal a plethora of interesting sources. At Galactic distances X-ray point sources may be cataclysmic variables, X-ray emitting massive stars and colliding wind binaries, low-mass X-ray binaries ([LMXBs], compact objects accreting from low-mass stars), HMXBs, or SNRs. At the distance of LG galaxies current X-ray observatories have the sensitivity to probe sources intrinsic to LG galaxies like LMXBs, HMXBs, SNRs, and colliding wind binaries, as well as foreground flaring stars, and background active galactic nuclei (AGN) and quasi-stellar objects (QSOs). Thus, extragalactic surveys in particular trace not only massive star evolution products (e.g. SNRs, HMXBs, and colliding wind binaries), but also the evolution of compact objects in binaries (e.g. LMXBs and HMXBs). In this way, observations of extragalactic X-ray sources are an integral piece of the puzzle for understanding massive star and binary evolution.

X-ray surveys of LG galaxies, such as M31, M33, and the MCs are key understanding the effects of host galaxy properties, such as metallicity and SFR, on X-ray source populations. In particular, M33, as discussed in Chapter 1, is an ideal target for studies of X-ray populations, as sources such as XRBs and soft, diffuse SNRs are resolvable at this distance. With advances in telescope design, M33 has been studied for decades in detail in X-rays, revealing an X-ray source population with a abundance of intriguing variable sources (e.g. Williams et al., 2008), a large population of SNRs (Dodorico et al., 1980; Long et al., 1990; Gordon et al., 1998; Long et al., 2010; Lee & Lee, 2014b; Garofali et al., 2017), and a rich population of candidate HMXBs

(Grimm et al., 2005, 2007). However, many of the past X-ray surveys have not allowed for in-depth characterization of individual sources on the basis of spectral characteristics, or measurement of a deep, intrinsic luminosity function, owing to their relatively short exposures ($\sim$ 10 ks) taken over long time baselines in order to survey large swathes of the galaxy (Pietsch et al., 2004a; Misanovic et al., 2006).

Most recently, a deep *Chandra* X-ray survey covering the central 15' of M33 with observations totaling 1.4 Ms generated a catalog of 662 discrete X-ray sources (Tüllmann et al., 2011, hereafter T11). In this Chapter, I extend these results making use of the large field-of-view (FOV) and higher soft sensitivity of *XMM-Newton* to characterize the results of a survey complementary to that of T11. The *XMM-Newton* survey is similar in depth to T11 but extends beyond the D_{25} isophote of M33, and has higher sensitivity in the soft band. This data was used in Williams et al. (2015, hereafter W15) to identify and characterize a number of new X-ray sources in M33.

Herein I present results on the characterization of the X-ray source population of M33 as seen with the deep *XMM-Newton* survey of W15. The survey is comprised of a deep 8 field mosaic of M33 that extends beyond the D_{25} isophote, and probes down to a limiting unabsorbed flux of 5×10^{-16} erg cm^{-2} s^{-1} ($L > 4 \times 10^{34}$ erg s^{-1}) in the 0.2–4.5 keV band. This extensive coverage and high soft sensitivity of this survey allows for the characterization of 1296 individual point sources in the 8 fields. These sources are matched to previous X-ray catalogs of M33 to note variable sources. In addition, I use the extensive source catalog to construct hardness ratios from custom X-ray colors to search for new soft sources, analyze the radial density profile of the sources, and characterize the XLF.

The remainder of this chapter is organized as follows: a brief description of the data and data reduction techniques from W15 is presented in Section 2.2. Classification of soft sources on the basis of custom hardness ratios (HRs) is discussed in Section 2.3. In Section 2.4 I discuss source variability based on matching the catalog of W15 to previous X-ray catalogs. In Section 2.5 I discuss the characteristics of the source population, namely the radial density distribution of sources, and the XLF. Finally, I present discussion and a synopsis for this chapter in Section 2.6.

2.2 Data

The W15 survey consists of an 8 field *XMM-Newton* mosaic of M33 with a summed exposure time of 900 ks extending beyond the D_{25} isophote and to a limiting 0.2-4.5 keV luminosity of 4×10^{34} erg s^{-1} at the distance of M33. The data consist of seven new fields with observation dates ranging from 2010 July 09 to August 15 and from 2012 January 10 to January 12, and one archival field with observation dates ranging from 2010-01-07 to 2010-02-24. Below, we briefly describe the data reduction, source detection, and final source catalog culling and selection process. Full details, including how source detection was carried out specifically for the multiple, overlapping fields that comprised this survey, can be found in W15.

2.2.1 Source Detection

The data were first filtered for background flares via the creation of good time intervals (GTIs), and clean images were created by correcting for out of time (OOT) events. The event lists were flagged in the standard way to exclude events near bad pixels or the CCD edge. Initial source detection on the full-stack of images was performed using the SAS tasks `emosaicproc` and `emosaicprep`. The task `emosaicproc` itself runs the task `eboxdetect` to determine source positions. These positions were then fed iteratively to the task `emldetect` to converge on a list of source detections. This source list was further culled on the basis of cuts determined using a combination of source S/N and detection likelihood. This analysis results in a catalog of 1296 sources. Finally, `emldetect` was run on the individual bands and cameras of interest, i.e. for both PN and MOS cameras in the 0.2-0.5, 0.5-1.0, 1.0-2.0, and 2.0-4.5 keV bands.

We next determined source fluxes by converting the on-axis equivalent count rates returned by `emldetect` into flux values using appropriate energy conversion factors (ECFs). ECFs were determined for the individual bands and instruments (PN and MOS) using `XSPEC` (Arnaud, 1996) assuming a power-law spectrum with photon index 1.7 and absorption 6×10^{20} cm^{-2}, chosen to match the spectral model assumed in Misanovic et al. (2006). The ECFs provide the unabsorbed fluxes assuming this spectrum and are listed in Table 2.1 for reference.

Table 2.1: Unabsorbed ECF values for different energy bands and instruments. Units are 10^{11} cm^2 erg^{-1}.

Energy Band (keV)	MOS1 Med Filter	MOS2 Med Filter	PN Thin Filter
0.2-0.5	0.5009	0.4974	2.7709
0.5-1.0	1.2736	1.2808	6.006
1.0-2.0	1.8664	1.8681	5.4819
2.0-4.5	0.7266	0.7307	1.9276

2.2.2 Spurious Sources

X-ray detectors are susceptible to false detections in the form of hot pixels or OOT streaks. To search for and flag such sources we inspected by eye all sources returned from `emldetect` in each individual observation using soft band images in detector coordinators. The soft band is of particular use in searching for false detections as it is most susceptible to hot pixel artifacts (Haberl et al., 2012).

We pre-flagged some sources for our visual inspections on the basis of detection likelihood criteria. To catch possibly hot PN pixels, we pre-flagged any source with soft band PN detection likelihood that was much higher than the value of any other band/camera detection likelihood. In addition, we noted any sources that had much higher detection likelihood in either MOS1 or MOS2 than any other band camera, as such entries may be artifacts due to high noise levels in the MOS CCDs. In particular, 75 sources in the final catalog were flagged as soft-band PN or OOT artifacts, and 138 sources were flagged as MOS artifacts.

In addition to these criteria, we found some sources that were not detected in all cameras in a given band, or that had combined flux measurements from all band/cameras that were more than a factor of 2 discrepant from the individual band/camera measurements. These sources are not considered spurious, but instead have less reliable total flux measurements than the rest of the catalog.

In total, we determined four different origins for spurious sources to flag. We found 27 sources that appeared to be due to hot pixels ("ip" flag), 29 sources that were associated with streaks from nearby bright sources ("is" flag), 138 sources that had high detect likelihoods in only one MOS camera ("m" flag), and 35 sources that had higher detection likelihood in the PN soft band

than any other band camera ("pn" flag). We also created two flags for sources with discrepant flux measurements. There were 167 sources that were not measured in all three cameras ("s" flag), and 44 sources that had total source counts more than a factor of two different from the sum of source counts measured in individual band cameras ("t" flag), suggestive of a problem with the merged measurement, or total counts in an individual band more than a factor of two different from the sum of the source counts measured in the individual cameras for that band, likely due to a limitation of the combining algorithm. Flagging such sources allows for quality cuts to be made for various analyses of the catalog.

2.3 Hardness Ratios

Hardness ratios are often used to discriminate between X-ray source types. By comparing X-ray fluxes across different bands one may hope to isolate different spectral shapes for sources with too few counts for reliable spectral fitting. We investigate the HRs of sources in our catalog computed using two different sets of bands. First, we computed the HRs from source fluxes for all unflagged sources, sources with the "s" or "t" flag, and flagged sources matched to T11 counterparts in the following bands: 0.2-1.0 keV (soft), 1.0-2.0 (medium), and 2.0-4.5 keV (hard). The HRs in these bands are computed from unabsorbed fluxes assuming a power-law spectrum with a photon index of 1.7, and absorption of 6×10^{20} cm^{-2}, and are computed using the following formulae:

$$HR1 = \frac{M - S}{S + M + H}, HR2 = \frac{H - M}{S + M + H} \tag{1}$$

where S, M, and H are the fluxes in the bands defined above.

The HRs in these bands are plotted in Figure 2.1 for the subset of sources mentioned above with > 50 counts. The triangular region denotes sources with positive flux measurements (or upper-limits in the cases of non-detections). The upper-right hand panel of Figure 2.1 displays HRs computed from count rates, where the fluxes in the left-hand panel are simply the count rates multiplied by the ECFs. The points are color-coded based on the number of source counts in the detection, with the SNRs in the sample outlined in purple. The SNRs stand out as a markedly soft (HR1 $<$ -0.3) population compared to the rest of the distribution. The distribution of sources ranging from soft, thermal sources (such as SNRs) to hard, absorbed power-law sources (e.g. XRBs) is evident in the sources with the most counts (> 300 counts). The spread of points

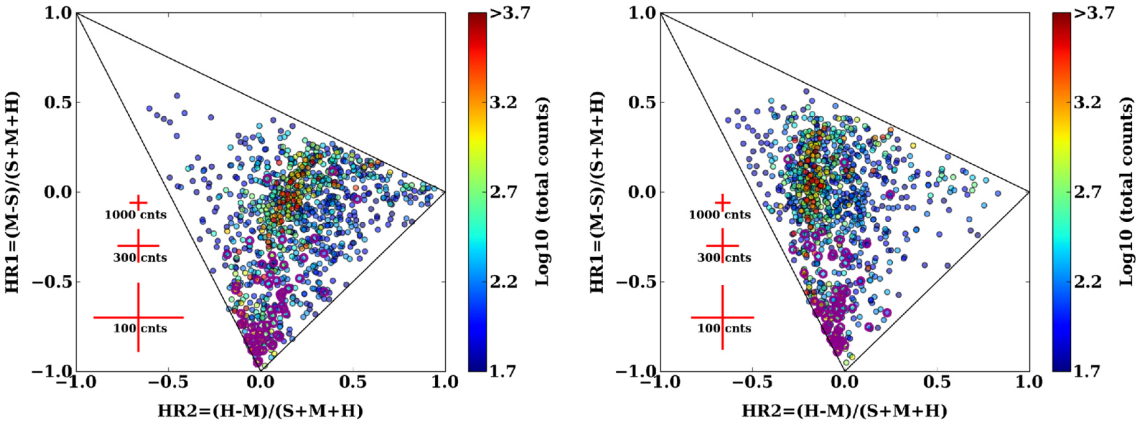

Figure 2.1: *Left*: hardness ratios from fluxes in the 0.2-1.0, 1.0-2.0, and 2.0-4.5 keV bands of all sources with > 50 source counts. These fluxes use the ECFs in Table 2.1, which assumes a power-law spectrum with index 1.7 and absorption 6×10^{20} cm^{-2}. H = 2.0-4.5 keV flux; M = 1.0-2.0 keV flux; S = 0.2-1.0 keV flux. Upper limits were applied in bands with 0 counts to calculate ratios, so that no sources fall outside of the area allowed by positive flux measurements. Blue to red colors show the number of counts in the measurement. Known SNRs are highlighted with purple circles. Approximate uncertainties for a range of total counts are shown with the red crosses. *Right*: same as left, but using ratios calculated from count rates.

around this sequence is due partially to measurement uncertainties (representative error bars in red), but also potentially to intrinsic differences in the assumed spectrum, and hydrogen column density.

To further separate the soft sources, we compute the HRs from source counts using custom HRs in bands < 2 keV. These ratios were developed specifically for use with *XMM-Newton* data to take advantage of the soft-band sensitivity. We compute these ratios using counts to make the same comparisons as Pietsch et al. (2004a) for separating SNRs and foreground stars from sources with harder spectra. They are computed as follows:

$$HR1_{\rm C} = (SCTS_{0.5-1.0keV} - SCTS_{0.2-0.5keV})/SCTS_{0.2-1.0keV} \quad (2)$$

$$HR2_{\rm C} = (SCTS_{1.0-2.0keV} - SCTS_{0.5-1.0keV})/SCTS_{0.5-2.0keV} \quad (3)$$

We only include sources with enough counts in these bands to have uncertainties on HR1$_{\rm C}$ and HR2$_{\rm C}$ of ≤ 0.2. In Figure 2.2 we outline a box that isolates SNRs well, as previously noted by Pietsch et al. (2004a) and verified here by the relative isolation of the SNRs (cyan triangles) from Long et al. (2010). Within this box are 89 sources (orange dots) not previously classified as SNRs

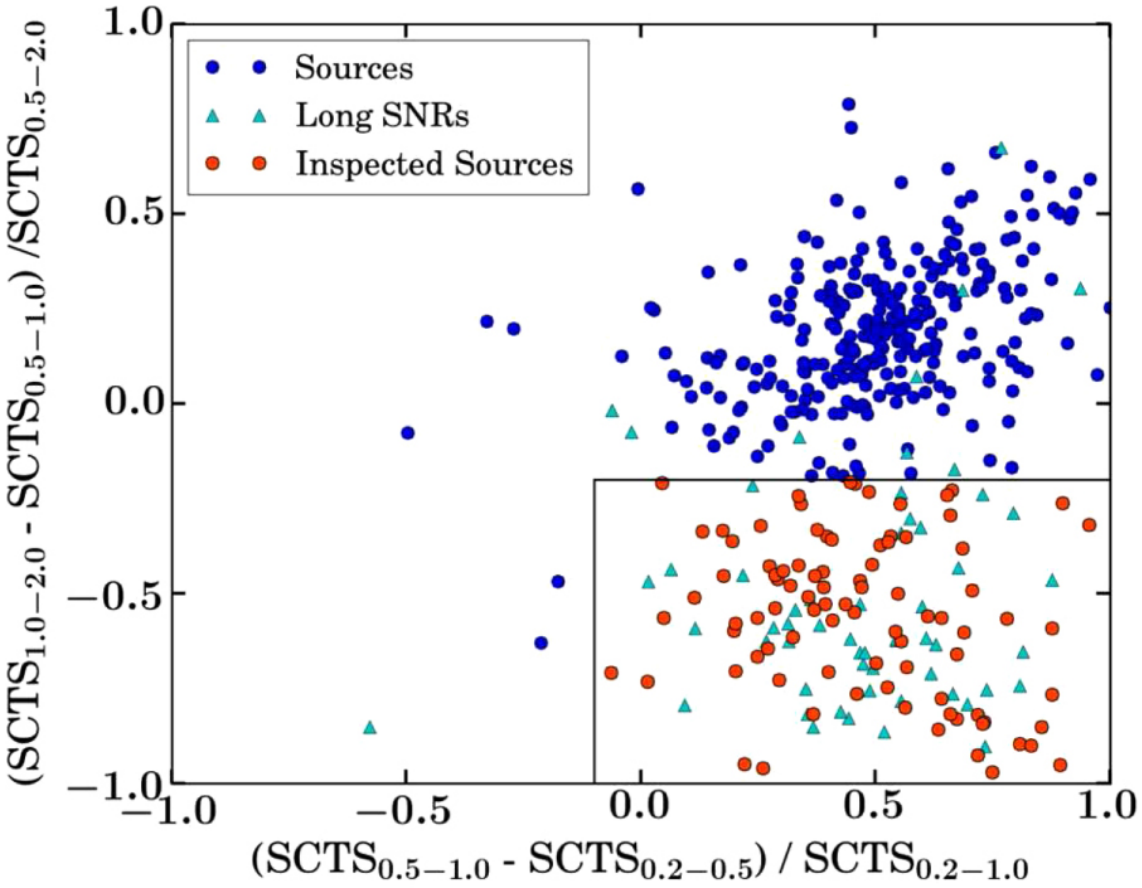

Figure 2.2: Hardness ratio from source counts (SCTS) in the 0.2-0.5, 0.5-1.0, and 1.0-2.0 keV bands of all sources with hardness ratio uncertainties ≤ 0.2 based on the number of counts in these bands. The black box indicates the region where most Long et al. (2010) SNRs (triangles) lie. The other sources in this box, indicated by the 89 orange dots, were not in the Long et al. (2010) catalog. These 89 were all investigated in optical images, and classified as SNRs if they coincided with gas emission or foreground stars if they coincided with a bright star. Sixty-two of the 89 remain unclassified.

or foreground stars. To further discern the nature of these soft sources, we visually inspected the source locations in the optical emission line and broadband images from the Local Group Galaxy Survey (LGGS; Massey et al., 2006). Those sources corresponding to bright stars are classified as foreground stars, while those sources corresponding to extended Hα shells are classified as SNRs. There were 23 foreground stars that were previously unclassified, four SNRs that were previously unknown, and confirmation of one of the brightest X-ray SNRs in M33 found via this analysis. Sixty-two of the 89 sources corresponding to orange dots remained unclassified after inspecting the optical data. The SNRs, and in particular the newly X-ray detected SNRs that resulted from this analysis, will be discussed in more detail in Chapter 3.

2.4 Source Matching & Variability

Long-term variability may be indicative of sources such as foreground flaring stars, intrinsic M33 sources in outburst (e.g. HMXBs and LMXBs), or possibly long-term variable background AGN. For this reason, we match the sources in the *XMM-Newton* catalog of W15 to all previous X-ray surveys of M33 to search for sources that show evidence of long-term variability.

2.4.1 Catalog Matching

We matched the sources from the catalog of W15 with the catalogs of Misanovic et al. (2006, hereafter M06) and T11 using the IDL software package `match_xy` in the Tools for ACIS Review and Analysis TARA package (Broos et al., 2007). This package determines the most likely match for each source in each catalog, and also reports sources that were not matched. The matching algorithm tests pairs of sources for spatial coincidence, i.e. that the sources are random samples drawn from Gaussians with identical means and variances. For the variances we assign the positional errors on the sources in each catalog. After computing individual source matches, the algorithm also returns the relative shift between the catalogs that maximized the number of source matches. In addition, the package has the advantage of providing visualization of matches via ds9 region files, forcing one-to-one matching, and allowing individual position errors to be specified (Broos et al., 2010). The `match_xy` package has been used by Broos et al. (2011) to match the Chandra Carina Complex Project catalog sources to their counterparts. Any failures in matching result in spurious matches and missed matches, which we address below.

Comparing the positions of pairs of matched sources, we found that the T11 positions were more precise than those of W15, and that we could improve the absolute astrometry of the W15 catalog by slightly shifting the positions of the entire catalog by +0.1" in R.A. and +0.7" in decl. After applying these shifts, the median difference between the R.A. and decl. of the matched sources is zero, with an associated 1σ uncertainty of 0.07" in both R.A. and decl. The rms of the matched sources was 2.2" and 1.7" in R.A. and decl., respectively, prior to shifting, and 2.2" and 1.6" in R.A. and decl., respectively, after shifting.

The positional uncertainties recovered straight from `emldetect` resulted in `match_xy` returning many unmatched sources that were clearly re-detections of T11 sources. For these sources to be properly matched we continued to add systematic error to the positional errors returned from `emldetect` until we matched all "close" unmatched sources to the counterpart found by eye but originally missed by the algorithm. Each time more systematic error was introduced, we checked the validity of the new matches and made certain that no obvious spurious matches were being introduced. We found that the matching routine performed best when we added a constant 1.5" to all of our position uncertainties. This result suggests that the uncertainties from `emldetect` can often be underestimated, especially when simultaneously measuring multiple observations with offset aimpoints. This extra uncertainty is included in the positional uncertainties reported in the final W15 catalog.

The well-tested matching routine from Broos et al. (2007) also allowed us to look for unmatched sources in regions that overlapped between various X-ray surveys of M33. This included matching the full catalog from W15 with the full catalog of M06, and with that of T11 for the area of the W15 catalog that was inside the T11 footprint. Figure 2.3 shows the number of unmatched sources as a function of S/N of the detection. Of the 1296 sources in the W15 catalog, 810 were unmatched to either the T11 or M06 survey.

We briefly break down the matching results in the following way: *Chandra* sources from T11 matched to W15, sources from W15 in T11 footprint not matched to *Chandra* sources, and sources from M06 matched to W15. Of the 662 *Chandra* sources in the T11 catalog, 348 were matched to the *XMM-Newton* sources from W15, while the other 314 were not detected by W15. Inside the T11 footprint, the W15 catalog contains 280 sources that did not match to any sources in T11. All of these sources have fluxes that were above the Chandra sensitivity limit during the observations

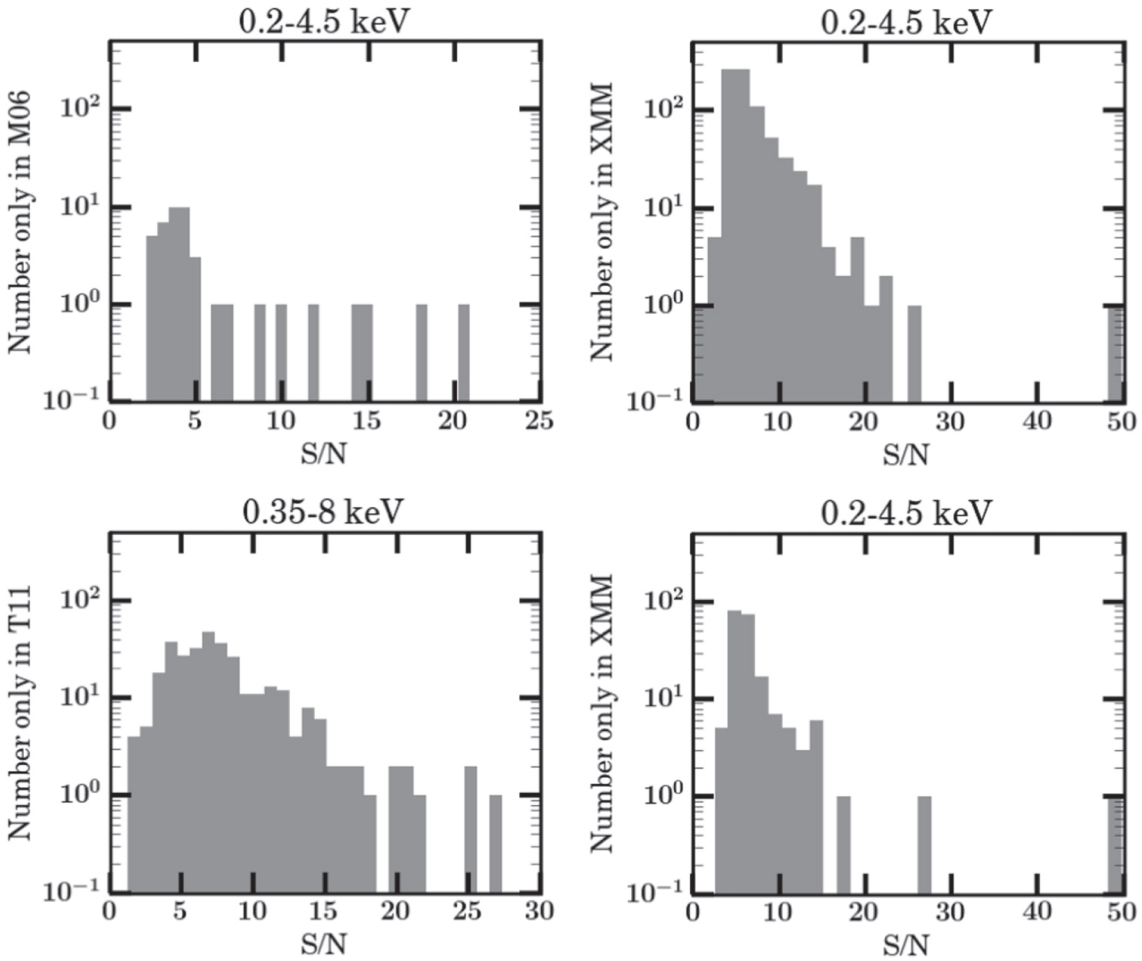

Figure 2.3: Unmatched sources as a function of signal-to-noise ratio of the detection in the three matched catalogs (M06, T11, W15). *Upper-left*: S/N of sources in M06 unmatched to W15. *Upper-right*: S/N of sources in W15 unmatched to M06. *Lower-left* : S/N of sources in T11 unmatched to W15. *Lower-right*: S/N of sources in W15 within the T11 footprint, but unmatched to any T11 source.

of W15; however, only 207 of these are not flagged as possible artifacts in W15 (see Section 2.2). Of the 350 sources in the M06 catalog, 306 were matched to W15 sources. Of these matched sources from W15, 162 were also matched to T11 sources. Thus of the 810 W15 sources that are new detections unaccounted for in these previous surveys, 280 are inside of the T11 footprint, and 207 are not flagged as possible artifacts. The other 542 unmatched sources are outside of the T11 footprint, and 425 of these are not flagged as possible artifacts.

2.4.2 Long-term Variability and Transients

With the W15 catalog matched to previous surveys of M33 as discussed above, we next searched for transient sources which were not detected in at least one survey where they should have been above the detection limit. In addition, we were able to assess long-term source variability through comparison of fluxes between catalogs. We found 51 sources that varied with $> 5\sigma$ significance between surveys and 21 sources detected only by W15 that were bright enough in W15 to require a factor of 10 change in brightness from previous surveys, for a total of 72 sources in our catalog with significant long-term variability.

First, we compare the catalog of W15 with the catalog of M06. As shown in the top panels of Figure 2.3 the lower S/N sources from W15 were not detected in the survey of M06. This result was expected, as the data from W15 are significantly deeper. However, there are five sources in the catalog of W15 with S/N > 20 that were not seen by M06. Three of these sources were matched to sources in T11, one is a known pulsar transient (Trudolyubov, 2013), and the fifth is just outside the observations of M06. On the other hand, eleven M06 sources with S/N > 5 in their catalog were not seen in our observations, which suggests variability by a factor of at least 10 in eight cases.

We next compare the catalog of W15 to the catalog of T11 inside the area common to both surveys. Here, we expect the data of T11 to be deeper, and thus expect that low S/N sources in their data will not be present in the catalog of W15. The bottom panels of Figure 2.3 display this comparison between W15 and T11. We find that four of the 41 sources with S/ N > 12 in T11 require variability in flux by a factor >10 to explain non-detection in W15. These sources, along with all other sources that required variations in flux by a factor > 10 between catalogs to explain non-detections are provided in Table 2.2.

Table 2.2: Possible Transients in M33 from *XMM-Newton*. Column 1 is the source ID number in M06, column 2 is the source ID in T11, column 3 is the source ID in W15, column 4 is the peak flux in erg cm^{-2} s^{-1} as measured in either of the three catalogs (M06,T11,W15), column 5 is the limit on the flux for the source to have not been observed in one or more catalogs, column 6 is the ratio between peak flux and flux limit, and column 7 is the peak S/N as measured in either M06, T11 or W15.

M06	T11	Source	Peak (erg cm^{-2} s^{-1})	Limit (erg cm^{-2} s^{-1})	Ratio	Peak S/N
41	···	···	6.56e-14	<8.95e-16	73.30	18.25
96	···	···	2.76e-13	<1.38e-15	200.12	20.89
134	···	···	1.59e-13	<3.12e-15	50.90	15.00
149	···	···	1.21e-14	<1.04e-15	11.68	5.08
180	···	···	3.63e-14	<1.66e-15	21.88	6.86
207	···	···	1.10e-13	<1.19e-15	92.79	14.44
246	···	···	1.81e-14	<1.53e-15	11.82	11.71
296	634?	···	5.29e-14	<1.32e-15	40.07	8.45
···	13	···	1.10e-14	<8.50e-16	12.98	14.15
···	26	···	9.70e-15	<9.16e-16	10.59	12.18
···	233	···	1.41e-14	<1.24e-15	11.37	20.05
···	283	···	1.96e-14	<1.43e-15	13.73	25.01
···	···	712	4.83e-14	<3.00e-16	161.10	49.80
113	···	426	5.39e-14	<3.00e-16	179.81	26.80
228	···	859	1.03e-14	< 3.00e-16	34.20	14.22
285	···	1032	7.07e-15	<3.00e-16	23.58	11.72
236	···	882	6.98e-15	<3.00e-16	23.26	12.39
···	···	633[a]	6.41e-15	<3.00e-16	21.37	12.83
···	···	551	1.30e-14	< 3.00e-16	43.30	14.38
···	···	556	1.91e-14	<3.00e-16	63.82	13.80
255	···	940	1.13e-14	<3.00e-16	37.83	13.65
312	···	1141	8.23e-15	< 3.00e-16	27.45	10.80
···	···	887[a]	5.11e-15	<3.00e-16	17.03	10.31
···	···	916	1.26e-14	<3.00e-16	41.89	12.15
···	···	17	8.49e-15	<3.00e-16	28.30	10.99
206	···	784	3.45e-15	<3.00e-16	11.50	8.06
···	···	1043	4.64e-15	<3.00e-16	15.47	8.62
···	···	637	4.34e-15	<3.00e-16	14.46	8.99
···	···	748	8.25e-15	<3.00e-16	27.50	9.61
···	···	475	3.78e-15	<3.00e-16	12.60	8.84
···	···	55	8.29e-15	<3.00e-16	27.65	8.37
···	···	514	8.21e-15	<3.00e-16	27.38	8.76
···	···	477	3.95e-15	<3.00e-16	13.17	9.05

[a]fgStar

Two of the non-detections reported in Table 2.2 correspond to transients reported in Williams et al. (2008, XRT-1 and XRT-6), and require a change in flux by a factor > 10 to explain their non-detections. Four of the other transients reported by Williams et al. (2008) were detected by W15. These detections are XRT-2, XRT-4 (foreground star), XRT-5, and XRT-7 as reported in Williams et al. (2008). The new detections in W15 suggest that these faint transients did not vary by more than a factor of 10 from their previous detections. Therefore they are not included in our list of transient candidates from the survey of W15. Another transient (XRT-3), fails to make it into Table 2.2 because its original detection was so faint that it requires only a factor of 6.5 change in flux to explain non-detection in W15.

As demonstrated in Figure 2.3 many sources detected by W15 at S/N $\sim$ 3–8 and located inside the T11 footprint were not detected in the *Chandra* survey even though they are brighter than the T11 limiting flux. To investigate the nature of these sources, we inspected the spatial and hardness distributions of the unmatched sources. In Figure 2.4 we plot the HRs based on soft-band source counts of these $3 <$ S/N < 8 sources unmatched to T11 along with all of the sources inside the footprint of their survey. The unmatched sources are peaked at significantly softer ratios than the matched sources, indicating that the dominant cause of the discrepancy between the catalogs is the *XMM-Newton* soft response. Because of this increased soft sensitivity, the W15 *XMM-Newton* survey has discovered more faint soft sources than the *Chandra* survey of T11.

Because many of the unmatched sources with S/N ≤ 8 in W15 appear to be due to increased soft sensitivity and not variability, we concentrated on separating out the most highly variable transients, which appear to be those with S/N > 8 in our catalog. There were 31 W15 sources inside the T11 footprint that were not seen by T11, but are detected at S/ N > 8 in W15. The flux upper limits, taken from the sensitivity of T11, suggest variability by a factor of 10. Of these, 21 are included in Table 2.2, with the other 10 omitted because we have classified them as probable SNRs. SNRs are not variable; instead their non-detections in T11 arise from the lower soft sensitivity of *Chandra*. Comparing these same 31 sources against M06, we find that 14 of the 21 non-SNR sources were also not seen in M06. One is again the transient pulsar reported by Trudolyubov (2013). Another interesting previously known variable source in W15 is the second eclipsing HMXB ([PMH2004] 47) known in M33.

As a final variability check, we compared the fluxes for all W15 sources with a match in T11. The

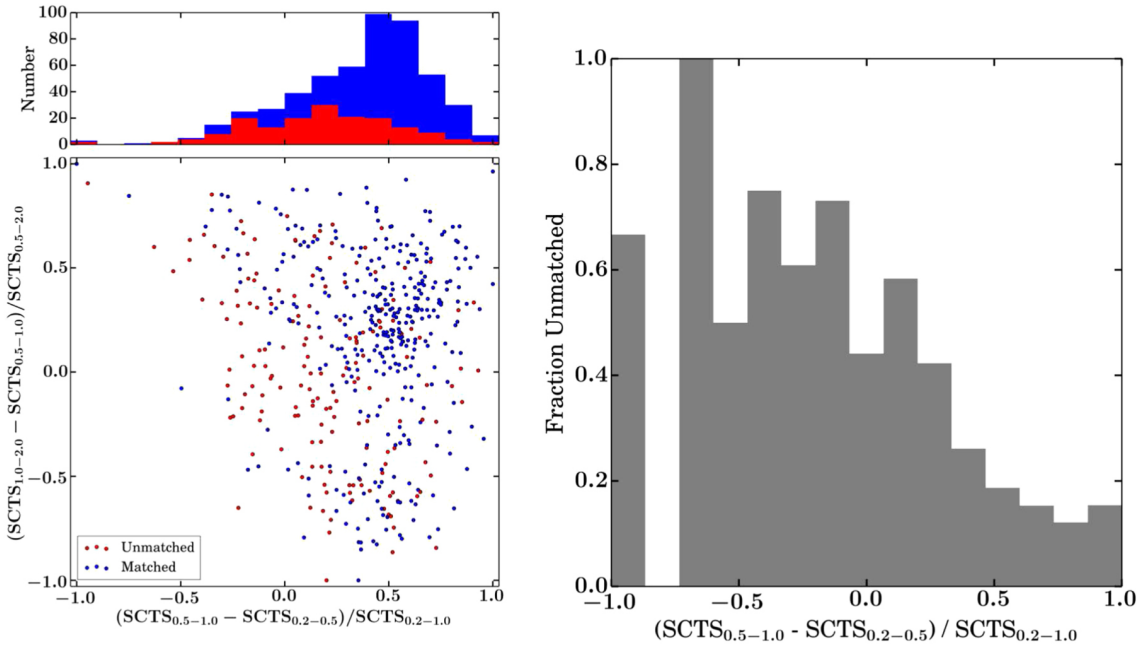

Figure 2.4: *Bottom-left:* Hardness ratios optimized for separating soft sources using source counts (SCTS) in the 0.2-0.5, 0.5-1.0, and 1.0-2.0 keV energy bands of all matched sources inside of the T11 footprint (blue circles) and unmatched sources with $3 < S/N < 8$ from W15 inside the T11 footprint (red circles). The median uncertainty on the X axis is 0.16 for the matched sources and 0.25 for the unmatched sources. The median uncertainty on the Y axis is 0.11 for the matched sources and 0.23 for the unmatched sources. *Top-left*: Sandpile histogram of all sources shown in left bottom so that the contribution of each to the total in each bin can be compared. The blue area shows the contribution of all matched sources; the red shows the contribution of unmatched sources. The unmatched sources have a softer distribution than the overall distribution. *Right:* Fraction of unmatched sources as a function of hardness ratio, showing that a high fraction of soft sources are not matched to a T11 source.

results are provided in Table 2.3. We fit an empirical relation between the fluxes in W15 and those in the T11 catalog in the 0.5–2 keV band, and then renormalized their fluxes to account for any systematic offset between our flux measurements. After renormalizing, we calculated the variability significance between the matched sources before accounting for any systematic uncertainty (σ), as well as the variability significance after adding in quadrature a 10% systematic uncertainty to all measured fluxes (revised σ). This estimate of the systematic uncertainty was consistent with the RMS scatter of matched sources as well as calibration tests in the literature (e.g. Plucinsky et al., 2012). There are 56 sources in Table 2.3 with revised $\sigma \geq 2.0$, and 76 sources with revised $\sigma \geq 3.0$. Seven of these sources showing evidence of variability between the two catalogs are discussed as HMXB candidates in Chapter 4.

2.5 Source Population Characteristics

With the broad coverage and depth of the W15 survey, we were able to measure the X-ray source surface density out to D_{25} and beyond, as well as the XLF accounting for the local background explicitly. These measurements are described in turn below.

2.5.1 Radial Source Density

With a survey covering as much of the galaxy as W15 with such high depth it is reasonable to expect detection of a non-negligible number of sources that are not intrinsic to M33, e.g. background AGN. In order to study the properties of the intrinsic M33 sources, we divided the catalog of W15 into elliptical annuli to investigate the radial density distribution for the bright sources. The annuli were computed assuming an M33 position angle of 23° and an inclination of 56° (Zaritsky et al., 1989). Figure 2.5 shows the source density as a function of semi-major axis of the ellipse (radius equivalent). We include only sources with 0.2–4.5 keV fluxes brighter than 4.5×10^{-15} erg cm^{-2} s^{-1} ($L_X > 3.6 \times 10^{35}$ erg s^{-1}), as faintward of this limit the catalog becomes increasingly background dominated. This cut includes the 391 brightest sources in the W15 catalog.

We fitted this radial profile with an exponential plus a constant:

$$\Sigma_{N_X} = Ae^{(r/r_s)} + B \tag{4}$$

Table 2.3: Variability of Matched T11 Sources. Column 1 lists the source ID in W15, column 2 is the source flux in W15 (erg s^{-1} cm^{-2}), column 3 is the source flux in T11 (erg s^{-1} cm^{-2}), column 4 is the revised flux in T11 after adding in quadrature 10% systematic uncertainty (erg s^{-1} cm^{-2}), column 5 is the variability significance between matched sources in W15 and T11, and column 6 is the variability significance between the two catalogs using the revised fluxes from column 4. Full table available electronically in Williams et al. (2015).

Source ID	XMM Flux	T11 Flux	Revised T11 Flux	Sigma	Revised Sigma
177	2.21e-15	3.64e-15	6.18e-15	3.26	2.87
189	2.07e-15	1.28e-15	2.17e-15	0.14	0.12
198	1.03e-14	2.84e-15	4.82e-15	4.46	3.27
200	3.38e-15	4.93e-15	8.36e-15	4.72	3.59
202	3.17e-15	2.16e-15	3.67e-15	0.66	0.55
203	1.24e-14	5.79e-15	9.82e-15	2.35	1.35
217	6.25e-16	6.75e-16	1.14e-15	1.10	1.06
222	3.78e-15	1.33e-15	2.25e-15	1.59	1.45
234	2.25e-15	2.76e-14	4.69e-14	24.45	8.86
252	1.18e-15	7.39e-16	1.25e-15	0.19	0.17
255	1.55e-15	1.97e-15	3.35e-15	3.61	2.90
259	9.29e-16	1.67e-15	2.83e-15	4.21	3.52
264	9.72e-15	9.33e-15	1.58e-14	6.07	2.89
274	1.65e-15	6.81e-16	1.16e-15	1.19	1.07
283	1.68e-15	1.12e-15	1.90e-15	0.46	0.41
285	1.36e-15	1.10e-15	1.86e-15	0.89	0.82
290	1.45e-15	1.65e-15	2.81e-15	2.77	2.32
293	2.65e-15	1.99e-15	3.38e-15	1.34	1.05
296	5.72e-15	5.29e-15	8.97e-15	4.27	2.48
297	5.05e-16	8.17e-16	1.39e-15	2.40	2.22
299	7.82e-16	5.93e-16	1.01e-15	0.59	0.56
309	3.97e-15	3.16e-15	5.37e-15	1.76	1.35
314	9.39e-14	6.57e-14	1.11e-13	6.80	1.19
316	5.22e-14	6.31e-14	1.07e-13	30.64	4.55
320	3.49e-15	3.10e-15	5.27e-15	2.63	1.92
323	4.91e-16	2.58e-16	4.38e-16	0.20	0.19
327	3.58e-15	1.57e-15	2.66e-15	0.89	0.81
329	4.68e-15	2.48e-15	4.21e-15	0.81	0.55
334	8.99e-16	8.77e-16	1.49e-15	1.53	1.40
336	2.12e-15	3.90e-15	6.63e-15	6.26	4.50
338	3.66e-15	1.97e-15	3.34e-15	0.56	0.42
339	8.29e-16	6.47e-16	1.10e-15	0.73	0.68
340	1.68e-14	6.77e-15	1.15e-14	5.22	2.34
346	3.60e-14	1.89e-14	3.20e-14	3.11	0.79
351	1.26e-14	6.63e-15	1.12e-14	1.71	0.74
355	2.43e-15	1.61e-15	2.72e-15	0.56	0.46
356	4.31e-16	6.03e-16	1.02e-15	1.86	1.76
360	1.26e-15	2.76e-15	4.69e-15	7.02	4.98
362	4.40e-15	3.74e-15	6.35e-15	2.82	1.88
375	4.96e-15	2.54e-15	4.31e-15	1.30	0.79
377	9.85e-16	7.47e-16	1.27e-15	0.74	0.68
379	9.68e-15	8.73e-15	1.48e-14	5.31	2.55
382	8.22e-16	2.86e-16	4.86e-16	1.14	1.09

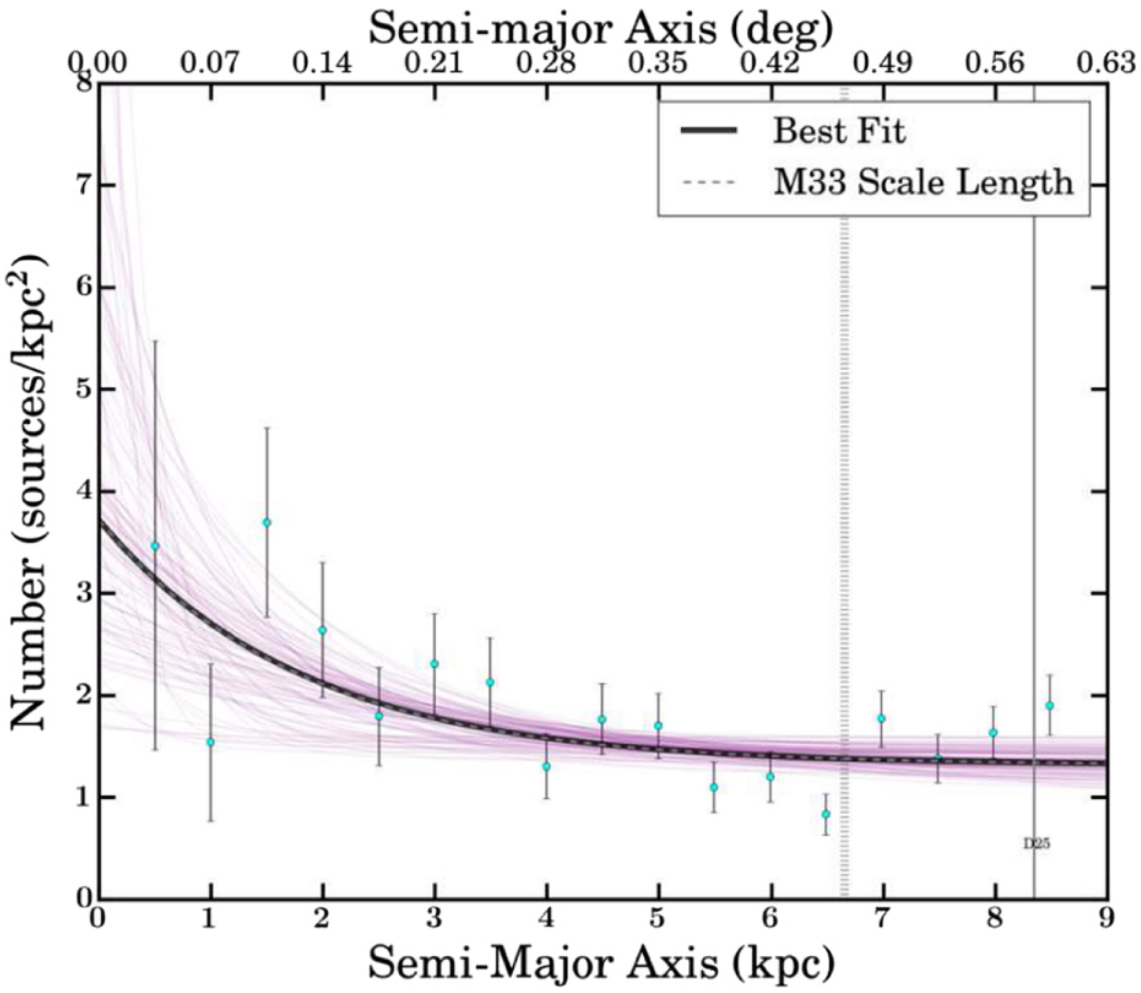

Figure 2.5: X-ray source surface density for all sources with L_X(0.2-4.5 keV) $> 3.6 \times 10^{35}$ erg s^{-1}. The thick black line shows an exponential with scale length 1.8 kpc (best fit) and constant background of 1.3 kpc^{-2}. For comparison, the optical scale length (1.8 kpc) is plotted with a gray dashed line, which lies on top of the black line. A random draw of 100 trials from the MCMC runs used for uncertainty determination is shown with the thin pink lines. A constant surface density, which we take to be the background surface density, is reached by 6.7 kpc (marked with the thick gray vertical dotted line) and is relatively well-constrained, while the scale length is less certain due to the large error bars in the inner disk. D_{25} is marked with the thin vertical gray line.

where Σ_{N_X} is the source density, A is the normalization of the exponential term, r is the galactocentric radius, r_s is the exponential scale length, and B is the constant background density. We assume the exponential term of the function represents the M33 population while the added constant term represents the AGN background. The fit was performed using a Markov Chain Monte Carlo technique, and specifically the `emcee` Python module (Foreman-Mackey et al., 2013). A random draw of 100 samples from the fitting used for uncertainty determinations is shown with the thin lines on the figure. The errors on data points are Poisson.

We find the source density falls with an exponential scale length (r_s) of $1.8^{+1.3}_{-0.8}$ kpc, indistinguishable from the optical scale length of the disk ($\sim$ 1.8 kpc Williams et al., 2009). The normalization (A) of the exponential source density term was $2.3^{+1.6}_{-1.0}$ sources kpc^{-2}. Integrating the M33 component (exponential term) out to D_{25} yields 50^{+40}_{-30} M33 sources down to a limiting luminosity of 3.6×10^{35} erg s^{-1}. Since there are 20 SNRs at this luminosity limit (Long et al., 2010) this analysis suggests that roughly 40% of the bright X-ray sources in M33 are SNRs. However, we note that this number of M33 sources is likely biased low, as we do not account for the loss of background sources due to absorption by M33 itself. Absorption effects would decrease the background contribution within D_{25}, thus increasing the number of M33 sources.

Our radial density profile fit also constrains the background source density (the constant added to the exponential) to 460^{+40}_{-70} deg^{-2}, which corresponds to B = $1.3^{+0.1}_{-0.2}$ kpc^{-2} corrected for inclination as in Figure 2.5. This value is roughly consistent with what would be inferred from the cosmic mean background densities at these flux levels (Cappelluti et al., 2009). This analysis yields a total of 290^{+30}_{-40} background sources inside D_{25} (0.59 $\times$ 0.37 degrees, 8.4 kpc deprojected radius).

2.5.2 X-ray Luminosity Function

The XLF is a powerful tool for analyzing extragalactic X-ray source populations. This is because it is often one of the few X-ray population diagnostics available in more distant galaxies. Most often, the XLF is presented as a cumulative distribution of the number of sources at each luminosity. Both the slope and normalization of the XLF distribution in turn provide insight into the characteristics of the underlying source population and its connection with the host galaxy (e.g. Grimm et al., 2003; Mineo et al., 2012).

We constructed an XLF (log(N)-log(S)) from the sources in the W15 survey within 6.7 kpc

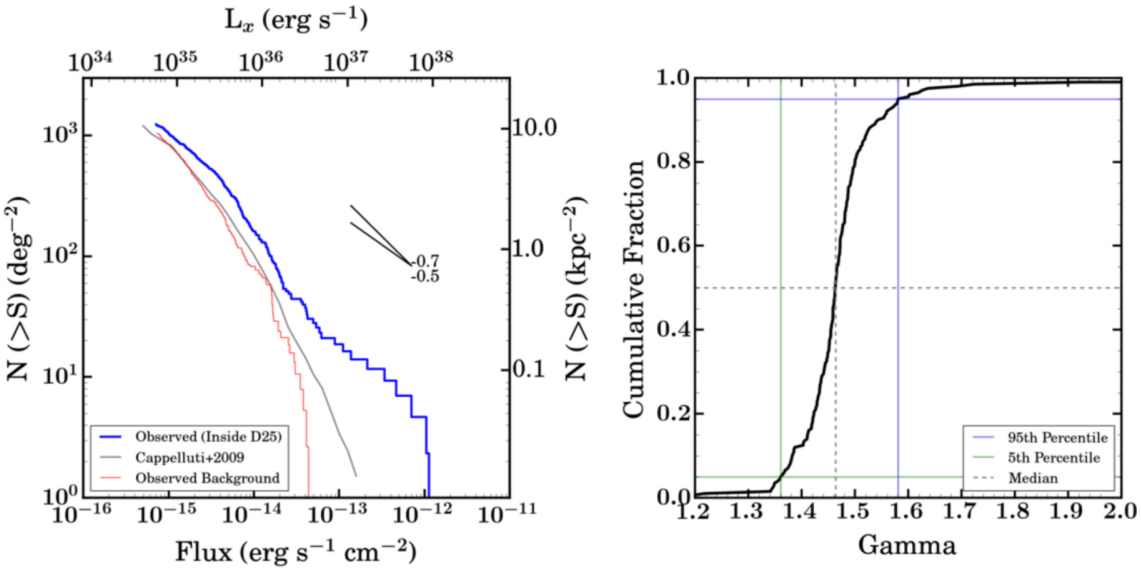

Figure 2.6: *Left:* Cumulative luminosity function of all sources with fluxes $> 6 \times 10^{-16}$ erg cm^{-2} s^{-1} inside of 6.7 kpc (deprojected) is shown in blue. Cumulative power-law indices of 0.5 and 0.7 (equivalent to 1.5 and 1.7 differential indices) are shown for comparison. The cosmic mean background shown in gray is taken from Cappelluti et al. (2009). The observed background, shown in red, is measured from our data outside of 6.7 kpc. *Right:* Cumulative distribution of the best-fit power-law index of the M33 component of the XLF from fits to our Monte Carlo draws from the catalog fluxes. The resulting 90% uncertainties to the best-fit are $1.50^{+0.08}_{-0.14}$.

(deprojected) of the center of M33 (just inside of D_{25}, as marked on Figure 2.5). The XLF is shown in Figure 2.6, where N has units of deg^{-2} and L is the 0.5-2.0 keV luminosity of the source assuming all sources are at the distance of M33. This XLF excludes sources that are known foreground stars.

Each source was corrected for completeness by calculating the amount of the W15 survey area inside of 6.7 kpc sensitive to the source's count rate. For this purpose we constructed a sensitivity map of the survey area from the exposure and background maps using the SAS task `esensmap`. The fractional area sensitive to each count rate is shown in Figure 2.7. The lowest 0.5–2.0 keV count rate on the area sensitivity plot (2.7×10^{-4} counts s^{-1}) corresponds to a 0.5–2.0 keV flux of $\sim 2\times 10^{-16}$ erg cm^{-2} s^{-1}. The luminosity function itself is limited to sources with 0.5-2 keV fluxes above 6×10^{-16} erg cm^{-2} s^{-1}, or 5×10^{34} erg s^{-1} ($\sim 8 \times 10^{-4}$ counts s^{-1} combined 0.5-2.0 keV count rate) for which the completeness corrections are small. Thus, the area corrections are not sensitive to the details of the sensitivity map; however, we do correct for completeness using the area corrections derived from our sensitivity function.

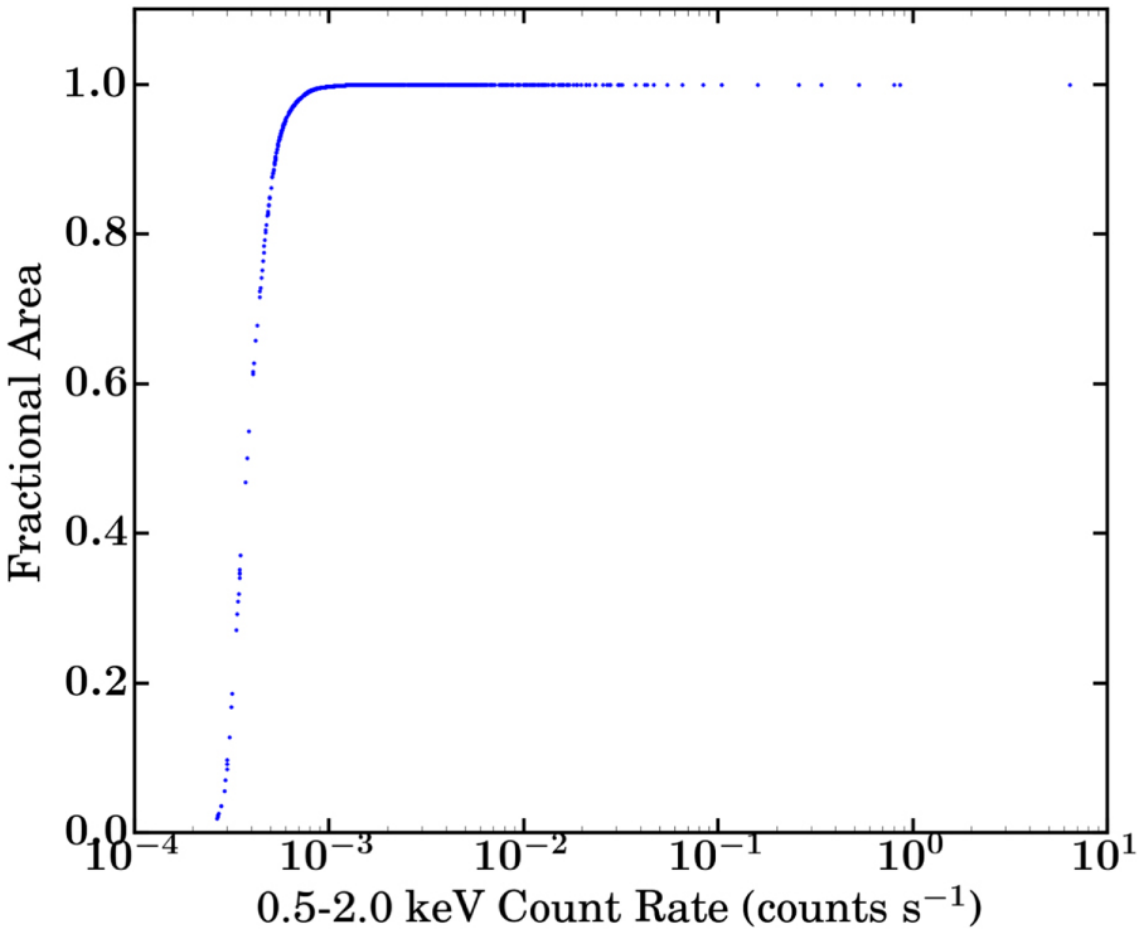

Figure 2.7: Fractional coverage of the area inside 6.7 kpc (deprojected) as a function of 0.5-2.0 keV count rate, as calculated from the combined sensitivity map. The entire area is covered down to a count rate of $\sim 8 \times 10^{-4}$ counts s^{-1}.

We also construct an background XLF from all the W15 sources outside 6.7 kpc (red distribution, Figure 2.6). This radius is chosen because of the enhanced surface density visible here (0.47 deg along major axis, marked on Figure 2.5), but because it is also a region within which there was at least 100 ks of exposure time in the W15 survey. We corrected for completeness using the same technique described above as for the inner regions, but with areas derived from the sensitivity map in this outer region of the survey. We also plot the background XLF as determined from (Cappelluti et al., 2009) (grey line, Figure 2.6). The agreement between the cosmic mean background and the observed backgrounds gives us confidence that the catalog of W15 is clean and the computed completeness function is accurate.

To extract more information about the inferred source population based on the XLF, we first fit the unbinned differential XLF with a sum of two power-law components using the `CIAO` package `Sherpa`. First, we fit the background component alone with a single power law using only sources measured outside of the surface density enhancement seen in the radial analysis. Then we fit the total XLF inside of the surface density enhancement by adding a second power-law component to the fixed background component. The second power law represents the intrinsic M33 XLF.

The best fit to the background XLF (323 sources outside of the area of enhanced surface density in the radial analysis) has a power-law index of 1.83. To assess the precision of this background power-law index, we performed 200 Monte Carlo draws from the fluxes, where each source was given a flux drawn from a Gaussian distribution centered at the measured flux with a width determined from the Poisson uncertainties. The 90% uncertainties from this method are $1.83^{+0.09}_{-0.05}$. We note that this background XLF represents the maximum expected background contamination in the M33 catalog because some of the sources directly behind M33 are likely lost due to absorption by M33 itself.

We then added a second power-law component to the model and fit the unbinned differential XLF for 523 sources inside of the radial surface density enhancement. The additional component, which we attribute to the X-ray source population intrinsic to M33, has a power-law index of 1.50. To estimate the uncertainties on this result, we again performed 200 Monte Carlo draws from our measured source fluxes, using the same technique applied to the background fits. However, in addition to applying uncertainties to the fluxes, for each draw, we also fixed the background component to a random draw from our 200 background fits. Thus, we also account for uncertainty

in the background XLF.

In the right panel of Figure 2.6 we show the cumulative distribution of the resulting power-law index values for the M33 component from these 200 fits. With the resulting 90% uncertainties, we measure the power-law index of the intrinsic M33 XLF to be $1.50^{+0.08}_{-0.14}$. Integrating this M33 component, we find 60^{+50}_{-30} M33 sources, consistent with the radial distribution analysis. As with the result of the radial analysis, this value is likely to be biased low because some background sources are likely lost to absorption by M33 itself. This XLF slope is consistent with that measured by T11 and similar to the "universal" XLF of HMXBs seen in several external galaxies (1.6; Grimm et al., 2003; Mineo et al., 2012), suggesting that the bright X-ray source population of M33 has a large fraction of HMXBs.

2.6 Synopsis

In this chapter, we detailed the analysis of the X-ray source population of M33 as seen with a deep *XMM-Newton* survey published in W15. The data provide increased soft sensitivity and cover beyond the D_{25} isophote of the galaxy to a similar depth as probed by the deep *Chandra* survey of T11 which covered the inner 15' of M33.

The increased soft sensitivity allows for the characterization of many new soft sources on the basis of custom hardness ratios. In particular, this analysis finds four new SNRs in M33. The extensive coverage of the survey allows the source catalog to be matched to previous X-ray source catalogs in M33 in overlapping regions to search for source variability. In addition to rediscovering several known transients (e.g. Williams et al., 2008), and a known pulsar (Trudolyubov, 2013), we find ~ 30 new possible transient sources, and ~ 75 sources that showed evidence of long term variability between surveys.

The depth and coverage of the survey allowed us to analyze an extended radial profile of the M33 X-ray source density out to D_{25} and beyond. We measured an X-ray scale length consistent with the optical scale length, similar to other nearby spiral galaxies (e.g. Binder et al., 2012). Our radial density profile suggests that a relatively low number of the sources from W15 (~ 50, 15%) with fluxes $>4.5\times 10^{-15}$ erg cm^{-2} s^{-1} belong to M33, and about 40% (20) of these are known SNRs. However, this number of M33 members from this survey is likely to be biased low since some background sources may be undetected through M33.

Finally, we performed a local characterization of the background XLF, which we measure to have a differential power-law index of $1.83^{+0.05}_{-0.09}$. When we account for this background, we find the differential XLF of M33 itself has a power-law index of $1.50^{+0.08}_{-0.14}$, consistent with previous measurements and the "universal" XLF for HMXB populations, suggestive of a large population of as-yet uncharacterized HMXBs in M33.

The next two chapters will discuss the detailed properties of subsets of the X-ray source population discussed and analyzed here. In particular, Chapter 3 discusses the SNR population in terms of the characteristics of the global population, as well as detailed spectral analysis of the brightest sources. Chapters 4 and 5 further discuss the identification and characterization of the population of candidate HMXBs in M33 via identification of their optical counterparts, and measurement of formation timescales using *HST* data.

Chapter 3:

Supernova Remnants as Tracers of Massive Star Evolution

3 Supernova Remnants in M33: X-ray Properties as Observed by *XMM-Newton*

Material from this chapter was previously published in collaboration with Benjamin F. Williams, Paul P. Plucinsky, Terrance J. Gaetz, Brian Wold, Frank Haberl, Knox S. Long, William P. Blair, Thomas G. Pannuti, P. Frank Winkler, and Jacob Gross in the November 2017 edition of the Monthly Notices of the Royal Astronomical Society ((Garofali et al., 2017); ©2017 Oxford University Press on behalf of the Royal Astronomical Society), and has been reproduced here with the permission of the Oxford University Press.

3.1 Introduction

As first discussed in Chapter 1, SNRs deposit energy and metals into ISM, and thus contribute strongly to galactic chemical evolution. Unlike the short-lived SNe that precede them, SNRs are available in abundance to study in the LG. However, despite their large numbers observable nearby, there are still open questions regarding the connection between SNR properties at optical, IR, X-ray, and radio wavelengths and their progenitor type. These open questions remain largely due to incomplete SNR surveys in different wavelength regimes, and the erasure and dilution characteristics signaling progenitor type as SNRs age and mix with the surrounding circumstellar material and ISM.

M33 is a prime target for extending previous works characterizing extragalactic SNRs owing to the detailed SNR surveys that have already been carried out at optical, X-ray, and radio wavelengths (Sabbadin, 1979; Dodorico et al., 1980; Gordon et al., 1998; Long et al., 2010; Sarbadhicary et al., 2017). These previous detailed multiwavelength surveys have revealed a extensive SNR population (218 candidates, 86 confirmed via multiwavelength detections) in optical, radio, and X-ray wavelengths. Using optical emission-line ratios Gordon et al. (1998) identified a population of 98 SNR candidates in M33. Recently, Long et al. (2010, hereafter L10) carried out a multiwavelength study of 131 of the previously known 137 SNRs in the galaxy; they detected 82 (58) at the 2σ (3σ) level with *Chandra*, and obtained upper limits for the rest. Most recently, Lee & Lee (2014b, hereafter LL14) boosted the number to 199 optically selected SNR candidates, of which 78 were not previously reported in L10's catalog. Here I carry out an analysis of the properties of all 218

known and suggested SNRs in M33. This includes the 137 sources described by L10 (of which 121 overlap with the sources discussed by LL14), the 78 new sources identified as candidates by LL14, and 3 X-ray candidates identified by W15.

In this chapter I will expand upon this work using the *XMM-Newton* data described in Chapter 2 to search for SNRs newly detected in X-rays in M33, as well as confirm previous SNR candidates on the basis of X-ray detection with *XMM-Newton*. Compared to past works, the data described in Chapter 2 is ideally suited for this purpose, given the soft sensitivity of *XMM-Newton*, and the wide coverage of the survey of W15. With this *XMM-Newton* survey, all 218 SNR candidates are within the field-of-view and refinements can be made to the properties of those SNRs already detected at X-ray and/or optical wavelengths.

The remainder of this chapter is laid out as follows: in Section 3.2, I describe the data used from this and previous surveys as well as the data reprocessing and reduction techniques. Section 3.3 outlines the SNR catalog, and details the characterization of the SNR population based on spectral fitting, HRs, and X-ray morphology. In Section 3.4 I discuss the results from this most recent X-ray survey of the M33 SNR population, including the shape of the X-ray luminosity function, and the implications for SNR detectability, and finally in Section 3.5 I present a synopsis of this chapter.

3.2 Survey Overview

The observations and analysis of the *XMM-Newton* survey data of M33 used in this paper are described by W15, and briefly summarized in Chapter 2. For the purpose of analyzing the SNR population, we have optimized our reduction of the survey data for extended sources, as we describe in Section 3.2.1. All 218 previously identified SNR candidates are within the field-of-view of W15, allowing for cross-correlation of the W15 X-ray catalog with both the existing X-ray and optical catalogs of L10 and LL14, as well as identification of 3 new X-ray selected SNRs (described in Section 3.3.1) based on X-ray HRs and visual inspection of LGGS data (Massey et al., 2006). The positions for all sources used in the remainder of this analysis come from the catalog of W15. The X-ray fluxes, and HRs reported in Table 3.2 and Table 3.3 come from custom measurements at the positions of all 218 SNR candidates using the *XMM-Newton* data in the bands described in Section 3.2.1. The *XMM-Newton* spectra used in the spectral fitting described in Section 3.3.2 were extracted specifically for this analysis.

In addition to the catalog of W15, we utilize high resolution observations from the ChASeM33 survey (T11). The SNR catalog from the ChASeM33 survey is described in L10, and, in addition to cross-correlating our SNR candidates with those of L10, we also use their ACIS spectra when available for spectral fits.

We also cross-correlate our sources with the optically selected SNR candidate catalog of LL14. Their survey used narrow-band images from the LGGS (Massey et al., 2006) to identify SNR candidates based on emission-line ratios ([S II]/Hα $>$ 0.4) and shell-like or circular morphology for sources smaller than 100 pc. The L10 survey, by contrast, did not initially cut candidates based on morphological or size considerations, focusing instead on evidence of shock-heating, and further used only portions of the LGGS within the ChASeM33 footprint. For the purposes of this chapter, we have kept all objects contained in both survey lists. We discuss our measurements at the locations of all sources in each catalog in Section 3.3.1.

In addition to finding SNR candidates, LL14 assign each candidate in their catalog a tentative progenitor classification of CC or Type Ia based upon the surrounding stellar population. CC SNe result from the explosion of a massive star and thus are expected to be in regions of recent star formation nearby other OB stars. Type Ia, or thermonuclear, SNe are caused by the detonation of a white dwarf that has reached its Chandrasekhar limit and are expected in regions of little to no recent star formation (i.e. few nearby OB stars). However, it is possible a Type Ia SN could occur near a region of OB stars in areas with multiple epochs of star formation, highlighting the need for a full SFH of the surrounding region to determine more reliably the progenitor class. Such classifications exist for a handful of SNRs in M33 from the work of Jennings et al. (2014). These SNR progenitor classifications are the result of measured progenitor masses from detailed SFHs of the stellar populations surrounding each SNR, and are considered robust determinations. When the classifications from Jennings et al. (2014) are unavailable, we instead use the LL14 tentative progenitor type labels. Together these classifications are used to explore the efficacy of measured HRs (Section 3.3.4) in typing SNR progenitors.

3.2.1 Reprocessing of *XMM-Newton* Data

While the vast majority of the reduction techniques for the analysis presented here was described in detail in W15, there were some special considerations that we employed for source detection and

background characterization when looking specifically for the SNRs in M33, which slightly differ from the description in W15.

For detecting and measuring extended sources, it is beneficial to use the software provided by the `Extended Source Analysis Software (ESAS)` (Kuntz & Snowden 2008), a package within `SAS` optimized for extended sources, which models the background light curves during an observation and identifies time periods when the background level is significantly enhanced compared to the quiescent background, allowing cleaner separation of extended sources from the background as well as spectra with less background contamination.

We selected GTIs using the `ESAS` tools `pn-filter` and `mos-filter`. Utilizing the unexposed corner sections of the CCDs, count thresholds are chosen by fitting a Gaussian peak at the quiescent count rate. A GTI file is produced which includes only time intervals where the count rate was within 2σ of the peak of the aforementioned Gaussian. Within the `ESAS` package `pn-filter` and `mos-filter` were applied to the `SAS` task `espfilt` to determine the GTIs. We then applied these GTIs to our event lists for spectral extraction. Our spectral extraction required a large amount of customization, which is described in more detail in Chapter 5. The extracted spectra are used for the spectral fitting described in Section 3.3.2.2.

When searching for soft and extended gas emission sources (such as large SNRs or H II regions), we applied the same `emosaicprep` and `emosaicproc` tasks as for the point sources, but using the `ESAS`-processed event lists. For the purposes of detecting SNRs, the energy range was set to 0.2-2.0 keV and the positions of the L10 and LL14 SNR candidates were input into `emldetect`. For the 0.2-2.0 keV band we ran `emldetect` simultaneously on the 0.2-0.5 keV, 0.5-1.0 keV, and 1.0-2.0 keV bands, and let `emldetect` calculate the full band (0.2-2.0 keV) totals based on the provided exposure times, background images, and masks. This energy range was chosen to leverage the soft sensitivity of *XMM-Newton* for SNR detection. The pn requires more conservative flagging be applied to the event list in the softest band (0.2-0.5 keV) to avoid spurious detections. For this reason, the individual bands were run separately with flagging as described in W15, and then combined to create a full band (0.2-2.0 keV). For the purposes of measuring and comparing luminosities, the energy range was also set to 0.35-2.0 keV to match the band of L10. These measurements at the locations of previously known SNRs are discussed in 3.3.1.

Another critical adjustment to make was the choice of ECF values. The list of source positions

from `emosaicproc` was fed to `emldetect` to calculate on-axis equivalent count rates and convert these values to a flux using ECFs selected during the detection script. Table 3.1 lists the ECFs used to calculate the fluxes in the 0.2-2.0 keV band (plus component bands) which was used for source detection, and the 0.35-2.0 keV band which was used for comparison to L10, and the 0.3-0.7 keV, 0.7-1.1. keV, and 1.1-4.2 keV bands, which were used for HR calculations in Section 3.3.4. The unabsorbed ECFs were calculated based on `XSPEC` simulations of an `apec` spectrum with absorption with parameters N_H=1x10^{21} cm^{-2}, kT = 0.6 keV, and elemental abundance set to half solar. This spectrum was also chosen to remain consistent with L10. Futhermore, we ensured that the locations of all SNR candidates were included in the candidate source list that was measured by the `emldetect` step of our analysis routine. Thus, we were able to obtain either detections or upper limits for all SNR candidates. Occasionally, `emldetect` fails to properly combine the individual bands to produce a reliable full band total. In these cases (8% of sources), the source counts in the full band (0.2-2.0 keV) are a factor of 2 discrepant from the sum total of the individual bands (0.2-0.5 keV, 0.5-1.0 keV, and 1.0-2.0 keV). We denote these sources with a 't' flag in Table 3.2 and Table 3.3. These sources still have reliable measurements in the individual bands, so for their full band 0.2-2.0 keV totals we report the counts, count rate, and flux values as the sum of the individual bands. For all other sources the total flux values are output from `emldetect` and represent the sum of the fluxes from each EPIC instrument weighted by the appropriate calibration files. All sources are listed in Table 3.2.

3.3 Results

Our goal is to provide the best possible characterization of the SNR population of M33 given all of the available data. Because *XMM-Newton* provides high soft-band sensitivity, this new survey provides further constraints on SNR spectral fits and HR measures which can potentially be used to constrain progenitor explosion type. We describe the sample of SNRs measured in this survey, as well as each of these methods as applied to that sample below.

3.3.1 Catalog of M33 SNRs

To measure fluxes or, where not possible, establish upper limits on the flux of SNRs in M33, we measured the locations of SNR candidates from L10, LL14, and W15 (218 total sources) in both

Table 3.1: Unabsorbed ECFs for the bands and instruments used in this survey. ECF units are counts erg cm^{-2}.

Energy Band (keV)	pn	MOS1	MOS2
0.35-2.0	1.8×10^{-12}	7.45×10^{-12}	7.44×10^{-12}
0.2-2.0	2.5×10^{-12}	8.2×10^{-12}	8.1×10^{-12}
0.2-0.5	4.2×10^{-12}	2.7×10^{-11}	2.8×10^{-11}
0.5-1.0	1.8×10^{-12}	7.8×10^{-12}	7.8×10^{-11}
1.0-2.0	1.9×10^{-12}	5.9×10^{-12}	5.8×10^{-12}
0.3-0.7	1.8×10^{-12}	1.1×10^{-11}	1.1×10^{-11}
0.7-1.1	1.9×10^{-12}	7.8×10^{-12}	7.7×10^{-12}
1.1-4.2	2.0×10^{-12}	6.1×10^{-12}	6.1×10^{-12}

the 0.2-2.0 keV band as well as the 0.35-2.0 keV band to be consistent with L10. We find that the average signal-to-noise is higher in the 0.2-2.0 keV band, and after verifying all measurements by eye to remove spurious detections in both bands, we found that using the 0.2-2.0 keV band results in 12 more 3σ detections than using the 0.35-2.0 keV band. We therefore conclude that the 0.2-2.0 keV band is better for detection of SNRs when using *XMM-Newton* and that only 3σ measurements should be taken as reliable detections, as there can be fluctuations in the background at the 2σ level in the 0.35-2.0 keV band on the size scale of SNRs in the *XMM-Newton* imaging.

We have also inspected all measurements at the locations of SNR candidates by eye to validate the detections and non-detections in our sample. In some cases, overlapping sources in the *XMM-Newton* data lead to erroneously high fluxes for a single SNR candidate. For these sources, if there is a previous X-ray detection of the SNR (i.e. from L10), the source is flagged as contaminated by the overlapping source ('c'), and the measured flux is likely too high and thus treated as an upper limit. If there is a nearby contaminating X-ray source, but no previous X-ray detection at the location of the SNR candidate, the source is denoted with the 'x' flag, and the flux is treated as an upper limit, and the source a non-detection. Those sources that did not appear to be reliable detections in the by-eye validation are denoted by the 'n' flag, and their fluxes are also reported as upper limits, and the sources treated as non-detections. As noted in Section 3.2.1 sources marked 't' have full band totals that come from the sum of the individual band runs from `emldetect`. Sources with erroneous `emldetect` count errors in at least one band are denoted by the 'e' flag, and their count errors are pegged to the total number of counts in that band.

All 218 sources are recorded in Table 3.2. We report ID numbers in this catalog, corresponding ID numbers in both L10 and LL14, *XMM-Newton* positions, counts in the 0.2-2.0 keV band, count

rates and associated errors in the 0.2-2.0 keV band in s^{-1}, fluxes from `elmdetect` (sum of all EPIC instruments) in the 0.2-2.0 keV band in erg cm^{-2} s^{-1} (used for detection), fluxes in the 0.35-2.0 keV band in erg cm^{-2} s^{-1} (used for comparison to L10), SNR sizes (in pc) from L10 and LL14, [S II]/Hα from both L10 and LL14, and the log of Hα luminosity in erg s^{-1} from both L10 and LL14. Individual source ID numbers are denoted with the 'c', 'x', 'n', 't', and 'e' flags as described above. Sources that are upper limit measurements in this survey have fluxes preceded by $<$.

In addition to listing all 218 sources in Table 3.2, we also list all 3σ detections only in Table 3.3, along with their associated counts (sum of all EPIC instruments) and count errors in the 0.2-2.0 keV, 0.35-2.0 keV, 0.3-0.7 keV, 0.7-1.1 keV, and 1.1-4.2 keV bands. The last three bands are used to compute HRs for all detected sources only as described in Section 3.3.4. The HRs in these bands, computed with counts using the Bayesian Estimation of Hardness Ratios (BEHR) method Park et al. (2006), are listed with their associated errors in columns 9-10 of Table 3.3. Columns 11-12 similarly list the HRs and associated errors calculated from the 0.2-0.5 keV, 0.5-1.0 keV, and 1.0-2.0 keV bands using BEHR. The final column of Table 3.3 denotes the level at which the source was measured in the 0.35-2.0 keV band in L10: $<$ for upper limit, 2σ, or 3σ. The comparison of this catalog with those of L10 and LL14 is described below.

The vast majority of extragalactic SNRs, including those in M33, were first identified optically based on elevated [S II]/Hα ratios as compared to H II regions. This technique works well in general, especially for brighter objects, but H II contamination for fainter objects, especially in complex regions, can affect the observed [S II]/Hα ratio and cause uncertainty in some optical identifications. We therefore view 3σ X-ray detection of a previously optically identified SNR to be a strong confirmation of SNR detection based on both the elevated [S II]/Hα as well as strong X-ray emission. Of course, some of the optically identified SNR candidates that are undetected in X-rays may simply fall below our detection threshold and thus still be SNR detections. However, for the reasons described here, and in Section 3.3.1, we consider sources that are identified optically as well as measured at 3σ confidence in X-rays to be well-confirmed SNRs. These sources, and those detected in X-rays at the 3σ level from L10, are regarded as X-ray confirmed SNRs in all subsequent detectability analyses, while any candidates measured less than 3σ are considered non-detections in the analysis that follows.

Table 3.2: All 218 SNR and SNR candidates in our sample. Columns 1-3: lD number from this catalog, ID number in L10, and ID number in LL14. Columns 4-5: source RA and Dec from this catalog. Columns 6-7: source counts and associated errors, and count rates and associated errors in the 0.2-2.0 keV band (used for detection). Columns 8-9: fluxes in the 0.2-2.0 keV band (used for detection), and fluxes in the 0.35-2.0 keV band (used for comparison to L10). Columns 10-11: optical SNR sizes from the L10 and LL14 catalogs. Columns 12-13: [SII]/Hα ratio from the L10 and LL14 catalogs (used for optical selection of candidates). Columns 14-15: log of the Hα luminosity from the L10 and LL14 catalogs. All units are given in the column headers.

ID	L10	LL14	RA	Dec	0.2-2.0 Cts	0.2-2.0 Ct Rate (s^{-1})	0.2-2.0 Flux (erg cm^{-2} s^{-1})	0.35-2.0 Flux (erg cm^{-2} s^{-1})	D(pc) L10	D(pc) LL14	[SII]/Hα L10	[SII]/Hα LL14	log(L(Hα) (erg s^{-1})) L10	log(L(Hα) (erg s^{-1})) LL14
XMM-001	–	1	1:32:25.78	30:30:04.03	21 ± 11	2.34e-04 ± 1.30e-04	<8.20e-16	<2.18e-16	–	81.0	–	0.74	–	36.16
XMM-002	–	2	1:32:27.85	30:35:44.58	25 ± 15	2.81e-04 ± 1.80e-04	<6.77e-16	<3.44e-16	–	72.0	–	0.98	–	36.05
XMM-003	1	–	1:32:30.83	30:27:45.99	107 ± 19	1.15e-03 ± 2.09e-04	1.40e-15	1.12e-15	123.0	–	0.77	–	36.98	–
XMM-004	2	3	1:32:31.41	30:35:32.90	66 ± 19	7.76e-04 ± 2.49e-04	1.09e-15	8.62e-16	29.0	28.0	0.44	0.59	36.20	36.02
XMM-005	–	4	1:32:35.36	30:35:19.81	27 ± 14	2.82e-04 ± 1.51e-04	<7.61e-16	<2.23e-16	–	85.0	–	0.50	–	36.36
XMM-006	–	5	1:32:37.36	30:18:03.10	296 ± 23	6.02e-03 ± 4.93e-04	8.49e-15	7.30e-15	–	85.0	–	0.60	–	36.15
XMM-007	–	6	1:32:39.78	30:27:54.95	11 ± 13	1.07e-04 ± 1.19e-04	<3.59e-16	<1.76e-16	–	36.0	–	0.93	–	35.36
XMM-008	–	7	1:32:40.23	30:16:21.24	4 ± 7	1.16e-04 ± 2.16e-04	<5.33e-16	<2.85e-16	–	44.0	–	0.52	–	35.65
XMM-009	–	8	1:32:40.53	30:16:37.20	74 ± 13	1.89e-03 ± 3.53e-04	1.76e-15	2.03e-15	–	42.0	–	0.79	–	35.36
XMM-010	–	9	1:32:40.94	30:31:51.05	39 ± 16	3.15e-04 ± 1.33e-04	7.98e-16	<3.35e-16	–	86.0	–	0.51	–	36.36
XMM-011	3	–	1:32:42.54	30:20:58.83	10 ± 10	1.22e-04 ± 1.33e-04	<5.59e-16	<1.31e-16	100.0	–	0.55	–	36.90	–
XMM-012[n]	–	10	1:32:42.71	30:36:20.06	51 ± 16	5.63e-04 ± 1.81e-04	<1.42e-15	2.85e-16	–	58.0	–	0.49	–	36.07
XMM-013[n]	4	11	1:32:44.83	30:22:14.54	47 ± 15	5.54e-04 ± 1.86e-04	<1.57e-15	4.93e-16	39.0	38.0	–	0.85	35.97	35.94
XMM-014[n]	–	12	1:32:45.47	30:23:14.15	15 ± 12	1.89e-04 ± 1.45e-04	<5.99e-16	<3.23e-16	–	45.0	–	0.59	–	35.84
XMM-015	5	13	1:32:46.61	30:34:37.00	253 ± 26	2.45e-03 ± 2.60e-04	4.89e-15	2.39e-15	45.0	42.0	0.78	0.89	36.08	35.97
XMM-016	–	14	1:32:51.84	30:51:08.98	19 ± 10	4.65e-04 ± 2.70e-04	<9.87e-16	1.03e-15	–	40.0	–	0.72	–	35.34
XMM-017[c]	6	15	1:32:52.76	30:38:12.57	55 ± 42	5.58e-04 ± 4.40e-04	<1.45e-15	<6.62e-16	56.0	56.0	0.55	0.57	36.38	36.28
XMM-018	–	16	1:32:52.80	30:31:34.23	15 ± 13	1.22e-04 ± 1.26e-04	<5.49e-16	<1.09e-16	–	68.0	–	0.56	–	36.37
XMM-019	7	18	1:32:53.36	30:48:23.06	53 ± 15	1.15e-03 ± 3.29e-04	1.61e-15	1.49e-15	73.0	56.0	–	0.81	35.88	35.78
XMM-020[x]	8	17	1:32:53.40	30:37:56.95	79 ± 31	8.88e-04 ± 3.54e-04	<1.23e-15	<6.10e-16	51.0	50.0	0.61	0.60	36.65	36.58
XMM-021	9	19	1:32:54.10	30:25:31.79	43 ± 19	4.37e-04 ± 2.43e-04	9.14e-16	<4.07e-16	39.0	42.0	–	0.81	36.18	36.15
XMM-022	10	21	1:32:55.96	30:40:33.57	134 ± 23	1.51e-03 ± 2.66e-04	2.68e-15	1.61e-15	93.0	96.0	0.81	0.87	36.83	36.79
XMM-023	–	20	1:32:56.12	30:33:30.44	68 ± 20	5.57e-04 ± 1.76e-04	8.14e-16	5.88e-16	–	80.0	–	0.85	–	36.30
XMM-024	11	22	1:32:57.10	30:39:25.87	474 ± 32	5.31e-03 ± 3.61e-04	8.80e-15	6.00e-15	20.0	22.0	0.84	0.83	36.46	36.42
XMM-025	–	23	1:32:57.18	30:39:14.69	31 ± 17	3.48e-04 ± 1.94e-04	<9.35e-16	<2.99e-16	–	37.0	–	0.47	–	35.93
XMM-026[t]	12	–	1:33:00.15	30:30:46.18	52 ± 41	3.96e-04 ± 3.17e-04	4.52e-16	<3.28e-16	52.0	–	–	–	37.43	–
XMM-027	13	24	1:33:00.40	30:44:07.57	407 ± 33	4.20e-03 ± 3.49e-04	6.37e-15	4.44e-15	33.0	34.0	0.47	0.56	35.72	35.73
XMM-028	14	25	1:33:00.67	30:30:59.28	31 ± 19	2.34e-04 ± 1.51e-04	<4.86e-16	<2.46e-16	46.0	46.0	–	0.56	37.20	37.21
XMM-029	15	26	1:33:01.51	30:30:49.59	45 ± 23	3.47e-04 ± 1.85e-04	<9.16e-16	<4.75e-16	28.0	26.0	–	0.54	36.32	36.43
XMM-030	16	27	1:33:02.93	30:32:29.65	93 ± 20	7.93e-04 ± 1.85e-04	1.04e-15	6.11e-16	51.0	49.0	0.97	0.74	36.40	36.34
XMM-031	17	28	1:33:03.58	30:31:18.27	225 ± 27	1.70e-03 ± 2.11e-04	3.15e-15	1.73e-15	33.0	34.0	1.07	1.10	36.15	36.11

ID	L10	LL14	RA	Dec	0.2-2.0 Cts	0.2-2.0 Ct Rate (s^{-1})	0.2-2.0 Flux erg s cm^{-2}	0.35-2.0 Flux erg s cm^{-2}	D(pc) L10	D(pc) LL14	[SII]/Hα L10	[SII]/Hα LL14	log(L(Hα) (erg s^{-1})) L10	log(L(Hα) (erg s^{-1})) LL14
XMM-032	18	29	1:33:04.07	30:39:51.65	217 ± 27	2.30e-03 ± 2.92e-04	3.07e-15	2.97e-15	30.0	33.0	0.49	0.66	36.64	36.62
XMM-033	19	–	1:33:07.55	30:42:52.51	71 ± 23	6.61e-04 ± 2.10e-04	1.22e-15	7.08e-16	71.0	–	–	–	36.82	–
XMM-034	–	30	1:33:08.77	30:12:15.64	928 ± 36	2.50e-02 ± 9.76e-04	4.28e-14	2.77e-14	–	27.0	–	0.60	–	35.60
XMM-035	20	31	1:33:08.93	30:26:57.31	181 ± 26	1.52e-03 ± 2.35e-04	2.21e-15	1.46e-15	51.0	50.0	–	0.79	36.26	36.22
XMM-036	–	32	1:33:09.69	30:16:39.01	21 ± 9	4.11e-04 ± 1.75e-04	7.12e-16	<3.27e-16	–	85.0	–	1.15	–	35.88
XMM-037	21	33	1:33:09.87	30:39:34.89	39 ± 22	4.25e-04 ± 2.35e-04	<8.31e-16	<5.73e-16	67.0	100.0	0.66	0.51	36.58	36.97
XMM-038	22	34	1:33:10.16	30:42:22.26	372 ± 35	3.61e-03 ± 3.45e-04	6.64e-15	3.95e-15	27.0	24.0	0.86	0.85	35.78	35.65
XMM-039	23	35	1:33:11.16	30:39:43.41	1807 ± 56	1.68e-02 ± 5.64e-04	2.88e-14	1.82e-14	25.0	24.0	0.78	0.68	35.93	36.00
XMM-040	24	36	1:33:11.28	30:34:23.46	15 ± 14	1.64e-04 ± 1.69e-04	<4.64e-16	<4.23e-16	99.0	92.0	0.49	0.45	37.08	37.05
XMM-041	25	37	1:33:11.80	30:38:40.48	21032 ± 190	1.89e-01 ± 1.76e-03	2.82e-13	2.18e-13	25.0	18.0	0.55	0.49	36.30	36.09
XMM-042	–	38	1:33:13.46	30:28:13.12	99 ± 22	7.04e-04 ± 1.58e-04	9.98e-16	6.20e-16	–	74.0	–	0.54	–	36.33
XMM-043	–	39	1:33:13.81	30:39:44.01	31 ± 20	2.89e-04 ± 1.95e-04	<7.41e-16	<4.31e-16	–	65.0	–	0.51	–	36.28
XMM-044	–	40	1:33:15.35	30:35:41.91	22 ± 18	2.12e-04 ± 1.68e-04	<4.84e-16	<2.51e-16	–	75.0	–	0.74	–	35.95
XMM-045	26	41	1:33:16.73	30:46:10.25	36 ± 17	4.70e-04 ± 2.45e-04	1.33e-15	9.01e-16	73.0	70.0	–	0.62	36.72	36.63
XMM-046	27	42	1:33:17.44	30:31:28.50	79 ± 22	5.17e-04 ± 1.46e-04	8.07e-16	5.74e-16	44.0	34.0	0.91	0.81	36.00	36.07
XMM-047	–	43	1:33:17.55	30:46:45.64	58 ± 19	6.50e-04 ± 2.23e-04	1.15e-15	9.53e-16	–	68.0	–	0.60	–	36.39
XMM-048	–	44	1:33:18.13	30:33:38.61	27 ± 15	2.17e-04 ± 1.26e-04	<6.57e-16	<2.53e-16	–	30.0	–	0.47	–	35.45
XMM-049	28	–	1:33:18.80	30:27:04.38	22 ± 17	1.67e-04 ± 1.23e-04	<4.60e-16	<1.63e-16	179.0	–	–	–	37.18	–
XMM-050	29	45	1:33:18.94	30:46:51.88	92 ± 19	1.21e-03 ± 2.55e-04	2.12e-15	7.01e-16	66.0	66.0	–	1.02	36.20	36.22
XMM-051	–	46	1:33:19.52	30:12:29.22	13 ± 8	3.57e-04 ± 2.08e-04	<7.96e-16	<3.80e-16	–	69.0	–	0.69	–	35.81
XMM-052	–	47	1:33:20.76	30:25:55.21	42 ± 18	2.75e-04 ± 1.24e-04	7.28e-16	<1.90e-16	–	16.0	–	0.46	–	35.27
XMM-053	–	48	1:33:21.19	30:19:20.61	35 ± 15	3.72e-04 ± 1.63e-04	9.76e-16	<3.18e-16	–	74.0	–	0.55	–	36.01
XMM-054[t]	–	49	1:33:21.33	30:30:31.63	1036 ± 341	6.54e-03 ± 2.18e-03	6.95e-15	5.19e-16	–	55.0	–	0.42	–	36.25
XMM-055[n]	30	50	1:33:21.64	30:31:31.09	79 ± 43	5.34e-04 ± 2.98e-04	6.12e-16	<4.80e-16	76.0	80.0	–	0.46	36.67	36.76
XMM-056	–	51	1:33:21.94	30:25:58.36	49 ± 19	3.15e-04 ± 1.23e-04	6.86e-16	<2.71e-16	–	36.0	–	0.51	–	36.05
XMM-057	31	52	1:33:22.67	30:27:04.00	87 ± 24	6.07e-04 ± 1.67e-04	8.09e-16	4.31e-16	20.0	20.0	0.95	1.00	35.84	35.78
XMM-058	32	53	1:33:23.85	30:26:13.53	66 ± 27	4.28e-04 ± 1.81e-04	7.63e-16	<5.65e-16	21.0	24.0	1.06	1.12	36.26	36.24
XMM-059	–	54	1:33:24.01	30:36:56.81	72 ± 21	6.53e-04 ± 1.96e-04	8.79e-16	6.35e-16	–	76.0	–	0.64	–	36.20
XMM-060	–	55	1:33:24.18	30:28:50.24	66 ± 22	4.10e-04 ± 1.39e-04	1.18e-15	<4.29e-16	–	50.0	–	1.05	–	35.69
XMM-061	33	56	1:33:27.07	30:47:48.65	36 ± 15	3.82e-04 ± 1.74e-04	1.10e-15	<3.84e-16	67.0	62.0	0.57	0.81	36.38	36.35
XMM-062	–	57	1:33:27.32	30:23:59.34	33 ± 16	2.49e-04 ± 1.28e-04	6.92e-16	<2.76e-16	–	34.0	–	0.48	–	35.60
XMM-063[n]	–	58	1:33:27.92	30:18:17.35	45 ± 14	5.70e-04 ± 1.90e-04	<9.07e-16	7.13e-16	–	40.0	–	0.93	–	35.69
XMM-064	–	59	1:33:28.00	30:16:01.14	10 ± 9	1.42e-04 ± 1.33e-04	<5.46e-16	<1.19e-16	–	37.0	–	0.81	–	35.28
XMM-065	34	60	1:33:28.11	30:31:33.53	749 ± 42	4.48e-03 ± 2.55e-04	7.23e-15	5.28e-15	32.0	32.0	0.55	0.55	36.38	36.31
XMM-066	35	–	1:33:28.92	30:47:43.95	736 ± 36	8.50e-03 ± 4.26e-04	1.50e-14	8.86e-15	19.0	–	0.36	–	35.76	–
XMM-067	36	61	1:33:29.08	30:42:15.99	3706 ± 78	3.29e-02 ± 7.08e-04	5.13e-14	3.88e-14	18.0	21.0	1.13	0.95	36.81	36.80
XMM-068	37	62	1:33:29.48	30:49:10.63	2170 ± 59	2.42e-02 ± 6.53e-04	4.04e-14	2.69e-14	32.0	31.0	0.75	0.78	35.86	35.81
XMM-069	–	63	1:33:29.79	31:01:53.00	52 ± 14	8.92e-04 ± 2.44e-04	3.78e-15	1.33e-15	–	47.0	–	0.79	–	35.71
XMM-070	38	64	1:33:30.21	30:47:43.83	27 ± 15	2.88e-04 ± 1.67e-04	<6.37e-16	<4.36e-16	51.0	40.0	0.31	0.45	36.43	36.26

ID	L10	LL14	RA	Dec	0.2-2.0 Cts	0.2-2.0 Ct Rate (s^{-1})	0.2-2.0 Flux erg s cm^{-2}	0.35-2.0 Flux erg s cm^{-2}	D(pc) L10	D(pc) LL14	[SII]/Hα L10	[SII]/Hα LL14	log(L(Hα) (erg s^{-1})) L10	log(L(Hα) (erg s^{-1})) LL14
XMM-071	–	65	1:33:30.64	30:21:01.49	57 ± 19	6.14e-04 ± 2.10e-04	1.63e-15	7.61e-16	–	88.0	–	0.79	–	36.40
XMM-072[n]	–	66	1:33:31.20	30:21:14.25	65 ± 19	6.39e-04 ± 1.91e-04	<1.35e-15	9.02e-16	–	58.0	–	0.78	–	36.09
XMM-073	39	67	1:33:31.30	30:33:32.42	7361 ± 106	5.16e-02 ± 7.56e-04	7.95e-14	6.00e-14	13.0	44.0	0.95	0.68	36.98	37.17
XMM-074	40	68	1:33:31.34	30:42:18.33	95 ± 27	8.40e-04 ± 2.34e-04	1.12e-15	1.05e-15	55.0	52.0	0.65	0.40	36.45	36.43
XMM-075	41	69	1:33:32.17	30:31:02.62	172 ± 30	1.04e-03 ± 1.81e-04	1.47e-15	1.28e-15	97.0	82.0	–	1.02	36.23	36.30
XMM-076	–	72	1:33:34.99	30:29:54.55	134 ± 26	8.38e-04 ± 1.61e-04	1.35e-15	6.54e-16	–	18.0	–	0.93	–	35.93
XMM-077	–	70	1:33:35.10	30:19:24.16	31 ± 15	3.38e-04 ± 1.65e-04	8.11e-16	<3.56e-16	–	63.0	–	0.81	–	35.78
XMM-078	42	71	1:33:35.14	30:23:07.44	96 ± 20	7.70e-04 ± 1.61e-04	9.27e-16	8.98e-16	43.0	42.0	–	1.51	35.98	35.47
XMM-079[t]	43	–	1:33:35.59	30:42:29.14	276 ± 56	2.49e-03 ± 5.10e-04	2.90e-15	5.45e-15	85.0	–	–	–	36.66	–
XMM-080	44	73	1:33:35.61	30:49:22.96	65 ± 18	7.11e-04 ± 1.98e-04	1.02e-15	7.51e-16	29.0	31.0	1.01	1.05	36.04	36.02
XMM-081[t]	–	–	1:33:35.81	30:31:13.67	322 ± 68	2.38e-03 ± 5.05e-04	2.54e-15	5.08e-15	–	–	–	–	–	–
XMM-082	45	74	1:33:35.97	30:36:26.68	1746 ± 56	1.43e-02 ± 4.73e-04	2.20e-14	1.73e-14	30.0	40.0	0.82	0.69	37.30	37.30
XMM-083[t]	46	76	1:33:36.92	30:32:54.24	3016 ± 531	2.19e-02 ± 3.79e-03	2.57e-14	6.86e-15	39.0	38.0	1.01	1.12	36.11	36.12
XMM-084	–	75	1:33:37.02	30:33:10.04	100 ± 27	6.78e-04 ± 1.88e-04	1.15e-15	7.27e-16	–	74.0	–	0.62	–	36.63
XMM-085	47	77	1:33:37.68	30:40:09.50	234 ± 30	2.01e-03 ± 2.58e-04	2.93e-15	2.63e-15	50.0	50.0	1.11	0.83	36.04	36.13
XMM-086	48	78	1:33:38.01	30:42:18.24	49 ± 21	5.34e-04 ± 2.12e-04	1.04e-15	<3.52e-16	21.0	27.0	0.66	0.57	35.99	36.10
XMM-087	–	79	1:33:38.65	31:02:38.78	25 ± 12	6.25e-04 ± 3.28e-04	1.63e-15	<7.02e-16	–	59.0	–	0.87	–	36.20
XMM-088	–	80	1:33:39.59	30:34:26.02	126 ± 28	8.35e-04 ± 1.93e-04	1.72e-15	3.75e-16	–	61.0	–	0.79	–	36.06
XMM-089	–	–	1:33:39.80	30:31:19.05	243 ± 30	1.99e-03 ± 2.64e-04	3.29e-15	2.15e-15	–	–	–	–	–	–
XMM-090	–	81	1:33:40.54	30:10:48.35	138 ± 17	5.39e-03 ± 6.81e-04	8.92e-15	5.41e-15	–	46.0	–	0.76	–	35.97
XMM-091[t]	49	82	1:33:40.66	30:39:40.85	67 ± 40	6.19e-04 ± 3.74e-04	6.67e-16	<1.60e-16	43.0	42.0	–	0.74	36.15	36.27
XMM-092	50	–	1:33:40.73	30:42:35.67	61 ± 22	6.32e-04 ± 2.33e-04	1.26e-15	6.84e-16	71.0	–	0.61	–	36.75	–
XMM-093	51	83	1:33:40.87	30:52:13.75	26 ± 13	2.69e-04 ± 1.67e-04	<7.77e-16	<2.13e-16	60.0	60.0	0.69	0.98	36.18	36.09
XMM-094	52	84	1:33:41.30	30:32:28.45	74 ± 32	4.91e-04 ± 2.09e-04	1.14e-15	<4.77e-16	33.0	40.0	–	0.51	35.95	35.96
XMM-095	–	–	1:33:41.44	30:42:20.77	696 ± 59	7.04e-03 ± 6.03e-04	1.17e-14	8.08e-15	–	–	–	–	–	–
XMM-096	53	85	1:33:41.71	30:21:04.10	7 ± 18	7.25e-05 ± 1.82e-04	<4.15e-16	<1.80e-16	34.0	36.0	0.44	0.62	36.71	36.68
XMM-097	54	86	1:33:42.24	30:20:57.75	24 ± 22	2.24e-04 ± 2.14e-04	<6.65e-16	<2.99e-16	45.0	44.0	–	0.83	36.52	36.49
XMM-098	55	87	1:33:42.91	30:41:49.51	110 ± 25	1.01e-03 ± 2.32e-04	1.34e-15	1.03e-15	44.0	74.0	–	0.50	36.08	36.74
XMM-099	56	88	1:33:43.49	30:41:03.76	61 ± 22	7.49e-04 ± 3.05e-04	1.82e-15	1.10e-15	23.0	26.0	0.89	0.78	35.92	35.99
XMM-100[t]	57	89	1:33:43.70	30:36:11.50	955 ± 161	6.42e-03 ± 1.07e-03	8.37e-15	1.11e-14	36.0	36.0	0.54	0.52	36.08	36.26
XMM-101	58	90	1:33:45.26	30:32:20.09	62 ± 23	4.88e-04 ± 1.76e-04	1.00e-15	<4.80e-16	67.0	70.0	–	0.54	36.86	36.88
XMM-102[c]	59	91	1:33:47.46	30:39:44.74	634 ± 74	6.07e-03 ± 7.15e-04	<6.88e-15	<1.65e-15	42.0	42.0	–	0.74	36.08	36.11
XMM-103[n]	–	92	1:33:47.52	30:17:13.75	57 ± 16	7.59e-04 ± 2.20e-04	<1.03e-15	7.80e-16	–	56.0	–	0.54	–	35.91
XMM-104	–	93	1:33:47.82	30:18:02.09	26 ± 15	3.40e-04 ± 2.04e-04	<9.04e-16	<3.23e-16	–	94.0	–	0.62	–	36.57
XMM-105	–	94	1:33:48.13	30:17:25.87	25 ± 12	3.30e-04 ± 1.62e-04	7.96e-16	<1.91e-16	–	19.0	–	0.46	–	34.85
XMM-106[c]	60	95	1:33:48.35	30:39:28.44	59600 ± 797	5.32e-01 ± 7.20e-03	<4.97e-13	<4.80e-13	14.0	14.0	0.74	0.63	36.00	35.95
XMM-107	61	96	1:33:48.49	30:33:04.39	1419 ± 62	1.03e-02 ± 4.59e-04	1.56e-14	1.28e-14	60.0	40.0	0.74	0.98	37.20	36.52
XMM-108[t]	62	97	1:33:49.75	30:30:49.66	54 ± 39	4.15e-04 ± 2.93e-04	4.94e-16	<3.59e-16	73.0	56.0	–	0.59	36.28	36.24
XMM-109	63	98	1:33:49.90	30:30:16.72	52 ± 17	4.43e-04 ± 1.44e-04	8.48e-16	<3.71e-16	54.0	46.0	–	0.95	35.74	35.69

ID	L10	LL14	RA	Dec	0.2-2.0 Cts	0.2-2.0 Ct Rate (s^{-1})	0.2-2.0 Flux erg s cm^{-2}	0.35-2.0 Flux erg s cm^{-2}	D(pc) L10	D(pc) LL14	[SII]/Hα L10	[SII]/Hα LL14	log(L(Hα) (erg s^{-1})) L10	log(L(Hα) (erg s^{-1})) LL14
XMM-110[t]	64	99	1:33:50.12	30:35:28.58	163 ± 55	1.34e-03 ± 4.61e-04	9.01e-16	5.77e-15	48.0	50.0	0.83	0.74	36.30	36.36
XMM-111	65	100	1:33:51.06	30:43:56.17	92 ± 21	7.26e-04 ± 1.71e-04	1.20e-15	6.56e-16	50.0	48.0	0.63	0.55	36.73	36.70
XMM-112	66	101	1:33:51.67	30:30:59.65	90 ± 22	6.65e-04 ± 1.62e-04	1.12e-15	7.42e-16	59.0	58.0	1.65	1.00	36.11	36.07
XMM-113	67	102	1:33:51.71	30:30:43.45	23 ± 16	2.00e-04 ± 1.35e-04	<4.78e-16	<2.52e-16	45.0	44.0	–	0.74	35.98	35.97
XMM-114	68	–	1:33:52.53	30:56:35.22	87 ± 19	8.80e-04 ± 1.95e-04	1.40e-15	9.14e-16	109.0	–	–	–	36.43	–
XMM-115	–	103	1:33:52.56	30:28:38.44	19 ± 14	1.31e-04 ± 1.02e-04	<2.89e-16	<1.96e-16	–	40.0	–	0.44	–	35.62
XMM-116	69	104	1:33:54.47	30:33:49.12	667 ± 53	4.99e-03 ± 4.11e-04	7.92e-15	5.99e-15	47.0	49.0	0.82	0.83	36.51	36.58
XMM-117	–	106	1:33:54.69	30:18:50.96	69 ± 16	8.27e-04 ± 2.04e-04	1.25e-15	8.58e-16	–	72.0	–	0.91	–	36.07
XMM-118	70	105	1:33:54.84	30:45:19.02	633 ± 43	3.91e-03 ± 2.72e-04	6.36e-15	3.66e-15	21.0	38.0	0.83	0.76	36.57	36.93
XMM-119	71	107	1:33:54.93	30:33:10.20	4344 ± 82	4.06e-02 ± 7.81e-04	6.82e-14	4.43e-14	20.0	26.0	0.83	0.87	36.91	36.91
XMM-120[c]	72	108	1:33:55.01	30:39:57.33	27602 ± 814	2.30e-01 ± 6.45e-03	<3.52e-13	<2.82e-13	32.0	32.0	–	0.79	35.65	35.74
XMM-121	–	109	1:33:55.29	30:16:48.95	26 ± 14	3.54e-04 ± 1.86e-04	<9.02e-16	<2.38e-16	–	31.0	–	0.54	–	35.28
XMM-122	73	110	1:33:56.44	30:21:24.72	177 ± 26	1.67e-03 ± 2.51e-04	2.17e-15	1.14e-15	57.0	58.0	–	0.93	36.34	36.32
XMM-123[t]	74	111	1:33:56.97	30:34:58.69	21 ± 40	1.29e-04 ± 2.62e-04	1.40e-16	<2.90e-16	31.0	31.0	0.67	1.02	36.08	36.25
XMM-124	75	112	1:33:57.13	30:40:48.54	23 ± 15	1.50e-04 ± 1.19e-04	<4.04e-16	8.68e-17	44.0	42.0	1.16	0.83	36.00	35.98
XMM-125	76	113	1:33:57.13	30:35:06.05	12 ± 22	7.32e-05 ± 1.44e-04	<4.23e-16	<2.30e-16	21.0	19.0	–	0.50	36.11	36.03
XMM-126	–	114	1:33:57.41	31:00:55.81	12 ± 11	1.55e-04 ± 1.59e-04	<5.64e-16	<3.00e-16	–	60.0	–	0.51	–	36.04
XMM-127	77	115	1:33:58.06	30:32:09.64	68 ± 21	5.08e-04 ± 1.68e-04	7.32e-16	6.73e-16	24.0	24.0	0.40	0.37	36.28	36.28
XMM-128	78	116	1:33:58.07	30:37:54.57	216 ± 32	1.88e-03 ± 2.77e-04	3.72e-15	9.02e-16	16.0	22.0	1.19	0.95	36.04	36.12
XMM-129	80	117	1:33:58.14	30:36:23.30	183 ± 31	1.18e-03 ± 2.05e-04	1.65e-15	1.13e-15	8.0	15.0	0.96	0.98	35.46	35.59
XMM-130	79	–	1:33:58.15	30:48:36.45	75 ± 21	6.83e-04 ± 1.96e-04	8.63e-16	8.87e-16	58.0	–	–	–	36.63	–
XMM-131	82	118	1:33:58.18	30:51:53.72	140 ± 23	1.32e-03 ± 2.19e-04	2.19e-15	1.31e-15	56.0	54.0	1.07	0.91	36.18	36.16
XMM-132	81	119	1:33:58.52	30:33:32.60	1152 ± 51	1.03e-02 ± 4.68e-04	1.80e-14	1.13e-14	34.0	48.0	0.73	0.52	36.23	36.48
XMM-133	–	120	1:33:59.15	30:32:42.06	52 ± 22	4.58e-04 ± 1.99e-04	8.37e-16	<3.78e-16	–	39.0	–	0.50	–	36.23
XMM-134	83	121	1:33:59.93	30:34:21.18	32 ± 26	1.98e-04 ± 1.78e-04	<6.25e-16	<4.27e-16	31.0	–	0.63	–	36.72	–
XMM-135	85	124	1:34:00.00	30:47:23.28	245 ± 31	1.72e-03 ± 2.26e-04	2.85e-15	1.79e-15	43.0	46.0	–	1.00	36.08	36.15
XMM-136	84	123	1:34:00.19	30:42:18.52	653 ± 40	4.43e-03 ± 2.77e-04	7.70e-15	4.72e-15	32.0	36.0	1.23	0.93	36.28	36.27
XMM-137[t]	–	122	1:34:00.25	30:39:28.87	451 ± 96	2.93e-03 ± 7.65e-04	3.69e-15	3.33e-14	–	40.0	–	0.81	–	36.09
XMM-138	–	125	1:34:00.58	30:50:42.87	77 ± 18	6.10e-04 ± 1.49e-04	5.29e-16	4.08e-16	–	23.0	–	0.93	–	35.04
XMM-139	86	126	1:34:00.60	30:49:04.29	259 ± 29	1.82e-03 ± 2.02e-04	3.28e-15	1.52e-15	13.0	12.0	0.80	0.60	34.98	34.88
XMM-140[t]	87	127	1:34:01.26	30:35:14.97	2298 ± 411	1.64e-02 ± 2.99e-03	2.05e-14	7.15e-15	48.0	48.0	0.90	0.85	36.04	36.19
XMM-141	–	128	1:34:02.10	30:28:34.52	25 ± 13	1.67e-04 ± 9.73e-05	<4.46e-16	<7.58e-17	–	37.0	–	0.48	–	35.44
XMM-142	88	129	1:34:02.58	30:31:02.62	81 ± 19	1.05e-03 ± 2.56e-04	1.66e-15	7.42e-16	60.0	53.0	0.96	0.89	36.23	36.24
XMM-143	89	130	1:34:03.23	30:36:26.53	1330 ± 97	8.78e-03 ± 6.48e-04	1.62e-14	8.79e-15	92.0	90.0	–	0.49	37.11	37.11
XMM-144	90	131	1:34:03.52	30:44:42.40	235 ± 31	1.38e-03 ± 1.84e-04	2.67e-15	1.27e-15	42.0	44.0	1.03	0.79	36.04	36.08
XMM-145	91	132	1:34:04.15	30:32:57.50	298 ± 30	2.08e-03 ± 2.13e-04	4.27e-15	2.14e-15	36.0	32.0	–	1.00	35.36	35.44
XMM-146	–	133	1:34:04.88	30:58:30.71	13 ± 12	1.24e-04 ± 1.25e-04	<5.69e-16	<9.22e-17	–	72.0	–	0.46	–	36.07
XMM-147	–	134	1:34:05.55	31:07:25.08	136 ± 16	3.84e-03 ± 4.75e-04	1.63e-14	6.97e-15	–	55.0	–	0.71	–	35.60
XMM-148	92	135	1:34:07.30	30:36:20.14	220 ± 33	1.62e-03 ± 2.44e-04	2.43e-15	1.49e-15	101.0	96.0	0.71	0.78	36.89	36.92

ID	L10	LL14	RA	Dec	0.2-2.0 Cts	0.2-2.0 Ct Rate (s^{-1})	0.2-2.0 Flux erg s cm^{-2}	0.35-2.0 Flux erg s cm^{-2}	D(pc) L10	D(pc) LL14	[SII]/Hα L10	[SII]/Hα LL14	log(L(Hα) (erg s^{-1})) L10	log(L(Hα) (erg s^{-1})) LL14
XMM-149	93	136	1:34:07.47	30:37:07.61	407 ± 36	2.26e-03 ± 1.99e-04	3.78e-15	2.48e-15	20.0	16.0	0.95	0.87	35.32	35.26
XMM-150[n]	–	137	1:34:07.98	31:01:03.72	42 ± 13	5.43e-04 ± 2.07e-04	<1.42e-15	9.61e-16	–	54.0	–	0.55	–	36.06
XMM-151	94	138	1:34:08.36	30:46:32.70	1267 ± 51	6.98e-03 ± 2.82e-04	1.26e-14	7.60e-15	20.0	19.0	0.75	0.50	35.71	35.63
XMM-152[t]	95	139	1:34:10.14	30:47:16.78	247 ± 56	1.46e-03 ± 3.41e-04	1.71e-15	1.64e-15	23.0	26.0	0.83	0.78	35.60	35.74
XMM-153	96	140	1:34:10.65	30:42:23.51	2947 ± 69	2.05e-02 ± 4.91e-04	3.75e-14	2.13e-14	18.0	23.0	1.25	1.17	36.70	36.70
XMM-154	97	141	1:34:10.92	30:39:00.70	139 ± 25	9.47e-04 ± 1.76e-04	1.53e-15	9.73e-16	14.0	16.0	1.15	0.74	35.40	35.56
XMM-155	–	142	1:34:11.21	30:24:15.32	46 ± 17	4.14e-04 ± 1.62e-04	9.80e-16	5.95e-16	–	42.0	–	0.62	–	35.45
XMM-156	–	143	1:34:12.28	31:02:43.42	14 ± 10	2.20e-04 ± 1.67e-04	<3.57e-16	<2.71e-16	–	55.0	–	0.48	–	35.81
XMM-157	98	–	1:34:12.69	30:35:11.98	44 ± 20	2.63e-04 ± 1.20e-04	6.50e-16	<2.69e-16	67.0	–	0.46	–	36.58	–
XMM-158	–	144	1:34:12.90	30:23:24.28	32 ± 14	2.83e-04 ± 1.32e-04	8.24e-16	<2.42e-16	–	46.0	–	0.50	–	35.63
XMM-159	99	145	1:34:13.02	30:48:36.11	99 ± 26	6.18e-04 ± 1.63e-04	9.80e-16	6.50e-16	51.0	46.0	–	0.69	36.49	36.48
XMM-160	100	146	1:34:13.65	30:43:27.01	98 ± 21	6.08e-04 ± 1.35e-04	9.70e-16	5.25e-16	26.0	27.0	0.87	0.79	35.62	35.63
XMM-161	101	147	1:34:13.71	30:48:17.47	106 ± 24	6.64e-04 ± 1.54e-04	8.99e-16	4.48e-16	58.0	62.0	–	0.76	36.51	36.70
XMM-162	–	148	1:34:13.85	30:30:39.82	17 ± 13	1.02e-04 ± 8.74e-05	<2.10e-16	<1.22e-16	–	16.0	–	0.39	–	35.22
XMM-163	102	149	1:34:14.10	30:34:30.92	70 ± 23	4.41e-04 ± 1.43e-04	5.47e-16	4.87e-16	39.0	40.0	0.46	0.52	36.71	36.74
XMM-164	103	150	1:34:14.35	30:41:53.59	53 ± 21	3.44e-04 ± 1.36e-04	1.11e-15	<3.93e-16	48.0	44.0	1.08	0.85	36.00	35.91
XMM-165	105	152	1:34:14.37	30:53:52.65	301 ± 28	2.73e-03 ± 2.63e-04	4.35e-15	2.85e-15	50.0	58.0	1.02	1.00	36.45	36.50
XMM-166	104	151	1:34:14.38	30:39:41.56	132 ± 24	9.10e-04 ± 1.75e-04	1.63e-15	7.52e-16	39.0	38.0	1.05	1.05	36.00	35.99
XMM-167	–	153	1:34:14.55	30:44:36.18	24 ± 16	1.44e-04 ± 1.04e-04	<3.24e-16	<1.29e-16	–	51.0	–	0.74	–	36.10
XMM-168	106	154	1:34:14.67	30:31:50.92	76 ± 20	5.81e-04 ± 1.56e-04	8.91e-16	6.66e-16	66.0	66.0	–	1.10	35.93	35.85
XMM-169	107	155	1:34:15.69	30:33:00.67	279 ± 31	1.60e-03 ± 1.83e-04	2.64e-15	1.97e-15	33.0	34.0	0.74	0.69	35.97	36.01
XMM-170	108	156	1:34:16.31	30:52:32.74	109 ± 23	7.47e-04 ± 1.61e-04	1.27e-15	6.49e-16	77.0	80.0	0.80	0.60	36.56	36.84
XMM-171	110	158	1:34:16.46	30:33:55.07	182 ± 30	1.16e-03 ± 1.96e-04	1.75e-15	1.26e-15	54.0	52.0	–	0.52	36.71	36.78
XMM-172[x]	109	157	1:34:16.50	30:51:53.86	937 ± 48	6.29e-03 ± 3.23e-04	<1.08e-14	<7.74e-15	25.0	32.0	0.28	0.40	36.72	36.86
XMM-173	111	159	1:34:17.50	30:41:22.64	436 ± 34	2.76e-03 ± 2.21e-04	5.02e-15	2.83e-15	51.0	52.0	1.04	0.89	36.38	36.38
XMM-174	112	160	1:34:18.32	30:54:05.78	27 ± 14	3.10e-04 ± 1.61e-04	<7.11e-16	<3.18e-16	84.0	80.0	–	0.98	36.15	36.08
XMM-175	113	161	1:34:19.28	30:33:45.91	19 ± 21	1.27e-04 ± 1.32e-04	<3.20e-16	<1.83e-16	38.0	40.0	0.62	0.46	36.81	36.89
XMM-176	–	162	1:34:19.45	30:52:48.89	91 ± 22	6.71e-04 ± 1.64e-04	8.95e-16	6.93e-16	–	75.0	–	0.87	–	36.09
XMM-177	–	163	1:34:19.68	30:33:41.51	53 ± 23	3.35e-04 ± 1.46e-04	6.82e-16	<4.30e-16	–	38.0	–	0.36	–	36.82
XMM-178	114	164	1:34:19.87	30:33:56.02	23 ± 21	1.36e-04 ± 1.40e-04	<4.85e-16	<1.94e-16	22.0	30.0	0.74	0.69	36.49	36.63
XMM-179	116	166	1:34:22.94	30:54:22.95	172 ± 25	2.49e-03 ± 3.81e-04	3.60e-15	2.92e-15	42.0	10.0	0.86	0.89	34.99	34.73
XMM-180	115	165	1:34:23.34	30:25:26.85	152 ± 22	1.36e-03 ± 2.01e-04	1.91e-15	1.57e-15	47.0	50.0	–	0.78	35.92	35.96
XMM-181	–	167	1:34:24.08	30:33:24.41	63 ± 23	3.88e-04 ± 1.44e-04	9.58e-16	<4.45e-16	–	60.0	–	0.44	–	36.32
XMM-182	–	168	1:34:24.48	30:48:58.35	23 ± 13	1.76e-04 ± 1.08e-04	<3.27e-16	<1.24e-16	–	80.0	–	0.48	–	36.56
XMM-183	117	169	1:34:25.40	30:54:57.44	110 ± 23	1.20e-03 ± 2.56e-04	1.44e-15	1.10e-15	66.0	64.0	0.78	0.87	36.78	36.63
XMM-184[n]	118	170	1:34:25.41	30:48:30.95	46 ± 19	3.69e-04 ± 1.47e-04	7.96e-16	<4.65e-16	53.0	44.0	1.06	0.93	35.95	35.88
XMM-185	119	171	1:34:25.82	30:33:17.02	342 ± 31	2.43e-03 ± 2.28e-04	2.87e-15	2.79e-15	33.0	26.0	–	0.49	35.38	35.15
XMM-186	120	172	1:34:29.61	30:41:33.38	27 ± 16	1.86e-04 ± 1.14e-04	<3.63e-16	<2.21e-16	43.0	42.0	0.82	0.59	36.08	36.22
XMM-187[t]	–	173	1:34:30.22	30:35:10.51	163 ± 46	9.79e-04 ± 2.92e-04	1.14e-15	4.40e-16	–	85.0	–	0.54	–	36.05

ID	L10	LL14	RA	Dec	0.2-2.0 Cts	0.2-2.0 Ct Rate (s^{-1})	0.2-2.0 Flux erg s cm^{-2}	0.35-2.0 Flux erg s cm^{-2}	D(pc) L10	D(pc) LL14	[SII]/Hα L10	[SII]/Hα LL14	log(L(Hα) (erg s^{-1})) L10	log(L(Hα) (erg s^{-1})) LL14
XMM-188	121	175	1:34:30.29	30:35:44.80	119 ± 26	7.07e-04 ± 1.54e-04	1.26e-15	4.97e-16	54.0	52.0	1.04	1.00	36.18	36.19
XMM-189	122	174	1:34:30.93	30:56:39.82	164 ± 22	1.82e-03 ± 2.44e-04	3.16e-15	1.78e-15	111.0	34.0	–	0.98	36.84	35.83
XMM-190	123	176	1:34:32.63	30:35:30.37	154 ± 25	8.41e-04 ± 1.42e-04	1.21e-15	9.19e-16	41.0	40.0	–	1.02	36.00	35.92
XMM-191	124	177	1:34:33.03	30:46:37.65	94 ± 32	7.88e-04 ± 3.30e-04	1.36e-15	9.95e-16	11.0	16.0	0.66	0.62	36.65	36.73
XMM-192	125	178	1:34:35.52	30:52:10.97	130 ± 23	1.33e-03 ± 2.51e-04	2.83e-15	1.25e-15	39.0	38.0	–	0.87	35.71	35.69
XMM-193	126	179	1:34:36.22	30:36:23.56	38 ± 20	2.19e-04 ± 1.19e-04	<4.85e-16	<1.91e-16	46.0	40.0	–	0.60	36.04	35.86
XMM-194	–	180	1:34:37.40	30:44:11.03	21 ± 13	1.82e-04 ± 1.13e-04	<4.29e-16	<2.39e-16	–	61.0	–	0.48	–	36.52
XMM-195	127	181	1:34:38.73	30:37:56.82	90 ± 23	5.27e-04 ± 1.38e-04	6.83e-16	4.86e-16	86.0	80.0	–	0.41	36.63	36.57
XMM-196	–	182	1:34:39.69	30:39:17.55	37 ± 15	2.42e-04 ± 1.10e-04	6.81e-16	<2.08e-16	–	64.0	–	0.71	–	35.95
XMM-197	–	183	1:34:39.94	31:06:02.72	12 ± 8	2.08e-04 ± 1.35e-04	<4.85e-16	<1.56e-16	–	53.0	–	0.93	–	35.76
XMM-198	128	184	1:34:40.74	30:43:36.44	62 ± 20	5.32e-04 ± 1.75e-04	7.17e-16	<3.25e-16	22.0	36.0	0.77	0.87	36.41	36.73
XMM-199	129	185	1:34:41.09	30:43:26.33	669 ± 36	5.45e-03 ± 2.96e-04	9.93e-15	6.70e-15	39.0	50.0	1.07	0.91	36.86	36.96
XMM-200	130	186	1:34:41.23	30:43:55.38	31 ± 16	2.99e-04 ± 1.55e-04	<4.38e-16	<2.36e-16	35.0	32.0	–	0.72	35.57	35.80
XMM-201	131	–	1:34:41.89	30:37:35.25	41 ± 17	2.16e-04 ± 1.13e-04	4.28e-16	<2.56e-16	156.0	–	–	–	36.92	–
XMM-202	–	187	1:34:42.68	30:40:51.50	21 ± 14	1.64e-04 ± 1.15e-04	<4.10e-16	<2.25e-16	–	39.0	–	0.62	–	35.58
XMM-203[t]	–	188	1:34:44.02	31:01:48.89	1 ± 12	2.39e-05 ± 1.76e-04	1.08e-17	<7.50e-17	–	80.0	–	0.66	–	35.86
XMM-204	132	–	1:34:44.62	30:42:38.79	11 ± 11	8.86e-05 ± 8.62e-05	<3.31e-16	<5.88e-17	55.0	–	–	–	36.46	–
XMM-205[x]	–	189	1:34:45.40	30:35:35.18	93 ± 24	6.12e-04 ± 1.62e-04	<1.26e-15	<6.01e-16	–	49.0	–	0.91	–	35.65
XMM-206	–	190	1:34:45.88	30:57:19.13	32 ± 13	3.52e-04 ± 1.65e-04	8.26e-16	4.52e-16	–	50.0	–	0.91	–	35.66
XMM-207	–	191	1:34:47.24	30:34:24.98	32 ± 14	2.89e-04 ± 1.33e-04	6.83e-16	<3.05e-16	–	37.0	–	0.44	–	35.59
XMM-208	–	192	1:34:50.48	31:07:38.63	13 ± 7	2.49e-04 ± 1.42e-04	<2.61e-16	<8.24e-17	–	55.0	–	0.45	–	35.76
XMM-209[t]	–	193	1:34:52.48	30:50:22.22	59 ± 33	7.29e-04 ± 4.31e-04	6.54e-16	<1.90e-16	–	84.0	–	0.98	–	35.89
XMM-210	133	–	1:34:54.88	30:41:16.95	47 ± 17	3.81e-04 ± 1.41e-04	8.78e-16	6.41e-16	75.0	–	–	–	36.84	–
XMM-211[n]	134	194	1:34:56.44	30:36:23.16	66 ± 18	7.32e-04 ± 1.97e-04	<1.36e-15	8.27e-16	58.0	56.0	–	0.91	35.83	35.81
XMM-212[n]	–	195	1:34:58.60	31:10:09.50	38 ± 12	1.13e-03 ± 3.50e-04	<1.57e-15	1.11e-15	–	44.0	–	0.60	–	35.66
XMM-213	–	196	1:34:59.19	30:40:16.49	43 ± 16	3.84e-04 ± 1.58e-04	8.01e-16	6.61e-16	–	36.0	–	0.79	–	35.60
XMM-214	135	197	1:35:00.36	30:40:04.97	47 ± 16	4.70e-04 ± 1.57e-04	9.16e-16	5.52e-16	65.0	58.0	–	0.68	36.32	36.27
XMM-215	–	198	1:35:00.40	31:02:36.37	7 ± 9	1.17e-04 ± 1.53e-04	<3.97e-16	<1.74e-16	–	72.0	–	0.52	–	35.94
XMM-216	136	–	1:35:01.22	30:38:17.07	23 ± 11	2.25e-04 ± 1.13e-04	4.79e-16	<2.76e-16	128.0	–	–	–	36.72	–
XMM-217[t]	–	199	1:35:01.82	30:39:53.94	24 ± 24	2.20e-04 ± 2.22e-04	1.26e-16	<1.48e-16	–	80.0	–	0.56	–	36.46
XMM-218[x]	137	–	1:35:02.80	30:37:08.60	181 ± 21	2.67e-03 ± 3.24e-04	<3.45e-15	<3.31e-15	127.0	–	–	–	36.67	–

[c] Flux is contaminated by nearby bright X-ray source, but source has a previous X-ray detection. Flux is an upper limit.

[b] Unrealistic source count errors from `emldetect` in at least one individual band. Source count errors pegged to total count values.

[n] Determined to be a nondetection via by-eye catalog checking. Flux is an upper limit.

[t] Total counts in the full band are discrepant by a factor of two from the summation of counts in each individual band due an `emldetect` merging issue. Total counts in the 0.2-2.0 keV band are reported as the sum of counts in the 0.2-0.5 keV, 0.5-1.0 keV, and 1.0-2.0 keV band.

[x] Flux is contaminated by nearby bright X-ray source, but source does not have a previous X-ray detection. Flux is an upper limit.

Table 3.3: All 105 3σ SNRs detected in our sample. Columns 1-3: lD number from this catalog, and the RA and Dec from this catalog. Column 4: source counts and associated errors in the 0.2-2.0 keV band (used for detection). Column 5: source counts and associated errors in the 0.35-2.0 keV band (used for comparison to L10). Columns 6-8: source counts and errors in the 0.3-0.7 keV, 0.7-1.1 keV, and 1.1-4.2 keV bands, which are used for computing the HRs shown in Figure 3.7. Columns 9-10: HRs and errors in the aforementioned bands (HR1 = (M-S)/(H+M+S), HR2 = (H-M)/(H+M+S)). Columns 11-12: HRs and errors computed from the 0.2-0.5 keV, 0.5-1.0 keV, and 1.0-2.0 keV bands ($HR1_{XMM}$ = (M-S)/(S+M), $HR2_{XMM}$ = (H-M)/(H+M)). Column 13: measurement level in L10: 3σ, 2σ, or upper limit (<).

ID	RA	Dec	0.2-2.0 keV Cts	0.35-2.0 keV Cts	0.3-0.7 keV Cts	0.7-1.1 keV Cts	1.1-4.2 keV Cts	HR1	HR2	$HR1_{XMM}$	$HR2_{XMM}$	L10 Detect
XMM-003	1:32:30.83	30:27:45.99	107 ± 19	98 ± 19	55 ± 13	48 ± 11	15 ± 11	-0.14 ± 0.02	-0.29 ± 0.01	0.49 ± 0.05	0.18 ± 0.04	–
XMM-004	1:32:31.41	30:35:32.90	66 ± 19	53 ± 18	10 ± 10	25 ± 9	13 ± 16	0.04 ± 0.02	-0.34 ± 0.02	–	–	<
XMM-006	1:32:37.36	30:18:03.10	296 ± 23	286 ± 22	45 ± 9	104 ± 12	222 ± 20	-0.16 ± 0.02	-0.31 ± 0.02	0.47 ± 0.01	-0.47 ± 0.01	–
XMM-009	1:32:40.53	30:16:37.20	74 ± 13	79 ± 13	12 ± 6	14 ± 6	91 ± 14	0.10 ± 0.03	-0.21 ± 0.03	0.90 ± 0.07	0.60 ± 0.03	–
XMM-015	1:32:46.61	30:34:37.00	253 ± 26	207 ± 25	163 ± 19	35 ± 10	27 ± 14	-0.31 ± 0.05	-0.16 ± 0.05	0.47 ± 0.22	0.79 ± 0.04	3σ
XMM-019	1:32:53.36	30:48:23.06	53 ± 15	41 ± 14	18 ± 9	22 ± 8	8 ± 9	0.02 ± 0.06	-0.33 ± 0.09	–	–	2σ
XMM-022	1:32:55.96	30:40:33.57	134 ± 23	123 ± 23	59 ± 14	32 ± 10	61 ± 18	-0.30 ± 0.07	-0.05 ± 0.10	0.60 ± 0.06	0.27 ± 0.04	<
XMM-023	1:32:56.12	30:33:30.44	68 ± 20	57 ± 18	32 ± 12	19 ± 10	23 ± 14	-0.73 ± 0.05	-0.01 ± 0.05	–	–	–
XMM-024	1:32:57.10	30:39:25.87	474 ± 32	443 ± 31	241 ± 21	203 ± 19	42 ± 15	0.18 ± 0.08	0.39 ± 0.09	0.57 ± 0.03	0.22 ± 0.02	3σ
XMM-027	1:33:00.40	30:44:07.57	407 ± 33	363 ± 32	245 ± 24	113 ± 17	100 ± 24	0.08 ± 0.01	0.75 ± 0.02	0.71 ± 0.04	0.41 ± 0.02	3σ
XMM-030	1:33:02.93	30:32:29.65	93 ± 20	83 ± 21	19 ± 11	66 ± 13	10 ± 12	0.04 ± 0.12	-0.40 ± 0.13	–	–	3σ
XMM-031	1:33:03.58	30:31:18.27	225 ± 27	192 ± 27	113 ± 19	58 ± 14	57 ± 17	-0.05 ± 0.08	-0.05 ± 0.12	0.43 ± 0.04	0.07 ± 0.04	<
XMM-032	1:33:04.07	30:39:51.65	217 ± 27	230 ± 28	53 ± 15	105 ± 16	66 ± 21	-0.07 ± 0.06	-0.25 ± 0.08	0.73 ± 0.11	0.55 ± 0.04	3σ
XMM-033	1:33:07.55	30:42:52.51	71 ± 23	50 ± 20	23 ± 11	7 ± 9	34 ± 19	-0.33 ± 0.10	-0.09 ± 0.12	–	–	<
XMM-034	1:33:08.77	30:12:15.64	928 ± 36	862 ± 35	584 ± 28	281 ± 19	41 ± 11	-0.61 ± 0.14	-0.05 ± 0.12	0.63 ± 0.01	-0.64 ± 0.01	–
XMM-035	1:33:08.93	30:26:57.31	181 ± 26	156 ± 25	59 ± 15	79 ± 14	55 ± 19	-0.05 ± 0.12	-0.34 ± 0.14	0.33 ± 0.53	0.94 ± 0.04	2σ
XMM-038[e]	1:33:10.16	30:42:22.26	372 ± 35	333 ± 33	145 ± 145	126 ± 126	114 ± 25	-0.13 ± 0.15	-0.14 ± 0.19	0.35 ± 0.02	-0.75 ± 0.03	3σ
XMM-039	1:33:11.16	30:39:43.41	1807 ± 56	1614 ± 54	1096 ± 42	515 ± 30	91 ± 21	0.03 ± 0.10	0.68 ± 0.14	0.43 ± 0.01	0.10 ± 0.01	3σ
XMM-041	1:33:11.80	30:38:40.48	21032 ± 190	20152 ± 190	8698 ± 133	9787 ± 137	2230 ± 60	-0.17 ± 0.12	-0.22 ± 0.14	0.54 ± 0.00	0.29 ± 0.00	3σ
XMM-042	1:33:13.46	30:28:13.12	99 ± 22	76 ± 21	33 ± 14	29 ± 11	45 ± 18	-0.26 ± 0.15	-0.20 ± 0.16	–	–	–
XMM-046	1:33:17.44	30:31:28.50	79 ± 22	61 ± 20	22 ± 13	13 ± 10	75 ± 19	0.30 ± 0.14	0.03 ± 0.17	–	–	<
XMM-050	1:33:18.94	30:46:51.88	92 ± 19	65 ± 19	46 ± 13	17 ± 8	61 ± 15	-0.08 ± 0.11	-0.11 ± 0.15	–	–	2σ
XMM-054[t]	1:33:21.33	30:30:31.63	1036 ± 341	68 ± 21	49 ± 16	910 ± 303	76 ± 22	-0.07 ± 0.19	-0.29 ± 0.19	–	–	–
XMM-057	1:33:22.67	30:27:04.00	87 ± 24	53 ± 20	42 ± 14	25 ± 13	27 ± 17	-0.34 ± 0.14	-0.11 ± 0.15	–	–	<
XMM-059	1:33:24.01	30:36:56.81	72 ± 21	47 ± 18	15 ± 11	18 ± 9	40 ± 20	-0.01 ± 0.19	-0.27 ± 0.19	–	–	–
XMM-065	1:33:28.11	30:31:33.53	749 ± 42	729 ± 42	430 ± 30	255 ± 23	81 ± 22	-0.06 ± 0.28	-0.06 ± 0.31	0.36 ± 0.02	-0.03 ± 0.02	3σ
XMM-066	1:33:28.92	30:47:43.95	736 ± 36	660 ± 35	464 ± 27	200 ± 19	57 ± 17	-0.11 ± 0.24	-0.02 ± 0.29	0.62 ± 0.02	0.24 ± 0.01	3σ
XMM-067	1:33:29.08	30:42:15.99	3706 ± 78	3568 ± 76	1546 ± 50	1692 ± 50	452 ± 34	-0.57 ± 0.22	0.16 ± 0.20	0.80 ± 0.01	0.44 ± 0.00	3σ
XMM-068	1:33:29.48	30:49:10.63	2170 ± 59	1987 ± 56	1127 ± 41	790 ± 34	149 ± 22	0.09 ± 0.20	0.23 ± 0.26	0.64 ± 0.01	0.31 ± 0.01	3σ
XMM-069	1:33:29.79	31:01:53.00	52 ± 14	43 ± 14	27 ± 9	8 ± 6	14 ± 10	0.25 ± 0.14	0.28 ± 0.22	–	–	–
XMM-073	1:33:31.30	30:33:32.42	7361 ± 106	7084 ± 118	3349 ± 71	2741 ± 63	1276 ± 51	-0.07 ± 0.46	0.06 ± 0.49	0.49 ± 0.00	0.19 ± 0.00	3σ
XMM-074	1:33:31.34	30:42:18.33	95 ± 27	103 ± 28	32 ± 16	43 ± 16	37 ± 17	-0.03 ± 0.39	0.20 ± 0.46	–	–	2σ
XMM-075	1:33:32.17	30:31:02.62	172 ± 30	172 ± 31	69 ± 17	77 ± 17	73 ± 23	-0.10 ± 0.38	0.32 ± 0.43	0.56 ± 0.06	0.17 ± 0.04	<

ID	RA	Dec	0.2-2.0 keV Cts	0.35-2.0 keV Cts	0.3-0.7 keV Cts	0.7-1.1 keV Cts	1.1-4.2 keV Cts	HR1	HR2	$HR1_{XMM}$	$HR2_{XMM}$	L10 Detect
XMM-076	1:33:34.99	30:29:54.55	134 ± 26	119 ± 24	84 ± 18	29 ± 12	35 ± 18	-0.06 ± 0.27	0.37 ± 0.33	–	–	–
XMM-078	1:33:35.14	30:23:07.44	96 ± 20	94 ± 20	22 ± 12	38 ± 10	57 ± 18	0.27 ± 0.41	-0.19 ± 0.47	–	–	<
XMM-079[t]	1:33:35.59	30:42:29.14	276 ± 56	571 ± 55	128 ± 20	113 ± 18	35 ± 17	-0.06 ± 0.38	0.31 ± 0.45	0.84 ± 0.07	0.50 ± 0.03	3σ
XMM-080	1:33:35.61	30:49:22.96	65 ± 18	57 ± 18	19 ± 9	23 ± 9	33 ± 14	-0.04 ± 0.26	0.54 ± 0.35	–	–	2σ
XMM-081[t]	1:33:35.81	30:31:13.67	322 ± 68	632 ± 74	116 ± 23	56 ± 17	149 ± 27	0.01 ± 0.39	0.09 ± 0.48	0.85 ± 0.10	0.55 ± 0.03	–
XMM-082	1:33:35.97	30:36:26.68	1746 ± 56	1718 ± 55	594 ± 33	782 ± 35	413 ± 35	0.15 ± 0.41	-0.05 ± 0.52	0.46 ± 0.01	0.09 ± 0.01	3σ
XMM-083[t]	1:33:36.92	30:32:54.24	3016 ± 531	788 ± 64	84 ± 22	338 ± 33	2592 ± 475	-0.06 ± 0.46	-0.01 ± 0.44	0.64 ± 0.03	0.30 ± 0.02	3σ
XMM-084	1:33:37.02	30:33:10.04	100 ± 27	66 ± 23	28 ± 17	23 ± 13	18 ± 18	-0.32 ± 0.34	0.30 ± 0.35	–	–	–
XMM-085	1:33:37.68	30:40:09.50	234 ± 30	251 ± 30	39 ± 15	106 ± 17	119 ± 23	-0.50 ± 0.28	0.07 ± 0.25	0.73 ± 0.06	0.37 ± 0.04	3σ
XMM-088	1:33:39.59	30:34:26.02	126 ± 28	87 ± 27	72 ± 19	38 ± 13	16 ± 18	-0.07 ± 0.45	0.10 ± 0.48	–	–	–
XMM-089	1:33:39.80	30:31:19.05	243 ± 30	209 ± 30	107 ± 19	54 ± 14	40 ± 18	0.33 ± 0.35	-0.41 ± 0.33	0.61 ± 0.04	0.24 ± 0.03	–
XMM-090	1:33:40.54	30:10:48.35	138 ± 17	117 ± 16	66 ± 11	44 ± 8	10 ± 9	-0.12 ± 0.36	0.30 ± 0.42	0.55 ± 0.02	-0.63 ± 0.03	–
XMM-095	1:33:41.44	30:42:20.77	696 ± 59	692 ± 61	253 ± 34	215 ± 28	81 ± 20	0.14 ± 0.36	-0.18 ± 0.39	0.56 ± 0.03	0.04 ± 0.03	–
XMM-098	1:33:42.91	30:41:49.51	110 ± 25	99 ± 25	44 ± 14	47 ± 14	30 ± 17	-0.03 ± 0.34	0.44 ± 0.42	–	–	<
XMM-100[t]	1:33:43.70	30:36:11.50	955 ± 161	1425 ± 181	825 ± 123	84 ± 19	46 ± 19	-0.02 ± 0.46	0.04 ± 0.50	–	–	3σ
XMM-107	1:33:48.49	30:33:04.39	1419 ± 62	1434 ± 60	628 ± 40	635 ± 36	113 ± 26	0.00 ± 0.32	0.37 ± 0.47	0.51 ± 0.01	-0.37 ± 0.01	3σ
XMM-110[t]	1:33:50.12	30:35:28.58	163 ± 55	816 ± 127	38 ± 18	70 ± 16	54 ± 20	0.24 ± 0.23	-0.17 ± 0.30	–	–	2σ
XMM-111	1:33:51.06	30:43:56.17	92 ± 21	77 ± 21	45 ± 14	10 ± 10	34 ± 16	0.04 ± 0.35	0.29 ± 0.48	–	–	<
XMM-112	1:33:51.67	30:30:59.65	90 ± 22	61 ± 21	36 ± 14	31 ± 13	22 ± 13	0.10 ± 0.39	-0.14 ± 0.42	–	–	<
XMM-114	1:33:52.53	30:56:35.22	87 ± 19	78 ± 19	69 ± 14	8 ± 8	33 ± 15	0.17 ± 0.29	0.18 ± 0.46	0.20 ± 0.56	0.89 ± 0.08	<
XMM-116	1:33:54.47	30:33:49.12	667 ± 53	676 ± 52	420 ± 43	153 ± 20	35 ± 17	0.02 ± 0.36	0.20 ± 0.48	0.61 ± 0.02	-0.62 ± 0.02	3σ
XMM-117	1:33:54.69	30:18:50.96	69 ± 16	45 ± 15	12 ± 9	17 ± 8	16 ± 10	-0.02 ± 0.47	0.10 ± 0.54	–	–	–
XMM-118	1:33:54.84	30:45:19.02	633 ± 43	488 ± 37	258 ± 25	195 ± 21	70 ± 19	0.03 ± 0.41	0.06 ± 0.50	0.55 ± 0.02	0.19 ± 0.02	3σ
XMM-119	1:33:54.93	30:33:10.20	4344 ± 82	4015 ± 97	2202 ± 58	1611 ± 48	402 ± 32	-0.07 ± 0.35	0.35 ± 0.44	0.41 ± 0.00	0.21 ± 0.00	3σ
XMM-122	1:33:56.44	30:21:24.72	177 ± 26	136 ± 25	81 ± 17	64 ± 14	48 ± 18	0.15 ± 0.32	0.09 ± 0.42	0.46 ± 0.03	-0.76 ± 0.04	<
XMM-127	1:33:58.06	30:32:09.64	68 ± 21	57 ± 20	15 ± 12	16 ± 11	32 ± 19	-0.10 ± 0.36	0.30 ± 0.46	–	–	<
XMM-128	1:33:58.07	30:37:54.57	216 ± 32	143 ± 30	137 ± 23	62 ± 18	10 ± 12	-0.31 ± 0.35	-0.03 ± 0.28	–	–	3σ
XMM-129	1:33:58.14	30:36:23.30	183 ± 31	184 ± 30	58 ± 18	88 ± 18	99 ± 23	0.09 ± 0.35	-0.30 ± 0.27	0.52 ± 0.04	0.15 ± 0.03	3σ
XMM-130	1:33:58.15	30:48:36.45	75 ± 21	59 ± 20	10 ± 12	34 ± 12	31 ± 17	0.01 ± 0.42	0.13 ± 0.52	–	–	3σ
XMM-131	1:33:58.18	30:51:53.72	140 ± 23	125 ± 23	74 ± 15	41 ± 12	25 ± 18	0.26 ± 0.33	-0.30 ± 0.37	-0.18 ± 0.03	-0.47 ± 0.05	2σ
XMM-132	1:33:58.52	30:33:32.60	1152 ± 51	1106 ± 50	726 ± 39	251 ± 24	152 ± 26	0.03 ± 0.32	0.10 ± 0.41	0.60 ± 0.01	-0.53 ± 0.01	3σ
XMM-135	1:34:00.00	30:47:23.28	245 ± 31	210 ± 29	63 ± 16	65 ± 14	125 ± 25	0.00 ± 0.47	0.03 ± 0.52	0.27 ± 0.04	-0.43 ± 0.04	3σ
XMM-136	1:34:00.19	30:42:18.52	653 ± 40	575 ± 38	269 ± 26	282 ± 23	83 ± 20	-0.23 ± 0.39	0.24 ± 0.42	0.47 ± 0.02	-0.69 ± 0.02	3σ
XMM-137[t]	1:34:00.25	30:39:28.87	451 ± 96	3937 ± 512	18 ± 16	85 ± 18	347 ± 62	-0.05 ± 0.39	0.24 ± 0.48	–	–	–
XMM-138	1:34:00.58	30:50:42.87	77 ± 18	43 ± 17	8 ± 6	14 ± 7	54 ± 17	0.10 ± 0.32	0.19 ± 0.46	–	–	–
XMM-139	1:34:00.60	30:49:04.29	259 ± 29	183 ± 27	137 ± 20	33 ± 11	36 ± 17	-0.27 ± 0.21	0.34 ± 0.25	0.35 ± 0.03	0.08 ± 0.02	3σ
XMM-140[t]	1:34:01.26	30:35:14.97	2298 ± 411	840 ± 70	1864 ± 351	245 ± 31	188 ± 29	-0.05 ± 0.43	0.16 ± 0.49	0.58 ± 0.05	0.35 ± 0.03	3σ
XMM-142	1:34:02.58	30:31:02.62	81 ± 19	72 ± 19	44 ± 15	41 ± 12	19 ± 11	0.23 ± 0.26	-0.36 ± 0.26	0.76 ± 0.08	0.35 ± 0.04	3σ
XMM-143	1:34:03.23	30:36:26.53	1330 ± 97	1176 ± 104	682 ± 58	76 ± 17	72 ± 22	0.85 ± 0.06	-0.84 ± 0.08	0.15 ± 0.02	-0.11 ± 0.02	3σ
XMM-144	1:34:03.52	30:44:42.40	235 ± 31	181 ± 28	98 ± 19	35 ± 13	83 ± 22	-0.07 ± 0.40	0.22 ± 0.47	0.69 ± 0.03	-0.38 ± 0.04	3σ
XMM-145	1:34:04.15	30:32:57.50	298 ± 30	254 ± 28	176 ± 22	72 ± 14	54 ± 17	0.23 ± 0.35	-0.21 ± 0.41	0.35 ± 0.03	0.01 ± 0.03	3σ

ID	RA	Dec	0.2-2.0 keV Cts	0.35-2.0 keV Cts	0.3-0.7 keV Cts	0.7-1.1 keV Cts	1.1-4.2 keV Cts	HR1	HR2	$HR1_{XMM}$	$HR2_{XMM}$	L10 Detect
XMM-147	1:34:05.55	31:07:25.08	136 ± 16	136 ± 16	59 ± 11	64 ± 10	15 ± 6	-0.08 ± 0.29	0.27 ± 0.38	0.48 ± 0.04	0.18 ± 0.03	–
XMM-148	1:34:07.30	30:36:20.14	220 ± 33	212 ± 33	128 ± 24	56 ± 17	41 ± 21	-0.06 ± 0.40	0.33 ± 0.43	0.56 ± 0.03	-0.34 ± 0.03	2σ
XMM-149	1:34:07.47	30:37:07.61	407 ± 36	371 ± 35	234 ± 25	102 ± 17	76 ± 22	0.07 ± 0.30	0.27 ± 0.42	0.49 ± 0.02	-0.70 ± 0.03	3σ
XMM-151	1:34:08.36	30:46:32.70	1267 ± 51	1130 ± 49	777 ± 38	384 ± 27	68 ± 21	0.03 ± 0.00	0.35 ± 0.00	-1.00 ± 0.00	0.09 ± 0.71	3σ
XMM-152[t]	1:34:10.14	30:47:16.78	247 ± 56	227 ± 30	109 ± 21	78 ± 15	60 ± 19	-0.29 ± 0.33	0.17 ± 0.32	0.52 ± 0.04	0.18 ± 0.03	3σ
XMM-153	1:34:10.65	30:42:23.51	2947 ± 69	2628 ± 77	1683 ± 51	903 ± 37	184 ± 25	-0.35 ± 0.16	-0.22 ± 0.13	0.63 ± 0.01	0.32 ± 0.00	3σ
XMM-154	1:34:10.92	30:39:00.70	139 ± 25	123 ± 25	55 ± 16	49 ± 14	47 ± 19	-0.03 ± 0.30	0.43 ± 0.40	0.93 ± 0.05	0.49 ± 0.04	2σ
XMM-159	1:34:13.02	30:48:36.11	99 ± 26	64 ± 23	21 ± 11	32 ± 12	77 ± 21	0.21 ± 0.41	-0.17 ± 0.45	–	–	$<$
XMM-160	1:34:13.65	30:43:27.01	98 ± 21	58 ± 20	57 ± 16	25 ± 10	18 ± 13	0.04 ± 0.41	0.08 ± 0.46	–	–	3σ
XMM-161	1:34:13.71	30:48:17.47	106 ± 24	57 ± 20	17 ± 13	37 ± 11	52 ± 17	0.09 ± 0.49	-0.13 ± 0.47	–	–	2σ
XMM-163	1:34:14.10	30:34:30.92	70 ± 23	60 ± 21	36 ± 14	20 ± 11	11 ± 16	-0.36 ± 0.31	0.10 ± 0.31	–	–	$<$
XMM-165	1:34:14.37	30:53:52.65	301 ± 28	255 ± 27	99 ± 17	144 ± 17	41 ± 15	0.10 ± 0.33	-0.20 ± 0.35	0.36 ± 0.03	-0.19 ± 0.02	3σ
XMM-166	1:34:14.38	30:39:41.56	132 ± 24	89 ± 23	46 ± 15	57 ± 14	15 ± 12	-0.30 ± 0.30	-0.08 ± 0.24	–	–	2σ
XMM-168	1:34:14.67	30:31:50.92	76 ± 20	53 ± 19	22 ± 11	40 ± 12	20 ± 12	0.49 ± 0.33	-0.47 ± 0.36	–	–	2σ
XMM-169	1:34:15.69	30:33:00.67	279 ± 31	276 ± 31	157 ± 22	106 ± 17	48 ± 18	-0.03 ± 0.49	0.09 ± 0.48	0.48 ± 0.03	-0.01 ± 0.03	3σ
XMM-170	1:34:16.31	30:52:32.74	109 ± 23	80 ± 22	67 ± 16	25 ± 11	20 ± 14	-0.10 ± 0.46	0.15 ± 0.47	–	–	$<$
XMM-171	1:34:16.46	30:33:55.07	182 ± 30	167 ± 29	67 ± 19	55 ± 15	48 ± 21	0.32 ± 0.28	-0.13 ± 0.40	0.46 ± 0.05	-0.21 ± 0.05	2σ
XMM-173	1:34:17.50	30:41:22.64	436 ± 34	368 ± 32	199 ± 22	129 ± 18	68 ± 20	-0.20 ± 0.36	-0.00 ± 0.37	0.39 ± 0.02	-0.44 ± 0.02	3σ
XMM-176	1:34:19.45	30:52:48.89	91 ± 22	57 ± 20	1 ± 10	31 ± 11	44 ± 16	-0.06 ± 0.41	0.21 ± 0.48	–	–	–
XMM-179	1:34:22.94	30:54:22.95	172 ± 25	185 ± 26	73 ± 16	53 ± 13	59 ± 19	-0.27 ± 0.39	0.19 ± 0.38	0.44 ± 0.03	-0.83 ± 0.04	3σ
XMM-180	1:34:23.34	30:25:26.85	152 ± 22	150 ± 22	43 ± 12	62 ± 12	71 ± 19	-0.13 ± 0.40	-0.10 ± 0.33	0.67 ± 0.07	0.42 ± 0.03	2σ
XMM-183	1:34:25.40	30:54:57.44	110 ± 23	86 ± 22	24 ± 11	33 ± 12	62 ± 20	0.02 ± 0.33	0.31 ± 0.45	0.50 ± 0.30	0.74 ± 0.07	3σ
XMM-185	1:34:25.82	30:33:17.02	342 ± 31	353 ± 30	43 ± 13	111 ± 16	272 ± 27	-0.09 ± 0.45	0.20 ± 0.48	0.69 ± 0.05	0.38 ± 0.02	3σ
XMM-187[t]	1:34:30.22	30:35:10.51	163 ± 46	52 ± 20	20 ± 11	10 ± 8	132 ± 26	-0.06 ± 0.40	0.18 ± 0.50	0.39 ± 0.04	-0.35 ± 0.04	–
XMM-188	1:34:30.29	30:35:44.80	119 ± 26	88 ± 24	52 ± 15	35 ± 12	26 ± 16	0.12 ± 0.50	-0.14 ± 0.49	–	–	2σ
XMM-189	1:34:30.93	30:56:39.82	164 ± 22	141 ± 22	87 ± 15	48 ± 11	20 ± 12	-0.01 ± 0.37	0.20 ± 0.50	0.55 ± 0.04	0.04 ± 0.03	2σ
XMM-190	1:34:32.63	30:35:30.37	154 ± 25	138 ± 26	61 ± 17	42 ± 13	53 ± 19	0.04 ± 0.44	0.06 ± 0.53	0.44 ± 0.05	0.16 ± 0.04	$<$
XMM-192	1:34:35.52	30:52:10.97	130 ± 23	106 ± 21	91 ± 17	46 ± 14	29 ± 16	-0.15 ± 0.44	0.15 ± 0.42	0.57 ± 0.05	0.15 ± 0.04	3σ
XMM-195	1:34:38.73	30:37:56.82	90 ± 23	66 ± 20	25 ± 12	34 ± 12	76 ± 20	-0.03 ± 0.38	0.21 ± 0.48	0.87 ± 0.09	0.41 ± 0.04	$<$
XMM-198	1:34:40.74	30:43:36.44	62 ± 20	19 ± 18	17 ± 14	16 ± 11	27 ± 13	-0.00 ± 0.40	0.24 ± 0.51	–	–	3σ
XMM-199	1:34:41.09	30:43:26.33	669 ± 36	668 ± 37	402 ± 27	224 ± 20	17 ± 12	-0.05 ± 0.37	0.27 ± 0.48	0.57 ± 0.02	-0.12 ± 0.02	3σ

[e] Unrealistic source count errors from `emldetect` in at least one individual band. Source count errors pegged to total count values.

[t] Total counts in the full band are discrepant by a factor of two from the summation of counts in each individual band due an `emldetect` merging issue. Total counts in the 0.2-2.0 keV band are reported as the sum of counts in the 0.2-0.5 keV, 0.5-1.0 keV, and 1.0-2.0 keV band.

We cross-correlate all our SNR candidates with measurements from LL14 and L10 to determine the number of newly X-ray detected SNRs in this catalog. The position of each of the 137 L10 sources was inspected by eye for a counterpart not already known to be a point source in the W15 catalog. To cross-correlate with LL14, we searched for counterparts in the W15 catalog out to a maximum separation of 10" for those sources not already matched to sources in L10. This resulted in 69 matches of the 78 newly reported sources in LL14. The remainder of the LL14 sources (121) were previously matched to counterparts in L10. For those sources in both L10 and LL14 that did not have a counterpart in W15 after cross-correlation we forced `emldetect` to make measurements at the locations of these sources to ensure that we would measure upper limits for all sources.

Although LL14 report 79 new SNR candidates over previous works, we find one of these 79 sources to have a potential counterpart in L10 (XMM-189, L10-122, LL14-174). As a result, our census of SNR candidates totals 218: 137 from L10, 78 from LL14, and three from W15. From our measurements of the locations of these SNRs we detect 105 at 3σ confidence and 145 at 2σ confidence. We measure upper-limits for the remaining 73 non-detections. Of our 105 3σ detections, 54 are newly detected in X-rays at 3σ, 3 are newly discovered in X-rays from this data set, 48 are 3σ detections in both L10 and this work, and 96 are reported in LL14. There are six SNRs that were detected in L10 but are not detected here. Of the six L10 detections that are undetected here, the majority have between 2-8 times more exposure in the ChASeM33 survey due to overlapping observations than the exposure times from W15. The other sources are on regions of the detector that are unfavorable to detection i.e. far off-axis, or near a chip gap on the detector. There are 25 SNRs which are upper limits in both L10 and this work. Of the 78 SNR candidates in LL14 and not in L10, we measure 18 as 3σ detections, 39 at 2σ confidence, and the remaining 39 as upper limits. In general, we are less likely to detect in X-rays the SNR candidates newly reported in LL14 compared to those SNR candidates reported in both L10 and LL14. This is very likely because the new LL14 objects have a lower mean surface brightness than the SNRs previously reported in L10, indicating that they are older and/or interacting with less dense ISM, both of which tend toward lower expected X-ray emission.

The three newly discovered SNRs were first reported in W15. The brightest of these is denoted as XMM-034 here. This SNR (source 383 in W15) is now the fifth brightest X-ray emitting SNR in M33 with a 0.35-2 keV flux of 2.77×10^{-14} erg cm^{-2} s^{-1} (L_x(0.35-2.0 keV) $= 2.2 \times 10^{36}$ erg s^{-1}).

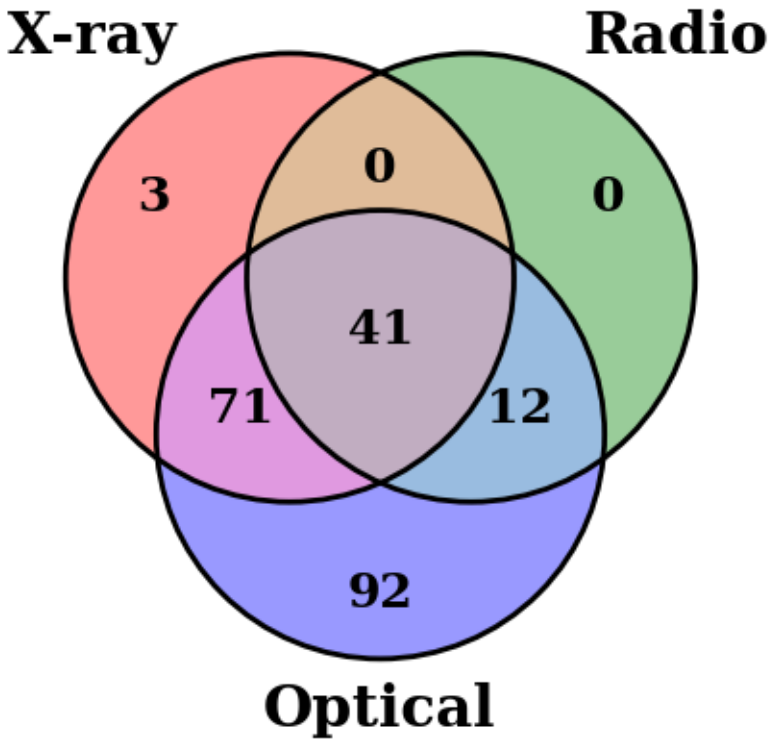

Figure 3.1: Venn diagram of the current multiwavelength sample of SNRs in M33. Optical detections are based on elevated [S II]/Hα ratios and come from the catalogs of L10 and LL14. X-ray detections are from this work and the work of L10. Radio detections are taken from Gordon et al. (1999).

The discovery of these new SNRs was facilitated by the larger survey area and increased soft sensitivity of *XMM-Newton*. In particular, any source that had strong emission below 1 keV compared to above 1 keV and was not already classified as an SNR was studied in the [S II] and Hα images of Massey et al. (2006) to see if the region hosted an SNR.

We provide an updated Venn diagram of the current multiwavelength detections of SNRs in M33 in Figure 3.1. The prevalence of optically detected SNRs with elevated [S II]/Hα is due primarily to the efficacy of this diagnostic ratio in separating SNRs from other contaminants. We boost the number of X-ray detections for the previously optically detected sources owing to our large survey area and increased soft sensitivity, which is particularly adept at detecting thermal X-ray

emission of extended sources. The lack of SNRs detected only in X-rays is due to the difficulty in separating SNR candidates from other sources of soft X-ray emission on the basis of X-rays alone. By selecting primarily for candidates with multiwavelength confirmation (optical and X-ray), we may be missing some young, X-ray emitting SNRs in the free expansion phase. The dearth of radio detected SNRs is affected by observational limits; most radio surveys do not furnish the requisite angular resolution and sensitivity to definitively identify SNRs without optical or X-ray follow-up. In the absence of a deep radio survey of M33, the combination of optical emission-line diagnostics and X-ray detections remains the most reliable way to identify SNRs, although such detection methods may be biased against detecting SNRs hosting pulsar wind nebulae (plerion-type SNRs), SNRs that are Balmer-dominated, and oxygen-rich SNRs.

3.3.2 Spectral Fitting

We attempt to type the progenitors for 15 of the SNRs in our sample by fitting their spectra using `XSPEC`. These 15 sources are some of the brightest X-ray emitting SNRs in M33 for which there is both *XMM-Newton* and *Chandra* data, and for which there are enough on-axis counts for detailed spectral fitting. We used both *XMM-Newton* and *Chandra* data in cases where *Chandra* data was available and provided $\approx 40\%$ more counts than *XMM-Newton* data alone (11 SNRs). All remaining SNRs were fit using *XMM-Newton* data only (four). For each of these SNRs we perform a simultaneous fit to both the unbinned source and background components. While this method for fitting is more computationally expensive than one in which the background is directly subtracted from the source spectrum before fitting, it avoids the problems with the non-Poisson nature of background-subtracted data and makes optimal use of the full spectral information of the SNRs. We describe the individual source and background models and fitting method in the following sections. For more details on how the spectral extractions themselves were carried out, see discussion in Chapter 5.

3.3.2.1 Background Model

Our background spectra were fitted with a two component model: a sky component, plus a detector component. The blank sky background was modeled as a pair of absorbed thermal plasma components (`tbabs`, $N_H = 5{\times}10^{20}$ cm^{-2}). The best-fit low-T component had kT= 0.16 keV,

and the higher temperature component had kT= 0.75 keV. When fitting the SNRs, all blank sky background parameters were frozen, except for an overall multiplicative constant factor which was allowed to vary for all instruments.

For the pn, the detector component was modeled as a broad (σ = 0.455 keV) Gaussian at 0 keV and a broken power-law. In addition, Gaussian components were added for the detector fluorescence lines near 1.49 keV (Al-Kα), 2.15 keV (Au-L complex), 5.4 keV (Cr-Kα), 5.9 keV (Mn-Kα), 6.4 keV (Fe-Kα), 7.47 keV (Ni-Kα), 8.04 keV (Cu-Kα), 8.62 keV (Zn-Kα), and 9.6 keV (Zn-Kβ). For the MOS1 and MOS2 detectors, the model consists of a pair of broken power-laws to model the continuum component. The fluorescence lines listed above were added, along with a line at 1.75 keV (Si-Kα). The detector plus blank sky background models were fit to spectra covering most of each detector with point sources removed. The detector fluorescence line energies were fitted, and the line widths allowed to vary. Finally, the line energies and widths were all frozen, and the normalizations were all tied to appropriate multiples of an overall multiplicative constant factor, one for each detector background model. In subsequent fitting, only the multiplicative constant was allowed to vary.

Thus, the complete background model spectra have a scaling factor for the blank sky component, and separate scaling factors for each of the MOS1, MOS2, pn, and ACIS detector models. The background spectra are fit first with this model, and the results of this fit are supplied as inputs for the background component of the subsequent total (source + background) fit. This method thus accounts for the background while performing fits to the source spectra, as opposed to subtracting any signal from the source data before fitting, which preserves the Poisson characteristics of the data and provides more reliable estimates of the contribution of the background.

3.3.2.2 Simultaneous Fitting of *Chandra* and *XMM*

We fit both the *Chandra* and *XMM-Newton* data simultaneously for 11 SNRs. The fits were carried out using `XSPEC` with a plane-parallel shock model (`vpshock`) (Borkowski et al., 2001). All parameters in the `vpshock` model were tied between all instruments. In the `vpshock` model the individual abundances of O, Ne, Mg, Si and Fe are allowed to vary for SNRs with a large enough number of spectral counts with all other abundances (aside from H and He) frozen to values of 0.5. The Galactic absorption was fixed using a `tbabs` model to a value of 0.5×10^{21} cm^{-2} (Wilms et al.,

2000), while the absorption in M33 was allowed to vary using a `tbvarabs` model; the metallicity for absorption in M33 was fixed at 0.5 times solar. The spectra were fit with unbinned channels and the C statistic was used. The absorption, shock temperatures, individual abundances, and ionization timescales were allowed to vary in the `vpshock` model. The remaining 4 SNRs did not have a significant contribution from the *Chandra* data to their total spectral counts, and thus were fit using *XMM-Newton* data only, though using the same model as above.

Each SNR was visually inspected prior to fitting to determine the number of useful spectral counts available for fitting. This involved examining SNR images, and removing fields in which spectral extraction regions fell on chip gaps or were far off axis. We find that > 300 useful counts are necessary for a reliable fit, while > 1200 counts are required to fit for individual abundances in a given SNR's spectrum. For the SNRs that had between 300–1200 counts, the individual abundances were frozen when performing the fit, or, O and Fe were allowed to vary, with all other abundances tied to O.

We provide the best-fitting spectral parameters and associated 90% confidence intervals from all of our fits in Table 3.4. The analysis of the spectral fitting results are discussed in the following section.

Table 3.4: Parameters from XSPEC fits for 15 SNRs in our sample with detailed spectral fits. Column 1: source ID number in this catalog. Column 2: source counts in the 0.35-2.0 keV band. Column 3: hydrogen column density for M33 from tbvarabs model. Column 4: plasma temperature from the vpshock model. Column 5: the ionization timescale from the vpshock model. Column 6: the normalization from the vpshock model. Columns 7-11: the elemental abundances from the vpshock model listed with respect to solar values. All units are given in the column headers.

ID	0.35-2.0 keV Cts	N_H 10^{22} cm^{-2}	kT_e keV	τ 10^{11} cm^{-3} s	K 10^{-4} cm^{-5}	O	Ne	Mg	Si	Fe
XMM-041	11878	$0.02^{+0.06}_{-0.02}$	$0.66^{+0.03}_{-0.02}$	$3.48^{+0.87}_{-1.02}$	> 0.18	$0.51^{+0.12}_{-0.15}$	$0.56^{+0.08}_{-0.10}$	$0.47^{+0.08}_{-0.10}$	$0.56^{+0.15}_{-0.12}$	$0.45^{+0.06}_{-0.08}$
XMM-073	4347	$0.21^{+0.12}_{-0.11}$	$0.69^{+0.21}_{-0.17}$	$1.35^{+0.80}_{-0.45}$	$0.39^{+0.56}_{-0.14}$	$0.34^{+0.15}_{-0.13}$	$0.33^{+0.07}_{-0.06}$	$0.86^{+0.21}_{-0.15}$	$0.50^{+0.25}_{-0.18}$	$0.27^{+0.22}_{-0.06}$
XMM-119	2665	$0.10^{+0.01}_{-0.10}$	$0.56^{+0.13}_{-0.08}$	$1.56^{+1.12}_{-0.88}$	$0.42^{+0.13}_{-0.15}$	$0.20^{+0.04}_{-0.03}$	$0.31^{+0.08}_{-0.05}$	$0.25^{+0.13}_{-0.08}$	$0.48^{+0.33}_{-0.22}$	$0.20^{+0.13}_{-0.03}$
XMM-067	2109	$0.11^{+0.19}_{-0.11}$	$0.54^{+0.05}_{-0.18}$	$7.73^{+5.27}_{-4.31}$	$0.34^{+0.59}_{-0.14}$	$0.27^{+0.17}_{-0.13}$	$0.40^{+0.19}_{-0.19}$	$0.19^{+0.2}_{-0.15}$	$0.48^{+0.52}_{-0.36}$	$0.18^{+0.07}_{-0.10}$
XMM-153	1910	$0.10^{+0.04}_{-0.10}$	$0.74^{+0.22}_{-0.23}$	$0.46^{+0.85}_{-0.23}$	$0.15^{+0.12}_{-0.05}$	$0.26^{+0.05}_{-0.07}$	$0.31^{+0.09}_{-0.11}$	$0.17^{+0.17}_{-0.14}$	$0.85^{+0.45}_{-0.50}$	$0.34^{+0.16}_{-0.17}$
XMM-068	1207	$0.00^{+0.03}_{-0.00}$	$0.48^{+0.09}_{-0.03}$	$5.62^{+8.38}_{-1.85}$	$0.23^{+0.04}_{-0.07}$	$0.43^{+0.19}_{-0.07}$	$0.57^{+0.21}_{-0.12}$	$0.36^{+0.12}_{-0.21}$	$0.39^{+0.51}_{-0.38}$	$0.15^{+0.03}_{-0.03}$
XMM-034	742	$0.10^{+0.06}_{-0.10}$	$0.65^{+0.89}_{-0.16}$	$0.27^{+0.38}_{-0.12}$	$0.03^{+0.02}_{-0.01}$	$0.67^{+0.19}_{-0.15}$	–	–	–	$0.36^{+0.33}_{-0.21}$
XMM-039	1820	$0.10^{+0.13}_{-0.10}$	$0.51^{+0.21}_{-0.18}$	$0.9^{+2.43}_{-0.52}$	> 0.03	$0.39^{+0.19}_{-0.13}$	$0.57^{+0.26}_{-0.24}$	$0.41^{+0.50}_{-0.30}$	$0.42^{+1.04}_{-0.42}$	$0.29^{+0.24}_{-0.14}$
XMM-082	2143	<0.14	$0.43^{+0.01}_{-0.03}$	>50.00	$0.14^{+0.08}_{-0.10}$	$0.20^{+0.23}_{-0.03}$	$0.40^{+0.13}_{-0.07}$	$0.70^{+0.08}_{-0.18}$	$0.36^{+0.29}_{-0.25}$	$0.10^{+0.02}_{-0.02}$
XMM-151	937	$0.10^{+0.04}_{-0.10}$	$0.36^{+0.24}_{-0.14}$	$1.04^{+1.13}_{-0.03}$	>0.39	$0.48^{+0.23}_{-0.14}$	–	–	–	$0.50^{+0.32}_{-0.22}$
XMM-066	982	$0.26^{+0.00}_{-0.01}$	$0.6^{+0.03}_{-0.4}$	$0.17^{+0.07}_{-0.01}$	>0.37	$0.54^{+0.06}_{-0.13}$	–	–	–	$1.20^{+1.17}_{-0.64}$
XMM-132	1070	$0.10^{+0.04}_{-0.10}$	$0.73^{+0.59}_{-0.28}$	$0.25^{+0.34}_{-0.15}$	>0.06	$0.64^{+0.24}_{-0.11}$	–	–	–	$0.60^{+0.53}_{-0.27}$
XMM-065	502	$0.28^{+0.31}_{-0.19}$	$0.92^{+1.59}_{-0.56}$	$0.14^{+0.21}_{-0.06}$	$0.03^{+-0.02}_{-0.01}$	–	–	–	–	–
XMM-136	585	$0.10^{+0.05}_{-0.10}$	$0.38^{+0.05}_{-0.07}$	>6.72	>0.09	$0.24^{+0.07}_{-0.13}$	–	–	–	$0.15^{+0.08}_{-0.07}$
XMM-118	310	$0.10^{+0.14}_{-0.10}$	$0.31^{+0.32}_{-0.07}$	>19.78	$0.04^{+0.03}_{-0.03}$	$0.56^{+0.77}_{-0.36}$	–	–	–	$0.31^{+0.3}_{-0.17}$

3.3.3 Spectral Fit Parameters

The parameters from the detailed spectral fitting are recorded in Table 3.4 for the model described in Section 3.3.2.2. The fitted parameters include the hydrogen column density (N_H), the electron temperature (kT_e), the ionization timescale (τ), and the normalization (K). The abundances of O, Ne, Mg, Si and Fe are reported relative to the solar value, and are allowed to vary for SNRs with $>$ 1200 counts. An example of the model fit to the data for a single SNR (XMM-041, L10-025) is plotted in Figure 3.2. Each set of two panels illustrates the total fit, associated components (left panel), and the background fit only (right panel) for each instrument (pn, MOS1, MOS2, and ACIS). Figure 3.2 demonstrates the robustness of the fitting technique by illustrating the strong contribution of the background component, and in particular the instrument background, at higher energies.

Along with the fitted parameters we derive inferred physical parameters from these values, such as pre-shock H density (n_o), ionization age (t_{ion}), dynamical age (t_{dyn}), shock velocity (v_s), initial explosion energy (E_o), and swept-up mass (M_{su}). These parameters are calculated based on a Sedov model, and assuming a volume-filling factor of one, spherically symmetric SNRs, strong shock jump conditions, and electron-ion equilibrium. The effects of some of these simplifying assumptions are discussed in the following paragraphs. The values for the above calculated physical parameters are reported for each SNR in Table 3.5 and represent spatially averaged quantities over the SNR. The `XSPEC` model fits provide estimates for the electron temperature (kT_e), the ionization timescale (τ), and the normalization (K) (see Table 3.4).

Following Hughes et al. (1998) and Gaetz et al. (2007) we can calculate the Sedov model parameters in Table 3.5 based on the observational values for the electron temperature, ionization timescale, normalization, and SNR radii. We use the radius for each SNR reported from L10 in our calculations (see Table 3.2), and assume errors of $\sim$ 9% on the reported radii, based on adding in quadrature an error of 5% in angular size and assuming azimuthal asymmetry, and an error of 7% in the assumed distance to M33. Errors on the derived physical quantities are calculated from the 90% confidence interval on the fitted parameters using 10,000 Monte Carlo draws from the error distribution, and the propagation of the previously stated errors on the radii and angular sizes of the SNRs.

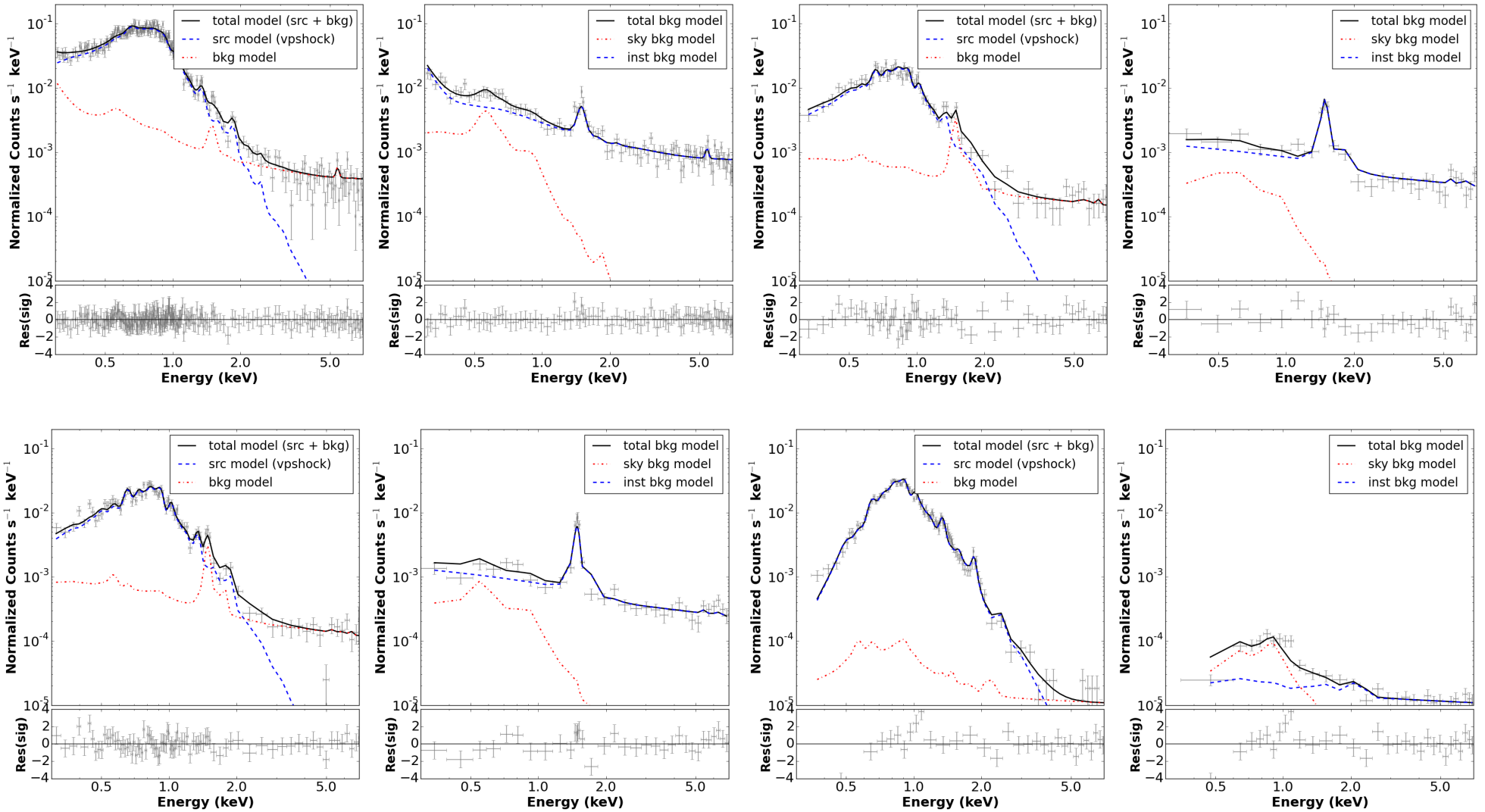

Figure 3.2: Sample fit for the SNR XMM-041 (L10-025) using a `vpshock` model for the source with O, Ne, Mg, Si and Fe abundances as free parameters. Panels a, b, c, and d represent fits the individual cameras: pn, MOS1, MOS2, and ACIS, respectively. Within each panel, the left-hand panel depicts the total fitted model in black, with the total model components, source (`vpshock`) and background shown in blue and red, respectively. The gray points show the data and residuals with associated errorbars. The right-hand panel shows the total fitted background model in black, and its components, sky and instrument background, in blue and red. The data and residuals are again plotted as gray points, with associated errorbars.

The pre-shock H density is calculated from the fitted normalization, distance to M33, and measured radii using the following equation from Gaetz et al. (2007):

$$n_o = 1.58 K_{-4}^{1/2} D_{800} R_{s,10}^{3/2} \ \ cm^{-3} \tag{5}$$

where K_{-4} is the normalization in units of 10^{-4} cm^{-5}, D_{800} is the assumed distance in units of 800 kpc, and $R_{s,10}$ is the source radius in units of 10 pc. Assuming strong shock jump conditions, this pre-shock H density can be used to calculate the post-shock density as follows: $n_e = 4.8 \times n_o$. The post-shock density, coupled with the ionization timescale (τ) gives an estimate of the ionization age. Following Borkowski et al. (2001), we note that at a given shock velocity the ionization timescale, τ, from a plane-parallel shock model, such as the `vpshock` model used in our fits, may be considerably larger than the emission-averaged ionization timescale, $<\tau>$, in the Sedov model. We calculate the ionization ages in Table 3.5 from the plane-parallel shock τ, and note that the ages based on the Sedov $<\tau>$ may be smaller, leading the ages reported in Table 3.5 to be an upper limit. The dynamical ages are proportional to the observed radii divided by the shock velocity ($v_s \sim \sqrt{kT_e}$), and we find that they are systematically much larger than the ages calculated based on the ionization timescale from the fits. This may imply that the simplifying assumptions of all SNRs in the Sedov phase and in electron-ion equilibrium as applied to our constant-temperature plane-parallel shock model fits are not appropriate for all SNRs. Despite this, we proceed with these assumptions to provide estimates of the explosion energies and swept-up masses for each fitted SNR. We derive an average explosion energy for all SNRs of $\sim 1.5 \times 10^{51}$ erg and swept-up masses that are all on the order of hundreds M$_\odot$. There is an uncertainty in the swept-up masses due to the distribution of circumstellar and interstellar material around the progenitor that is not accounted for here. The Sedov model assumes a point explosion in a uniform medium, however for a CC SN the stellar winds of the progenitor will have sculpted the surrounding medium, meaning that the density currently being encountered by the blast wave may be larger than the density encountered at an earlier stage, leading to a general overestimate of the swept-up mass. For this reason, we consider the swept-up mass calculations to be an upper bound.

Table 3.5: Physical parameters for SNRs calculated from fitted parameters in Table 3.4. Column 1: source ID number in this catalog. Column 2: pre-shock H density. Column 3: ionization age for the SNR. Column 4: dynamical age for the SNR. Column 5: shock velocity. Column 6: explosion energy. Column 7: swept-up mass. All units are given in the column headers.

ID	n_o	t_{ion} 10^3	t_{dyn}	v_s	E_o	M_{su}
	cm^{-3}	yrs	10^3 yrs	km s^{-1}	10^{51} erg	$M_\odot$
XMM-041	>0.40	$5.00^{+1.20}_{-5.00}$	$6.70^{+0.40}_{-0.50}$	740^{+20}_{-20}	>1.50	>180
XMM-073	$2.39^{+1.44}_{-0.57}$	$0.40^{+0.30}_{-0.20}$	$3.40^{+0.60}_{-0.50}$	760^{+110}_{-100}	$1.00^{+0.80}_{-0.40}$	120^{+80}_{-40}
XMM-119	$1.04^{+0.24}_{-0.25}$	$1.00^{+0.90}_{-0.50}$	$5.80^{+0.60}_{-0.70}$	680^{+80}_{-50}	$1.60^{+0.60}_{-0.50}$	230^{+70}_{-80}
XMM-067	$1.17^{+0.81}_{-0.30}$	$4.40^{+3.70}_{-2.70}$	$5.30^{+1.30}_{-0.40}$	670^{+30}_{-130}	$1.20^{+0.80}_{-0.50}$	180^{+140}_{-60}
XMM-153	$0.78^{+0.30}_{-0.17}$	$0.40^{+0.70}_{-0.20}$	$4.60^{+1.00}_{-0.60}$	780^{+110}_{-140}	$1.10^{+0.60}_{-0.40}$	120^{+60}_{-40}
XMM-068	$0.30^{+0.06}_{-0.07}$	$12.30^{+20.50}_{-4.10}$	$10.00^{+0.70}_{-1.00}$	630^{+60}_{-30}	$2.10^{+0.70}_{-0.60}$	350^{+100}_{-110}
XMM-034	$0.16^{+0.06}_{-0.04}$	$1.10^{+1.80}_{-0.50}$	$7.30^{+1.20}_{-2.60}$	730^{+400}_{-100}	$0.80^{+1.20}_{-0.30}$	110^{+50}_{-40}
XMM-039	>0.15	$2.70^{+6.50}_{-2.70}$	$7.60^{+1.90}_{-1.30}$	650^{+130}_{-130}	>0.40	>70
XMM-082	$0.27^{+0.09}_{-0.11}$	>103.40	$9.90^{+0.80}_{-0.60}$	600^{+10}_{-30}	$1.30^{+0.50}_{-0.60}$	250^{+100}_{-110}
XMM-151	>1.36	$0.30^{+0.5}_{-0.3}$	$7.2^{+2.0}_{-1.7}$	550^{+160}_{-120}	>1.1	>270
XMM-066	>1.02	$0.10^{+0.00}_{-0.10}$	$5.30^{+3.00}_{-0.30}$	710^{+20}_{-260}	>0.90	>180
XMM-132	>0.14	$0.90^{+1.20}_{-0.90}$	$8.70^{+2.50}_{-2.30}$	780^{+270}_{-170}	>1.40	>180
XMM-065	$0.11^{+0.03}_{-0.03}$	$0.90^{+1.50}_{-0.40}$	$7.30^{+3.90}_{-2.90}$	870^{+570}_{-310}	$1.40^{+2.60}_{-0.90}$	130^{+50}_{-50}
XMM-136	>0.18	>31.30	$11.30^{+1.40}_{-1.00}$	560^{+40}_{-60}	>1.00	>200
XMM-118	$0.29^{+0.11}_{-0.12}$	>46.20	$8.20^{+1.30}_{-2.50}$	510^{+220}_{-70}	$0.30^{+0.40}_{-0.10}$	80^{+40}_{-40}

The large swept-up masses for the fitted sample imply that the majority of these SNRs are older and therefore ISM-dominated. Given the derived ages and swept-up masses, we expect the SNR ejecta to be well-mixed with the surroundings, leading to fitted abundances that more closely resemble that of their surroundings, as opposed to the ejecta distributions expected for individual Type Ia or CC SNe. Because of this, we are unable to definitively type any of the SNRs in our fitted sample. We do note, however, that one of the SNRs in this fitted sample—XMM-068 (L10-037, LL14-062)—has an elevated O/Fe value of ~ 3, which is markedly in excess of the O/Fe ratios for the rest of the fitted sample as demonstrated in Figure 3.3. In a CC SNR, we would expect that if O is enhanced, Ne and Mg would also be enhanced. Because Ne line energies overlap Fe L-shell lines there will be some blending at the resolution of the CCD, and one might expect an elevated O/Fe value simply based on an anti-correlation between Ne and Fe. We do not see a strong anti-correlation between the fitted Ne and Fe values for this SNR based on a contour plot generated with the `XSPEC steppar` command, and further the Ne value is not overly abundant in the fit compared to the expected M33 metallicity abundance. This implies that the Fe abundance is actually deficient compared to O in this SNR, as opposed to simply *appearing* less abundant due to being masked by an enhanced Ne abundance based on lines at energies similar to those of the Fe L-shell lines which are not resolved at CCD resolution. We plot the spectral fit results for this SNR in Figure 3.4 for the pn, MOS1, and ACIS instruments, as well as for the pn compared to four other pn spectra for SNRs with O/Fe < 2 (bottom-right panel). Qualitatively, there is no marked difference between the high O/Fe SNR (blue line), and the rest of the sample (grey lines), though without more SNRs at higher O/Fe values it is difficult to classify based on spectral shape alone.

Based on the swept-up mass of SNR XMM-068, which is in excess of 300 $M_{\odot}$, we note that it is most likely ISM-dominated, but may still originate from an environment with generally more CC ejecta enrichment. Interestingly, XMM-068 is the only SNR in the fitted sample that was given a progenitor classification of Type Ia by LL14 based on the surrounding stellar population. By contrast, we see evidence that O is enriched compared to Fe, even within the errors, for XMM-068, suggesting that this SNR's environment contains relics of more high-mass, CC ejecta.

The only SNR to be designated as CC in L10 is XMM-073 (L10-039, LL14-067) based on elevated O, Ne, and Mg as compared to Fe from an X-ray spectral fit. We see only slight enhancement

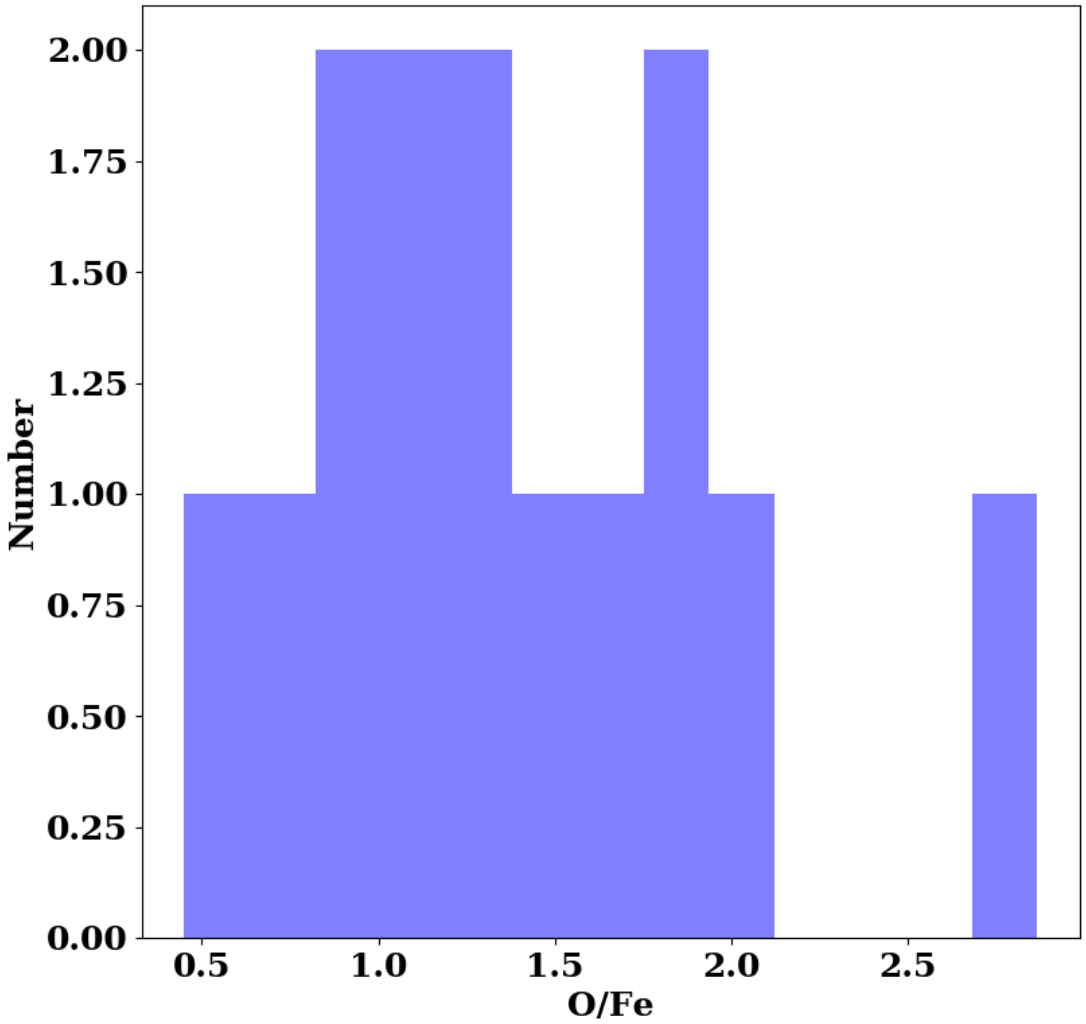

Figure 3.3: Histogram of the O/Fe values for all 15 fitted SNRs. There is one clear outlier (XMM-068) from the overall distribution, with highly elevated O/Fe, which may be indicative of CC ejecta enrichment in the vicinity of this SNR.

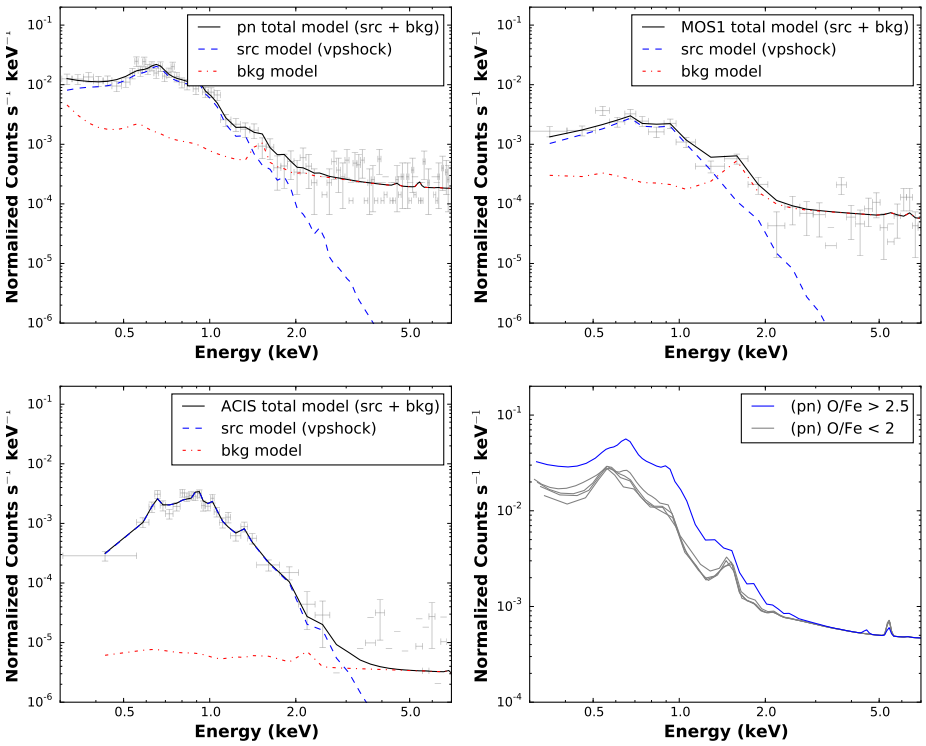

Figure 3.4: `XSPEC` `vpshock` model fit for SNR XMM-068 for the pn (top-left), MOS1 (top-right), and ACIS (bottom-left) instruments. The model components are labeled in each panel. The bottom right panel compares the fitted pn spectrum for XMM-068 to the pn spectra for four SNRs in this sample with similar numbers of counts, but lower O/Fe values. All spectra have been normalized to have the same number of counts at 5 keV.

of O, Ne, and Mg relative to Fe in our fits for XMM-073, but L10's classification is consistent with our spectral fits within the errors on the fitted abundances. However, the light element abundance enhancements relative to iron coupled with the large swept-up mass preclude the possibility of assigning a progenitor type based on our spectral fits alone.

M33, a star-forming spiral galaxy, is expected to have a much higher fraction of CC SNe than Type Ias. Mannucci et al. (2005) report a Type Ia SNe rate of $0.17^{+0.068}_{-0.063}$ per century per 10^{10} $M_{\odot}$ and a CC SNe rate of $0.86^{+0.319}_{-0.306}$ per century per 10^{10} $M_{\odot}$. Given these rates, we expect about 17% of the SNRs in M33 to be Type Ias, or around 37 of the 218 candidates. Therefore, we expect the vast majority of our sample to be CC SNe, and in particular we would expect only ~ 2 of the sample of bright SNRs with detailed spectral fits to be of Type Ia. LL14 tentatively type XMM-068 with this designation based on the surrounding stellar population, but we find no evidence in the X-ray spectral fits to support this designations (e.g. broad Fe L-shell complexes), and in fact we find evidence of enhanced O/Fe, though this SNR is likely ISM-dominated. XMM-066 (L10-035) is the only fitted SNR for which we measure O/Fe < 0.5, but this SNR was left out of the LL14 catalog due to its low [S II]/Hα value, so it has no assigned progenitor type in that catalog, and in addition, it has an extremely high swept-up mass, implying again that it would likely not retain much of the progenitor ejecta signature.

Finally, we compared both the fitted and derived parameters to physical quantities of the SNRs such as size, luminosity, and HR measure. In doing so, we find some evidence for a correlation between the pre-shock H density and the X-ray luminosity, as can be seen in Figure 3.5. Variations in the density of the ISM surrounding the SNR progenitor will lead to differences in the resultant SNR X-ray luminosity, with higher luminosities expected from SNRs whose progenitors explode in denser environments, so evidence of such a relation is not unexpected assuming an ISM that is not spatially uniform. One might expect a correlation between X-ray HR, SNR temperature, and SNR size, as those SNRs that are cool, and evolved will have stronger emission in the soft band and be larger in size, while hotter SNRs will have more emission in the medium band. Only very high temperature, young SNRs will have strong hard band emission (Maggi et al., 2016).

Ultimately, we do not find any significant correlations between HR1 (M-S/(H+M+S)) and the temperatures, nor between the fitted temperatures and SNR sizes, as illustrated in Figure 3.6, though the errors on the fitted temperatures are similar to the range of measured values. Nearly

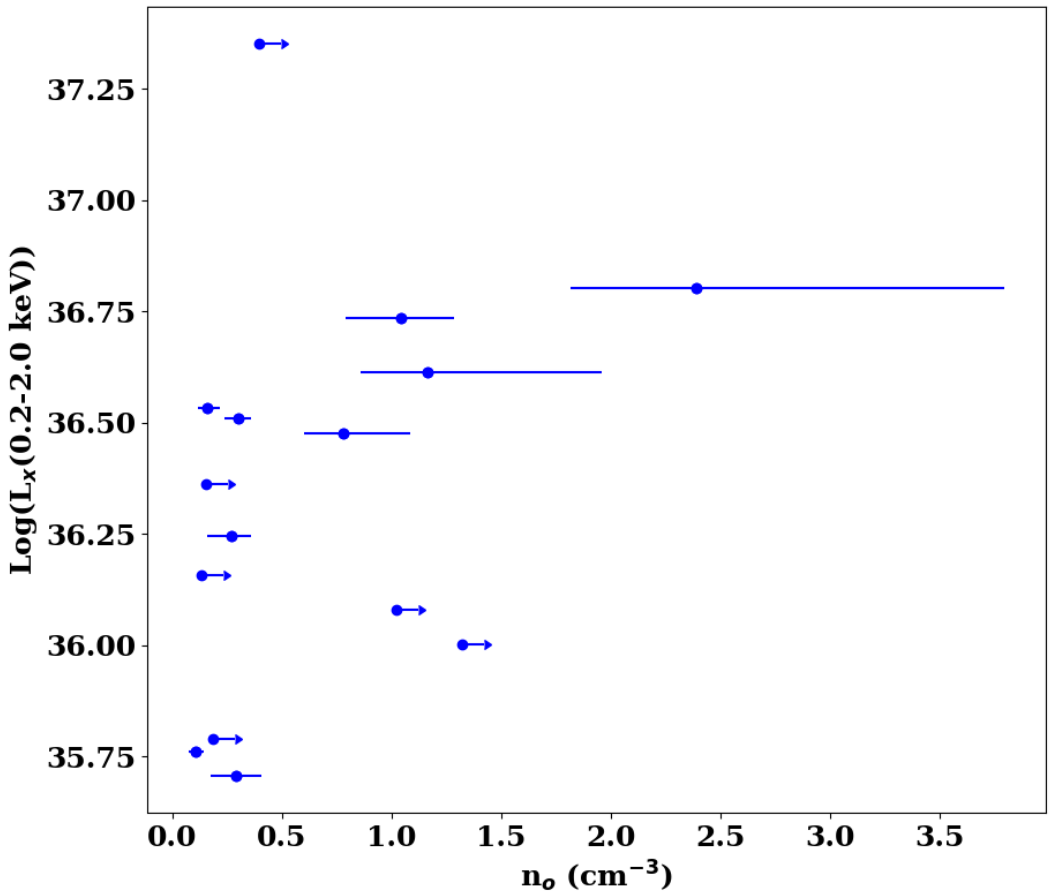

Figure 3.5: Pre-shock H densities derived for the 15 SNRs with spectral fits versus their X-ray luminosities in the 0.2-2.0 keV band.

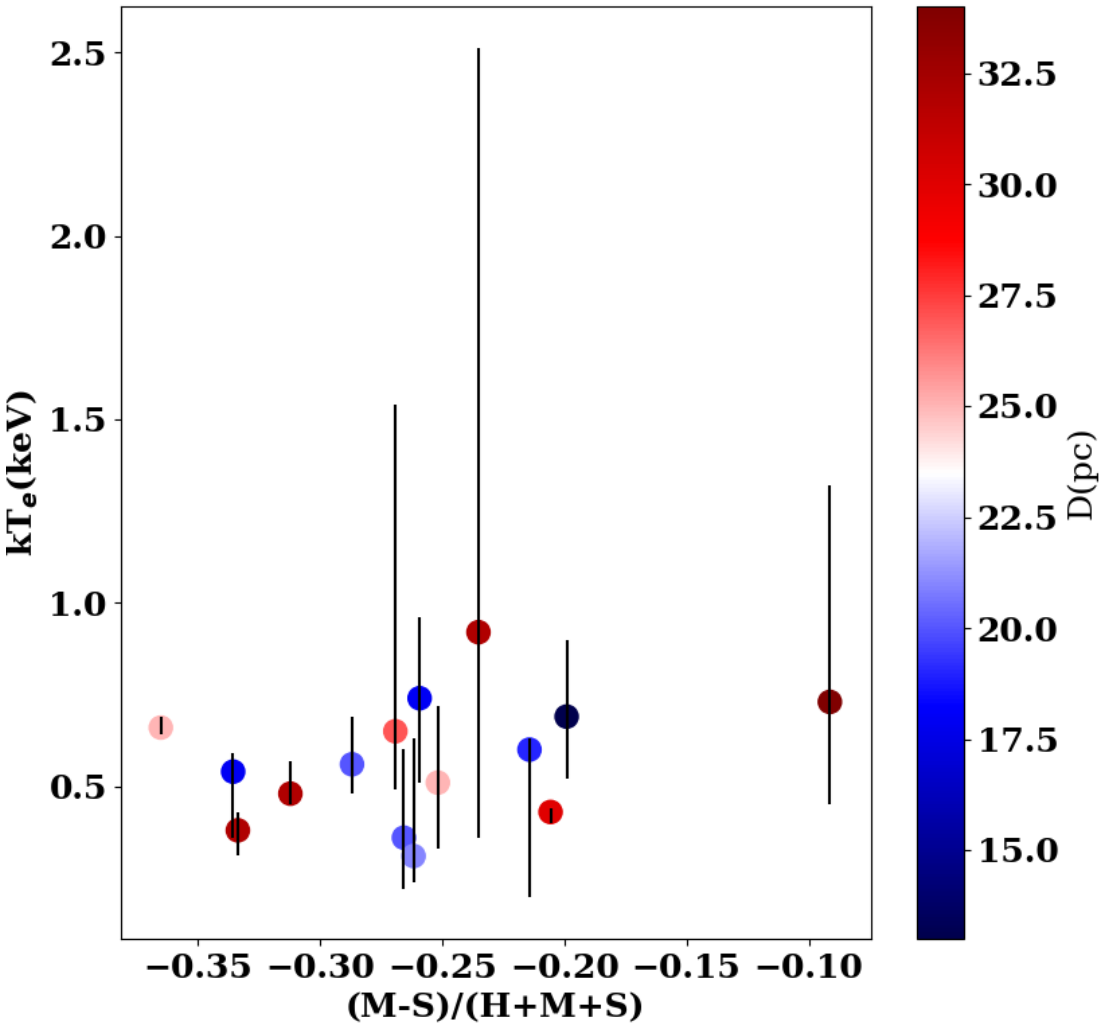

Figure 3.6: HR1 = (M-S)/(H+M+S), where H= 1.1-4.2 keV, M = 0.7-1.1 keV, and S = 0.3-0.7 keV versus the electron temperature from spectral fits. The points are color-coded by SNR size. We find no strong correlation between SNR temperature and HR, or SNR temperature and size.

all of the fitted SNRs have abundances that are similar to the M33 ISM abundance. This implies that most of the bright SNRs are ISM-dominated, and no longer display strong evidence of the ejecta signature of their progenitor. This may also indicate that fitting a global model to the entire SNR—as opposed to separately fitting and analyzing individual features—will yield fitted parameters that represent global averages of the ejecta structure of the SNR, which generally leads to some loss of information.

3.3.4 Hardness Ratios

As first discussed in Chapter 2, HRs can be used to differentiate different X-ray source types for those sources that lack the requisite counts for a detailed spectral analysis. We attempted to type the sample of X-ray detected SNRs by HRs in bands defined in Maggi et al. (2014). These bands are selected to highlight specific features in a SNR's thermal spectrum. The soft band is from 0.3 keV to 0.7 keV and is dominated by oxygen lines. The medium band ranges from 0.7 keV to 1.1 keV and includes both Fe L-shell lines indicative of a Type Ia progenitor as well as Heα lines from Ne XI and Ne X, themselves indicative of a CC progenitor. The hard band goes from 1.1–4.2 keV and is comprised of thermal continuum plus lines from Mg, Si, S, Ca, and Ar. The HRs also yield valuable information in the form of temperature; hotter SNRs should exhibit harder HRs, while more evolved objects with cooler plasmas should be more evident in the soft band (Maggi et al., 2014). We calculate HRs based on counts in the soft, medium and hard bands above with the following equations:

$$HR1 = \frac{M - S}{S + M + H}, \quad HR2 = \frac{H - M}{S + M + H} \tag{6}$$

We first simulate SNR spectra in `XSPEC` using a `vpshock` model, a fixed Galactic absorption component (`tbabs`, 0.5×10^{21} cm^{-2}), and a varying M33 absorption component (`tbvarabs`). We then compute the HRs from counts in the bands defined above from the simulated SNR spectra allowing only the temperature, M33 absorption component, and abundances of O and Fe to vary, with the abundances of Ne and Mg tied to the O abundance.

The HRs computed from these simulated spectra are plotted in the top-right, bottom-left, and bottom-right panels of Figure 3.7. In each panel the triangular region denotes the allowed HR values for positive count measurements. The top-right panel depicts the simulated HRs for a low

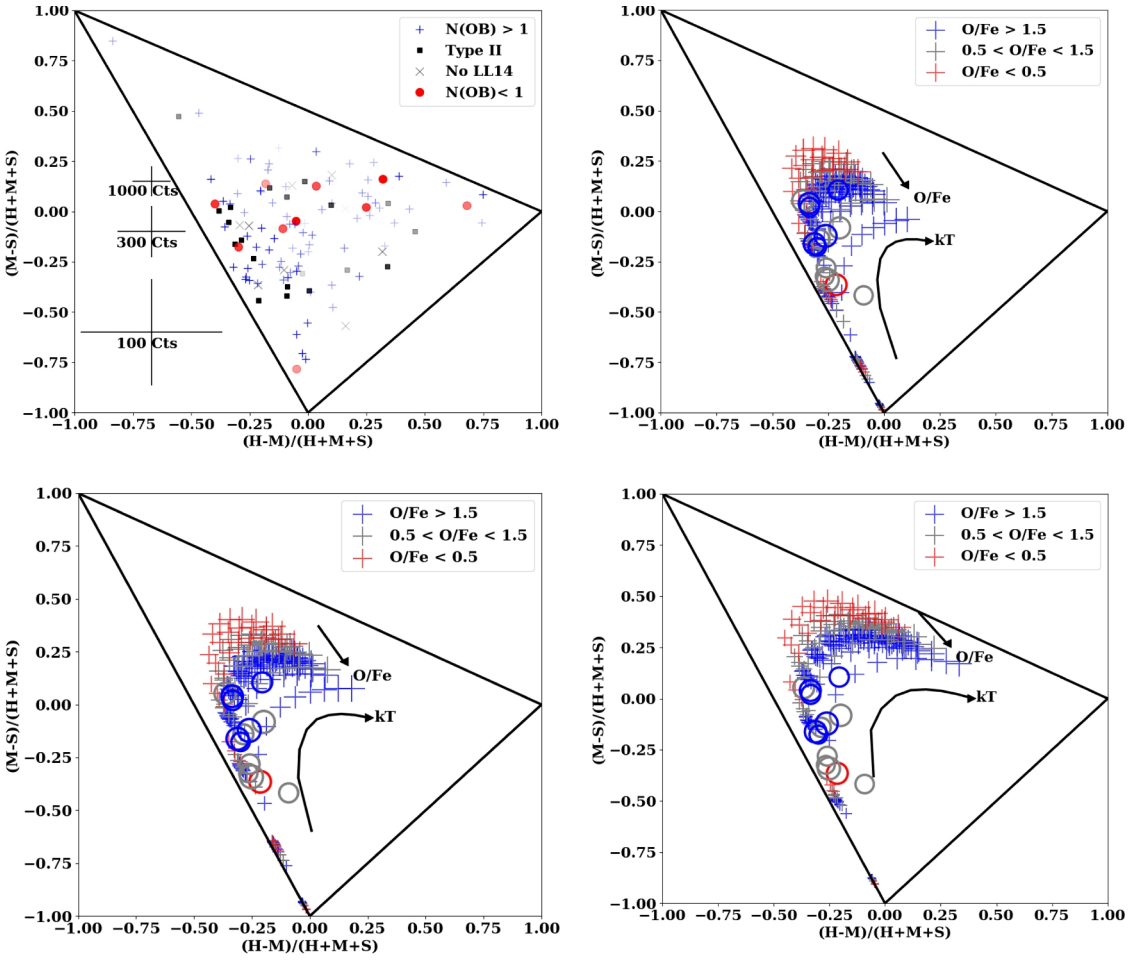

Figure 3.7: *Top-Left*: HR from counts in the 0.3-0.7 (soft), 0.7-1.1 (medium) and 1.1-4.2 (hard) keV bands for all SNRs detected at 3σ. Representative errors for bins of 1000 counts, 300 counts, and 100 counts are displayed for reference. Candidate Type Ia SNRs based on LL14 classifications are denoted by red circles, candidate CC SNRs from LL14 are denoted by blue crosses, and black squares are SNRs with CC progenitors based on analysis of the surrounding stellar population by Jennings et al. (2014). Those without an LL14 or Jennings et al. (2014) match are in gray. The transparency of the points is related to signal-to-noise, with the boldest points have the highest signal-to-noise values. *Top-Right*: HRs from a suite of SNR spectra simulated in `XSPEC` with a `vpshock` model and temperatures ranging from 0.1-1.0 keV, a range of O and Fe abundances, and with a fixed M33 absorption value of $N_H = 1 \times 10^{20}$ cm^{-2} (low N_H). Points are color-coded based on abundance ratio: red for low O/Fe, grey for O/Fe close to unity, and blue for elevated O/Fe. The 15 fitted SNRs are overplotted as unfilled circles using the same color scheme. The point size denotes temperature, with smaller crosses having lower temperatures. Arrows are added for reference to show the direction of increasing temperature, and increasing O/Fe ratio. *Bottom-Left*:: HRs from a suite of SNR spectra simulated in `XSPEC` with a `vpshock` model and temperatures ranging from 0.1-1.0 keV, a range of O and Fe abundances, and with a fixed M33 absorption value of $N_H = 1.2 \times 10^{21}$ cm^{-2} (intermediate N_H). *Bottom-Right*:: HRs from a suite of SNR spectra simulated in `XSPEC` with a `vpshock` model and temperatures ranging from 0.1-1.0 keV, a range of O and Fe abundances, and with a fixed M33 absorption value of $N_H = 3.5 \times 10^{21}$ cm^{-2} (high N_H). The fitted SNRs align most closely with the simulated sample at low N_H.

M33 absorption ($N_H = 1{\times}10^{20}$ cm^{-2}) from low temperatures ($\sim$ 0.1 keV, smaller crosses) to high temperatures ($\sim$ 1 keV, larger crosses) at a range of abundance ratios. Points are color-coded based on the abundance ratio of O/Fe: blue crosses are those SNRs with high O/Fe ratios, indicating O enrichment, grey crosses are those SNRs for which the O/Fe ratio is near unity, and red crosses are SNRs for which the O/Fe ratio is low and thus indicative Fe enrichment. The unfilled circles are the 15 SNRs for which we were able to perform detailed spectral fits (Table 3.4), and are also color-coded based on their fitted abundance ratios. The bottom-left panel displays the simulated HRs for an intermediate M33 absorption value ($N_H = 1.2{\times}10^{21}$ cm^{-2}), while the bottom-right has a high M33 absorption value ($N_H = 3.5{\times}10^{21}$ cm^{-2}), both with the same spread of temperatures and abundance ratios as the top-right panel. The size of the points (both simulated and fitted) indicates temperature, with smaller crosses having lower temperatures.

There is a clear trend with temperature in the simulated SNR HRs, wherein SNRs at a given O/Fe and N_H move to the left and down (softer HRs) in Figure 3.7 as their temperatures go from high ($\sim$ 1 keV) to low ($\sim$ 0.1 keV). This is denoted by the black arrow labeled "kT" on each panel. The progression of the panels illustrates the changes to simulated HRs with changing absorption values, with increasing absorption moving SNRs at a given temperature and abundance ratio to generally harder HRs (up and to the right). At a given temperature and value of N_H the O/Fe abundance ratio can move the HR diagonally downwards on the plot, as indicated by the black arrow labeled "O/Fe". Some separation between abundance ratios is evident in the simulated sample, with SNRs at low O/Fe exhibiting larger HR1 values, possibly indicative of their stronger Fe L-shell lines and thus a Type Ia progenitor.

The fitted sample (unfilled circles) is more consistent with the simulated sample at low N_H ($N_H = 1{\times}10^{20}$ cm^{-2}) for the majority of the fitted SNRs. The only SNR with low O/Fe in our fitted sample (red unfilled circle) is roughly consistent with the simulated sample assuming a lower temperature. There is one outlier in the fitted sample that does not clearly follow any of the simulated trends. This SNR has an intermediate abundance ratio value (grey unfilled circle) and is separated from the bulk of the population with the largest HR2 value. This is source XMM-132 (L10-081, LL14-119), and is classified as a CC SNR by LL14, and by Jennings et al. (2014) with a derived progenitor mass of $\sim$14M$_\odot$.

We next look for correlations between SNR progenitor type and HR in our sample of 3σ

detections by cross-correlating our sources with those from LL14 and Jennings et al. (2014) and assigning to each SNR, when available, a possible progenitor type based on their analyses of the surrounding stellar population. We illustrate this comparison between HRs and tentative progenitor type in the top-left panel of Figure 3.7, with HRs and their associated errors calculated from counts in the above bands using BEHR (Park et al., 2006). Each point is color-coded based on potential progenitor type: blue crosses represent potential CC classifications (nearby OB stars found in LL14), black squares are sources with CC classification from Jennings et al. (2014), gray x's are sources for which there is no counterpart in LL14 or Jennings et al. (2014), and filled red circles are sources with potential Type Ia progenitors (no nearby OB stars found in LL14). More transparent points have lower signal-to-noise ratios. The typical HR errors for sources with 1000 counts, 300 counts, and 100 counts are displayed for reference. We find no correlation between HR in these bands and potential SNR progenitor type.

Ultimately we are far from the idealized case in the other panels of Figure 3.7, and the range of temperatures, column densities, and abundance ratios probed, coupled with uncertainties on the HRs, do not allow for any kind of quantitative separation for SNR progenitor type based on HRs alone. In addition, it is perhaps not surprising to find no strong separation given that we expect only 17% of the SNRs in M33 to be of Type Ia origin (Mannucci et al., 2005), which is about 18 total out of all 3σ detections.

It is also true that some Type Ia SNRs in the LMC are Balmer-dominated, with little to no enhancement of [S II] emission (Hughes et al., 1995). As noted by Tuohy et al. (1982) this effect arises due to a fast shock propagating into a region of neutral hydrogen and giving rise to strong Balmer emission, while [S II] emission is suppressed in the high temperature region behind the shock due to low collisional rates. This implies that we may be missing the sample of young, ejecta dominated Type Ia SNRs in M33 by selecting SNRs mainly through their enhanced [S II]/Hα ratios; however, we expect the population of young, Balmer-dominated Type Ia SNRs in particular to be quite small, as only 4 are reported in the LMC (Tuohy et al., 1982; Hughes et al., 1995; Ghavamian et al., 2007; Maggi et al., 2016). For older SNRs, the ejecta will be well-mixed with the surrounding circumstellar material, so evidence of the progenitor's ejecta signature would be diluted or erased.

In addition to the bands defined by Maggi et al. (2014) we also test the correlation between

potential SNR progenitor type (derived from LL14) and HRs based on counts in the < 2 keV bands. This particular set of HRs was developed to take advantage of the soft-sensitivity of *XMM-Newton*. The ratios are calculated as follows:

$$\begin{aligned} HR1_{XMM} &= (M_{XMM} - S_{XMM})/(M_{XMM} + S_{XMM}) \\ HR2_{XMM} &= (H_{XMM} - M_{XMM})/(H_{XMM} + M_{XMM}) \end{aligned} \tag{7}$$

Here, the soft band is defined as 0.2-0.5 keV, the medium band is 0.5-1 keV, and the hard band is 1.0-2.0 keV. As outlined in W15 we used these HRs to isolate new SNR candidates based on the HR cuts described by Pietsch et al. (2004a), which are designed to take advantage of *XMM-Newton's* soft sensitivity. This method, combined with visual inspection of the SNR candidates in [S II]and Hα, yielded the discovery of three new SNRs in M33 (first reported in W15). As before, we first compute the HRs in these bands based on SNR spectra simulated in `XSPEC` with the model outlined above. The HRs computed from these simulated spectra are plotted with the same color-scheme as before in the top-right ($N_H = 1{\times}10^{20}$ cm^{-2}), bottom-left ($N_H = 1.2{\times}10^{21}$ cm^{-2}), and bottom-right ($N_H = 3.5{\times}10^{21}$ cm^{-2}) panels of Figure 3.8. The thick black arrow indicates the direction of increasing temperature (smaller to larger crosses). There is no clear distinction between abundance ratio values in these bands based on simulated spectra. The top-left panel of Figure 3.8 displays the HRs calculated from source counts in the above bands using BEHR (Park et al., 2006). Typical errors from BEHR for sources with 1000 counts, 300 counts, and 100 counts are displayed for reference. The points are again color-coded based on potential progenitor type from Jennings et al. (2014) or LL14. Similarly to the simulated data, there is no separation by progenitor type based on HRs in these bands.

3.3.5 X-ray Morphology: Power-Ratios

A basic question about an SNR is the nature of the SN explosion and the progenitor itself. One way to tackle this question is through the X-ray morphology of the SNR. Specifically, Lopez et al. (2009, 2011) showed that the X-ray morphologies of young, ejecta-dominated SNRs are correlated with SN progenitor type as determined from other methods, like spectral fits. Lopez et al. (2009, 2011) determined progenitor type (Type Ia versus CC) for a subsample of Milky Way and MC

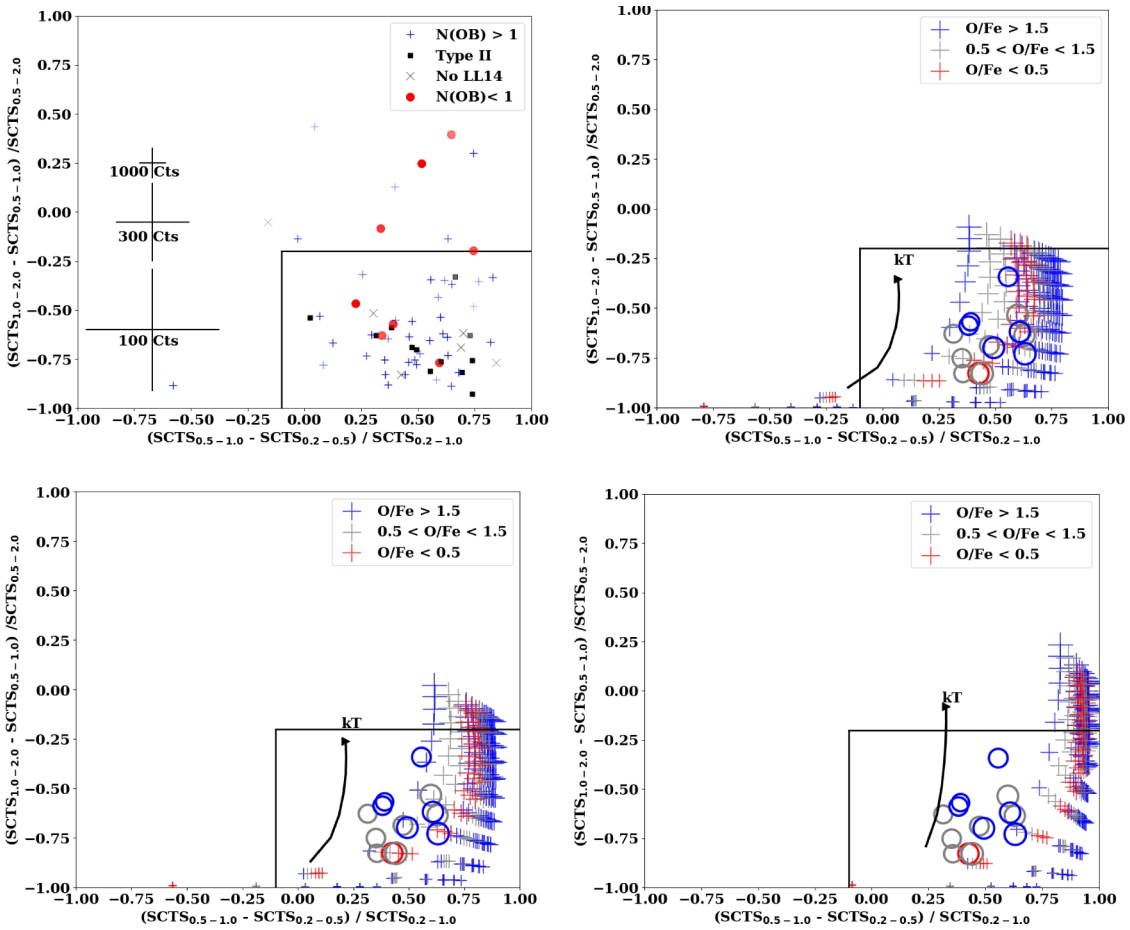

Figure 3.8: *Top-Left*: HR from source counts for the 0.2-0.5 (soft), 0.5-1.0 (medium) and 1.0-2.0 (hard) keV bands for SNRs detected at 3σ. Representative errors for bins of 1000 counts, 300 counts, and 100 counts are displayed for reference. Candidate Type Ia SNRs based on Lee & Lee (2014b) classifications are denoted by red circles, while the candidate CC SNRs from this same study are denoted by blue crosses. Those without a Lee & Lee (2014b) match are in gray. The majority of sources lie within the box defined by Pietsch et al. (2004a) where we expect most SNRs to fall, but there is not clear separation within this between Type Ia and CC SNRs. *Top-Right*: HRs from a suite of SNR spectra simulated in `XSPEC` with a `vpshock` model and temperatures ranging from 0.1-1.0 keV, a range of O and Fe abundances, and with a fixed M33 absorption value of $N_H = 1 \times 10^{20}$ cm^{-2} (low N_H). SNRs are color-coded based on abundance ratio: red for low O/Fe, grey for O/Fe close to unity, and blue for elevated O/Fe. The 15 fitted SNRs are overplotted as unfilled circles using the same color scheme. The point size denotes temperature, with smaller crosses having lower temperatures. Arrows are added for reference to show the direction of increasing temperature. *Bottom-Left:* HRs from a suite of SNR spectra simulated in `XSPEC` with a `vpshock` model and temperatures ranging from 0.1-1.0 keV, a range of O and Fe abundances, and with a fixed M33 absorption value of $N_H = 1.2 \times 10^{21}$ cm^{-2} (intermediate N_H). *Bottom-Right:* HRs from a suite of SNR spectra simulated in `XSPEC` with a `vpshock` model and temperatures ranging from 0.1-1.0 keV, a range of O and Fe abundances, and with a fixed M33 absorption value of $N_H = 3.5 \times 10^{21}$ cm^{-2} (high N_H). The fitted SNRs align most closely with the simulated sample at low N_H, though there is no clear trend with abundance ratio and HRs in these bands.

SNRs through a multipole expansion of the X-ray surface brightness of each source. This method produces quantitative measurements of morphological asymmetry for SNRs, and is referred to as the "power-ratio" method. Lopez et al. (2009, 2011) find that for ejecta dominated SNRs, Type Ia SNe are "statistically more spherical and mirror symmetric" than CC SNe, particularly in the 0.5-2.1 keV band.

The powers of the multipole expansion are found by integrating the magnitude of the mth multipole moment over the aperture radius for the source of interest. Each power is normalized by the zeroth moment, P_0, which yields the power-ratios P_m/P_0. In particular, the morphological information of interest for SNRs is encoded the P_2/P_0 (quadrupole) and P_3/P_0 (octopole) ratios. The quadrupole ratio measures the ellipticity or elongation of a source, while the octopole ratio is able to discriminate between objects that have asymmetric surface brightness from those that do not. As described above, this implies that the more spherical and mirror symmetric Type Ia SNe tend to have lower P_2/P_0 and P_3/P_0 values than CC SNe, though the quadrupole ratio appears to be the more robust indicator of type. A more detailed description of the equations used for the multipole expansion as well as the power-ratio method itself can be found in Lopez et al. (2009).

Because this method has thus far only been applied to relatively nearby SNRs, we have performed a series of tests on a subset of the Lopez et al. (2011) data to determine the spatial resolution and number of counts necessary for determining SN progenitor type via the power-ratio method at distances greater than the MCs. Our tests are performed on a series of SNRs in the LMC from Lopez et al. (2011) obtained from *Chandra* archive. Our selection of SNRs all have between 30–60 ks of exposure time. The data from the *Chandra* archive is processed using `CIAO`. The aspect histograms are made using the `CIAO` task `asphist`, the instrument maps are creating using `mkinstmap`, and the exposure maps are created using `mkexpmap`. We use `dmcopy` to create images in the soft band (0.5-2.1 keV) and `dmextract` with custom regions to extract background images for each SNR. Following Nurgaliev et al. (2013), we quantify the morphology in terms of sums over counts within a selected aperture radius. With the data processed in this way we are able to reproduce the results for six SNRs from Lopez et al. (2011), namely the top-left panel of their Figure 2. With a successful reproduction of the method, we are next able to test the limits of morphological measurements in terms of both spatial resolution, and count thresholds, as described in turn below.

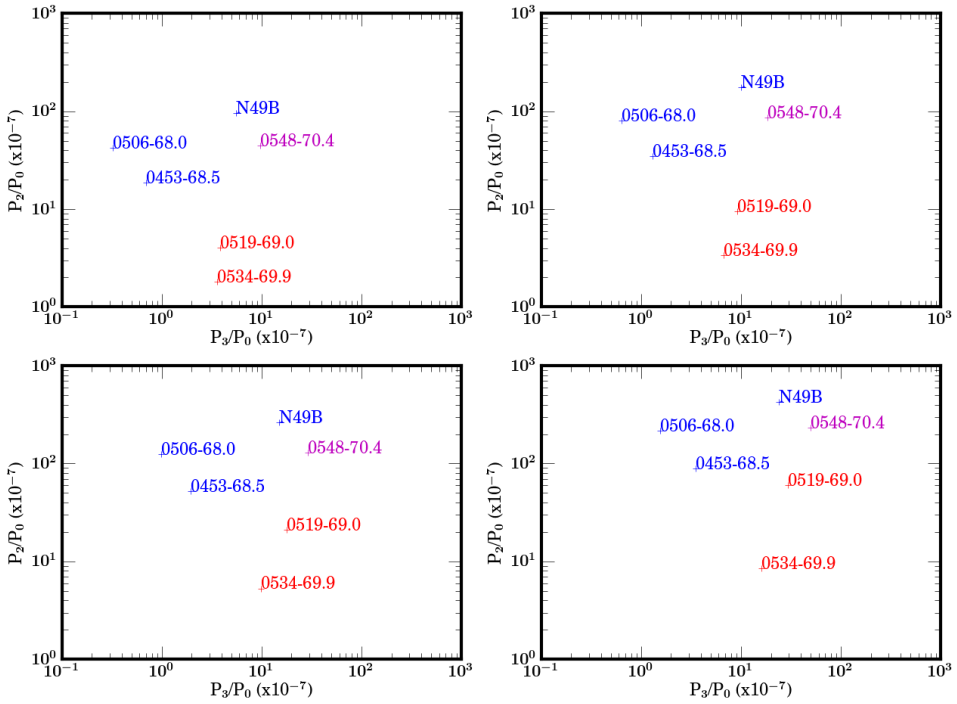

Figure 3.9: Power-ratios in the 0.5-2.1 keV band using six sources from Lopez et al. (2011). Core-collapse SNe are denoted in blue, and Type Ia SNe are denoted in red, and SNRs of unknown type are denoted in magenta. *Top-left*: SNRs at LMC distance. *Top-right*: SNRs at four times the LMC distance. *Bottom-left*: SNRs at eight times the LMC distance. *Bottom-right*: SNRs at M33 distance.

To test the spatial resolution limits, we bin the data for a subsample of LMC SNRs sequentially until the resulting values change the quantitative morphologies. With each binning we recalculate the SNR centroid based on the new image. We find that binning the data by four, eight, and sixteen and recalculating the power-ratios preserves the separation between the two types. Our tests reveal that the decreased spatial resolution at the distance of M33 should not affect our ability to type SNRs based on morphology as long as the SNRs possess enough counts. However, at high enough binning, it becomes apparent that there are too few pixels to extract robust morphological information. The results become significantly unreliable when all the counts are contained in less than roughly 100 pixels, depending on number of counts. Thus the maximum distance at which we can apply this technique depends on the size of the SNR as well as the distance. The results of this test, with binning factors equivalent to LMC, 4× LMC, 8× LMC, and M33 distance, are

displayed in Figure 3.9. We find a limiting distance for this method of $\sim$ 1200 kpc for the 0.5" *Chandra* pixel size and the largest SNR radius in Lopez et al. (2011) (r $\sim$ 30 pc). Adopting more conservative radii for young, ejecta-dominated SNRs of 20 pc and 10 pc yields limiting distances of $\sim$ 830 kpc, and $\sim$ 410 kpc, respectively, which puts M33 (817 kpc) at the threshold for efficacy of this method, assuming there are SNRs with the requisite number of sizes, and large enough number of counts, as described below.

To test the count threshold, we take a random sampling of between 1 and 10% of the original counts from a sample of LMC SNRs keeping the images at full resolution and recalculating the power-ratios. We are motivated to take such small fractions of the overall counts because the brightest SNRs in M33 have between 10^4–10^5 total counts, which is on the order of 10% of the total counts of bright SNRs in the LMC as used in Lopez et al. (2011). We find that the method produces reliable results down to 2×10^3 counts for Type Ia and down to 3×10^2–4×10^2 counts for CC SNe. Below these count thresholds the method begins to produce unphysical results, i.e. power ratios with errors that include negative values. The results of this test on LMC SNRs with 1%, 3%, 7%, and 10% of their original counts are displayed in Figure 3.10. CC SNe are more robust to this effect because they initially have higher power ratios for both the octopole and quadrupole moments; SNRs that have lower power-ratios with larger error bars require more counts to get a robust typing. Therefore, we find that at least 2×10^3 counts are needed to robustly separate CC SNR progenitors from Type Ia SNR progenitors.

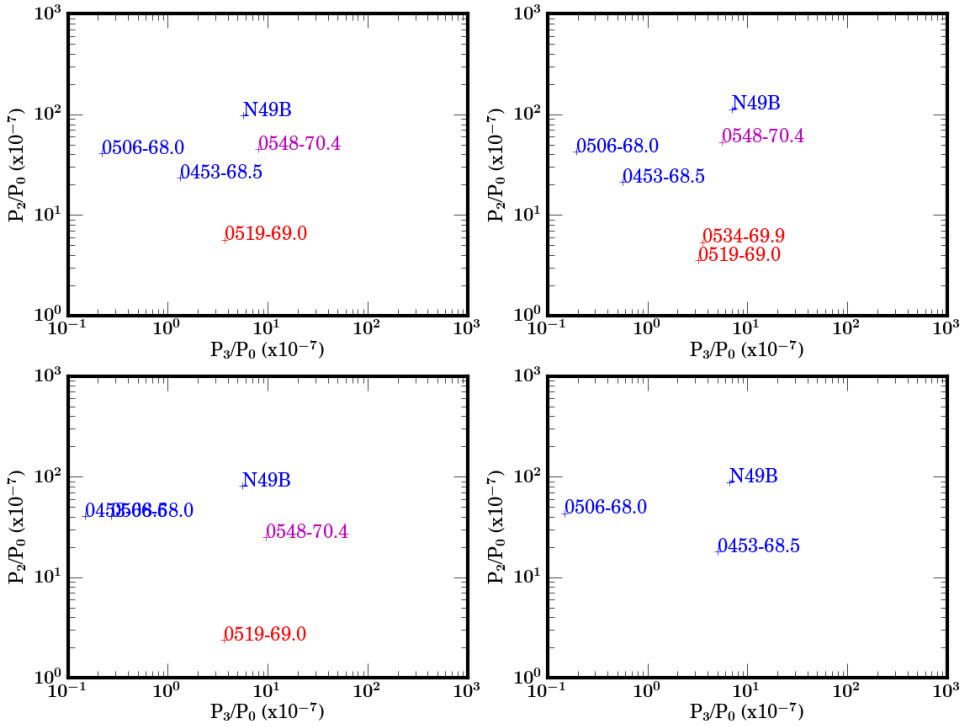

Figure 3.10: Power-ratios in the 0.5-2.1 keV band for six LMC SNRs from Lopez et al. (2011). CC SNe are denoted in blue, Type Ia SNe are denoted in red, and SNRs of unknown type are denoted in magenta. *Top-left*: SNRs at LMC distance with 10% of the original counts. *Top-right*: SNRs at LMC distance with 7% of the original counts. *Bottom-left*: SNRs at LMC distance with 3% of the original counts. *Bottom-right*: SNRs at LMC distance with 1% of the original counts.

Taken collectively, our tests demonstrate that SNRs with a radius of 20 pc and $\geq 2\times 10^3$ counts can have their progenitors typed via the power-ratio method out to the distance of M33. While there are a handful of SNRs in M33 with the requisite number of counts, none of these are large enough (r $>$ 20 pc) to utilize the power-ratio method for robust typing. We have verified this by testing the method on a few of the largest and brightest SNRs from the ChASeM33 survey and finding unphysical answers. In order to determine the quantitative morphologies of a large enough sample ($\sim$ 50) of SNRs in M33, our analysis suggests we would need an X-ray telescope with $\sim$ 0.03" resolution (17$\times$ the resolving power of *Chandra*), and with a 0.4 m^2 collecting area (10$\times$ the collecting area of *Chandra*).

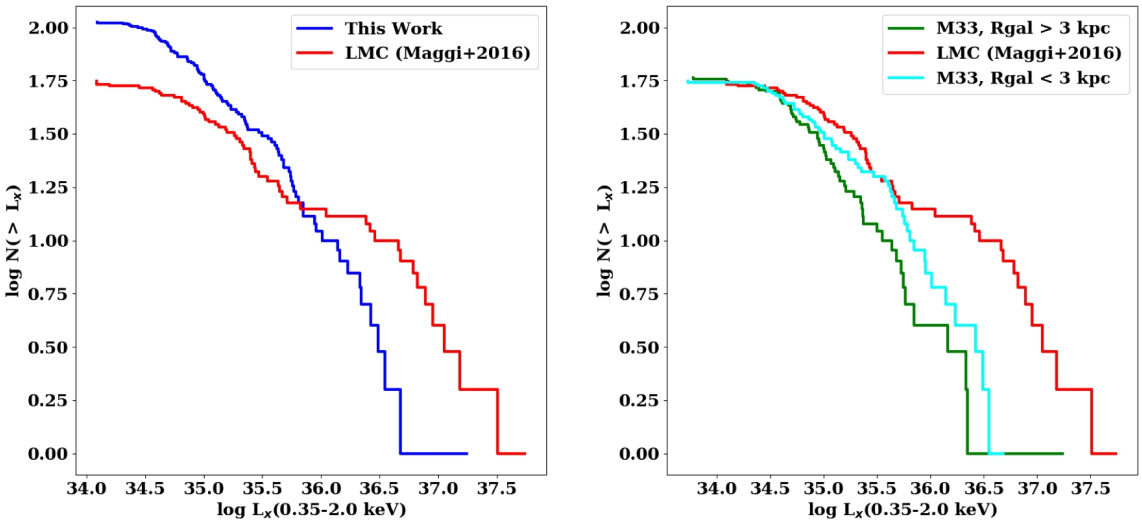

Figure 3.11: *Left*: Cumulative X-ray luminosity function (XLF) for all 3σ SNR detections from this work in blue. Cumulative XLF for the LMC from Maggi et al. (2016) in red. *Right*: Cumulative XLF for the inner 3 kpc of M33 (cyan, solar metallicity) and the outer 3 kpc (green, LMC-like metallicity) with the LMC XLF (red) for reference.

3.4 Discussion

Our deep XMM-Newton survey of M33 complements the high spatial resolution of the SNR candidates measured by the ChASeM33 survey with increased counts for spectral fitting, expanded survey area, and increased soft sensitivity for SNR detection. In this section we explore the implications of our results for the SNR X-ray luminosity function, and the X-ray detectability of SNRs.

3.4.1 Supernova Remnant X-ray Luminosity Function

We first construct the X-ray luminosity function (XLF) in the 0.35-2.0 keV band for all detections in this work (3σ measurements) as shown in Figure 3.11. We overplot the XLF from Maggi et al. (2016) in red for comparison, transforming their 0.3-8.0 keV luminosities into the 0.35-2.0 keV band using WebPIMMS, and assuming an `apec` spectrum with kT=0.6 keV, M33 hydrogen column density of of $1{\times}10^{21}$ cm^{-2}, and a galactic absorption component of $6{\times}10^{20}$ cm^{-2}. This SNR catalog has 11 detections with $L_x > 10^{36}$ erg s^{-1}, as compared to 13 in the LMC, but fewer sources (three) at luminosities greater than $> 10^{36.5}$ erg s^{-1} than are found in the LMC (eight). The limiting luminosities for this survey and that of Maggi et al. (2016) are of the same magnitude:

L_x(0.2-2.0 keV) = 7.2×10^{33} erg s^{-1}, and L_x(0.3-8.0 keV) = 7.0×10^{33} erg s^{-1}, respectively.

The shape of the LMC XLF, as discussed by Maggi et al. (2016) is clearly complex, and differs from the simple power-law distribution that can be used to describe the M33 XLF. At the faintest end, there are likely incompleteness effects for both catalogs, but such claims cannot be made at the bright end, thus necessitating an explanation of the discrepancies for the population of bright SNRs. We discuss several possible explanation below.

The explanation is unlikely to be the current SFR. The SFRs of the two galaxies are similar: between 0.2–0.4 $M_\odot$ yr^{-1} in the LMC over the last 100 Myr, with an increase to a rate of 0.4 $M_\odot$ yr^{-1} occurring in the last 12 Myr (Harris & Zaritsky, 2009b), and an average rate of 0.3 $M_\odot$ yr^{-1} in M33 over the last 100 Myr (Williams et al., 2013a). Given these SFRs, both galaxies would be assumed to have close to the same rate of CC SNe production.

Another possible explanation, as discussed by Maggi et al. (2016) is metallicity effects. In particular, a lower metallicity environment will host stars with weaker line-driven stellar winds. The consequence is smaller wind-blown cavities for massive stars such that the SN explosion is running into a dense shell of material earlier in its evolution, leading to brighter SNRs at earlier times (Dwarkadas, 2005). It is clear that the LMC has more SNRs at the bright end than M33, but to test whether this is solely a metallicity effect with respect to M33 one needs to take into account the metallicity gradient in M33. To do so we construct the XLF for SNRs in M33 that are within 3 kpc of the galactic center, and the XLF for SNRs that are at galactocentric radii larger than 3 kpc, as the metallicity in M33 goes from near-solar values within 3 kpc to LMC-like metallicity outside 3 kpc (Magrini et al., 2007). The two M33 XLFs are depicted in the right-hand panel of Figure 3.11. In M33 the SNRs at higher metallicity ($<$ 3 kpc, cyan curve) have higher luminosities than those at lower metallicity ($>$ 3 kpc, green curve), which is exactly the opposite of the expected behavior if the luminosity differences are due to differences in progenitor wind mass-loss rates alone. If metallicity was the primary driver of differences in the SNR XLF one might expect the SMC, as the lowest metallicity galaxy, to host even more SNRs at the bright end than the LMC. As noted in Maggi et al. (2016) this is not the case. Furthermore, at later times the effects of SNe exploding into environments of differing densities would be largely erased, so metallicity effects on the surrounding medium would only be distinguishable for a younger population of SNRs.

Maggi et al. (2016) also found that SN type and ISM structure did not seem to play a strong

role in the SNR XLF shape in the LMC. The ratio of Type Ia versus CC SNRs in the XLF is difficult to compare across galaxies, as we do not have a definitive set of SN types for a large sample of M33 SNRs; however, both galaxies are likely dominated by core-collapse events. Maggi et al. (2016) note that the ratio of CC to Type Ia SNRs is slightly higher at the bright end of the LMC XLF, but not strongly so. Furthermore, while differences in the SNR brightness distribution could also arise from SNe that are exploding into non-uniform interstellar medium, Maggi et al. (2016) found no significant spatial correlation between SNRs in different luminosity bins and HI maps of the LMC. However, HI maps may be an imperfect indicator of "local" density around an SNR, so we cannot fully rule out that local density variations in the vicinity of SNRs contribute to different SNR luminosity distributions. In fact, one may even expect a more uniform ISM in a large, spiral galaxy like M33, as compared to LMC, which would result in SNRs with lower X-ray luminosities in an M33-like galaxy.

Finally, it may be that the most plausible explanation for the differences in SNR XLF shapes is that the SFHs are different on a 50 Myr timescale, which would be relevant for SNe production. The total LMC SFR has increased by a factor of 2 over the past 50 Myr (Harris & Zaritsky, 2009b) which could result in a top-heavy progenitor mass distribution compared with a constant SFR. For example, SN1987A had a relatively massive progenitor (20 M$\odot$; Woosley et al. (1988)). We do not possess a global and resolved star formation history for M33, but based on the SNR progenitor mass distribution in M33 with peak mass at around 8 $M_\odot$ from Jennings et al. (2014) it is likely that M33 has a near constant SFR on this timescale. Furthermore, M33 is relatively high-mass and isolated compared to the LMC, making it less likely to change its global SFR significantly on timescales as short as 50 Myr. Thus, it is possible that differences in the XLF distributions at the bright end between the LMC and M33 are due the progenitor mass distributions leading to more bright, young SNRs in the LMC than in M33.

3.4.2 Detectability

The M33 XLF appears to flatten around 3×10^{34} erg s^{-1}, implying that our sample may still be incomplete at the faintest luminosities, and that with increased sensitivity the entire SNR population of M33 could be detected. To explore X-ray detectability we first compare the luminosities in the 0.35-2.0 keV band for all sources to the Hα luminosities from LL14. In Figure 3.12 we

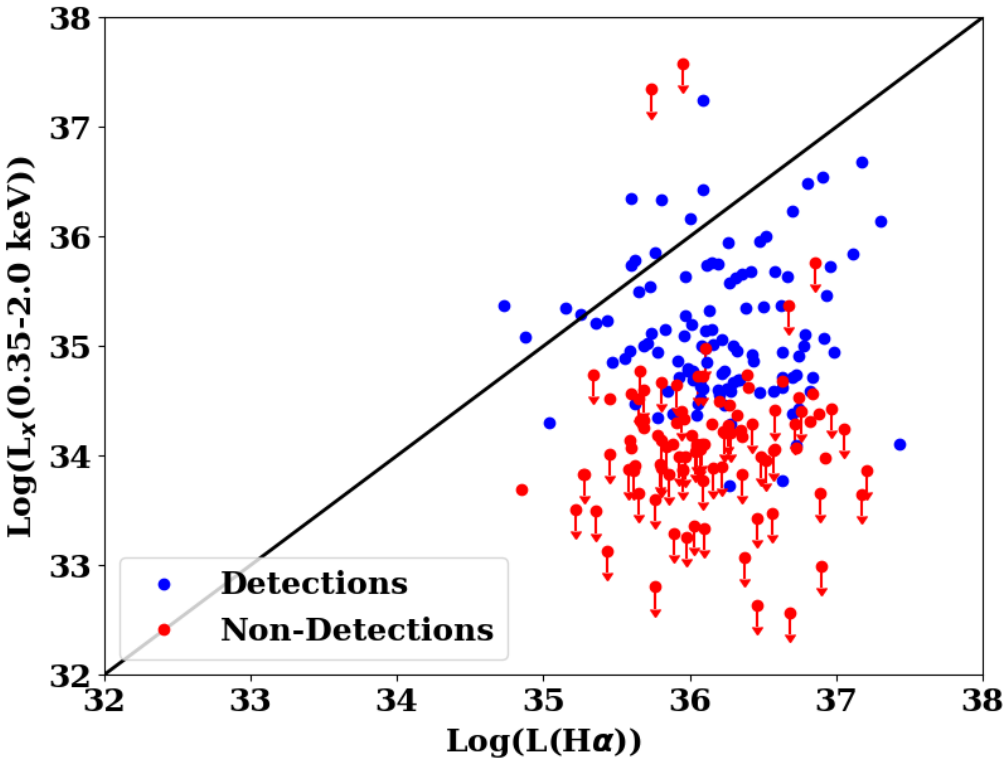

Figure 3.12: Comparison between the luminosities in 0.35-2.0 keV band from this work and the Hα luminosities from LL14. Red circles are SNR candidates non-detected in X-rays, and blue circles are SNRs detected at the 3σ level in X-rays. Sources that lie to the left and above the black diagonal line have X-ray luminosities greater than their Hα luminosities.

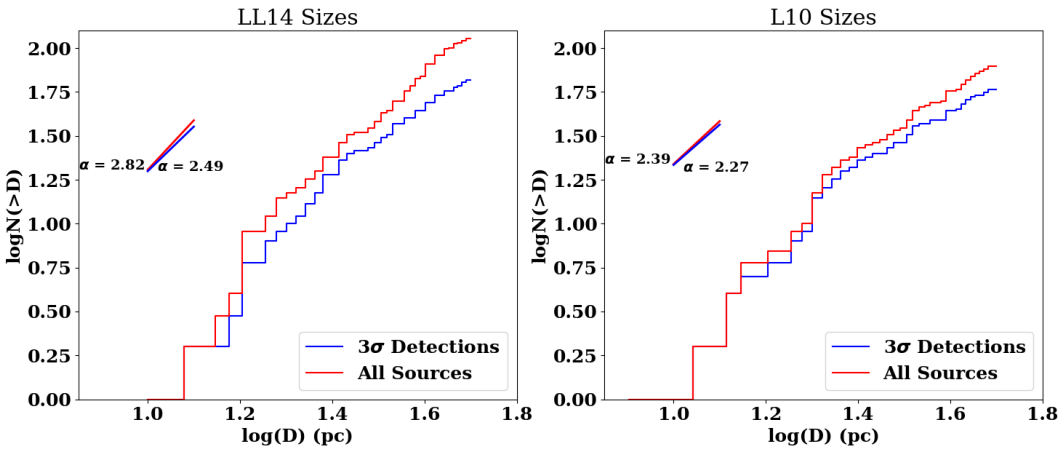

Figure 3.13: Cumulative size distribution for all 3σ detections (blue) versus all candidates (red) with D $<$ 50 pc in the sample for sizes measured by LL14 (left panel) and sizes measured by L10 (right panel). We measure slopes of $\alpha \sim 2.8$ and $\alpha \sim 2.5$ for all sources and all detections, respectively, using LL14 sizes. We find slopes of $\alpha \sim 2.4$ and $\alpha \sim 2.3$ for all sources and all detections, respectively, using L10 sizes. The slopes for all detections are in good agreement with the slope of $\alpha = 2.5$ expected of a population of SNRs in the Sedov phase.

plot the X-ray luminosity in this band versus the Hα luminosity and find no significant correlation between the luminosities for either X-ray detections (blue points) or X-ray non-detections (red points, sources from the optical catalogs that were measured at the 2σ or upper-limit level in X-rays). Similarly to L10, we find that only one SNR has an X-ray luminosity significantly higher than its Hα luminosity (i.e. falls above the black line), and this is the brightest SNR in the sample, XMM-041 (L10-025). While it does appear that SNRs that are brighter at X-ray wavelengths also have generally higher Hα luminosities, there is a large spread in the X-ray to Hα luminosity comparison. The lack of strong correlation between luminosities can be explained by differences in the regions of the SNR being probed by each diagnostic. Namely, the X-ray luminosity is probing the region of the reverse shock, which is generally a region of higher temperature that cools more slowly. The Hα luminosity, by contrast, originates from recombination in the cooler, more dense shell region, which tends to cool on shorter timescales (Long et al., 2010; Leonidaki et al., 2013). The lack of correlation may also be due to the presence of non-uniform ISM, rather than regions of differing temperatures (Pannuti et al., 2007).

We also compare the cumulative size distribution for all X-ray detected SNRs versus all sources (detections and candidates) in our catalog with D $<$ 50 pc to look for differences between the slopes

of the distributions of each population. We choose this size cutoff, because the population of SNRs and SNR candidates is not complete above D $\sim$ 50 pc. Our results are plotted in Figure 3.13 both for sizes from LL14 (left panel) and sizes from L10 (right panel). We find that the addition of 2σ and upper-limit measurements to the cumulative distribution tends to steepen the slope. This is likely because the population of SNR candidates non-detected in X-rays are biased towards larger diameter sources, as can also be seen in Figure 3.14. Likewise the slope of the cumulative distribution when using the LL14 sizes is steeper than the slope when using only L10 sizes, owing to the fact that the LL14 radii are systematically larger than those measured by L10. The slopes of the cumulative distributions for the 3σ SNR detections only are $\alpha \sim 2.5$ and $\alpha \sim 2.3$ when using LL14 and L10 size measurements, respectively. Both measured slopes are consistent with $\alpha = 2.5$, which is the slope expected for a population of SNRs in the Sedov phase. However, there are also various selection effects that can lead to biases in the sample of SNRs in a cumulative size distribution. For example, ISM conditions can strongly affect both the size and luminosity evolution of an SNR, though without detailed constraints on local ISM conditions we are unable to quantify the impact of such an effect. Surveys such as this one that confirm SNR candidates primarily on the basis of both optical and thermal X-ray emission are also liable to miss some young, X-ray emitting SNRs, thus biasing an optically selected and X-ray confirmed sample towards larger diameter SNRs.

In addition to the cumulative size distribution of the sample, we also look at the overall size distribution of all detections versus non-detections at all diameters. We plot this distribution in Figure 3.14, with all sources at D $>$ 100 pc placed in the rightmost bin. The X-ray detected SNR sample extends to smaller diameters, implying that most small diameter SNRs are detected in X-rays. By contrast, the X-ray non-detections display a bias towards larger sizes, and have a sharper cutoff at smaller diameters than the population of sources detected in X-rays. The difference in diameters between the X-ray detected and X-ray non-detected sample may be attributed to age, or evolutionary effects, as young SNRs in the free expansion phase are likely to display X-ray emission, while older SNRs in the radiative phase show stronger optical emission (e.g. Leonidaki et al., 2010). This difference in sizes between the two populations leads to a steepening of the slope of the cumulative distribution when SNR candidates that are non-detected in X-rays are included.

Finally, we compare the distribution of [S II]/Hα ratios for SNRs detected in X-rays versus those candidates undetected in X-rays in this catalog. The [S II]/Hα ratio is typically used as

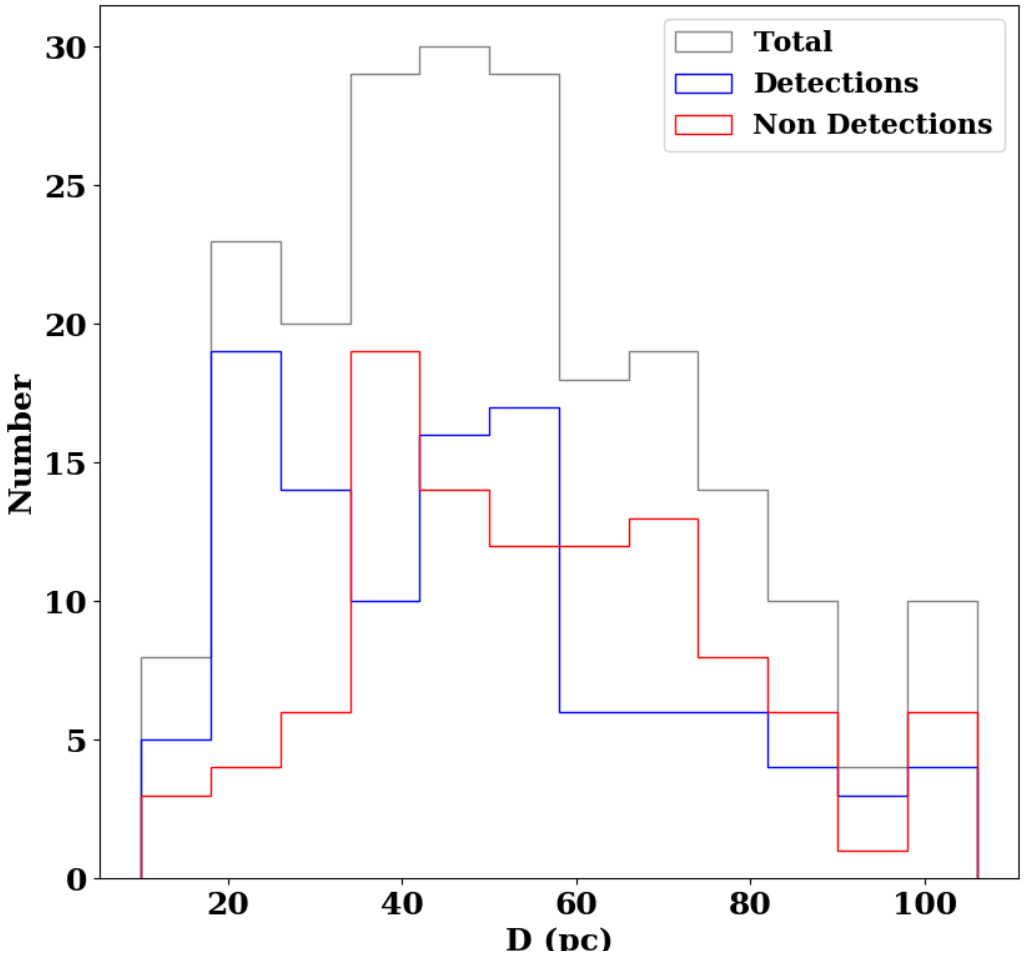

Figure 3.14: Histogram of sizes from L10 and LL14 for all non-detections (red) and detections (blue) in this sample. All sources with D> 100 pc are put into the rightmost bin.

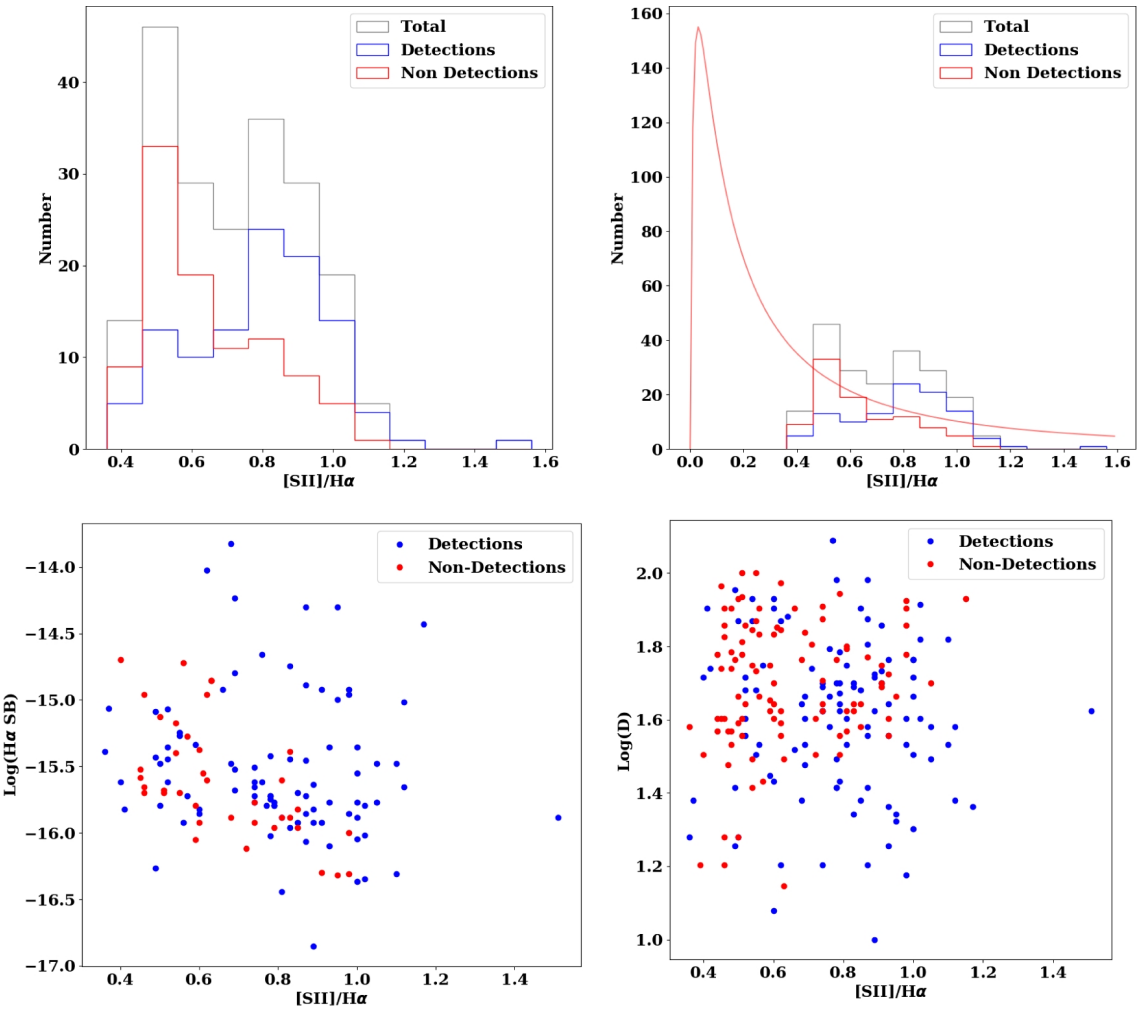

Figure 3.15: *Top left*: Histogram of [S II]/Hα ratios from L10 and LL14 for all SNR candidates non-detected in X-rays (red) versus X-ray detected SNRs (blue) in the sample. *Top right*: A log-normal error distribution of line ratios with a mean of 0.1 and σ value of 0.1 overplotted with respect to the population of X-ray non-detections. *Bottom left*: [S II]/Hα ratios from L10 and LL14 for all SNR candidates non-detected in X-rays (red) versus X-ray detected SNRs (blue) versus the measured Hα surface brightness values from L10. *Bottom right*: [S II]/Hα ratios from L10 and LL14 for all SNR candidates non-detected in X-rays (red) versus X-ray detected SNRs (blue) versus SNR diameters in pc.

a way to distinguish optical emission from shocked regions in SNRs from emission from H II regions, with a cutoff at > 0.4 for classification as an SNR candidate. Higher [S II]/Hα values are indicative of regions with radiative shocks where enough recombination has occurred to produce significant [S II] emission, as in SNRs. In Figure 3.15 we demonstrate that there are two distinct populations in the [S II]/Hα distribution, with the SNR candidates non-detected in X-rays being drawn from a distribution with on average lower measured [S II]/Hα than the population of X-ray detected SNRs. To determine if these populations are physically distinct, we look for correlations between [S II]/Hα and object size and surface brightness as shown in the bottom two panels of Figure 3.15. We find no strong correlation between [S II]/Hα ratio and object size, and only a slight correlation between surface brightness and this ratio, with the lower surface brightness non-detections displaying on average higher [S II]/Hα values (bottom-left panel of Figure 3.15). It is possible that some of the X-ray non-detections at low [S II]/Hα (but above the 0.4 SNR candidate threshold) could represent the tail-end of a log-normal error distribution of line ratios of ionized nebulae. An example of such a distribution containing ~ 480 sources with a mean [S II]/Hα value of 0.1 and $\sigma \sim 0.1$ is over plotted in red on the top-right panel of Figure 3.15.

The application of the cutoff at [S II]/H$\alpha \sim 0.4$ for optically identifying SNR candidates should not be discounted based on a number of X-ray non-detected SNR candidates that also fall above this threshold, as this may be due to differences in varying shock conditions, or circumstellar environment on small scales. For example, SNRs that have not encountered enough dense material may not form radiative shocks, and would therefore not display high [S II]/Hα values. Similarly, if the metallicity of the ISM is non-uniform one might expect different distributions of [S II]/Hα depending on location in the galaxy. To test for environmental differences we construct a histogram of the galactocentric radii for all X-ray detected SNRs (blue) and X-ray non-detected SNR candidates (red) in Figure 3.16. The population of X-ray detections (sources with higher [S II]/Hα, as can be seen from the upper left plot of Figure 3.15) are located at preferentially smaller galactocentric distances than the population non-detected in X-rays (sources with lower [S II]/Hα). We find no evidence that this separation is due to a gradient in exposure time or detector location in the observations. Instead, the separation may point to a metallicity effect, as there is a known chemical abundance gradient in M33, with the highest metallicities occurring at galaxy center and decreasing outwards (Magrini et al., 2007; Neugent & Massey, 2014). In particular, (Magrini et al.,

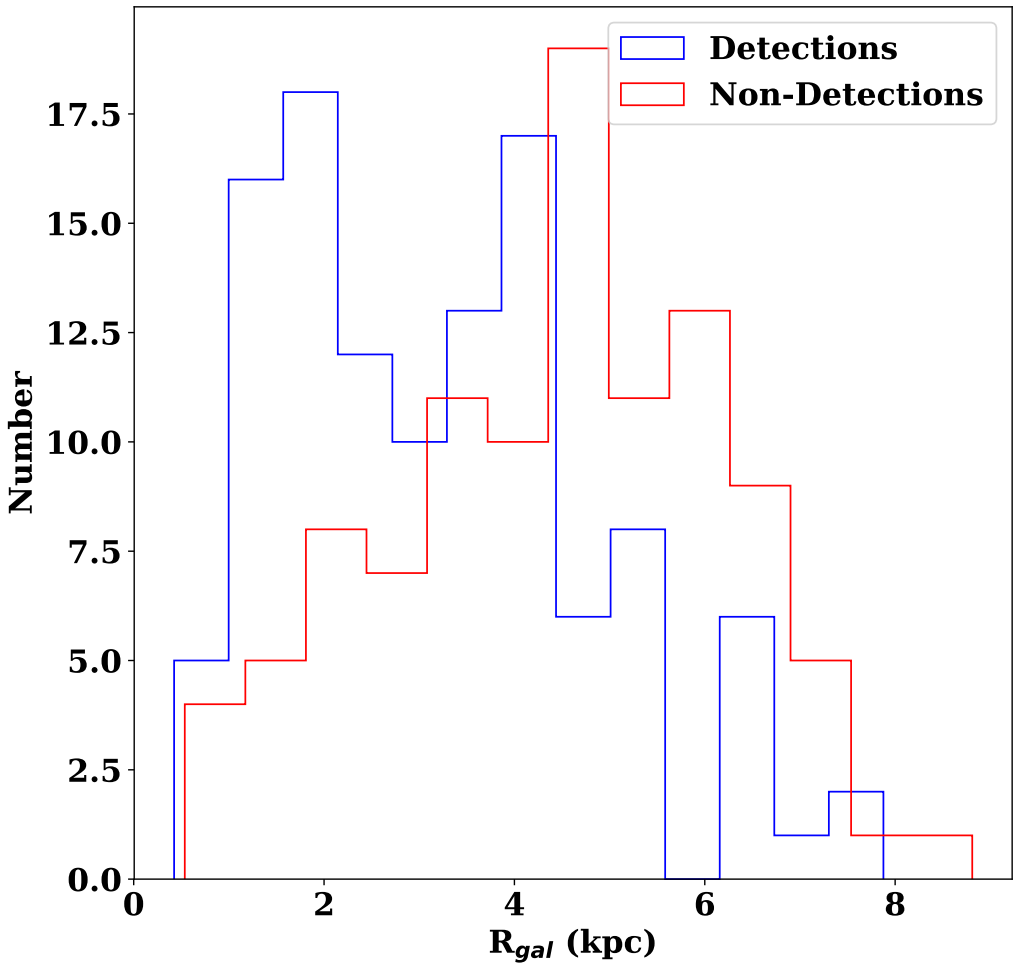

Figure 3.16: Histogram of galactocentric radii for all X-ray non-detections (red) and X-ray detections (blue) in this sample.

2007) measure this gradient as comprised of two slopes with the break occurring at R $\sim$ 3 kpc, similar to the radius at which we see the separation between the two histograms in Figure 3.16. Alternatively, this separation could be due to the effects of differing densities, with higher densities in the inner parts of the galaxy leading to stronger X-ray emission, and high [S II]/Hα values.

3.5 Synopsis

We have carried out a deep *XMM-Newton* Survey of M33 to complement the one performed by *Chandra*. With the power of both datasets we have detected at 3σ confidence $\approx$ 50% of the SNR candidates in M33 from previous X-ray and optical surveys (e.g. L10, LL14). These 105 sources are all robust SNR detections verified by both optical and X-ray measurements. We performed detailed spectral fitting for 15 SNRs, twice the number possible than with the *Chandra* data alone. We find evidence of elevated O/Fe values from X-ray spectral fits for one SNR (XMM-068), implying that this SNR exploded in a region generally enriched by CC ejecta. Based on the fitted spectral parameters we also determine that the majority of the brightest SNRs are old (t $>$ 1000 yrs), ISM-dominated SNRs.

To complement the spectral fitting analysis we have also tested the ability to type SNRs based on HRs in custom energy bands and X-ray morphology. We conclude that HRs or colors alone are too coarse as methods for detailed typing due to uncertainties in HRs coupled with degeneracies between the lines contributing to specific energy bands, SNR temperatures, and absorption values. In addition, due to current limits on telescope collecting area and resolving power we are unable to distinguish the SN progenitor type for a large sample of SNRs in M33 using quantitative morphology. However, the combination of quantitative morphology with HRs for SNRs in the much nearer MCs yields promising results for typing extragalactic SNRs independent of detailed spectral analysis for all SNRs in a sample.

We also use our large sample of SNRs to construct an XLF in both the inner ($<$ 3 kpc, solar-like metallicity), and outer ($>$ 3kpc, LMC-like metallicity) portions of M33 to test for metallicity effects on the luminosity distribution of the SNR population. In comparing XLFs in the inner and outer regions to one another, and also to the LMC SNR XLF, we find that while metallicity may play a role in SNR population characteristics, differing SFHs on short timescales, and small-scale environmental effects appear to cause more significant differences between X-ray luminosity

distributions.

Finally, we perform an analysis of the X-ray detectability of the M33 SNRs based on their physical properties. We compare this X-ray detected population of SNRs to the population of SNR candidates for which we have 2σ or upper-limit measurements in X-rays. The latter population is larger in diameter, located at preferentially larger galactocentric radii, and has lower measured [S II]/Hα values than the former. These differences suggest that the X-ray non-detected SNRs are likely comprised of a mixture of larger and/or fainter SNRs that potentially exploded into less dense, lower metallicity mediums that fall below our detection threshold, and some photoionized regions (H II regions or regions of diffuse ionized gas) whose measurement errors in the optical place them above the [S II]/Hα ratio cut used by most surveys. If we include only the X-ray detected SNRs in the cumulative size distribution, the distribution has a slope of 2.5, in accordance with a population of SNRs in the Sedov phase of evolution.

Future work will expand upon this large sample of well-characterized SNRs by exploring in more detail the interplay between host galaxy environmental factors and the resulting SNR properties. In particular, a more systematic study of surrounding ISM properties, coupled with resolved SFHs in the vicinities of M33 SNRs will further quantify the dominant drivers behind SNR detectability, and add to the sample of SNRs with determined progenitor types.

Chapter 4:

High-Mass X-ray Binaries as Tracers of Massive Star Evolution

4 Formation Timescales for High-Mass X-ray Binaries in M33

Material from this chapter was previously published in collaboration with Benjamin F. Williams, Tristan J. Hillis, Karoline M. Gilbert, Andrew E. Dolphin, Michael Eracleous, and Breanna Binder in the September 2018 edition of the Monthly Notices of the Royal Astronomical Society (Garofali et al., 2018); ©2018 Oxford University Press on behalf of the Royal Astronomical Society), and has been reproduced here with the permission of the Oxford University Press.

4.1 Introduction

Massive stars are catalysts in many astrophysically important processes, including star formation, feedback, compact object formation, and nucleosynthesis of heavy elements. Still, many unknowns regarding the late stage evolution of high-mass stars remain. Modeling and observationally constraining this late stage evolution is complicated yet further by the impact of binaries on massive star evolution. Understanding the favored evolutionary pathways that lead to close compact object-compact object binaries is a key area of research, especially in the era of multi-messenger astronomy.

HMXBs in particular are an important observational touchstone for massive star and binary evolution, as they can be used to probe everything from compact object and accretion physics to massive star mass loss and winds. In addition, they offer a possible snapshot in time in the evolution of a massive binary into a close compact object-compact object system, providing insight into the environment and conditions under which such objects might form.

M33 is an excellent nearby galaxy in which to study HMXBs as a population given its combination of deep *Chandra*, *XMM-Newton*, and *HST* coverage. Despite this coverage, M33 is a notable exception to recent LG surveys for HMXBs. M33 does not suffer from the same distance and extinction uncertainties that can hinder Galactic HMXB studies, and it has the deepest and most spatially resolved *Chandra* and *XMM-Newton* surveys to date of any nearby spiral galaxy (T11, W15) coupled with extensive archival *HST* coverage. To date, there are still only three HMXBs that have been robustly characterized in M33, and all are of great interest: the nucleus of M33 (Long et al., 2002), and two X-ray eclipsing binaries (Pietsch et al., 2004c, 2006, 2009). Of these,

M33 X-7 hosts one of the most massive stellar mass black holes (15.65 $M_\odot$) observed pre-LIGO (Orosz et al., 2007).

As described in Chapter 2, the M33 XLF has a slope that is consistent with the universal slope expected for a population of HMXBs (Mineo et al., 2012), suggesting that the M33 source population is dominated by HMXBs (Williams et al., 2015). The normalization of the XLF, and therefore number of HMXBs expected, is related to the SFR of the host galaxy (Grimm et al., 2003; Gilfanov et al., 2004; Mineo et al., 2012). This can we used to provide a rough estimate of the expected size of the HMXB population in M33 using the known SFR of M33 and the N_{HMXB}–SFR relation from Grimm et al. (2003). Adopting a SFR of 0.3 $M_\odot$ yr^{-1} for M33 (Williams et al., 2013b) implies that there are likely $\sim$ 109 HMXBs in M33 assuming a limiting luminosity of $\sim$ 1 $\times$ 10^{35} erg s^{-1}. This suggests that there are an order of magnitude more HMXBs in M33 yet to be discovered, characterized, and compared to models of massive binary formation and evolution.

The focus of this chapter is on the identification and characterization of candidate HMXBs in M33 on the basis of existing multiwavelength data. The candidate HMXBs are identified using available archival *HST* and *Chandra* imaging to find blue stars associated with X-ray positions. The *HST* photometric data is further used to model the color-magnitude diagrams (CMDs) in the vicinity of each candidate HMXB to measure a resolved recent SFH, and thus a formation timescale, or age for the source.

The remainder of this chapter is structured as follows: in Section 4.2 I describe the catalogs used in this analysis, the image alignment and SFH recovery technique, and the HMXB classification scheme. In Section 4.4 I describe the population of candidate HMXBs in M33 identified in this work, and discuss the age measurements for individual sources of interest, as well as the entire population. In Section 4.5 I discuss the effects of spurious sources on the results, how the HMXB age distribution compares to measurements of HMXB ages in other LG galaxies, models of massive binary evolution, and the implications for compact object binary formation. Finally, in Section 4.6 I present a synopsis of this work.

4.2 Data Acquisition & Analysis Techniques

In this section, we describe the catalogs used in this analysis, namely *Chandra* data from the ChASeM33 survey (T11), for localizing X-ray point sources, archival *HST* data for identifying

optical counterparts to X-ray sources, and the *Spitzer* catalog of Khan et al. (2015) for cross-correlating with our X-ray catalog to refine source characterization. In addition, we describe the technique used to align the *Chandra* and *HST* data to a common frame so that we can determine candidate optical counterparts to X-ray sources within *Chandra* error circles. We then describe how this multiwavelength coverage can be leveraged to find candidate HMXBs in M33. Finally, we discuss the CMD fitting technique used to recover resolved SFHs, and thus ages, in the vicinities of HMXBs.

4.2.1 *Chandra* Catalog

All X-ray sources used in this analysis come from the high resolution ChASeM33 survey (T11), which had a total exposure time of 1.4 Ms and covered about 70% of the D_{25} isophote of M33 down to a limiting 0.35-8.0 keV luminosity of 2.4×10^{34} erg s^{-1}. This catalog contains 662 X-ray sources for which there are positions that have been aligned to 2MASS (Cutri et al., 2003), fluxes, HRs, variability information, and spectral information for the subset containing enough counts. Based on the analysis of T11 $\sim$ 200 of the sources in their catalog were assigned tentative classifications.

In this analysis we primarily used the X-ray source positions from T11 for localizing candidates of interest, in addition to HRs, variability information, and past classifications to narrow down the catalog of HMXBs in M33. The HRs in particular were used for separating soft sources, foreground stars and SNRs, from harder sources like background AGN and XRBs, both HMXBs and LMXBs. An example of HR cuts used to roughly categorize sources is shown in Figure 4.1 using HR cuts from Binder et al. (2012). The energy bands from T11 used are 0.35-1.1 keV (S), 1.1-2.6 keV (M), and 2.6-8.0 keV (H). AGN and XRBs occupy the same locus in the HR plot, outlined in black, while soft sources, and harder (typically absorbed) sources are found outside this region.

We further characterized sources using the source variability flags from T11 designed to separate non-variable from both short- and long-term variable sources. Sources like SNRs should not be highly variable in time, while XRBs, AGN and foreground stars can be variable on both short and long timescales. In particular, AGN may be variable on short timescales, of order hours and possibly shorter (Moran et al., 2005; Shu et al., 2017; Hernández-García et al., 2017), while XRBs may be variable on extremely short (e.g. millisecond) timescales to relatively long timescales for systems that display aperiodic outbursts (van der Klis, 2004). Thus sources that display rapid

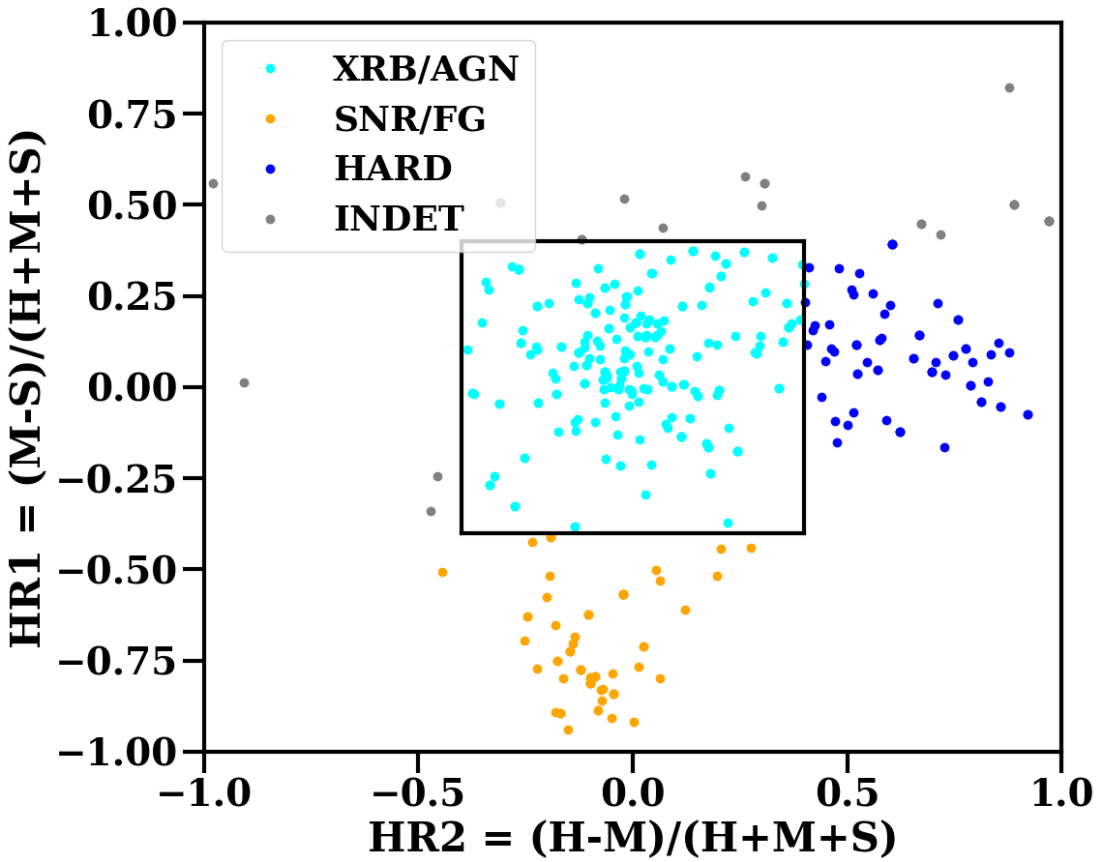

Figure 4.1: Hardness ratios for sources from the T11 catalog in the soft (0.35-1.1 keV), medium (1.1-2.6 keV), and hard (2.6-8.0 keV) bands. Sources are color-coded and labeled by their likely type based on HRs. AGN and XRBs (both LMXBs and HMXBs) are in cyan and occupy the same locus outlined in black. Soft sources (SNRs and foreground stars) are in orange, while hard sources (e.g. those behind large column densities) are in blue. Sources of indeterminate type based on HRs are in grey.

variability are potential HMXB candidates, while those sources with longer term variability may be AGN or XRBs, which can further be distinguished by their candidate optical counterpart colors where *HST* data is available.

In this analysis we also used the pre-determined source classifications from T11 that were made on the basis of cross-correlation with pre-existing catalogs to determine potential optical counterparts, and X-ray and optical spectra (where available). The T11 catalog was cross-correlated with the *XMM-Newton* catalogs of Pietsch et al. (2004b) and Misanovic et al. (2006), the SNR catalog of Long et al. (2010), the 2MASS All-Sky point source catalog (Cutri et al., 2003), the USNO-B1.0 catalog (Monet et al., 2003), and most recently with the deep *XMM-Newton* catalog of M33 from Williams et al. (2015) for which there are X-ray HRs and X-ray timing analysis. In addition, the T11 catalog contains X-ray spectral fits for $\sim$ 250 sources using the *Chandra* data, as well as optical spectroscopy for 116 sources using Hectospec on the MMT. For sources without Hectospec spectra T11 utilized archival *Spitzer*, *GALEX* and Local Group Galaxy Survey (LGGS; Massey et al., 2006) data to make preliminary source classifications. They classified $\sim$ 200 sources as either foreground stars, "stellar" sources, background galaxies/QSOs/AGN, XRBs, SNRs, and "non-stellar" sources. Of these, 14 were classified as XRBs.

4.2.2 *Spitzer* Catalog

We cross-correlated all X-ray sources from T11 with the *Spitzer* catalog of Khan et al. (2015) to leverage the mid-IR colors of sources where available. As shown in Khan et al. (2015) galaxies display a color excess in $m_{3.5\mu m} - m_{4.6\mu m}$, while sources like foreground stars fall along a nexus of zero color excess in these same bands. We used *Spitzer* colors, where available, as a coarse cut for separating X-ray sources that are most likely background galaxies, from other sources of interest (e.g. "stellar" type sources).

Sources with *Spitzer* colors ≤ 0 are most likely to be foreground stars and SNRs, while sources with *Spitzer* color excess (e.g. > 0) are more likely to be background galaxies. We tested the efficacy of using *Spitzer* colors to separate X-ray sources of different types by first cross-correlating all *Spitzer* sources from Khan et al. (2015) in M33 with all T11 sources. We found 172 unique matches within search radii of 0.5". We then separated the sources based on their T11 classifications, as described in Section 4.2.1, and binned the sources according to *Spitzer* colors as shown in Figure 4.2.

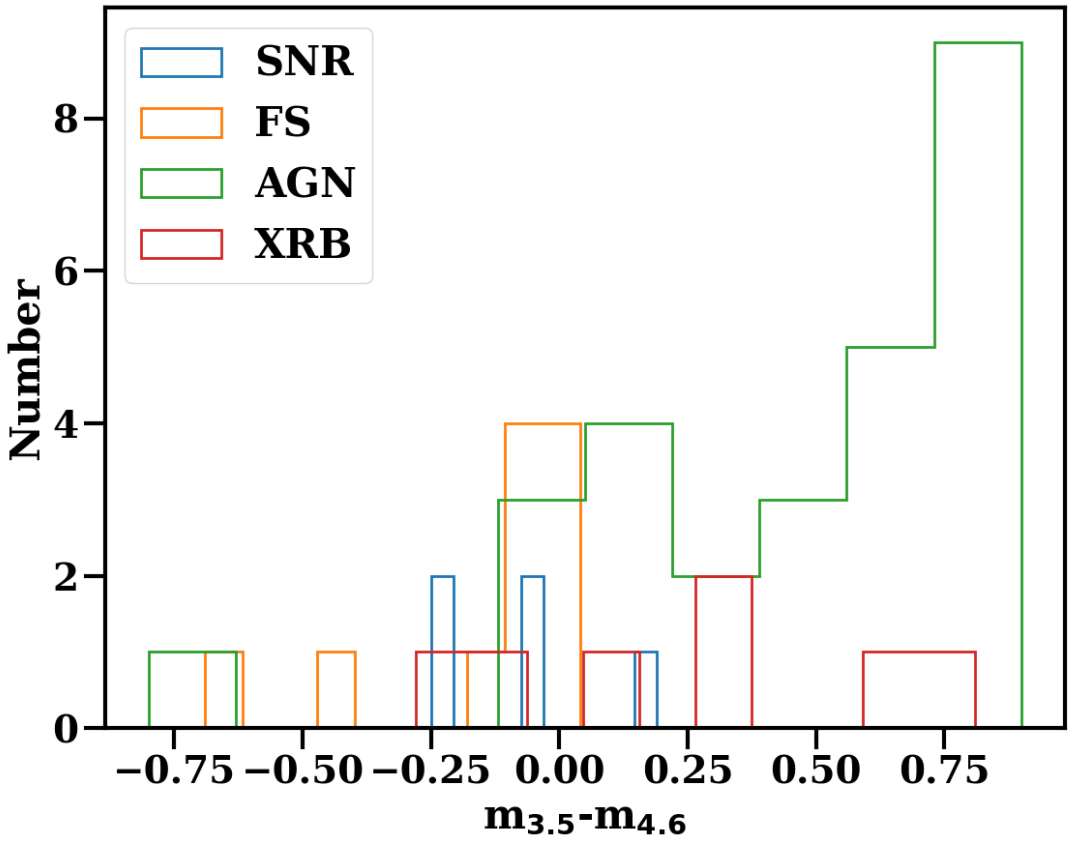

Figure 4.2: Histogram of *Spitzer* $m_{3.5\mu m} - m_{4.6\mu m}$ colors for X-ray sources from T11 with classifications as SNRs (blue), foreground stars (orange), XRBs (red), or AGN (green). The AGN generally have a larger color excess than other sources.

We found that X-ray sources with the classifications of galaxy/QSO/AGN from T11 had *Spitzer* colors that were systematically higher than sources of other classifications. We therefore made a *Spitzer* color cut of $m_{3.5\mu m} - m_{4.6\mu m} > 0.5$ to select X-ray sources that are likely background galaxies/AGN. This AGN color selection criteria may contain a small fraction of XRBs, but we combine the *Spitzer* color cuts with other criteria as described in Section 4.3 to avoid excluding possible XRBs. Sources that are classified as SNRs or foreground stars in T11 unsurprisingly cluster around $m_{3.5\mu m} - m_{4.6\mu m} \leq 0$, as shown in Figure 4.2. By contrast, sources that are classified as "stellar", "non-stellar," and XRB in T11 are spread across a range of *Spitzer* colors in this sample. Thus *Spitzer* colors, where available, are useful in narrowing down the set of X-ray sources that may be candidate HMXBs.

4.2.3 *HST* Photometry

To search for optical counterparts to the X-ray sources in T11 we used all available archival *HST* data in M33 with coverage in at least two broad-band filters. This amounted to 89 fields covering about $\sim 40\%$ of the T11 X-ray catalog (270 unique sources). The full archival *HST* coverage of M33 (grey and green regions) and its overlap with the X-ray point source catalog (cyan crosses) is shown in Figure 4.3. We reduced the *HST* data using the photometry pipeline developed as part of the ACS Nearby Galaxy Treasury Program (Dalcanton et al., 2009) and the PHAT Program (Dalcanton et al., 2012), measured photometry using `DOLPHOT` and `HSTPHOT` (Dolphin, 2000), and ran artificial star tests as described in Williams et al. (2014b). All optical magnitudes reported here are Vega magnitudes.

For the artificial star tests, stars of known color and magnitude were inserted into the images, and the photometry was repeated to compare the output and input photometry. The resulting comparisons allow us to accurately model the photometric bias, uncertainty, and completeness as a function of color and magnitude. We used the photometry to construct CMDs of the stars within 50 pc of sources of interest (Section 4.4.1), and artificial stars within 250 pc of sources in order to account for completeness and photometric uncertainties. Because the artificial star tests are performed on the whole field we choose this larger 250 pc region for the artificial stars to ensure that we have a large enough sample to quantify completeness.

We aligned all *HST* fields to a common frame with the X-ray data as described in Section 4.2.4,

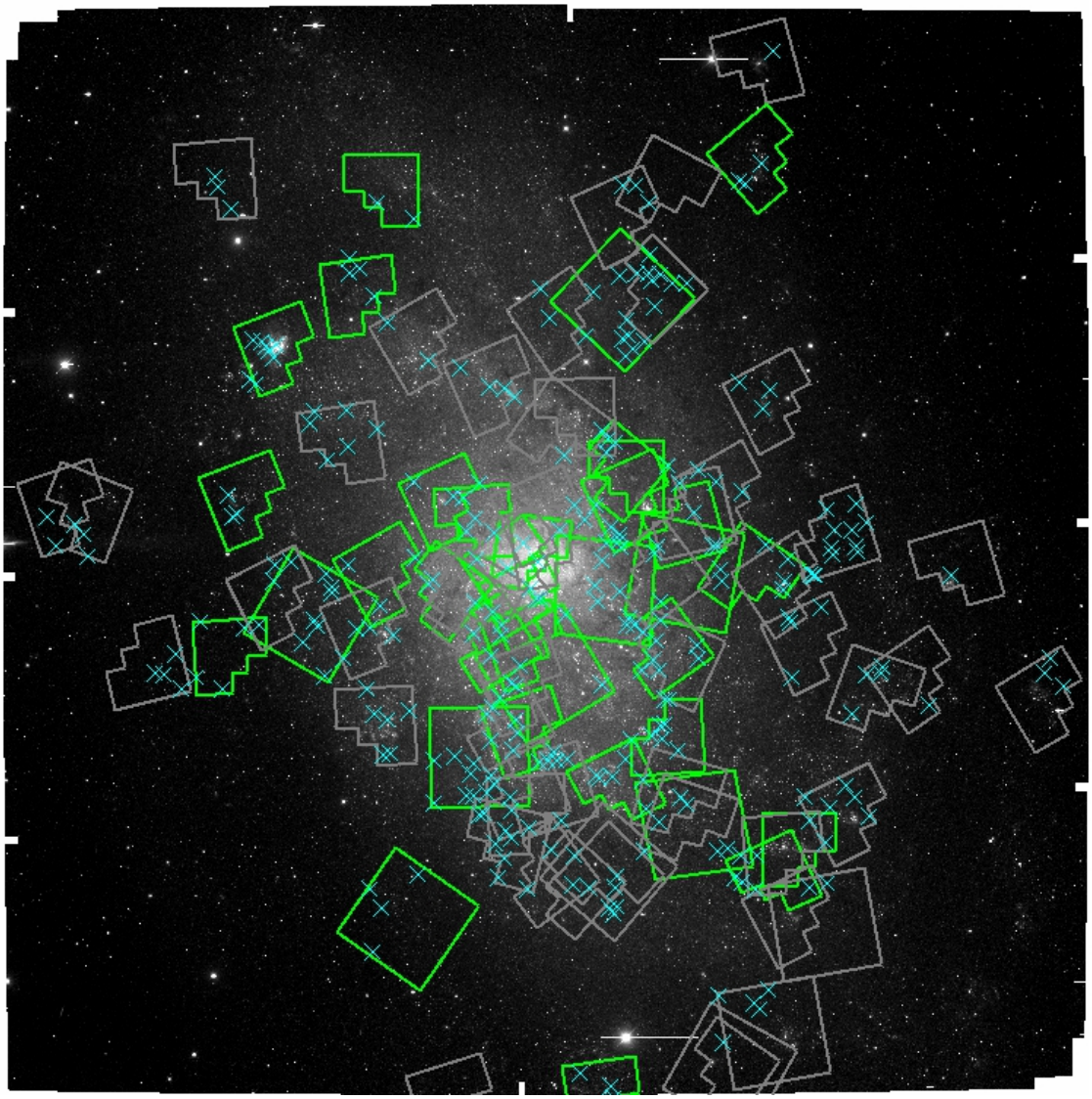

Figure 4.3: R band Local Group Galaxy Survey (Massey et al., 2006) image of M33 overlaid with all 89 archival *HST* fields (grey and green), and all 36 fields used in this analysis (green only). Cyan crosses are X-ray sources from Tüllmann et al. (2011) that fall within the current archival *HST* coverage. There are 270 X-ray sources covered by 89 *HST* fields.

which allows us to search for optical counterparts within the X-ray error circles for all sources with overlapping *Chandra* and *HST* coverage. Although we inspected all 89 archival fields for optical counterparts to X-ray sources to look for candidate HMXBs as described in Section 4.3, we ultimately present here only those fields in which there are HMXB candidates, which amounts to a subset of 36 of the 89 fields. This subset of 36 is displayed as green regions in Figure 4.3. For reference, we list in Table 4.1 the proposal ID, field name, camera, filter set, exposure time, 50% completeness magnitudes in both filters, and density of OB stars for all 36 *HST* fields used in this analysis.

Table 4.1: All archival *HST* fields used in this analysis. Column 1 lists the proposal ID number, column 2 is the field name, column 3 lists the camera, columns 4-5 are the *HST* filters available, columns 6-7 are the exposure times in seconds for each filter, columns 8-9 are the 50% completeness limits in each filter for each field, and column 10 is the density of OB stars in each field.

Proposal ID	Name	Camera	$Filter_1$	$Filter_2$	$Exposure_1$ (s)	$Exposure_2$ (s)	$m_1^{50\%}$	$m_2^{50\%}$	OB star density (arcsec^{-2})
10190	M33-DISK1	ACS	F606W	F814W	2480	2480	25.80	25.10	0.09
10190	M33-146sw-26505	ACS	F606W	F814W	2160	2160	26.20	25.60	0.27
10190	M33-301sw-25900	ACS	F606W	F814W	2400	2500	26.10	25.40	0.19
10190	M33-626sw-28004	ACS	F606W	F814W	2160	2160	26.96	26.31	0.05
10190	M33-784se-549	ACS	F606W	F814W	2160	2160	27.60	26.80	0.04
9873	M33-267nw-31659	ACS	F606W	F814W	8800	17600	25.27	25.51	0.17
10190	M33-419se-160	ACS	F606W	F814W	2400	2500	27.48	26.81	0.03
9873	NGC598-U49	ACS	F606W	F814W	10414	20828	27.21	26.37	0.21
9873	NGC598-M9	ACS	F606W	F814W	10414	20828	28.21	27.37	0.12
5998	M33-FLD4	WFPC2	F336W	F439W	800	800	23.23	23.90	0.05
6640	NGC598-SRV2[s]	WFPC2	F555W	F814W	2240	2080	24.33	23.38	0.06
5464	NGC598-1[s]	WFPC2	F555W	F814W	1600	1200	24.43	23.49	0.13
5237	M33-FIELDN604	WFPC2	F555W	F814W	400	400	24.33	24.21	0.04
5384	M33-NEB1[s]	WFPC2	F336W	F439W	320	360	22.22	22.85	0.08
5998	M33-FLD3	WFPC2	F336W	F439W	800	800	23.10	23.18	0.12
6640	NGC598-SRV3	WFPC2	F555W	F814W	2240	2080	24.98	24.13	0.18
8207	M33-PAR-FIELD7	WFPC2	F336W	F439W	800	600	22.71	23.51	0.14
6640	NGC598-SRV5	WFPC2	F555W	F814W	2240	2080	25.12	24.22	0.11
11079	M33-OB127	WFPC2	F336W	F439W	600	490	21.81	23.80	0.16
8207	M33-PAR-FIELD2	WFPC2	F336W	F439W	800	600	22.59	23.36	0.11
8207	M33-PAR-FIELD4	WFPC2	F336W	F439W	800	600	22.75	23.36	0.08
11079	M33-OB137	WFPC2	F336W	F439W	300	260	21.81	23.74	0.05
11079	M33-OB90	WFPC2	F336W	F439W	600	490	21.62	23.80	0.18
6431	NGC598-FIELD	WFPC2	F555W	F814W	520	460	25.08	24.10	0.02
5914	NGC598-R12	WFPC2	F555W	F814W	4800	5200	25.31	24.67	0.12
5914	NGC598-R14[s]	WFPC2	F555W	F814W	4800	5200	24.75	23.92	0.13
5914	NGC598-U137	WFPC2	F555W	F814W	4800	5200	26.25	25.62	0.11
6038	M33-AM6-FIELD	WFPC2	F336W	F439W	1800	600	23.64	23.37	0.07
8018	M33	WFPC2	F555W	F814W	3800	3800	25.60	24.80	0.10
11079	M33-OB39S[s]	WFPC2	F336W	F439W	600	490	21.77	22.37	0.17
11079	M33-OB77[s]	WFPC2	F336W	F439W	600	490	21.73	22.46	0.12
11079	M33-OB94[s]	WFPC2	F336W	F439W	600	490	21.76	22.33	0.22
11079	M33-OB101[s]	WFPC2	F336W	F439W	600	490	21.65	22.39	0.20
9127	M33-PAR-FLD1[s]	WFPC2	F336W	F439W	520	600	22.14	22.86	0.12
5384	M33-NEB6[s]	WFPC2	F336W	F439W	320	360	22.40	23.00	0.22
5494	M33-OB6-5-FIELD[s]	WFPC2	F300W	F555W	350	300	22.44	25.19	0.20

[s] Field depth does not reach 80 Myr MSTO.

4.2.4 Image Alignment

Robustly identifying optical counterparts to X-ray sources requires precise astrometric alignment between the archival *HST* data and the pre-existing *Chandra* catalog from T11. We chose 2MASS as a common frame for the alignment procedure, as the source positions in the T11 catalog are already aligned to 2MASS.

We used the R-band photometry from the LGGS (Massey et al., 2006) with source positions updated as prescribed in Massey et al. (2016) as the standard reference for aligning all *HST* fields. This choice was made to ensure that there were enough stars in each *HST* field with counterparts in the reference image on which to align. To use the R-band photometry from the LGGS as the standard reference for aligning each *HST* field, we first had to make sure that the LGGS positions were also aligned to 2MASS. To do so we chose ~ 1000 sources from the R-band photometry between 18th and 20th magnitude and found each source's corresponding reference source in 2MASS. We then aligned the two images using the `PyRAF` task `CCMAP` with 2MASS as the reference. The ΔRA and ΔDec fit RMS values from this procedure were 0.19", and 0.16", respectively.

We next aligned each archival *HST* field to the pre-aligned R-band image, which results in *HST* fields that are aligned to 2MASS, and thus a common frame as the X-ray data from T11. We chose stars between 18th and 22nd magnitude in each *HST* field, with the exact magnitude limits depending on the depth of the field. In general, we set the limits so that we found at least three R-band counterparts to the *HST* stars on which to align. We again aligned the images using the `PyRAF` task `CCMAP` with the 2MASS aligned R-band image as the new reference frame for each *HST* field. We performed this procedure in an iterative fashion, so outlier source matches were culled from the `CCMAP` input, and the task repeated prior to computing the final plate solution.

We then assessed by eye the alignment between each archival field and the R-band image to ensure good agreement between source centroids in the images, as well as the distribution of separations for *HST* sources and their reference counterparts in the R-band image. Examples of the efficacy of the alignment procedure are shown in Figures 4.4–4.6 for a number of different X-ray sources. Figure 4.4 shows a foreground star, both pre- and post-alignment, with the X-ray error circle in green. The alignment procedure was not performed using foreground stars, however, foreground stars serve as good checks of alignment as demonstrated in Figure 4.4. In Figure 4.5

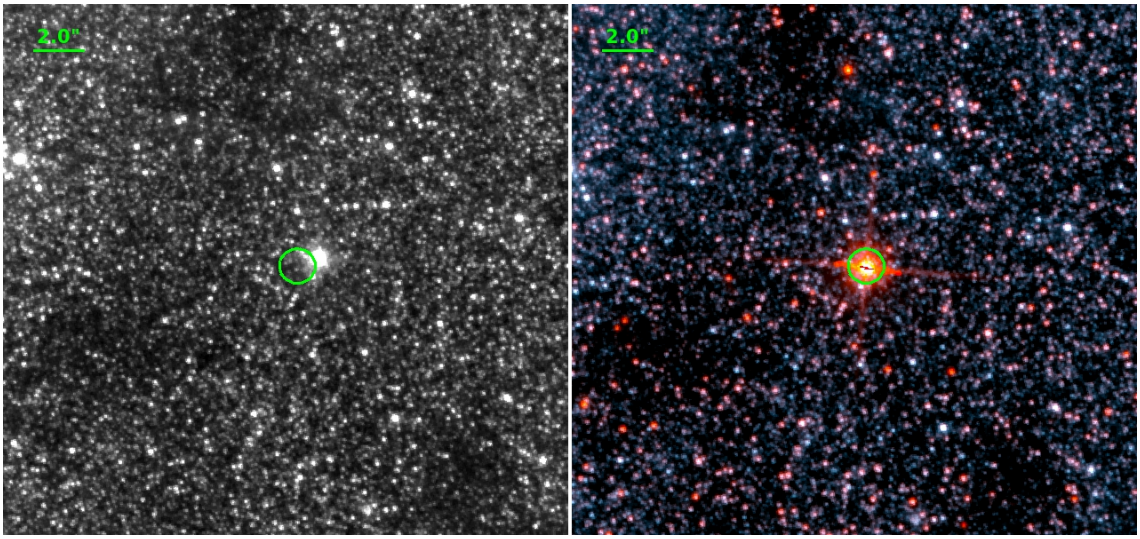

Figure 4.4: *Left*: *HST* ACS F606W image of a foreground star pre-alignment. The X-ray error circle is in green, mis-aligned relative to the position of the source in *HST*. *Right*: *HST* ACS three color image (red: F814W, green: F606W, blue: combination of F814W and F606W) of a foreground star post-alignment with the error circle, now encompassing the optical source position, in green.

we show a background AGN pre- and post-alignment (source denoted by green x in both panels), with the X-ray error circle in green. In the pre-aligned image the source is significantly offset from the X-ray error circle, demonstrating the varying shifts required in each *HST* field to bring the *HST* and *Chandra* imaging into alignment. Finally, Figure 4.6 shows a candidate HMXB from this work, again pre- and post-alignment. Pre-alignment the candidate counterpart star (marked by white arrow) falls outside the X-ray error circle, demonstrating the need for alignment in order to effectively identify candidate HMXBs via bright donor star counterparts.

In general, the ΔRA and ΔDec RMS fit values from the alignment process were < 0.1", and often smaller. We added in quadrature the ΔRA and ΔDec fit RMS from the Rband to 2MASS and *HST* to R band alignment procedures, which makes the positional error due to the full alignment process ~ 0.2" for most sources. This alignment error is smaller than the X-ray source position error itself. The X-ray positional error for each source comes directly from the T11 catalog, which has an error floor of 0.5", though the position errors may be larger depending on off-axis angle and source intensity. The total error due to the alignment procedure (~ 0.2") is then added to the *Chandra* position error from T11 (~ 0.5" for the majority of sources considered here, but sometimes higher for sources that are far off-axis), so the final X-ray position errors are a combination of both

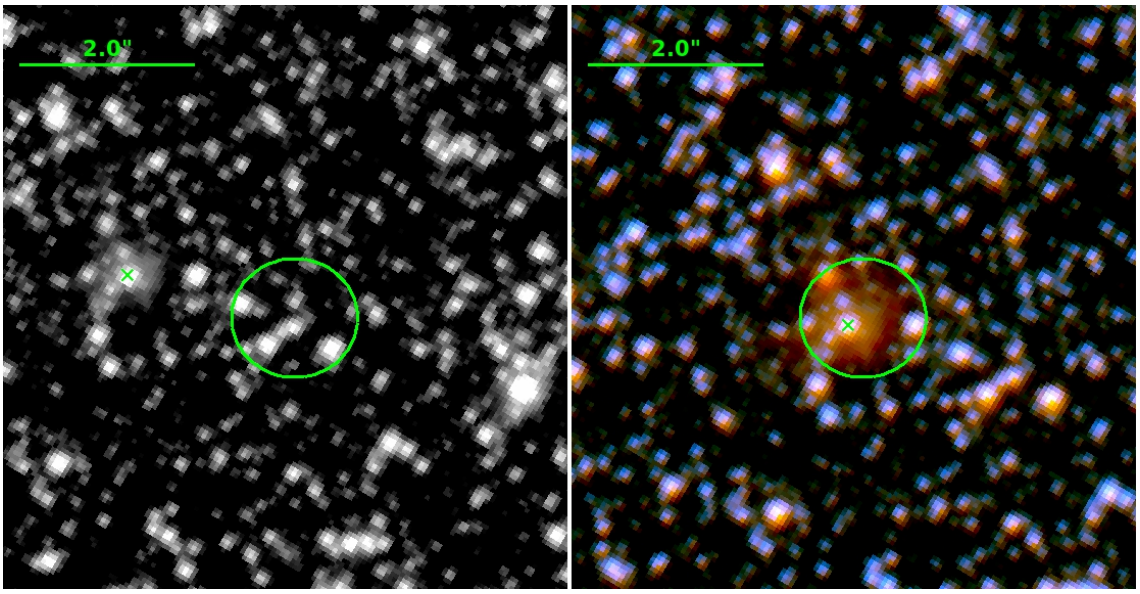

Figure 4.5: *Left*: *HST* ACS F606W image of a background AGN, marked with the green x, pre-alignment. The source is significantly offset from the position of the X-ray error circle (green) in this field. *Right*: *HST* ACS three color image (red: F814W, green: F606W, blue: combination of F814W and F606W) of the same AGN now post-alignment with the error circle, now encircling the optical source, again in green.

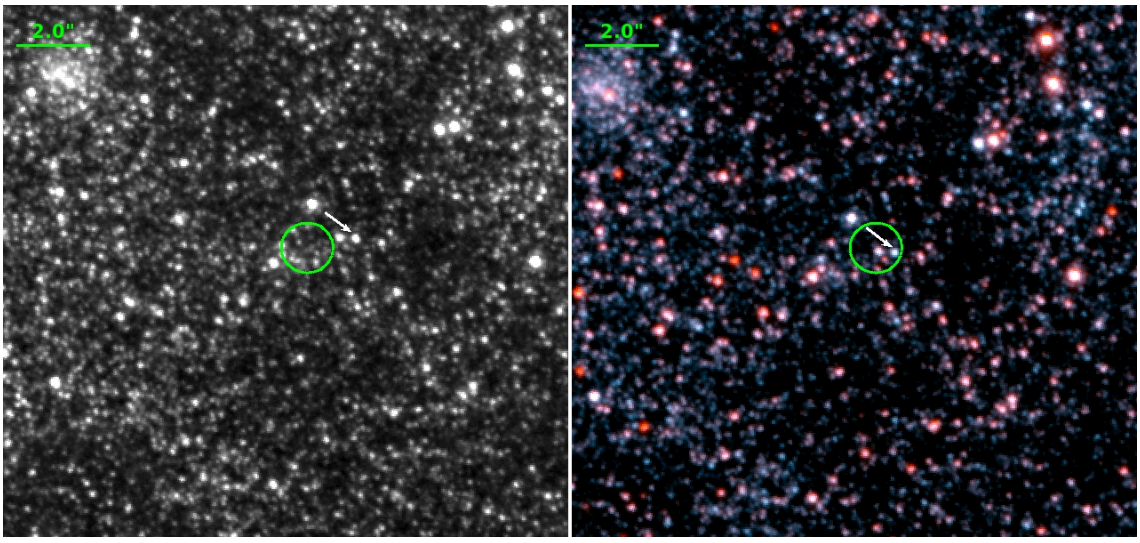

Figure 4.6: *Left*: *HST* ACS F606W image of a candidate HMXB, counterpart in *HST* marked with a white arrow, pre-alignment. The source is outside the X-ray error circle (green) in this field. *Right*: *HST* ACS three color image (red: F814W, green: F606W, blue: combination of F814W and F606W) of the same candidate HMXB now post-alignment with the X-ray error circle in green. The candidate donor star, marked by the white arrow, is now well within the X-ray error circle.

intrinsic source position uncertainty, and uncertainty from the alignment process. This results in X-ray error circles that are typically < 0.7" in radius for our sources. With this kind of precision astrometric alignment is possible to search for optical counterparts to the X-ray sources from T11.

4.3 Identifying Counterpart Candidates

After aligning all available *HST* images to a common frame with the T11 catalog, and cross-correlating the Khan et al. (2015) *Spitzer* catalog with the X-ray source catalog we leveraged the multiwavelength coverage to identify candidate HMXBs in M33. We separated HMXBs from other X-ray bright sources, including foreground stars, SNRs, and AGN based on a combination of X-ray HRs, *Spitzer* colors (if available), magnitude and color of the *HST* source or sources within the X-ray error circle, X-ray variability, and classification based on visual inspection of the *HST* images (e.g. for extended sources) as described in turn below.

We first made cuts on X-ray HRs as defined in Figure 4.1 to separate sources broadly into the categories of "soft" (SNRs and foreground stars), "intermediate" (AGN, HMXBs, and LMXBs), and "hard" (potentially AGN and HMXBs behind large column densities). For sources with *Spitzer* counterparts (65 sources) the categorization as SNR or foreground star was strengthened if the *Spitzer* colors were ≤ 0. Foreground stars can sometimes be identified by visual inspection, and SNRs were likewise easily identified via cross-correlation with the SNR catalogs of Long et al. (2010) and Garofali et al. (2017).

If the *Spitzer* color was in excess of 0.5 we considered the source a strong AGN candidate, while if the *Spitzer* colors were between 0–0.5, or if there were no *Spitzer* counterparts available we relied on further measures, such as variability, optical counterpart color, and the aforementioned HRs to further classify the source as either an AGN or XRB candidate. The efficacy of the *Spitzer* color cuts is demonstrated in Figure 4.2 as compared to previous source classifications from T11. We considered detection of short or long term variability from T11 to be indicative of a possible HMXB, though AGN may also be variable on such timescales (Paolillo et al., 2004).

XRBs (both LMXBs and HMXBs) and AGN are not easily separated from one another based on one measure alone. All such sources fall within the same general area of the X-ray HR plot (black box, Figure 4.1), and may both be time variable, but should be associated with markedly different optical counterparts in terms of their spectroscopic and photometric characteristics. As

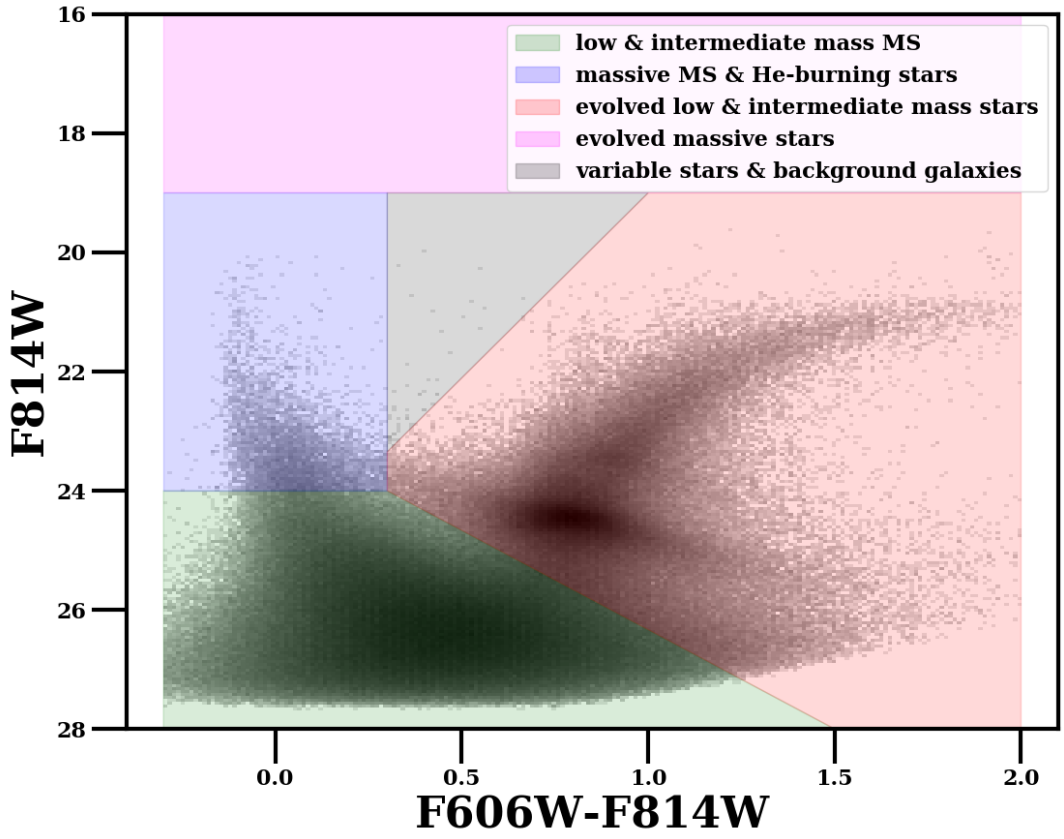

Figure 4.7: A Hess diagram constructed using all the stars in one of the *HST* ACS fields binned by 0.05 magnitudes in both color and magnitude space. The shaded regions delineate sources in different mass ranges and stages of stellar evolution: green: low and intermediate mass main sequence stars; blue: massive main sequence stars (e.g. OB stars) and He-burning stars; red: evolved low and intermediate mass stars (e.g. red giant branch, red clump, and asymptotic giant branch stars); magenta: evolved massive stars (e.g. supergiants); grey: variable stars and background galaxies. Optical counterparts for HMXBs would lie in the blue and magenta shaded regions.

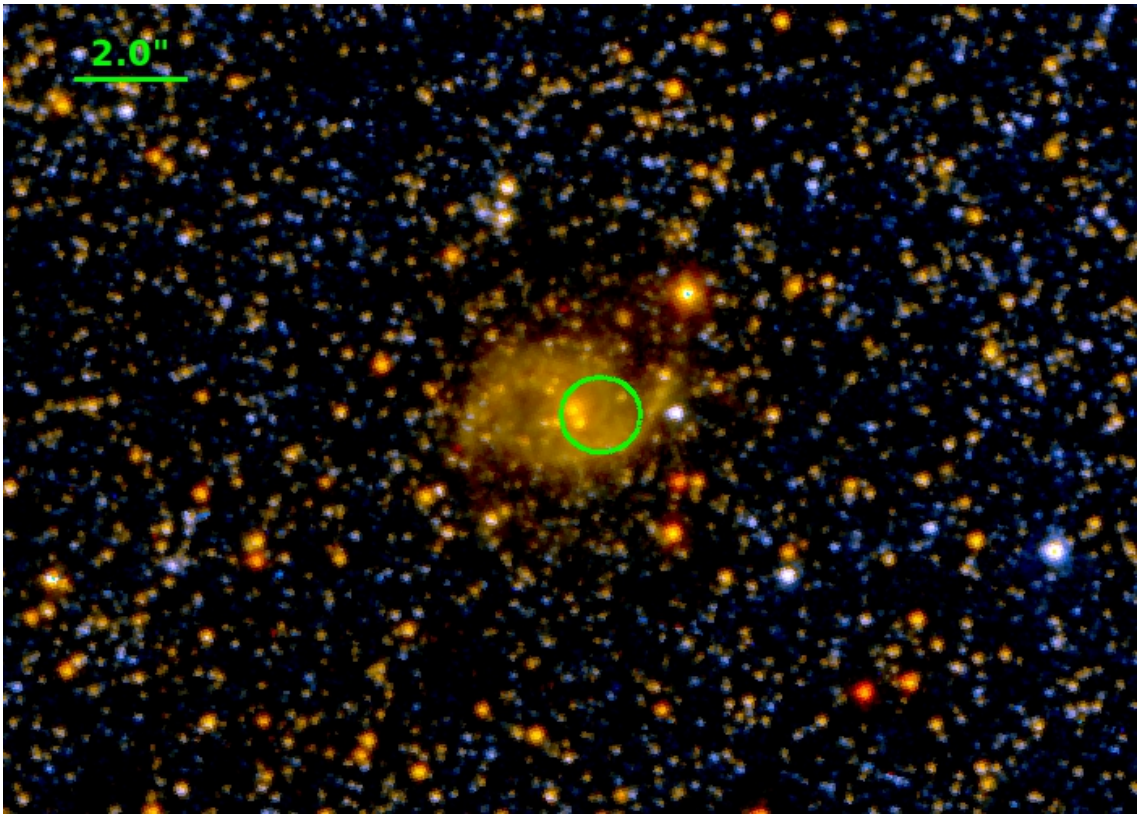

Figure 4.8: *HST* ACS three color image (red: F814W, green: F606W, blue: combination of F814W and F606W) of a background galaxy. The X-ray error circle (post-alignment procedure) is in green.

Hectospec data is only available for a small subset of the T11 catalog we rely primarily on a photometric classification scheme, using the complementary Hectospec spectra where available. In this way, the *HST* data are crucial for separating HMXBs, which should have relatively bright, blue stars as their optical counterparts, from background AGN and LMXBs, whose counterparts should appear much redder, and in the case of AGN, sometimes more extended. In Figure 4.7 we show the loci for optical sources in different mass ranges and stages of stellar evolution as shaded regions overlaid on a Hess diagram constructed from one of the ACS fields used in this work. An optical counterpart in the blue or magenta regions of the Hess diagram in Figure 4.7 that falls within the error circle of an X-ray source makes that X-ray source a strong HMXB candidate. Figures 4.8–4.11 also show examples of the *HST* counterparts for X-ray sources of different types: a background AGN, an HMXB, an SNR, and an X-ray source with no secure optical counterpart.

With all X-ray and *HST* data aligned to a common frame we constructed CMDs for regions

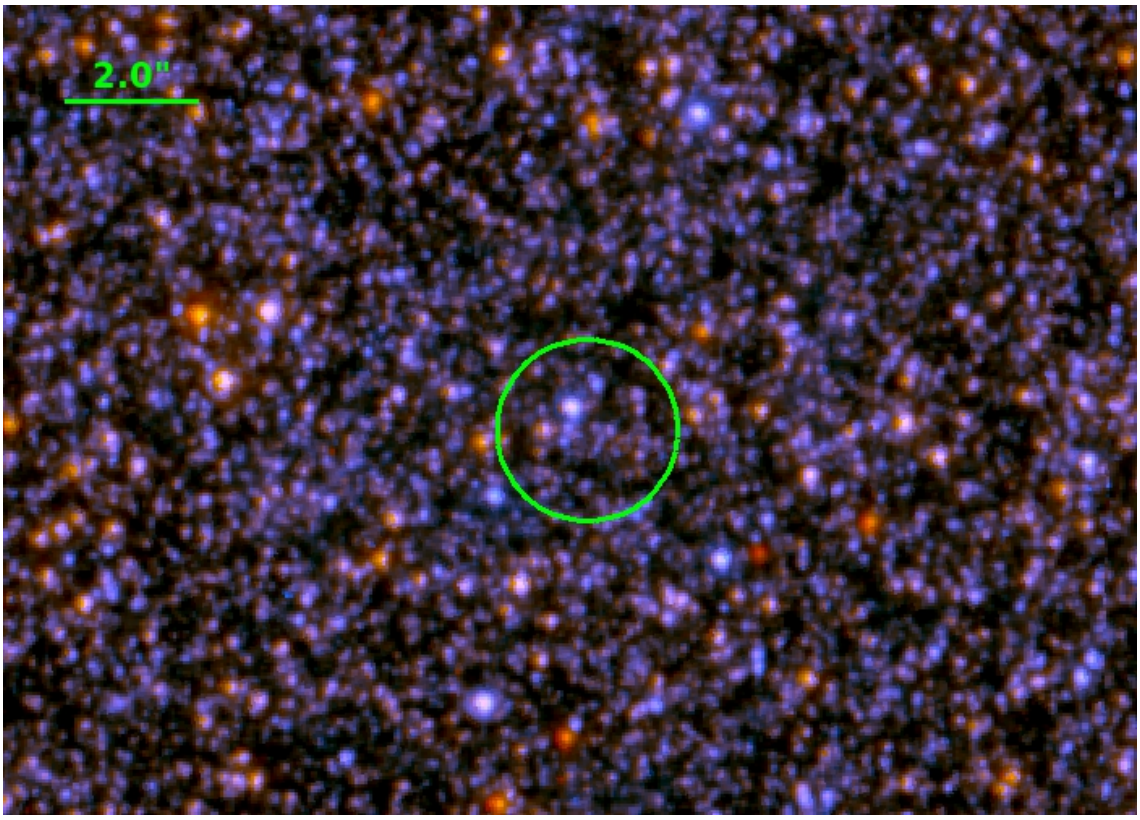

Figure 4.9: *HST* ACS three color image (red: F814W, green: F606W, blue: combination of F814W and F606W) of an HMXB candidate identified in this work. A bright, blue candidate counterpart is visible within the X-ray error circle (green).

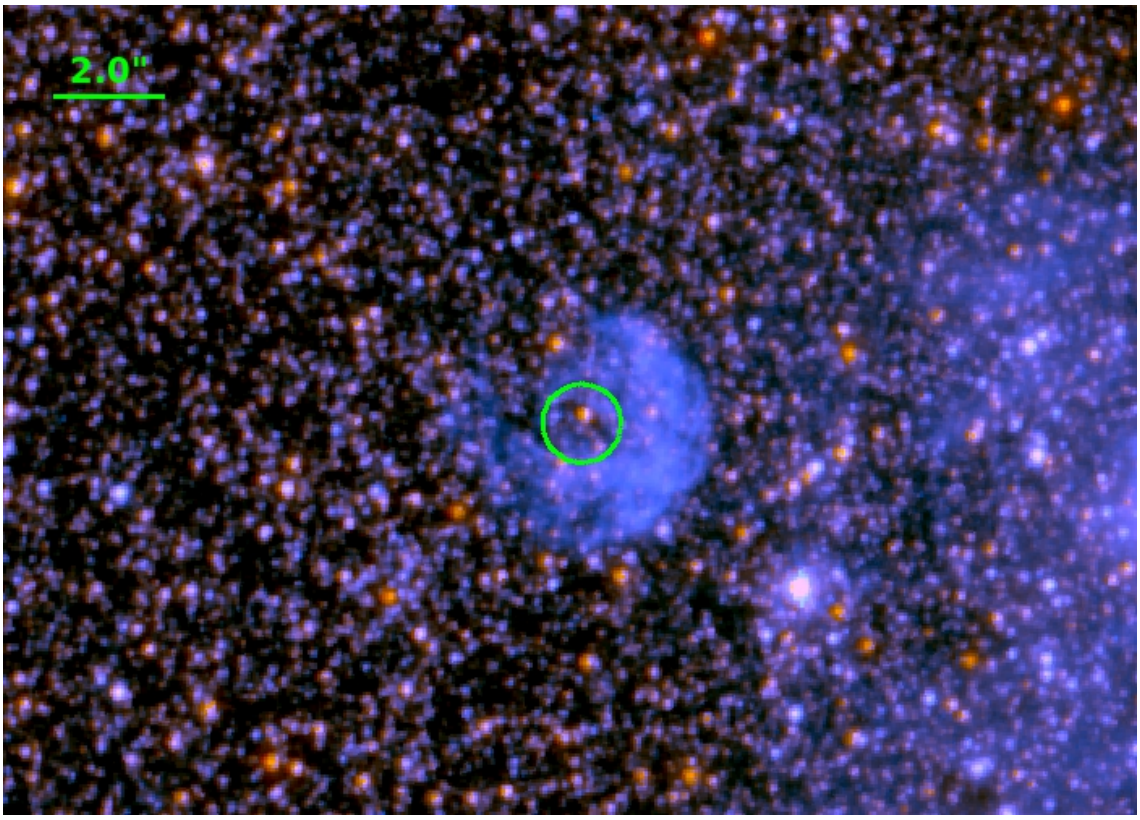

Figure 4.10: *HST* ACS three color image (red: F814W, green: F606W, blue: combination of F814W and F606W) of an X-ray and optically detected SNR. The X-ray error circle (assuming an X-ray point source) is in green, though extended emission is resolvable in the *HST* imaging.

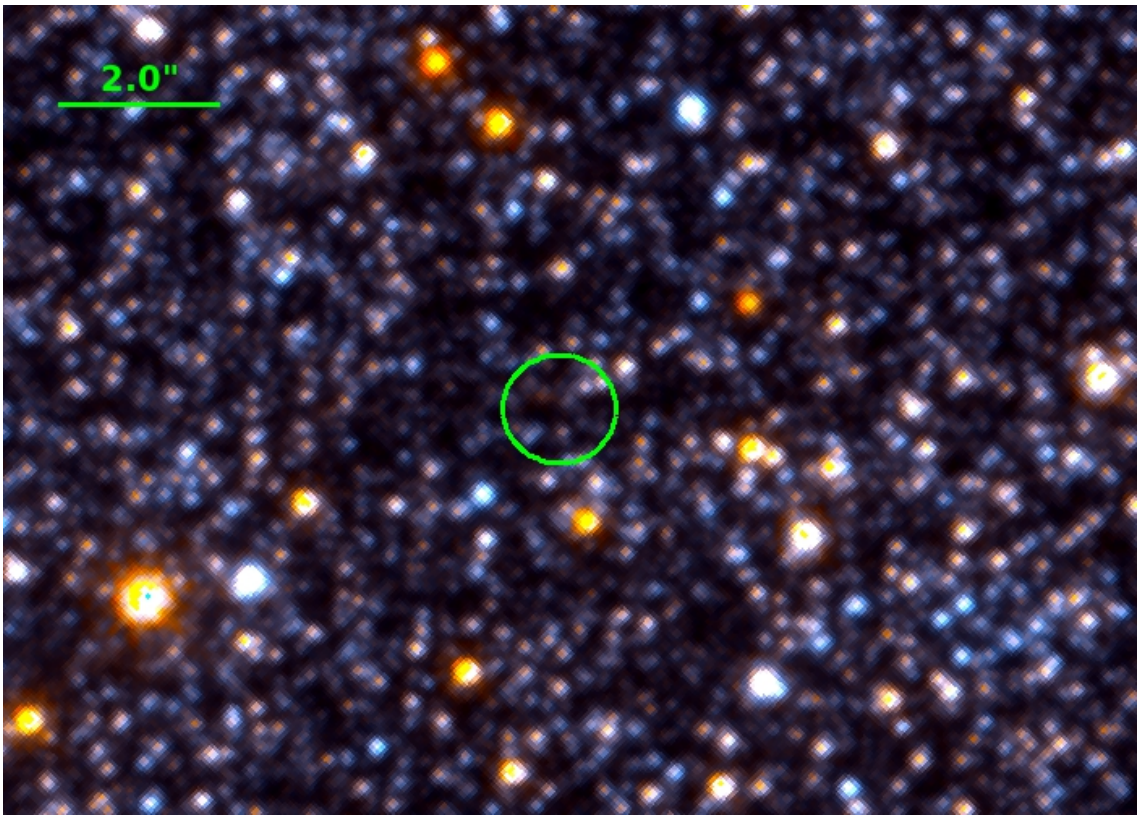

Figure 4.11: *HST* ACS three color image (red: F814W, green: F606W, blue: combination of F814W and F606W) of an X-ray source of unknown type. No unique optical counterpart is discernible within the X-ray error circle (green).

within 50 pc of all X-ray sources, and noted the positions on the CMD of any *HST* sources that were within the X-ray error circle, where the error circle is derived from a combination of the individual source positional uncertainties from T11, which account for off-axis angle and source intensity, and the uncertainty due to alignment, as described in Section 4.2.4. Because we are interested primarily in good HMXB candidates we selected optical counterparts within the X-ray error circle that were brighter than 24th magnitude (roughly the magnitude of a B star at the distance of M33), and had F606W-F814W, or F555W-F814W colors ≤ 0.3 (bluer than the red giant branch). Assuming a Milky Way like extinction curve (i.e. $R_v = 3.1$), this color cut allows for about one magnitude of extinction for stars on the main sequence.

Identification of a bright, blue star within the X-ray error circle does not denote a unique optical counterpart to the X-ray source, however because bright OB stars have low surface density the presence of such a star within the X-ray error circle suggests the source is a good candidate HMXB. We estimate the chance coincidence probability, and thus the number of possible spurious sources by first calculating the density of bright, blue stars in each field by selecting stars brighter than 24th magnitude and bluer than F606W-F814W, or F555W-F814W = 0.3. The density of OB stars for each field is listed in the last column of Table 4.1. These densities taken in conjunction with a typical X-ray error circle of 0.7" yield the chance coincidence probability for each field. To provide a representative value for the whole sample, we calculate a weighted average of the chance coincidence probabilities in each field, weighted by the number of candidate HMXBs in that field. Based on this calculation we expect 0.21 bright, blue stars are chance coincidences with the typical X-ray error circle. This implies that of our 55 candidate HMXBs 11 ± 3 may be chance coincidences of blue stars with the X-ray source position, and thus spurious HMXB candidates. Further discussion of potential spurious HMXB candidates in our sample, and their effects on our results are presented in Section 4.5.1.

The above color and magnitude cuts will select relatively bright, blue sources, but will miss any bright sources that are slightly more red in color. Sources much redder than these color cuts that fall within our X-ray error circles may either be background AGN, evolved massive stars, or otherwise potentially stars with strong emission lines (e.g. emission line stars with strong Hα). For this reason, we also included as candidate HMXBs sources that had optical counterparts in their error circles that were brighter than $\sim$ 21st magnitude, but nominally more red than

F606W-F814W or F555W-F814W = 0.3, though not as red as the red giant branch stars. Again assuming $R_v = 3.1$ this more lenient color cut allows for about two magnitudes of extinction for main sequence stars. We then checked special cases for any further classification from T11 on the basis of available Hectospec spectra. If the X-ray source had an *HST* counterpart brighter than $\sim$ 22nd magnitude, but bluer than the red giant branch as well as corresponding Hectospec data with classification "stellar" in T11 we include it as an HMXB candidate. If the source was classified as "QSO/AGN" in T11 on the basis of available optical spectroscopy then it was excluded. Sources that were classified as "XRB" in T11 were also automatically included, even if they did not pass the above color cuts. Finally, to determine our list of candidate HMXBs all sources were inspected visually, and compared against the classification determined from the color cuts at X-ray, optical, infrared wavelengths, and previous classifications available from T11. Notes on individual sources are provided in Table 4.2.

4.3.1 Age Constraints from Surrounding Populations

We measure ages, or formation timescales for the HMXB candidates in this sample using the stars surrounding each candidate. This process involves first extracting photometry of stars in the vicinity of HMXB candidates, and then fitting the photometry using stellar evolution models. We detail both of these steps below.

4.3.1.1 Selecting Stellar Samples

For young sources it should be possible to determine the age, or formation timescale of the source based on the surrounding stellar population. Most stars are known to form in clusters, and thus in relatively co-eval populations that stay associated in regions of $\sim$50 pc on timescales < 60 Myr (Lada & Lada, 2003; Gogarten et al., 2009; Eldridge et al., 2011). In the case of HMXBs, the system age is limited to be less than the lifetime of the secondary, which is a high-mass star with a lifetime of $\lesssim$50 Myr. Thus, we can potentially determine ages for HMXBs by fitting the CMDs of the stellar population within 50 pc of the source. This population age is the *total* age of the binary, which is a combination of the time to formation for the compact object from the primary, the delay time between compact object formation and the onset of the X-ray emission, and the time since the start of X-ray emission.

Such measurements of the ages of young objects have been performed successfully to constrain the ages and masses of the progenitors of SNe and SNRs (e.g. Jennings et al., 2012, 2014; Williams et al., 2018), which have similar maximum ages (and therefore associated region sizes) as HMXBs as set by the lifetimes of massive stars. We therefore adopt this same methodology for attempting to constrain the ages of HMXB candidates.

While the 50 pc region is commonly-used for constraining ages of young populations, because the HMXB phase may occur millions of years after the formation of the compact object, there is some possibility that it could have moved farther from its associated young population following compact object formation. Namely, there is some possibility that the binary could have received a significant kick during compact object formation. While the nature and strength of such kicks is highly uncertain (Lipunov et al., 1997; Podsiadlowski et al., 2004; Janka, 2012), such a kick could potentially send an HMXB into isolation, or, more problematically for this kind of analysis, into a neighboring star-forming region which contains a young stellar population not representative of the true HMXB age. This scenario is possible, but theory and observations suggest that large natal kicks and long delays between compact object formation and the onset of X-ray emission may not be common (e.g. Pfahl et al., 2002; Mirabel & Rodrigues, 2003; Linden et al., 2009, 2010; Repetto & Nelemans, 2015; Mandel, 2016). The offsets between HMXBs and nearby young clusters in the SMC are $\sim$65 pc (Coe et al., 2005), roughly consistent with a 50 pc association region. Similarly, Sepinsky et al. (2005) find median distances between XRBs and their natal clusters of 30-100 pc for 15-50 Myr age clusters in binary population synthesis simulations that assume simple cluster models. For potential cases of very large kicks and long travel times, we would expect to see at least some sources kicked into regions without any young stars (i.e. no recent star formation), but we do not find evidence of this in our M33 sample.

We test that our results are not highly dependent on our choice of extraction region size by extracting and fitting samples from two different region sizes for each HMXB candidate. The first sample corresponds to the 50 pc region typically used in studies of young population ages, while the second is double this radius. We find that the results are consistent in both cases, and so primarily discuss the results using the 50 pc regions in Section 4.4.3.

4.3.1.2 Color-Magnitude Diagram Fitting

In order to measure resolved SFHs and thus recover ages for HMXB candidates we modeled the CMDs of the stellar population within 50 pc of the X-ray source of interest using the software `MATCH` (Dolphin, 2002). `MATCH` fits the observed CMD by building up synthetic diagrams using the stellar evolution models of Girardi et al. (2002) and Marigo et al. (2008) for a range of ages and metallicities and finding the combination that best fits the observed distribution. For this analysis we assumed a distance modulus of 24.67 for M33 (Rizzi et al., 2007), a Kroupa initial mass function (IMF), and a binary fraction of 0.35. For sources within 3 kpc of the nucleus we modeled the CMDs over a range of metallicities from [Fe/H] = -0.4 to 0.00 with steps of 0.1 in log Z, while for sources outside 3 kpc we chose a range of [Fe/H] = -0.6 to -0.3 in accordance with the measured metallicity gradient in M33 (Magrini et al., 2007). We used bin sizes of 0.2 in magnitude space, and 0.1 in color space for binning the CMD. Our age bins were of width 0.1 dex and range from 4.0 Myr–14.1 Gyr. `MATCH` places any star formation < 5 Myr in the 4-5 Myr time bin, therefore age measurements in the youngest time bins are actually upper limits on the age (e.g. < 5 Myr), and provide lower limits on the progenitor mass when mapping from age to mass. We fit for a range of extinction values, and included a prescription for differential reddening.

In fields with very shallow depth the CMD may not be sensitive to stellar populations at older ages, which means the CMD fitting routine will not be able to place strong constraints on the star formation in older age bins. For each field we used artificial stars to quantify the field depth as the 50% completeness magnitude limit (Section 4.2.3). The completeness limits for each field are listed in columns 7-8 in Table 4.1. To ensure that we are sensitive to the main sequence turn-off (MSTO) for various population ages we compared the 50% completeness magnitudes in each field to the MSTO magnitudes at ages from 6-80 Myr from the stellar evolution isochrones of Girardi et al. (2002) in the same filters used here. As shown in the left-hand panel of Figure 4.12 we are sensitive to MSTO at 80 Myr for all ACS fields. The center and right-hand panels of Figure 4.12 display the same comparison between 50% completeness magnitude limits in each field (grey x's) and MSTO magnitudes at various ages in the WFPC2 filters used. Here, there are several fields where the depth is so shallow that we are not quite sensitive to the magnitudes of the oldest MSTO ages. We have flagged these fields (11) for which we are not sensitive to the MSTO at 80 Myr with s in Table 4.1 and Table 4.2, and note that the age estimates for sources in these fields may have

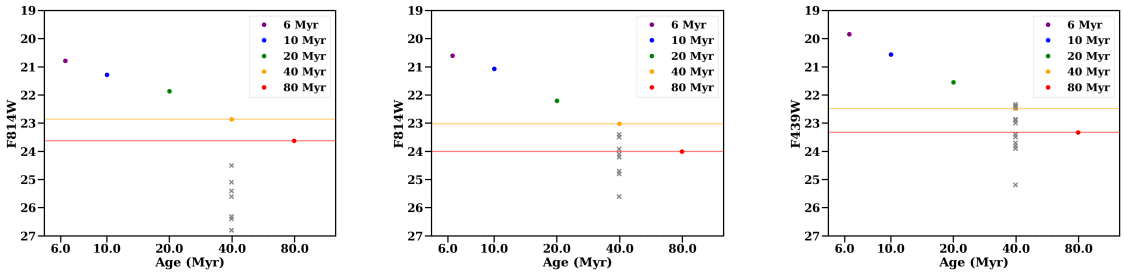

Figure 4.12: *Left*: The 50% completeness magnitudes in the F814W filter for all ACS fields (grey points) at a MSTO of $\sim$ 40 Myr. The MSTO magnitudes for ages from 6-80 Myr are plotted in color and labeled for reference. The 50% completeness limits for all ACS fields are well above the MSTO magnitude at 80 Myr, indicating that we are sensitive the MSTO at 80 Myr in these fields. *Center*: The 50% completeness magnitudes in the F814W filter for all WFPC2 fields (grey points) at a MSTO of $\sim$ 40 Myr. Three fields (6640-NGC598-SRV2, 5464-NGC598-1, 5914-NGC598-R14) have 50% completeness magnitude limits fainter than the MSTO magnitude at 80 Myr, indicating that we are not sensitive to the MSTO of the oldest populations in these fields. *Right*: The 50% completeness magnitudes in the F439W filter for all WPC2 fields (grey points) at a MSTO of $\sim$ 40 Myr. There are eight fields (5384-M33-NEB1, 11079-M33-OB39S, 11079-M33-OB77, 11079-M33-OB94, 11079-M33-OB101, 9127-M33-PAR-FLD1, 5384-M33-NEB6, and 5494-M33-OB6-5-FIELD) with a completeness limits fainter than the MSTO magnitude at 80 Myr, indicating that these fields are not sensitive to the MSTO of the oldest populations

large errors toward older ages.

In addition to quantifying errors based on photometric depth we quantified systematic errors by randomly resampling the CMD and refitting with model isochrones shifted in both bolometric magnitude as well as effective temperature (Dolphin, 2012). We quantified random errors from the fitting technique itself using `MATCH's hybridMC` routine which uses a Markov Chain Monte Carlo approach to quantify uncertainties on the amount of star formation in a given age bin by sampling from the probability density distribution of the fit values (Dolphin, 2013). The random error from the fit method most often affects the relative amount of star formation in a particular age bin rather than the relative age bin localization of a star formation burst.

The SFH returns the SFR in each time bin, and we use this to derive the cumulative distribution of stellar mass using the SFR at each time step to calculate first the total stellar mass formed in the timespan of interest, and then the fraction of this total stellar mass formed in each time bin. The cumulative distribution of stellar mass that is returned is akin to a probability distribution function with the most likely age for the source being the time bin with the highest fraction of stellar mass formed. Errors on the overall cumulative distribution are computed by resampling the errors on the SFRs in each time bin 1000 times using a Gaussian distribution with mean of the

best SFR and sigma of the rate of uncertainty.

We report the most likely age for a given source as the time bin with the highest fraction of stellar mass formed. The errors on this age are given here as the narrowest 68th percentile confidence interval, calculated using 1000 realizations of the SFH from `MATCH's hybridMC` routine (Dolphin, 2013). As described in Murphy et al. (2018), the more common use of the 16th and 84th percentiles as the confidence interval on a measurement introduces biases in the cases where the probability distribution function has large "wings." As this is sometimes the case for data such as this, the use of the narrowest 68th percentile tempers the effects that such biases would have on the reported age and associated errors.

Even in the case of multiple star formation events we are therefore able to measure the most likely age using the time bin with the highest fraction of stellar mass formed, and report the narrowest 68th percentile confidence interval using the full probability distribution function spanning the full 80 Myr. We determined the age for a source using only the last 80 Myr of the SFH as we are interested in young systems hosting neutron stars or black holes. Given that at least a ~ 8 $M_{\odot}$ progenitor is needed to produce a neutron star (Jennings et al., 2012, 2014) all neutron stars should be formed within ~ 50 Myr of the star formation episode. We therefore probed out to 80 Myr to allow for some delay of the onset of the HMXB phase given considerations of binary evolution, but note that we are not particularly sensitive to ages much older than this because dynamical mixing of populations means we are limited by photometric depth. Furthermore, contamination begins to drown out signal at older ages.

An example the cumulative stellar mass fraction and associated SFH for HMXB candidate 013341.47+303815.9 is shown in the center and right panels of Figure 4.13. The most likely age (dotted line) based on the time bin with the highest fraction of stellar mass formed in the last 80 Myr is 7.1 Myr (narrowest 68th percentile confidence interval in red). The CMD of stars within 50 pc of this source is shown on the left with stellar isochrones overlaid for reference. The most likely optical counterpart within the X-ray error circle is denoted by the cyan star, and is consistent with a young age based on the isochrones.

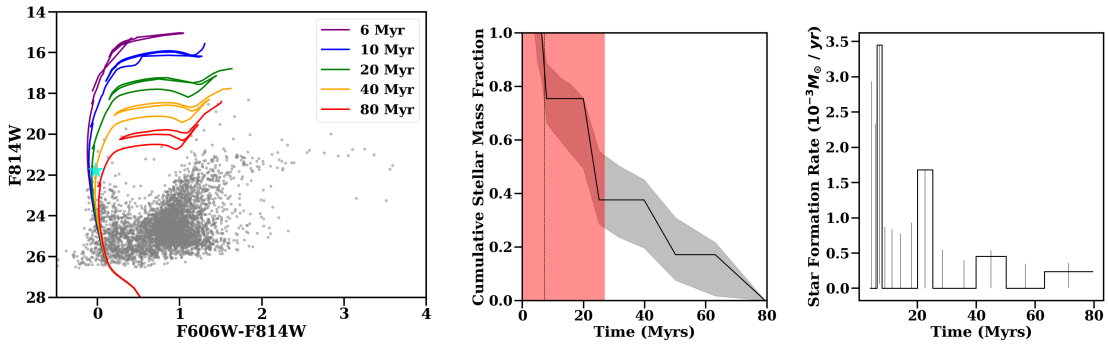

Figure 4.13: *Left*: The CMD of stars within 50 pc of the HMXB candidate 013341.47+303815.9 (grey points), with the candidate optical counterpart denoted by the cyan star. Padova group isochrones shifted to the distance and extinction of M33 are overlaid for reference. *Center*: The cumulative stellar mass fraction (black line) formed over time based on modeling the CMD of the stars within 50 pc of the HMXB candidate. The Monte Carlo derived errors on this distribution are in grey. The most likely age is the bin with the highest fraction of stellar mass formed, and is denoted by the dotted line. The narrowest 68th percentile confidence interval on the most likely age are denoted in red. *Right*: The SFH for this candidate HMXB based on modeling the CMD, indicative of a young source.

4.4 Results

We identified 55 candidate HMXBs in M33 based on their X-ray, optical, and infrared characteristics as described in Section 4.3. The majority ($\sim$ 75%) were previously unclassified as potential XRBs. We measured an age for each source using the CMD fitting method described in Section 4.3.1. Here we describe the sample of HMXB candidates that fall within our archival *HST* coverage, their optical counterparts, the age measurement results for interesting sources in M33, and the resulting combined age distribution for all HMXB candidates in M33 within the archival *HST* coverage.

4.4.1 Candidate HMXBs in M33

Based on the XLF measured by Williams et al. (2015) and T11, M33 is expected to host a large HMXB population. 14 sources in the T11 catalog (662 sources) were classified as possible XRBs. Our technique has allowed us to nearly triple the number of candidate HMXBs in M33.

We identified 55 HMXB candidates from the 270 X-ray sources in T11 for which there is overlapping *HST* coverage. Given the relation between the number of HMXBs and SFR from Grimm et al. (2003), we infer that there are likely $\sim$ 109 HMXBs in M33 above a limiting luminosity

of $\sim 1 \times 10^{35}$ erg s^{-1}, roughly consistent with the limiting luminosity at 90% completeness in T11. Considering that the overlapping *HST* coverage accounts for only 40% the T11 survey area we therefore expect to find around 43 HMXBs in our sample, consistent with the 55 sources with 11 ± 3 spurious candidates reported here.

Of the 55 candidate HMXBs reported here, eight were previously classified as possible XRBs by T11 (with the remaining six T11 XRBs outside this survey area). All candidate HMXBs from this study are listed in Table 4.2 with corresponding T11 catalog identifier, *HST* field name, RA/Dec from T11, deprojected galactocentric radius in M33, source type from T11, match from Grimm et al. (2005) (described below), and source notes.

Table 4.2: All candidate HMXBs in M33 identified in this work. The T11 identifier is in column 1, the corresponding *HST* field is listed in column 2, the RA and Dec positions for the X-ray source from T11 are in columns 3-4, column 5 lists the deprojected galactocentric radius in kpc, the source classification from T11 is in column 6, the Grimm et al. (2005) match is in column 8, and any notes on the source are in column 9.

T11 Name	Field	RA	Dec	R_{gal} (kpc)	T11 Class	Grimm Match	Notes
013305.14+303001.4	11079-M33-OB127	23.27145611	30.50041000	3.90	XRB	–	no *HST* counterpart, low SFR
013314.68+304012.2	9127-M33-PAR-FLD1[s]	23.31116694	30.67008000	3.30	USNO-0626	–	no SFH
013315.16+305318.2	11079-M33-OB137	23.31316694	30.88839000	5.86	XRB?,X-4	J013315.1+305317	$> 3\sigma$ var
013318.34+302840.4	5914-NGC598-U137	23.32641694	30.47789000	3.29	–	–	low SFR
013320.80+302948.0	10190-M33-626sw-28004	23.33666694	30.49669000	2.99	–	–	red counterpart
013330.19+304255.6	8207-M33-PAR-FIELD4	23.37579194	30.71547000	2.37	stellar	–	–
013331.32+303402.2	6038-M33-AM6-FIELD	23.38050000	30.56728000	1.83	–	–	–
013331.86+304011.7	10190-M33-301sw-25900	23.38275000	30.66994000	1.77	–	–	low SFR
013332.19+303656.8	6431-NGC598-FIELD	23.38412500	30.61578000	1.54	stellar	–	red counterpart
013332.23+303955.5	8018-M33	23.38429194	30.66544000	1.70	XRT-2	–	–
013332.71+303339.3	6038-M33-AM6-FIELD	23.38629194	30.56094000	1.83	–	–	
013334.13+303211.3	5998-M33-FLD4	23.39223389	30.53648000	2.02	XRB,X-7	J013334.1+303210	–
013334.54+303556.1	6431-NGC598-FIELD	23.39392611	30.59894000	1.42	XRB	–	–
013336.04+303332.9	5998-M33-FLD4	23.40018889	30.55914000	1.69	–	J013336.0+303333	low SFR, $> 3\sigma$ var
013336.84+304757.3	9873-NGC598-U49	23.40350000	30.79925000	3.05	–	–	low SFR
013337.90+303837.2	10190-M33-146sw-26505	23.40791694	30.64369000	1.08	stellar	–	red counterpart
013339.01+302115.0	5998-M33-FLD3	23.41254194	30.35417000	4.80	XRT-3	–	–
013339.46+302140.8	5998-M33-FLD3	23.41444694	30.36136000	4.70	–	–	–
013340.09+304323.1	9873-M33-267nw-31659	23.41705611	30.72310000	1.68	–	–	–
013340.81+303524.2	10190-M33-DISK1	23.42004194	30.59006000	1.17	–	–	–
013341.26+303213.4	5998-M33-FLD4	23.42191694	30.53706000	1.90	XRB,XRT-4	–	–
013341.47+303815.9	10190-M33-146sw-26505	23.42279194	30.63775000	0.78	–	–	–
013341.56+304136.4	5384-M33-NEB6	23.42320500	30.69345000	1.17	–	–	–
013342.54+304253.3	9873-M33-267nw-31659	23.42725000	30.71483000	1.39	XRB	–	no *HST* counterpart
013344.17+302205.4	5998-M33-FLD3	23.43404194	30.36817000	4.70	–	–	–
013350.50+303821.4	6640-NGC598-SRV2[s]	23.46044306	30.63930000	0.34	stellar	–	–
013350.89+303936.6	5464-NGC598-1[s]	23.46208306	30.66017000	0.00	XRB,X-8	–	nucleus, no *HST* counterpart
013351.13+303823.7	6640-NGC598-SRV2[s]	23.46304194	30.63994000	0.35	–	–	–
013354.28+303347.8	6640-NGC598-SRV5	23.47617500	30.56330000	1.77	L10-069	–	SNR?
013354.47+303414.5	10190-M33-DISK1	23.47698000	30.57070000	1.65	stellar	–	–
013355.24+303528.6	10190-M33-DISK1	23.48016694	30.59128000	1.37	–	–	–
013356.77+303729.7	6640-NGC598-SRV2[s]	23.48654194	30.62492000	0.93	QSO/AGN?	–	$> 2\sigma$ var
013356.82+303706.7	6640-NGC598-SRV3	23.48675000	30.61853000	1.03	XRB	–	red counterpart
013358.07+303754.5	8207-M33-PAR-FIELD7	23.49197889	30.63182000	0.93	L10-078	–	SNR?
013358.23+303438.2	10190-M33-419se-160	23.49265194	30.57730000	1.76	stellar	–	–
013358.50+303332.2	10190-M33-419se-160	23.49378000	30.55896000	2.06	L10-081	J013358.4+303333	SNR?
013400.75+303944.9	5384-M33-NEB1[s]	23.50313694	30.66248000	0.87	–	–	–
013401.16+303242.3	10190-M33-419se-160	23.50484111	30.54511000	2.44	stellar	–	red counterpart, $> 2\sigma$ var
013402.37+303136.2	10190-M33-419se-160	23.50990389	30.52674000	2.81	–	–	–
013402.86+304151.2	5914-NGC598-R14[s]	23.51191694	30.69756000	1.00	stellar	J013402.8+304151	red counterpart, $> 3\sigma$ var
013407.63+303902.4	5914-NGC598-R12	23.53179194	30.65067000	1.56	stellar	–	–
013408.32+303851.7	5914-NGC598-R12	23.53466694	30.64772000	1.65	–	–	–
013410.03+302856.2	10190-M33-784se-5499	23.54179194	30.48228000	3.98	–	–	low SFR
013410.51+303946.4	5494-M33-OB6-5-FIELD[s]	23.54379194	30.66289000	1.74	stellar	–	no SFH
013410.69+304224.0	11079-M33-OB94[s]	23.54457111	30.70667000	1.63	L10-096	–	SNR?
013416.50+305156.5	11079-M33-OB39S[s]	23.56878306	30.86571000	3.30	stellar	J013416.3+305154	–
013417.08+303426.6	11079-M33-OB101[s]	23.57116694	30.57408000	3.20	stellar	–	$> 3\sigma$ var
013417.17+304843.8	11079-M33-OB77[s]	23.57154194	30.81217000	2.70	–	–	–
013421.15+303930.7	5494-M33-OB6-5-FIELD[s]	23.58812500	30.65853000	2.71	–	–	no SFH
013423.86+303847.6	9873-NGC598-M9	23.59941694	30.64656000	3.04	stellar	–	red counterpart, $> 2\sigma$ var
013426.14+303726.6	9873-NGC598-M9	23.60891694	30.62406000	3.43	–	–	–
013432.60+304704.1	5237-M33-FIELDN604	23.63586806	30.78448000	3.48	stellar	–	–
013435.09+304712.0	5237-M33-FIELDN604	23.64622000	30.78668000	3.67	–	–	–
013438.89+304117.4	11079-M33-OB90	23.66204194	30.68819000	4.10	–	–	–
013444.71+303732.9	8207-M33-PAR-FIELD2	23.68631306	30.62581000	5.06	USNO-2664	–	–

[s] Field depth does not reach 80 Myr MSTO.

Table 4.3: The list of candidate optical counterparts for each candidate HMXB in this work. The T11 identifier for the HMXB candidate is in column 1, the *HST* magnitudes in the F336W, F439W, F555W, F606W, and F814W filters (where available) are in columns 2-6, and the RA and Dec positions for the candidate optical counterpart from *HST* are in columns 7-8.

T11 Name	m_{F336W}	m_{F439W}	m_{F555W}	m_{F606W}	m_{F814W}	*HST* RA	*HST* Dec
013305.14+303001.4	–	–	–	–	–	–	–
013314.68+304012.2	19.0	20.71	–	–	–	23.31123066	30.67003304
013315.16+305318.2	20.8	21.84	–	–	–	23.31316801	30.88824967
013315.16+305318.2	22.12	23.16	–	–	–	23.31324241	30.88826482
013315.16+305318.2	21.5	23.34	–	–	–	23.31323366	30.88829689
013315.16+305318.2	20.01	21.84	–	–	–	23.31316791	30.88827283
013315.16+305318.2	20.15	20.6	–	–	–	23.31323992	30.88841399
013315.16+305318.2	18.0	19.51	–	–	–	23.31324649	30.88843833
013318.34+302840.4	–	–	23.73	–	23.47	23.32647866	30.47776002
013320.80+302948.0	–	–	–	21.0	20.14	23.33678044	30.4967935
013330.19+304255.6	22.21	23.78	–	–	–	23.37579808	30.71524818
013331.32+303402.2	21.93	23.17	–	–	–	23.38042429	30.56740602
013331.86+304011.7	–	–	–	23.87	23.72	23.38275139	30.67001082
013332.19+303656.8	–	22.26	21.64	–	20.88	23.38404693	30.61581187
013332.23+303955.5	–	–	24.2	–	24.19	23.38421691	30.66537972
013332.23+303955.5	–	–	24.31	–	24.17	23.38433879	30.66532402
013332.71+303339.3	22.72	23.71	–	–	–	23.38628803	30.56084971
013332.71+303339.3	22.4	23.11	–	–	–	23.3861842	30.56078041
013334.13+303211.3	17.84	19.33	–	–	–	23.39227098	30.53648949
013334.54+303556.1	–	23.62	23.46	–	23.78	23.39396567	30.59878273
013336.04+303332.9	21.83	23.27	–	–	–	23.40019675	30.55918211
013336.84+304757.3	–	–	–	23.97	24.05	23.40356797	30.79936029
013337.90+303837.2	–	–	–	21.72	21.23	23.4078521	30.64373483
013339.01+302115.0	22.28	23.84	–	–	–	23.41247503	30.35454243
013339.01+302115.0	22.62	23.82	–	–	–	23.4129489	30.35427171
013339.46+302140.8	20.68	22.2	–	–	–	23.41426396	30.36155868

T11 Name	m_{F336W}	m_{F439W}	m_{F555W}	m_{F606W}	m_{F814W}	*HST* RA	*HST* Dec
013339.46+302140.8	20.11	21.22	–	–	–	23.41471594	30.36120084
013340.09+304323.1	–	–	–	23.22	23.03	23.41715764	30.72309722
013340.81+303524.2	–	–	–	22.92	22.96	23.42018113	30.59010136
013340.81+303524.2	–	–	–	23.74	23.75	23.41984718	30.59000306
013340.81+303524.2	–	–	–	23.62	23.51	23.42012371	30.58999796
013341.26+303213.4	20.89	22.11	–	–	–	23.42179328	30.53689766
013341.26+303213.4	20.55	22.07	–	–	–	23.42200047	30.53714006
013341.47+303815.9	–	–	–	21.76	21.79	23.422621	30.6377089
013341.56+304136.4	19.26	19.40	–	–	–	23.422970	30.693422
013342.54+304253.3	–	–	–	–	–	–	–
013344.17+302205.4	20.16	21.42	–	–	–	23.43386426	30.36753758
013350.50+303821.4	–	–	21.0	–	21.14	23.4605127	30.6394515
013350.89+303936.6	–	–	–	–	–	–	–
013351.13+303823.7	–	–	23.9	–	23.68	23.46296903	30.63977172
013351.13+303823.7	–	–	23.12	–	23.01	23.46308108	30.63981074
013354.28+303347.8	–	–	20.62	–	20.78	23.47624293	30.56341926
013354.28+303347.8	–	–	23.3	–	23.22	23.47612905	30.56351518
013354.47+303414.5	–	–	–	24.22	24.12	23.47717516	30.57069537
013354.47+303414.5	–	–	–	22.59	22.71	23.47681386	30.57079985
013355.24+303528.6	–	–	–	23.91	23.89	23.48011294	30.59113955
013356.77+303729.7	–	–	21.34	–	21.24	23.48658666	30.62479502
013356.82+303706.7	–	–	22.18	–	21.29	23.48681041	30.6184458
013358.07+303754.5	22.02	23.27	–	–	–	23.49218916	30.63184171
013358.07+303754.5	22.73	23.97	–	–	–	23.49230198	30.63170482
013358.23+303438.2	–	–	–	23.89	23.92	23.49263863	30.57743719
013358.23+303438.2	–	–	–	23.7	23.71	23.49267909	30.5772012
013358.50+303332.2	–	–	–	24.15	23.88	23.49362144	30.55902244
013358.50+303332.2	–	–	–	22.75	22.83	23.49366451	30.55899361
013358.50+303332.2	–	–	–	23.25	23.29	23.49389244	30.55884499

T11 Name	m_{F336W}	m_{F439W}	m_{F555W}	m_{F606W}	m_{F814W}	*HST* RA	*HST* Dec
013358.50+303332.2	–	–	–	23.49	23.49	23.4938756	30.55890179
013358.50+303332.2	–	–	–	23.85	23.68	23.49375081	30.55915164
013400.75+303944.9	21.55	22.76	–	–	–	23.50302704	30.66263685
013401.16+303242.3	–	–	–	22.32	21.34	23.50485367	30.54517402
013402.37+303136.2	–	–	–	23.96	23.89	23.50993725	30.52692941
013402.86+304151.2	–	–	22.44	–	22.05	23.51192991	30.6977246
013407.63+303902.4	–	–	23.74	–	23.73	23.53177081	30.65053608
013407.63+303902.4	–	–	23.95	–	23.95	23.53186385	30.65073564
013407.63+303902.4	–	–	23.79	–	23.52	23.53161125	30.6505667
013408.32+303851.7	–	–	23.67	–	23.82	23.53472254	30.64788787
013408.32+303851.7	–	–	23.3	–	23.39	23.5348752	30.64767036
013410.03+302856.2	–	–	–	23.83	23.7	23.54181895	30.48218697
013410.51+303946.4[x]	–	–	22.19	–	–	23.543699	30.662796
013410.69+304224.0	21.21	22.78	–	–	–	23.54455387	30.7066734
013416.50+305156.5	20.51	20.54	–	–	–	23.56864113	30.86553403
013416.50+305156.5	21.25	22.39	–	–	–	23.56905053	30.86585631
013417.08+303426.6	20.13	21.13	–	–	–	23.57127714	30.57405008
013417.08+303426.6	19.64	21.0	–	–	–	23.57106813	30.57402997
013417.17+304843.8	20.23	22.03	–	–	–	23.57150248	30.81218826
013421.15+303930.7[x]	–	–	22.15	–	–	23.58817549	30.6586403
013423.86+303847.6	–	–	–	22.45	21.82	23.59941327	30.6465382
013426.14+303726.6	–	–	–	23.74	23.77	23.60887814	30.62418809
013432.60+304704.1[+]	–	–	19.84	–	19.6	23.63573839	30.78461361
013435.09+304712.0	–	–	23.75	–	23.65	23.64633193	30.78652903
013438.89+304117.4	22.11	23.67	–	–	–	23.66212068	30.68814925
013438.89+304117.4	22.18	23.5	–	–	–	23.66208939	30.68815607
013444.71+303732.9	21.03	22.33	–	–	–	23.68623071	30.62583536
013444.71+303732.9	19.6	21.13	–	–	–	23.68636008	30.62576648

+ Two saturated sources within the error circle are not recovered in the *HST* photometry, so only the faintest candidate counterpart in the error circle is listed here. The LGGS magnitudes of the saturated sources are listed in Section 4.4.2.

x Optical counterpart only recovered in one filter; color cuts made on the basis of LGGS photometry.

Fields where the depth was not sufficient for our CMD fitting routine to be sensitive to the MSTO of stellar populations older than 80 Myr are denoted by *s* in Table 4.2 next to the field name. As noted in Section 4.3.1.2 the age measurements for such sources will have larger errors at older ages, and thus are not as reliable as measurements from deeper fields.

We compared our catalog of candidate HMXBs in M33 with those of Grimm et al. (2005, 2007) to look for any previous classifications. The Grimm et al. (2005) catalog contains, as a subset, 16 unique X-ray sources with optical counterparts in M33, i.e. candidate HMXBs. Of these 16, all are in the T11 coverage area, but only 12 are also in our archival HST fields, so we matched only to these 12. We found matches for these sources to T11 positions by adopting a search radius of 4.5". Six of these 12 matches are also classified as candidate HMXBs in this work (noted in column seven of Table 4.2, candidate optical counterparts in Table 4.3), while the remaining six sources from Grimm et al. (2005) are classified here as either background AGN (two sources), SNRs (three sources), or foreground stars (one source).

The notes column in Table 4.2 lists more detailed information on each source: "no *HST* counterpart" if the source had no reliable *HST* optical counterpart either due to shallow exposures in available filters or issues of stellar crowding, "low SFR" if the source had SFR $< 4 \times 10^{-4}$ $M_{\odot}$ yr^{-1} in all time bins, or < 1000 $M_{\odot}$ formed in 80 Myr, "no SFH" if there were too few stars in the field to recover a SFH,"red counterpart" if the source had a bright ($<$ 21st magnitude) counterpart in its error circle that did not pass our blue color cuts, or similarly a $<$ 22nd magnitude counterpart with previous classification as "stellar", "SNR?" if the source was previously classified as an SNR in T11 and Long et al. (2010), or "$> 2\sigma$ var or $> 3\sigma$ var" if the source showed variability between the deep observations of T11 and those of Williams et al. (2015).

As noted in Section 4.3, 11 $\pm$ 3 out of the 55 HMXB candidates may be misclassified due to a chance coincidence between the X-ray error circle and a bright, blue star. In column 9 of Table 4.2 we list some of the source properties for each candidate HMXB, which may be used to cull the population down to the most reliable candidates. For the purposes of the analysis in Section 4.4.3 we remove only those sources present in shallow fields (i.e. field depth not sensitive to MSTO at 80 Myr), as these sources will have large errors towards old ages (11 sources), as well as those sources for which there were too few stars in the field to recover a SFH (3 sources). Culling on these sources removes 14 sources, bringing the number of HMXB candidates above our field depth

cuts to 41 sources. In Section 4.4.3 we present the age distribution for the full sample including sources in shallow fields (52 sources), as well as this culled sample (41 sources).

Using the *HST* photometry and the color and magnitude cuts described in Section 4.3 we also ascribed a most likely optical counterpart candidate to each candidate HMXB. For each HMXB candidate we list the likely optical counterpart candidate's position in the aligned *HST* catalog and magnitudes in all available *HST* filters in Table 4.3. For some sources there was more than one bright source that passed our color and magnitude cuts within the X-ray error circle, in which case we list the multiple candidate counterparts to the X-ray source. It is impossible to reliably determine any candidate counterpart for the nucleus of M33, so there are no counterparts listed for this source (013350.89+303936.6) in Table 4.3. If a source was denoted as "XRB" in T11, but we found no optical counterpart in the *HST* images within the X-ray error circle it is still included in Table 4.3 but without a counterpart listed. For these sources it is possible that the *HST* filters available (e.g. F336W) were too shallow and blue to pick up optical counterparts that might otherwise be visible in ground-based imaging or with IR imaging for more heavily extincted sources.

4.4.2 Individual Sources

While most of our candidates are either previously unclassified, or previously classified as associated with bright stars some have interesting history in the literature. Below we present notes on individual sources of interest, including any prior source classifications.

013334.13+303211.3: M33 X-7: This source is the known eclipsing X-ray binary in M33 consisting of a 15.65 $M_\odot$ black hole and a $\sim$ 70 $M_\odot$ O star secondary in a 3.45 day orbit (Pietsch et al., 2004c, 2006; Orosz et al., 2007). The source has been well-observed and modeled, with binary evolution models suggesting it could form within $\sim$ 4 Myr (Valsecchi et al., 2010). We identified a unique optical counterpart within the X-ray error circle ($\sim$ 0.7") for this source with an F336W magnitude of 17.84 and a F439W magnitude of 19.33. The SFH in the vicinity of M33 X-7 is shown in Figure 4.14, with an inset showing the location of the optical counterpart secondary within the X-ray error circle. The SFH recovered for this source yields a most likely age of < 5 Myr, with the narrowest 68th percentile confidence interval encompassing an age up to 11.8 Myr, consistent with the binary components, and the evolution models.

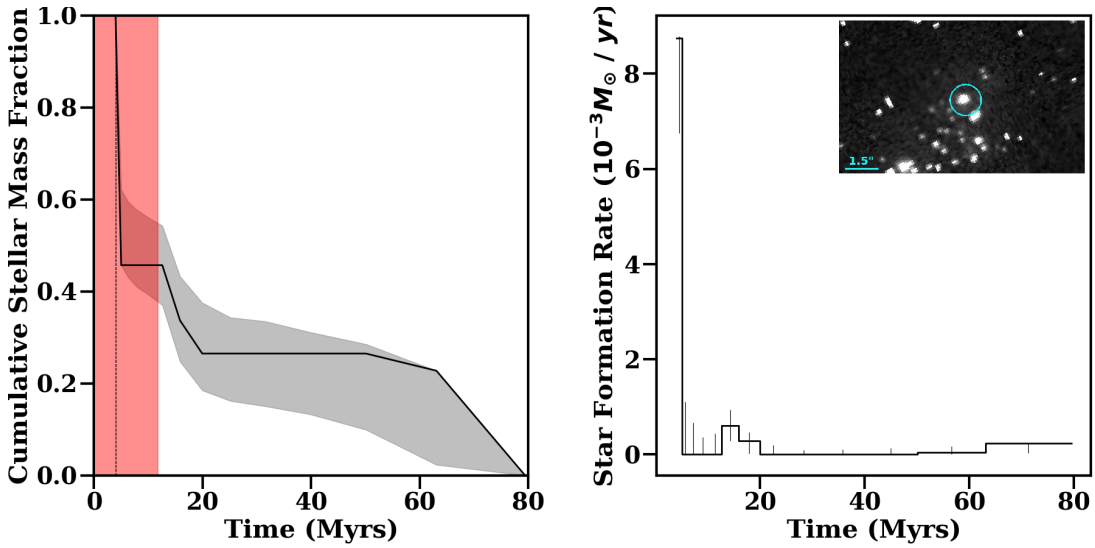

Figure 4.14: *Left*: The cumulative stellar mass fraction formed as a function of time for the stars in the vicinity of the HMXB 013334.13+303211.3 (M33 X-7). The most likely age ($< \sim 5$ Myr) is denoted by the dashed line, with narrowest 68th percentile confidence interval in red. The Monte Carlo derived errors on the cumulative stellar mass fraction are denoted in grey. *Right*: The corresponding SFH for M33-X7. *Right-inset*: F457W WFPC2 image of M33-X7, with the *Chandra* error circle (0.7") shown in cyan.

013354.28+303347.8: This source was classified as an SNR in Long et al. (2010) (L10-069). Although its X-ray colors are consistent with a soft source (e.g. SNR), it has two bright, blue potential optical counterparts within the X-ray error circle (1.3"). Even with a much smaller error circle (assuming the source is not extended), both counterparts are well within the X-ray position uncertainty. The brightest source within the X-ray error circle has a F555W magnitude of 20.62 and and F814W magnitude of 20.78. Although rare, HMXBs found residing in their natal SNR are not unknown (e.g. Heinz et al., 2013). The narrowest 68th percentile confidence interval suggests a progenitor mass between 8–13.4 $M_\odot$, consistent the mass and age derived in Jennings et al. (2014), and a core-collapse progenitor. We note that the measured SFH also has a peak in the SFR in one of the youngest time bins, indicating that the source could have an age as young as $\sim$ 6 Myr, suggestive of a progenitor > 50 $M_\odot$. Further spectral analysis is necessary to determine if an HMXB truly does reside within this SNR, and to discern the nature of the optical counterpart.

013358.07+303754.5: This source was classified as an SNR in Long et al. (2010) (L10-078). The X-ray colors for this source are consistent with it being quite soft, but it has two bright, blue stars within the X-ray error circle (1.1"). We note that a significantly smaller error circle would not include these same bright optical candidates. If this source is indeed just an SNR, with no

embedded HMXB, the age from its SFH suggests a progenitor mass > 9.7 $M_{\odot}$, which is consistent with a core-collapse supernova progenitor.

013358.50+303332.2: This source was classified as an SNR in Long et al. (2010) (L10-081), but an HMXB candidate in Grimm et al. (2005). This source is also included in the SNR catalog of Garofali et al. (2017), where it was found to have X-ray HR values that did not follow the expected trend for an SNR of its temperature, hydrogen column density, and abundance ratio values based on simulated HRs assuming an appropriate SNR spectral model. There are five candidate optical counterparts from *HST* within the X-ray error circle (0.7 "). If this source is an SNR the age from its SFH suggests a progenitor mass > 11.7 $M_{\odot}$, consistent with classification as a core-collapse supernova by Jennings et al. (2014); Lee & Lee (2014b).

013410.69+304224.0: This source was classified as an SNR in Long et al. (2010) (L10-096). Its X-ray colors from T11 are consistent with it being a soft X-ray source, but there is one bright, blue star within the X-ray error circle (0.7"). If this source is an SNR the age from its SFH suggests a progenitor mass of > 12.4 $M_{\odot}$, which suggests a core-collapse progenitor. This source is in one of the shallow fields, so the young age and high progenitor mass may be the result of limited field depth.

013432.60+304704.1: This source was not previously classified as an HMXB candidate, but is located in the highly star forming region NGC 604 in M33. The only candidate optical counterpart recovered from the *HST* photometry has an F555W magnitude of 19.84 and an F814W magnitude of 19.6 (as listed in Table 4.3), however there are two other bright stars visible within the error circle that are saturated, and thus not recovered in the *HST* photometry. All three sources within the X-ray error circle are blended in the LGGS imaging, but photometry is catalogued for two. These are J013432.63+304704.5 (V magnitude = 17.39, B-V=0.022), and J013432.64+304704.0 (V magnitude=17.19, B-V=0.006), neither of which have confirmed spectral types in the LGGS (Massey et al., 2006). The SFH for this source suggests an extremely young age of < 5 Myr, consistent with the most massive possible compact object progenitor in our models (> 50 $M_{\odot}$).

4.4.3 HMXB Age Distribution

Resolved SFHs in the vicinity of individual sources allow for constraining HMXB candidate ages, and thus the relevant timescales for feedback, particularly from massive stars and their end-

products. Using the CMD fitting technique described in Section 4.3.1 we measured ages, and thus formation timescales for individual sources, and also built up a distribution of ages for the entire HMXB source population in M33.

We constructed the age distribution for all 41 candidate HMXBs in fields with depth sensitive to the MSTO at 80 Myr. The full age distribution is the sum of the stellar-mass weighted star formation in each time bin, normalized so that the total mass for each candidate summed to 80 Myr is one. Summing these normalized probability functions yields the number of expected candidate HMXBs in each time bin. The errors on the number of candidates in each bin are the Monte Carlo derived errors on the star formation weighted by the stellar mass in each age bin. Stacking the normalized probability distribution functions for all sources in this way makes use of the entire SFH for each source, and thus does not rely on calculating specific ages for individual sources as is described in Section 4.3.1.2. Instead, the stacked distribution gives a measure of the likely HMXB formation timescales based on the SFHs from all sources included in the population analysis.

The HMXB age distribution for the subsample of 41 sources that pass our field depth cuts is displayed in the left-hand panel Figure 4.15 as the solid blue histogram, with the distribution for all 52 sources for which we were able to measure SFHs plotted as a dashed light green line. These results are based on using an extraction region of 50 pc for recovering the SFHs, as discussed in Section 4.3.1.1. Doubling the extraction radius resulted in the same age peaks discussed below, but with an increase in the percentage contribution in the oldest age bins, which we attribute to dilution of the signal. For comparison, we show the age distribution using these 100 pc regions for the subsample of 41 deep field sources, and all 52 sources in the right-hand panel of Figure 4.15. For reference, we also overplot as light grey lines 100 realizations of the age distribution for a "control" sample recovered from SFHs in the vicinities of the same number of non-HMXB sources measured in fields where we did not find any candidate HMXBs (grey regions, Figure 4.3); the median of these 100 draws is plotted as a dash-dot line in black.

The HMXB age distribution contains two prominent peaks that stand out from the control sample: notably a young population at < 5 Myr and an older population at ~ 40 Myr. Both populations can be reproduced in binary population synthesis models, but the young population at < 5 Myr is unusual, as the only known analogues to such a population are a handful of young SG-XRBs in the LMC (Antoniou & Zezas, 2016), the supernova impostor SN 2010da (Binder et al.,

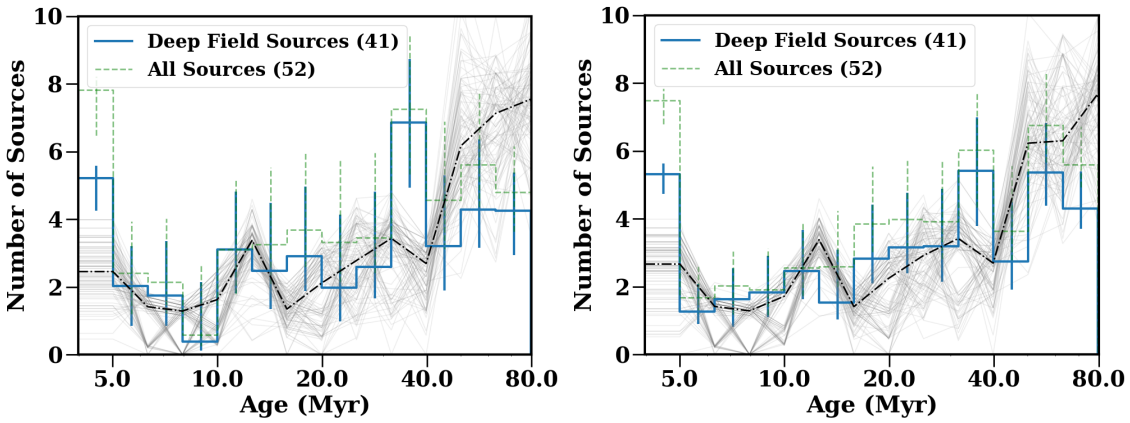

Figure 4.15: *Left*: The age distribution calculated using 50 pc regions for all 41 HMXBs in M33 that are in fields sensitive to the MSTO at 80 Myr plotted as a solid blue line. The solid blue histogram represents the number of systems expected in each age bin given the SFHs for all sources. The histogram is derived from summing the normalized stellar mass probability distribution functions for each source in each time bin. The distribution is normalized for each source as the sum of the stellar-mass weighted star formation in each time bin where the total mass for each candidate summed to 80 Myr. The errors on the number of candidates in each bin are the Monte Carlo derived errors on the star formation weighted by the stellar mass in each age bin. The light grey lines are the control sample: the equivalent age distribution for 100 random draws of 41 non-HMXB X-ray sources in M33, with the median of these 100 draws as a dash-dot line in black. The HMXB age distribution shows two peaks in HMXB formation efficiency that stand out from the control sample: a peak at very young ages (< 5 Myr), and one at older ages (~ 40 Myr). The age distribution for all 52 sources in the sample for which we were able to measure SFHs is overplotted as a light green dashed line for reference. *Right*: The age distribution calculated using 100 pc regions for all 41 sources in fields sensitive to the MSTO at 80 Myr as a solid blue histogram, with the age distribution for all 52 sources in the sample for which we were able to measure SFHs plotted again as a dashed green line. The light grey lines are the control sample as before.

Table 4.4: The full SFH probability distribution for all HMXB candidates in M33. Column 1 lists the T11 identifier, column 2 is the left edge of the age bin in Myr, column 3 is the right edge of the age bin in Myr, column 4 is the percentage chance that the source was formed in the corresponding age bin (stellar mass fraction in a given bin), and columns 5-6 are the positive and negative errors on that percentage. The full table is available in electronically in Garofali et al. (2018).

T11 Name	Age_{left} (Myr)	$\text{Age}_{\text{right}}$ (Myr)	Probability	Probability^{+}	Probability^{-}
013334.13+303211.3	0.0	5.0	0.543	0.000	0.169
013334.13+303211.3	5.0	6.3	0.000	0.187	0.000
013334.13+303211.3	6.3	7.9	0.000	0.190	0.000
013334.13+303211.3	7.9	10.0	0.000	0.185	0.000
013334.13+303211.3	10.0	12.6	0.000	0.194	0.000
013334.13+303211.3	12.6	15.8	0.120	0.169	0.120
013334.13+303211.3	15.8	20.0	0.072	0.171	0.072
013334.13+303211.3	20.0	25.1	0.000	0.200	0.000
013334.13+303211.3	25.1	31.6	0.000	0.191	0.000
013334.13+303211.3	31.6	39.8	0.000	0.200	0.000
013334.13+303211.3	39.8	50.1	0.000	0.211	0.000
013334.13+303211.3	50.1	63.1	0.037	0.206	0.037
013334.13+303211.3	63.1	79.4	0.228	0.000	0.190
013341.47+303815.9	0.0	5.0	0.000	0.100	0.000
013341.47+303815.9	5.0	6.3	0.000	0.174	0.000
013341.47+303815.9	6.3	7.9	0.246	0.093	0.246
013341.47+303815.9	7.9	10.0	0.000	0.253	0.000
013341.47+303815.9	10.0	12.6	0.000	0.262	0.000
013341.47+303815.9	12.6	15.8	0.000	0.285	0.000
013341.47+303815.9	15.8	20.0	0.000	0.321	0.000
013341.47+303815.9	20.0	25.1	0.378	0.120	0.378
013341.47+303815.9	25.1	31.6	0.000	0.334	0.000
013341.47+303815.9	31.6	39.8	0.000	0.309	0.000
013341.47+303815.9	39.8	50.1	0.205	0.184	0.205
013341.47+303815.9	50.1	63.1	0.000	0.306	0.000
013341.47+303815.9	63.1	79.4	0.171	0.039	0.171

2016), and a number of nearby ULXs (Poutanen et al., 2013; Berghea et al., 2013). We discuss possible explanations for the populations at both ages based on host galaxy properties and stellar and binary evolution in Section 4.5.2 and Section 4.5.3.

The full probability distributions for the age of each individual source are listed in Table 4.4 (full version available electronically). For a given source each line displays percentage probability that the source was formed in that particular time bin, as well as the corresponding errors in both directions. While we do not ascribe a particular age to each source the most likely age and associated errors can be recovered from the full probability distributions presented in Table 4.4 using the method described in Section 4.3.1.2.

4.5 Discussion

In this section we discuss the population of candidate HMXBs in M33 in terms of the effect of spurious sources on the results, how the age distribution for candidate HMXBs in M33 compares to different LG populations of HMXBs, and how the age distribution relates to massive binary evolution.

4.5.1 Effect of Spurious Sources

Because HMXBs and background AGN often look very similar in terms of their X-ray spectra and colors it can be hard to distinguish them in the absence of a clearly identified optical counterpart. Even with optical photometry, however, distinguishing the two classes may not be trivial. Reliable source typing may be achieved with the addition of a spectroscopically confirmed counterpart. In this way, false positives, e.g. spectroscopically identified AGN that appear photometrically like HMXB counterparts, may be weeded out from the sample. Because we lack spectroscopic identifications for the entirety of this sample the effect of false positives on the results must be considered.

As can be seen in Figure 4.15, the age distribution derived from the sample of "control" sources has star formation spread across all time bins, with increasing contribution from contamination at the latest times post-starburst. The low level star formation across all time bins can be thought of as a "background," while the inflated star formation rate in the oldest age bins comes from higher contribution from contamination that arises due to the effects of stellar mixing when measuring the SFH around sources that are not in exclusively young regions. Thus the contribution of spurious sources to the full age distribution will be to increase the overall "background" SFR in all time bins, increase the contribution from contamination at old ages, and inflate the error bars on the SFR in each bin accordingly. We address each of these effects on the overall results in turn.

Increased contribution from contamination at 80 Myr is not a strong concern for HMXB studies, as formation of HMXBs on this timescale is somewhat unphysical given considerations of single star evolution timescales. Therefore, a large signal in this age bin will be a noticeable contaminant. Inflated contribution from contamination in this latest age bin will also have the effect of diluting the signal in adjacent bins, i.e. weakening any discernible signal between $\sim$ 60-80 Myr, if present. This timescale is also unphysical for the formation of HMXBs, so again we would not expect false

positives to mask a signal of true physical significance in this time bin.

The presence of false positives in the sample will also increase the SFR (and associated errors) in all other time bins. The effect of this will be primarily to dilute the true age distribution from the population of interest. False positives are unlikely to preferentially boost the contribution to the full age distribution in one of the time bins < 60 Myr unless they all happen to be closely clustered in one region. Therefore, even with a modest fraction of spurious sources included here we do not expect the results to be affected substantially given that we do not have highly clustered candidates.

4.5.2 Comparison with Local Group HMXB Populations and Environment

Resolved SFHs have been used in a number of other nearby galaxies, including the SMC, LMC, NGC 300, and NGC 2403, to look at the age distribution of the HMXB population. In particular, a preferred age of $\sim$ 40-55 Myr was found for HMXBs in NGC 2403 and NGC 300 by Williams et al. (2013a) using *HST* data, and 25-60 Myr (peaked strongly at 42 Myr) for HMXBs in the SMC by Antoniou et al. (2010) using the SFH maps of Harris & Zaritsky (2004). More recently, Antoniou & Zezas (2016) looked at the age distribution for known HMXBs in the LMC using the SFH maps of Harris & Zaritsky (2009a). This analysis revealed a peak in the age distribution between 6-25 Myr for the LMC HMXBs. The most likely explanation for differences in the number of HMXBs present at different times is the underlying SFH of the host region, and namely how the SFR varies in regions of the host galaxy on short timescales, as has been demonstrated in other works, both theoretical and observational (e.g. Antoniou et al., 2010; Linden et al., 2010; Fragos et al., 2013; Antoniou & Zezas, 2016). In this section we discuss the preferred formation timescales for HMXBs in M33 as compared to other LG galaxies in the context of stellar evolution timescales and the role of metallicity.

The 40 Myr peak in the age distribution as seen in the SMC, NGC 300, NGC 2403, and now M33 is not unexpected assuming the population is strongly dominated by Be-XRBs containing NS companions, as this age coincides with both the peak rate of core-collapse events forming NS assuming standard models of stellar evolution (e.g. Marigo et al., 2008), as well as an observed peak in B star activity (McSwain & Gies, 2005). The preferred age for these Be-XRBs populations implies that there is an efficient formation pathway for these systems due to binary evolution (see

further discussion in Section 4.5.3). As these systems are potential precursors to NS-NS binaries (Tauris et al., 2017), this implies that the immediate precursors to these gravitational wave sources may form very efficiently on these timescales across a range of metallicities from significantly sub-solar (e.g. SMC) to solar (M33).

The < 5 Myr peak that is seen in M33 is observed for a subset of the LMC HMXBs, and in particular most prominently for the SG-XRBs in the LMC. The existence of such a young population, if it is indeed composed primarily of SG-XRBs, may be influenced by host galaxy metallicity. Both M33 and the LMC are higher metallicity environments than the SMC, and in these higher metallicity environments the line-driven winds of massive stars will generally be stronger than in low metallicity environments such as the SMC (Kudritzki et al., 1987).

The effect of metallicity on the line-driven winds of massive stars has been invoked as a factor in HMXB formation and evolution in terms of its effects on both mass loss and orbital evolution through loss of angular momentum (Dray, 2006; Linden et al., 2010). In particular, low metallicity environments where the stellar winds are weaker should produce more massive compact objects, as less mass will be lost from the primary via winds, and also possibly systems with different evolutionary pathways, e.g. tighter orbits, due to differences in how much angular momentum is lost from the system. However, in the case of wind-fed accretion onto compact objects as in SG-XRBs the population may be always in a low-luminosity, and thus undetected state in low metallicity environments where there are weak stellar winds, so it is reasonable to expect that this population would not be prevalent in low-metallicity environments (e.g. Linden et al., 2010).

As M33 has a known metallicity gradient which ranges from roughly solar in the interior to LMC-like at larger galactocentric radii with a break at 3 kpc (Magrini et al., 2007) we tested for any further metallicity effects by constructing the candidate HMXB age distribution separately for all 41 sources that pass our field depth cuts with galactocentric radii < 3 kpc (dashed orange line), and those with radii > 3 kpc (dotted green line) as shown in Figure 4.16. Although there appear to be fewer 40 Myr sources at radii > 3 kpc, the small number of sources at these larger galactocentric radii means that we cannot determine any significant differences between the age distributions of the higher metallicity (inner) versus lower metallicity (outer) regions of the galaxy.

While there are too few sources to make a definite statement about the differences between the candidate HMXBs at solar versus LMC metallicities we can note that there is not a strong

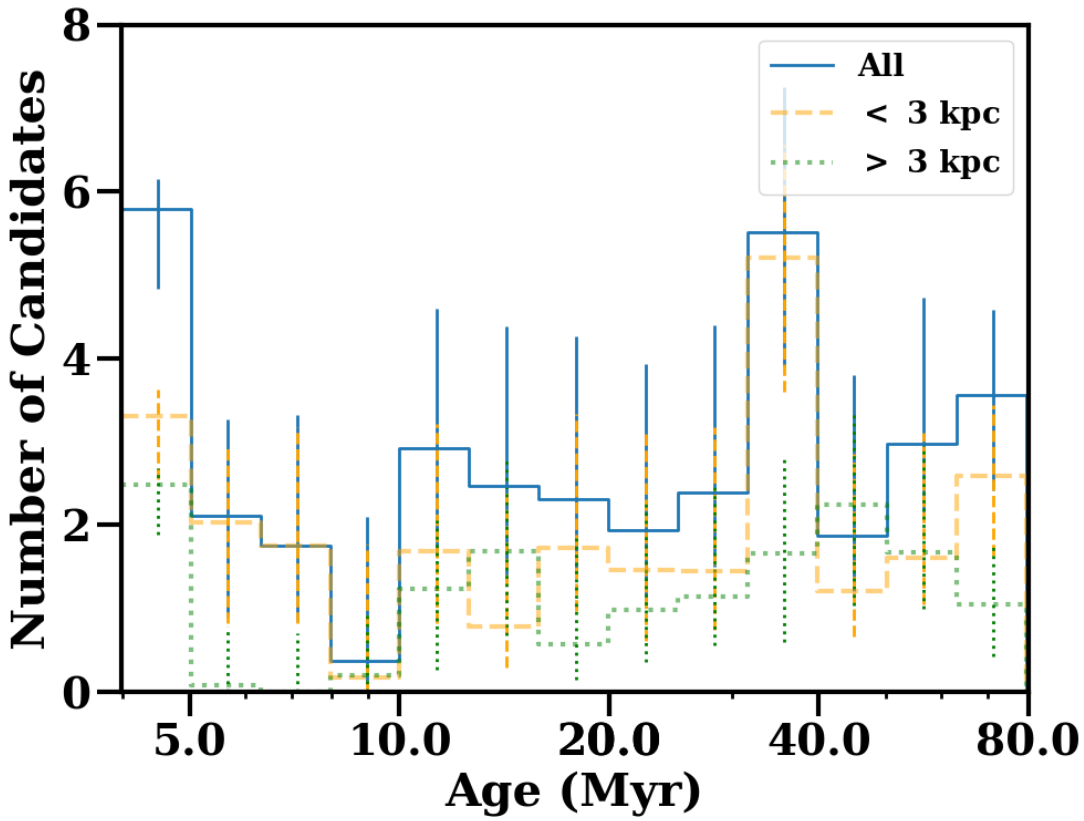

Figure 4.16: The age distribution broken down by galactocentric radius for the 41 candidate HMXBs in M33 that pass our field depth cuts. The full distribution is plotted as a solid blue line, while the distribution for sources within 3 kpc (solar metallicity) of M33's center is plotted as a dashed orange line, and the distribution for sources outside 3 kpc (LMC-like metallicity) is displayed as the dotted green line.

preference for young sources originating in one region of the galaxy. In particular, we find that there is no significant difference between the spatial distribution of young HMXB candidates and candidates found at older ages when compared to supergiants in M33 taken from the catalog of Massey et al. (2016). If we expect that SG-XRBs dominate the younger population in M33 as is the case for the LMC these systems may only require a metallicity threshold (roughly $\frac{1}{3}$ solar) to be observable as bright X-ray sources.

4.5.3 Implications for Massive Binary Evolution

Ages derived from resolved SFHs can help constrain binary evolution scenarios by restricting the formation timescale for HMXBs of various subtypes. There are three main features to the age distribution recovered for HMXB candidates in M33, namely a peak in the number of sources at intermediate ages ($\sim$ 40 Myr), a peak in the number of sources at very young ages ($<$ 5 Myr), and a "valley" where few, to no sources exist ($\sim$ 6-10 Myr). We discuss each of these features in turn, and their implications for binary evolution.

4.5.3.1 Delayed Onset HMXBs: Be-XRBs

The peak in HMXB formation around $\sim$ 40 Myr has already been attributed to Be-XRBs, both observationally and based on theoretical understanding of binary evolution (Linden et al., 2009; Antoniou et al., 2010; Williams et al., 2013a). As explained in Williams et al. (2013a), Be-XRBs form on these timescales based on neutron star formation and B star mass loss activity.

In these systems the initially more massive star (the primary) evolves away from the main sequence and expands to fill its Roche Lobe, in the process transferring mass to its companion (the secondary). The more massive star will end its life first, leaving behind a compact object, most often a neutron star. If the binary survives the death of the primary the result is a secondary that has been spun up by mass transfer that is now orbiting a compact object. Assuming enough material has been transferred such that the secondary is now rapidly rotating it may either liberate material from its poles, which can be funneled down towards the equator to form an equatorial disk, or otherwise directly liberate material around its equatorial regions if its rotation is close enough to the critical velocity (Bjorkman & Cassinelli, 1993). In either case, an equatorial disk of material is formed around the star, making the star an active Be star (Porter & Rivinius, 2003).

As mass from this outflowing disk is transferred back to the compact object the system becomes bright in X-rays, and observable as a Be-XRB.

There are several aspects to the formation of Be-XRBs described above that make the roughly 40 Myr timescale for the appearance of Be-XRBs preferential. Observationally B stars have been shown to have a peak in their activity (the Be phenomenon) between $\sim$ 25-80 Myr, implying that a majority of these stars are spun up by mass transfer in a binary on these timescales (McSwain & Gies, 2005). This also fits with the preferred timescale for neutron star formation. Assuming a standard Kroupa IMF and a minimum mass threshold for compact object formation, there will be an abundance of neutron stars that form from stars $\sim$ 8 $M_{\odot}$. Assuming standard stellar isochrones this mass corresponds roughly to a 40 Myr timescale for formation of neutron stars in the greatest numbers (Marigo et al., 2008).

We therefore expect Be-XRBs to be prevalent on this 40 Myr timescale given the above formation scenario, with the caveat that the binary needs to survive the death and supernova explosion of the primary. The binary population synthesis models of Linden et al. (2009) demonstrated that such Be binaries would survive to the HMXB phase if they were preferentially the result of primaries undergoing electron capture supernovae, which would impart smaller kicks to the system. The models of Linden et al. (2009) displayed a prominent peak in the number of HMXBs from $\sim$ 20-60 Myr post-starburst, which they dubbed the electron capture supernovae "bump," though the strength and age of this bump may be a function of metallicity (e.g. Podsiadlowski et al., 2004). While our samples do not contain enough sources to definitively compare to their models for electron capture supernovae kick distributions, or pre-explosion core masses, the timescales for formation from simulations are in line with what has been observed here in M33. These HMXB candidates would be those that avoided disruption, and may therefore be made up mainly of systems where the primary underwent an electron capture supernova.

4.5.3.2 Early Onset HMXBs

The HMXB candidates in M33 with formation timescales < 5 Myr post-starburst are more likely to have compact objects that originate from very massive progenitors based solely on considerations of single star evolution timescales (Marigo et al., 2008). At such young ages, however, the models become somewhat degenerate, so we are not able to ascribe a particular progenitor mass to the

stars that form compact objects this early, but rather a lower limit of ~ 50 $M_{\odot}$ for anything formed in the youngest age bins.

As mentioned in Section 4.4.3, a similarly young population is seen for a small number of interesting sources: the supernova impostor SN 2010da in NGC300 (Binder et al., 2016), a number of nearby ULXs (Poutanen et al., 2013; Berghea et al., 2013), as well as a handful of SG-XRBs in the LMC. The formation of SG-XRBs in particular on these timescales is bolstered by binary population synthesis models, like those of Linden et al. (2009), which predict a large number of massive black holes fed by wind accretion from supergiant companions at early times post-starburst.

Arguments based on single star evolution would suggest that HMXBs present at very young ages should host black holes as compact objects, as these would be systems originating from the most massive progenitors (> 40 $M_{\odot}$) (e.g. Fryer et al., 2012). There is some evidence for an upper mass cutoff for stars that produce black holes versus neutron stars (Jennings et al., 2012, 2014), however, binary evolution may make it possible for massive progenitors to form neutron stars $\sim$ 5 Myr post-starburst some small fraction of the time if the massive primary undergoes copious amounts of mass transfer or stripping in a binary (Belczynski & Taam, 2008). Thus, while it is likely that most of the HMXB candidates at these youngest ages host black holes we cannot state so definitively for any source but M33 X-7, for which the mass of the compact object has been measured (Orosz et al., 2007). In the future, *NuSTAR* observations of candidate HMXBs in M33 will help delineate between compact object type where dynamical mass measurements are lacking.

While we cannot state with certainty what the nature of the compact object is based on HMXB age alone we can make some inferences bolstered by the combination of system age, candidate optical counterpart color and magnitude, and X-ray luminosity. Based on the *HST* magnitudes of the candidate counterparts for the youngest HMXB candidates in M33 the majority of the systems at young ages are likely not systems hosting supergiant donors, though again we cannot say anything definitively about the nature of the compact object. There is likewise no trend with X-ray luminosity and age to indicate a preferred donor–compact object configuration at either young or old HMXB ages. The distribution of X-ray luminosities for sources at young ages ($<$ 5 Myr) is consistent with the luminosity distribution for sources in all other age intervals. Only two of the sources in the youngest time bin have candidate optical counterparts with magnitudes brighter than 20th magnitude, sources 013334.13+303211.3 (M33 X-7) and 013432.60+304704.1

(in NGC604).

The remainder of the candidate HMXBs in this youngest time bin therefore either represent systems with less massive (possible B star) donors to originally very massive primaries, or otherwise their relatively faint candidate optical counterparts suggest they were in fact formed in later time bins and are therefore older sources, or that the faint photometry of their optical counterpart is the result of past binary interactions (e.g. common envelope phase).

The possibility that these systems have B star donors to originally very massive primaries is somewhat refuted by current models of binary evolution, which suggest that close binaries with very high mass ratios may not survive the common envelope phase (i.e. would merge), and therefore systems such as Be-BH XRBs should be extremely rare (Belczynski & Ziolkowski, 2009). There is only one such Be-BH binary known in the Milky Way, albeit it is a very low luminosity source (Casares et al., 2014; Ribó et al., 2017).

Instead, it is more likely that these systems may in fact be older, though there is a high probability that they formed during the most recent star formation episode, or that the optical counterpart is fainter than expected due to binary evolution. The expected photometric class of the counterpart given the past history of interactions with a companion is difficult to quantify, as it depends on the unknown initial conditions of the system, as well as uncertain prescriptions for mass loss, mass transfer, common envelope phase, spin-up, and more. We can, however, quantify the likelihood of different formation timescales based on the measured SFHs for each source. In particular, the following four sources do not have candidate supergiant optical counterparts, but have high probabilities of being younger than 5 Myr: 013354.47+303414.5, 013339.01+302115.0, 013330.19+304255.6, 13358.23+303438.2, and 013426.14+303726.6. While the best fits for these sources have most of the stellar mass forming < 5 Myr after the initial burst of star formation there are uncertainties on these best fit values that make it plausible for these sources to have formed at later times, and therefore be older. The full SFH probability distributions and their associated errors are listed for each of these sources in Table 4.4. These sources will make interesting candidates for optical follow-up to classify their candidate optical counterparts and *NuSTAR* X-ray colors to classify their compact objects.

4.5.3.3 HMXB Valley

The distribution of sources in M33 shows a distinct lack of sources between the ages of $\sim$ 6-10 Myr. This feature is seen as well, to a certain extent, for HMXBs in the LMC (Antoniou & Zezas, 2016), and is consistent with the binary population synthesis models Linden et al. (2009), where the HMXBs appearing at the earliest times post-starburst are the systems containing black holes fed by the stellar winds of massive supergiant secondaries, which rapidly disappear once the O stars die out (e.g. Van Bever & Vanbeveren, 2000).

However, as shown in Figure 4.15, the age distribution for our "control" sample also shows a steady decrease and minimum between 6-10 Myr, which means that this particular feature is consistent with the SFH elsewhere in M33. Because of this we cannot definitively attribute this feature to binary evolution. It may be that HMXB formation is disfavored on these timescales, but, at least for the case of M33, the SFH also suggests that the star formation rate in general is low on these timescales.

4.6 Synopsis

We identified 55 candidate HMXBs in M33 using a combination of deep archival *Chandra* and *HST* imaging. After precise astrometric alignment between the X-ray and optical data we found their candidate optical counterparts. We then used *HST* data to construct CMDs in the vicinity of each HMXB candidate. Because HMXBs are young sources still associated with their natal regions we modeled these CMDs to find the best fitting SFHs and probability distribution for the age, or formation timescale of each source. The combination of probability distributions for all sources yields an age distribution for the population of candidate HMXBs, which can be used to infer the preferred formation timescales for HMXBs in M33.

The age distribution in M33 has three distinct features: a peak in HMXB production at < 5 Myr, a valley where there are few, if any, sources between 6-10 Myr, and another peak in HMXB production at $\sim$ 40 Myr. The 40 Myr peak has been seen in other nearby galaxies, and can be attributed to an efficient formation pathway for Be-XRBs across a range of metallicities. In particular, this peak is expected given increased production of neutron stars from 8 $M_\odot$ progenitors on this timescale, possibly via electron capture supernovae, and a peak in the Be star phenomenon from $\sim$ 25-80 Myr, possibly due to spin up by mass transfer in a binary. The young population

seen in M33 is unique compared to what has been observed in other LG galaxies, but given binary population synthesis models and stellar evolution timescales it is expected assuming a population of massive progenitors that result in relatively massive black holes accreting from the winds of supergiant companions at very early times (e.g. M33 X-7). The distinct lack of sources between 6-10 Myr may be attributed simply to the particular SFH of M33, which exhibits low a SFR on these timescales.

This sample of candidate HMXBs with measured ages provides not only a population ripe for further observational follow-up, but also a unique set of sources to help place constraints on binary population synthesis models. In particular, this population of candidate HMXBs can help constrain models by requiring them to reproduce the observed HMXB sample not only in terms of numbers of systems, but also when they must be formed relative to the known host galaxy properties of M33. Models that seek to reproduce these candidate HMXBs as an intermediate step in binary evolution can then be used to infer the population of compact object binaries and potential gravitational wave sources that would result by evolving this local population of HMXBs forward in time.

Future work will expand upon this catalog of HMXB candidates to refine the system characteristics using detailed X-ray spectral fits, and X-ray timing analysis for sources with enough counts. In addition, full spectral energy distribution fitting to determine optical counterpart spectral class will be possible using the upcoming M33 Legacy Survey (PI: Dalcanton). Forthcoming *NuSTAR* data for M33 will also yield compact object types from X-ray colors for some candidate HMXBs. Taken together, this will yield the first large sample of HMXBs with known system characteristics in a large spiral galaxy outside the Milky Way. Such a population is of great interest in understanding the potential local analogue precursors to gravitational wave sources.

Chapter 5:

Multiwavelength Properties of High-Mass X-ray Binaries in M33

5 Multiwavelength Properties of High-Mass X-ray Binaries in M33

5.1 Introduction

Of the hundreds of HMXB candidates in the Galaxy and MCs, $\sim 70\%$ have been classified into sub-types on the basis of their donor star counterparts (e.g. Negueruela & Coe, 2002; Coe et al., 2005; Liu et al., 2006; Coe & Kirk, 2015; Haberl & Sturm, 2016). These are limited mainly to Be-XRBs in the MCs, or sources with unobscured companions in the Milky Way (Walter et al., 2015; Haberl & Sturm, 2016; Antoniou & Zezas, 2016). A smaller percentage ($< 60\%$) of these sources have known compact object types (i.e. NS or BH), or furthermore, compact object masses that have been measured. This often incomplete picture of the characteristics of both binary components in an HMXB hinders the ability to leverage HMXB population studies to their full potential in the context of massive binary evolution, and in particular as these systems relate to compact object-compact object binary formation.

The sources for which in-depth characterization of the binary components is achievable have individually contributed multitudes to constraining binary evolution scenarios. As discussed in Chapter 1, the measured rotation periods and distribution of spectral types for donor stars in Be-XRBs are indicative of a preferred evolution scenario, namely "rejuvenation" of the donor companion via mass transfer (Rappaport & van den Heuvel, 1982; van Bever & Vanbeveren, 1997; Negueruela, 1998; Negueruela & Coe, 2002; McSwain & Gies, 2005). Individual systems, like M33 X-7, have also been fully described observationally, furnishing prescriptions for theoretical unknowns like common-envelope phase evolution, mass-transfer history, and even evolution timescale (Pietsch et al., 2006; Orosz et al., 2007; Valsecchi et al., 2010). Similarly, a small number of WR X-ray binaries (WR-XRBs) have had orbital periods, compact object masses, and donor star spectral types measured from optical and X-ray data (Prestwich et al., 2007; Silverman & Filippenko, 2008; Crowther et al., 2010). The high compact object masses, coupled with massive WR companions and short orbital periods suggest WR-XRBs are precursor systems to the BH-BH binary mergers that have been observed with aLIGO at higher redshifts (Bulik et al., 2011; Belczynski et al., 2013; van den Heuvel et al., 2017).

Beyond characterization of individual systems, specifying traits for large HMXB populations across the LG provides theoretical models of massive binary evolution with statistical checks. To obtain a full description of an observed population of HMXBs it is necessary to first identify the potential donor star relative to the X-ray source position. In Chapter 4, I described this first step in the process towards characterizing HMXBs. With a sample of candidate HMXBs such as the one produced in Chapter 4, it is then possible to perform targeted follow-up to not only confirm the nature of the sources as HMXBs, but also further describe the systems in terms of the donor star spectral type, and possibly compact object type and accretion state. In this Chapter, I present ongoing work using multiwavelength data to confirm and characterize the population of HMXBs in M33 first presented in Chapter 4.

The remainder of this chapter is organized as follows: in Section 5.2 I discuss the multiwavelength data, namely from *Chandra*, *XMM-Newton*, and *HST*, used to characterize the candidate HMXBs from Chapter 4. In Section 5.2.5 I describe the X-ray spectral fitting technique first introduced in Chapter 3, and used here to characterize HMXBs on the basis of *Chandra* and *XMM-Newton* spectra. In Section 5.3 I present updated characterizations for five candidate HMXBs on the basis of X-ray spectral fits, optical spectra, and six band photometry from *HST*. Finally, in Section 5.4, I provide a synopsis of these results.

5.2 Data & Analysis Techniques

An in-depth analysis of individual sources necessitates leveraging all available multiwavelength data. I have chosen five candidate HMXBs from Chapter 4 for further study on the basis of their unique optical colors or spectral characteristics, and the availability of multiwavelength data for detailed characterization. The data available for classifying these five sources includes X-ray spectral data from *Chandra* and *XMM-Newton* for characterizing the physical source of X-ray emission, as well as ground-based optical spectroscopy from Hectospec, where available, for classifying the optical sources associated with the X-ray emission, and finally photometry from *HST* for localizing candidate optical counterparts on color-magnitude and color-color diagrams. Each of these data sources will be presented in turn below.

5.2.1 *Chandra* Spectra

The *Chandra* data used here are from the high-resolution observations of the ChASeM33 survey (T11). Spectral products were extracted using the `CIAO` tool `dmextract` (part of the `ACIS Extract (AE)` package). Response matrix files (RMFs) and ancillary response files (ARFs) were created using `mkacisrmf` and `mkarf`. As the survey had overlapping fields, summed spectral products were created for any sources that were in more than one observation, with the spectral products from each observation weighted by exposure times.

Although the catalog contains 662 sources, spectral products were only extracted for sources with sufficient S/N for spectral fitting. Spectra were grouped such that there would be at least S/N = 2 in each spectral bin, with at least eight bins available for fitting. This constraint produces spectral products for 254 sources from the full catalog. In T11, these 254 sources were fit automatically using both an absorbed power-law model and an absorbed thermal plasma (`apec`) model to determine a best-fit. More detailed, multi-component models were only performed for a subset of the brightest sources in the catalog (those with > 2000 counts).

In this chapter, we use the spectral products extracted in T11 to perform spectral fits for a subset of the brightest HMXB candidates from Chapter 4. The fits are performed simultaneously using data from ChASeM33 as described above, as well as the *XMM-Newton* survey of W15, as described in Chapter 2. The X-ray spectral fitting technique is described in Section 5.2.5.

5.2.2 *XMM-Newton* Spectra

The *XMM-Newton* data are taken from the survey of W15, with spectral extraction techniques optimized for the complexity of the survey, as described below. Source spectra were extracted using the `SAS` task `evselect` with custom selection expressions for both source and background regions.

The structure of the survey of W15 allows for a source to be detected not only in multiple fields, but also with different combinations of instruments. For this reason, WCS source locations in each camera and field are inspected to determine the image coordinates for source extraction to be used in the selection expression in `evselect`. Background region selections must also be defined for each field and instrument combination. We do so manually using criteria recommended by the *XMM-Newton* Calibration Technical Notes. For the EPIC-MOS instruments, we select a

background region on the same CCD as the source, but in a different location with an equivalent off-axis angle to account for the effects of vignetting. For the EPIC-pn, we choose a background region again on the same CCD with close to an equivalent readout distance on the CCD (the same RAWY value) to account for the fact that different RAWY positions have different response matrices. We determined the optimal background size is double the area of the source region by examining spectra using three differently sized background regions: same extraction area as source, double the area, and ten times the area.

Beyond extraction region coordinates, the `evselect` selection expression requires parameter values such as binning factor (number of spectral bins), energy range (maximum and minimum channels), and pattern keywords for including different photon events. The specifics of the selection expressions vary slightly between the MOS and pn instruments. As suggested by the *XMM-Newton* Calibration Technical Notes, for the EPIC-MOS instruments we use a spectral bin size of 15, spectral channels from 0 to 11999, and the PATTERN keyword set to ≤ 12 to account for single, double, triple, and quadruple photon events. For the EPIC-pn we use a bin size of 5, spectral channels from 0 and 20479, the FLAG==0 keyword to exclude events on the edge of the CCD or bad pixels, and set the PATTERN keyword to ≤ 4 to account for single and double photon events only.

The source and background extraction regions in image coordinates are then fed to `evselect`, and once source and background spectra are extracted, RMFs and ARFs can be generated using the tasks `rmfgen` and `arfgen`. The spectral data products produced from this process are fit simultaneously with the spectra extracted from the *Chandra* data, using the fitting technique described in Section 5.2.5.

5.2.3 Hectospec Spectra

As part of the ChASeM33 survey (T11) follow-up spectroscopy was performed using Hectospec, a fiber-fed spectrograph on the 6.5-m MMT Observatory, for > 100 of the X-ray sources in the T11 catalog down to a limiting magnitude of R ~ 21. The Hectospec follow-up to the X-ray survey was performed by placing the 1.5" diameter Hectospec fibers either on a visible optical counterpart to the X-ray source, or otherwise, if no candidate optical counterpart was observed, on the source of X-ray emission itself.

The spectra were reduced and flux calibrated as part of the ChASeM33 survey. The resulting spectra cover a range from 3700 $\AA$ to 9150 $\AA$ with sufficient spectral resolution to classify sources as either SNRs, foreground stars, massive stars, or background AGN. For the purposes of this chapter, the spectra are used to bolster candidate HMXBs classification via spectral typing of optical counterparts.

Sources in T11 for which there is Hectospec data were broadly classified as either "stellar" type spectra, background galaxies/AGN, foreground stars, SNRs, or H II regions. This first pass classification was conducted on the basis of visual inspection: stellar sources display blue continua, and either narrow absorption lines and/or emission lines, AGN display a relatively flat continua with broad emission lines, foreground stars are typically M and K dwarfs which have red continua, while SNRs and H II regions both display strong emission lines of Hα and [S II].

To further classify sources of type "stellar", we use the `IRAF` routine `FXCOR` to determine spectral types. The `FXCOR` routine cross-correlates spectra against custom input spectral templates and, after Fourier cross correlation, returns a peak cross-correlation strength and radial velocity. These values are used to determine the spectral template that most closely matches the input source spectrum, and thus a most likely spectral type for the source based on the known spectral class of the template star. The spectral standard stars used here for cross-correlation come from Williams et al. (2014a) and are listed in Table 5.1.

5.2.4 Six Band *HST* Photometry

As already demonstrated in Chapter 4, *HST* photometry can be used to broadly classify optical counterpart candidates to X-ray sources using CMDs. With at least two broad-band filters bright, massive star counterparts can be identified on the basis of their very blue colors. With only two filters, however, there is still the chance for false positives, namely sources that photometrically appear to be massive stars, but spectroscopically are found to be background AGN. As spectroscopic follow-up of counterparts for all X-ray sources is prohibitive without a large diameter telescope with multi-object spectrograph, photometric characterization of counterparts still remains the most viable option for securing classifications for the largest number of sources down to the faintest limits.

Photometric coverage over a wider range of broad-band filters than those discussed in Chapter 4

Table 5.1: Spectral standard stars used for cross-correlation with donor star spectra. Column one lists the star name, column two lists the right ascension, column three lists the declination, and the final column notes the spectral type.

Name	RA	Dec	Spectral Type
HD 188001	19:52.4	+18.40	07.5 Iaf
B+60 447	02:11.7	+60:43	O9 Ia
B+61 154	00:43.3	+61:55	O9.5 V
B+57 153	00:49.0	+58.26	B0 V
B+63 33	00:21.8	+64:36	B1 V
B+58 351	02:00.7	+58:59	B1 III
B+61 191	01:14.5	+61:20	B2 IV
VOR+59 97	02:18.9	+59:59	B2 V
VOR+59	02:16.8	+59:46	B3 V
B+57 18	00:10.6	+58:45	B3 IV
B+57 58	00:19.9	+58:35	B5 V
L+60221	02:10.5	+61:07	B5 III
HD 13799	02:16.8	+62:57	B6 III
BSD 285	00:52.6	+59:41	B7 V
B+59 6	00:10.9	+60:26	B8 V

is forthcoming via the M33 *HST* Legacy Survey (PI: Dalcanton), which will consist of 54 fields covering the disk of M33 in six filters, from the UV to the near-IR. As the data for this survey are still being taken and reduced, we briefly introduce the survey here, and discuss the larger range of applications for the data set in Section 5.4.

The M33 Legacy Survey employs an observing strategy very similar to the PHAT survey of M31 (Dalcanton et al., 2012), which covered a third of the disk of M31 in six filters. Like the PHAT survey, the M33 Legacy Survey will consist of WFC3/UVIS imaging in the F275W (central $\lambda = 2750$ $\mathring{A}$) and F336W (central $\lambda = 3375$ $\mathring{A}$) filters, ACS/WFC imaging in F475W (central $\lambda = 4750$ $\mathring{A}$) and F814W (central $\lambda = 8353$ $\mathring{A}$), and WFC3/IR imaging in F110W (central $\lambda = 1.545$ μ) and F160W (central $\lambda = 1.15$ μ). With homogeneous UV to near-IR coverage, color-color diagrams can be constructed for candidate counterparts. These diagnostic diagrams make it possible to separate UV bright sources from those sources that have colors consistent with a flat SED (e.g. QSOs and background AGN), or foreground stars.

Furthermore, the six band photometry can be used to construct and model CMDs, and thus measure formation timescales for HMXBs, and progenitor masses for SNRs using the CMD modeling technique described in Chapter 4. Beyond this, the photometry can also be used to construct

spectral energy distributions (SEDs) for counterparts of interest. A well-tested tool for SED fitting has already been developed for a similar survey in M31 (PHAT Dalcanton et al., 2012): the Bayesian Extinction and Stellar Tool (BEAST) (Gordon et al., 2016). This SED fitting technique can derive stellar effective temperature and surface gravity over a wide range of values. From the effective temperature and surface gravity a further set of characteristics, including line-of-sight extinction, stellar age, and stellar mass can be inferred for the HMXB donor star. The M33 Legacy Survey will cover many of the same sources already discussed in this previous chapter, as well as an additional 50 X-ray sources from T11, bringing the overlapping *HST* coverage of this *Chandra* survey to $\sim$ 50%. Future work will expand upon the work discussed in Chapter 4 and in this chapter with more candidate HMXBs, more homogenous coverage, and better constraints on the spectral characteristics of the donor star population.

5.2.5 X-ray Spectral Fitting Technique

In order to determine the physical parameters of the X-ray emitting sources we use `XSPEC` to simultaneously fit both *XMM-Newton* and *Chandra*. Similar to the X-ray spectral fitting technique described in Chapter 3 for SNRs, we perform a simultaneous fit to the unbinned source and background components with a source model appropriate to the inferred source type (i.e. HMXB) and a background model that accounts for both the sky and instrument background. The efficacy of this method lies in the treatment of the background, which is not subtracted before fitting, thus making use of all available spectral information. We briefly reiterate the components of the background model below (as first described in Chapter 3), and save detailed discussions of individual source models for Section 5.3.

The model for background spectra consists of two components: a sky component as well as a detector, or instrumental component. The sky background is modeled as an absorbed thermal plasma with two components `tbabs*(apec + apec)`, with the absorption value set to $N_H = 5{\times}10^{20}$ cm^{-2}, and the low and high temperature components, normalizations, and overall multiplicative constant allowed to vary. Once fit for, these values are frozen in subsequent source plus background fits, with only the overall multiplicative constant allowed to vary. The EPIC-pn detector component is modeled as multiple Gaussian components (as described in Chapter 3), as well as a broken power-law. The model for the EPIC-MOS detectors has a continuum component (two broken

power-laws), as well as the Gaussian profiles to represent the detector fluorescence lines. The ACIS instrument model is again a series of Gaussians in addition to a power law component. To derive the background model components the detector fluorescence line energies are first fit, with the line widths allowed to vary. Next, the line energies and widths are frozen, and the normalizations are fixed as multiples of a multiplicative constant, one for each detector background model. With the background model determined, the multiplicative constants are the only parameters allowed to vary in subsequent model fits.

The multi-component background model, once fit, is added as a frozen component in the total (source plus background) model. The only free parameters in the total fit are therefore the overall multiplicative constants for the background components, as well as the source components of interest (i.e. photon index for power-law model). As discussed in Chapter 3, this method preserves the Poisson characteristics of the data, as the background is folded into the fit, as opposed to being subtracted prior to fitting. The characteristics of the source models for each individual source will be discussed in Section 5.3 below.

5.3 Results & Discussion

In this section, we describe the results of further characterization of five of the HMXB candidates from Chapter 4 on the basis X-ray and optical spectra, as well as optical color-color diagrams. The discussion includes two sources with no prior X-ray source classification, two sources previously classified by T11 broadly as "stellar", and one source classified by T11 as an XRB. Where possible, we tentatively determine the donor star stellar type on the basis of the optical spectrum. For the sources with six band photometry in *HST* (four), we show preliminary results using color-color diagrams to characterize the most likely donor star counterpart to the HMXBs. We also fit the X-ray spectra for each source using the technique described in Section 5.2.5, and report the parameters recovered from the best-fit models.

5.3.1 Source 013336.04+303332.9: Be-XRB

Source 013336.04+303332.9, first classified as a candidate HMXB in Chapter 4 on the basis of a bright, blue star in the X-ray error circle, had no previous X-ray source classification prior to this work. Below we present the optical and X-ray spectrum, as well as six band colors from *HST* in

support of source classification as a Be-XRB in M33.

The candidate HMXB can be further classified on the basis of the donor star characteristics, determined from both the optical spectrum, as well as the six band photometry from *HST*. Figure 5.1 displays the optical spectrum (two epochs from Hectospec) with insets depicting, from left to right, the three-color X-ray image from *Chandra*, the ground-based narrow-band image from the LGGS, and the *HST* WFPC2 image with X-ray error circle overlaid. There is one optical counterpart, marked by the white arrow, visible with the X-ray error circle. The Hectospec spectrum displays a blue continuum, and the presence of Balmer absorption lines, indicative of an early-type star. This, along with the fact that the source is a hard X-ray point source (left inset in Figure 5.1), further strengthens the source's classification as an HMXB.

Constraints can be placed on the donor star spectral type using the `IRAF` task `FXCOR`. Comparing the spectrum to the template stars listed in Table 5.1 returns a peak cross-correlation strength for donor star spectral type between B3 IV and B5 V. The majority of Be-XRBs have donor stars with slightly earlier spectral types, peaking around B2, (Negueruela, 1998; Negueruela & Coe, 2002), though later donor star spectral types (e.g. B3) are not absent from the population. Given the dependence of `FXCOR` on spectral resolution and choice of standard star spectral template inputs, this donor star spectral type inferred from `FXCOR` is consistent with donor star expected in a Be-XRB.

In addition to the Balmer absorption lines, the spectrum also shows strong Hα emission, which may be stellar in origin, or instead nebular emission from a surrounding star-forming region, or SNR. The ratio of [S II]/Hα in the spectrum suggests the emission originates from an H II region, as opposed to a SNR (Mathewson & Clarke, 1973). The middle inset in Figure 5.1 shows narrow-band imaging from the LGGS in Hα, [S II], [O III] in the vicinity of the source, which appears roughly consistent with the background. It is therefore possible that the Hα in the spectrum is a stellar feature, possibly originating from a circumstellar disk, however, Hα coupled with the other emission features in the spectrum (i.e. [O III] and [S II]) is more likely to originate from a surrounding star forming nebula.

The optical and IR color-color diagrams of the donor star counterpart from the *HST* six band photometry are shown in Figures 5.2–5.3. In both diagrams, the optical counterpart falls outside the region expected for background AGN, and foreground stars. The candidate donor star, however,

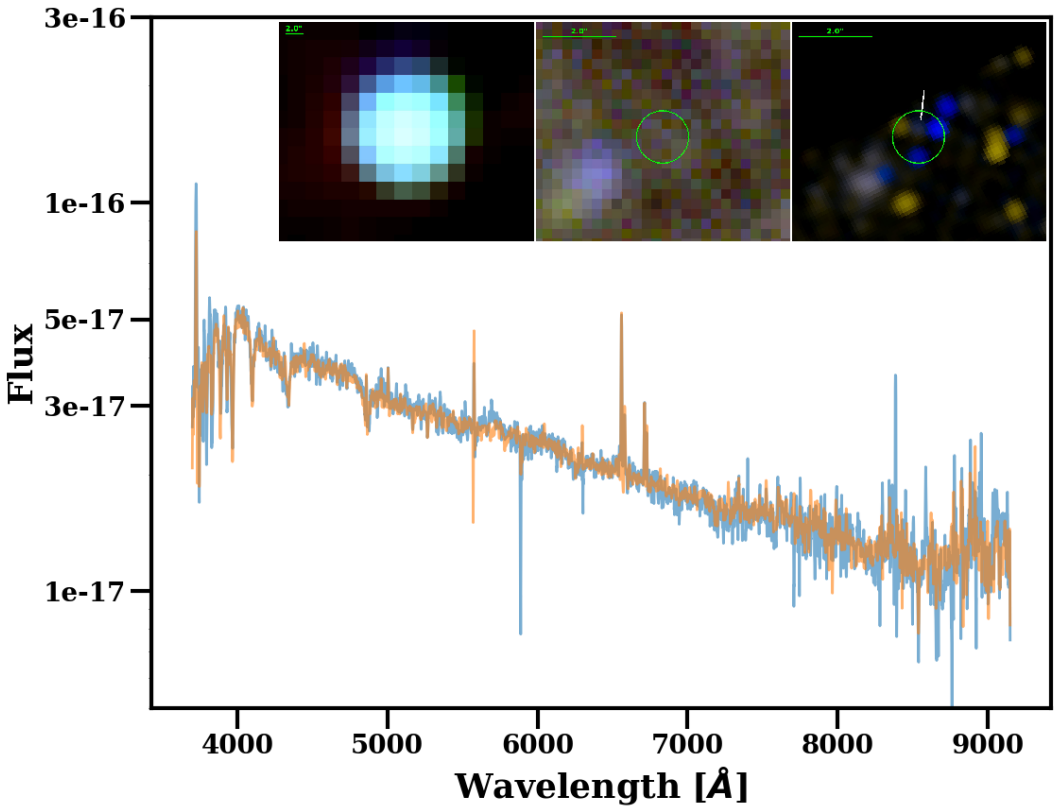

Figure 5.1: Hectospec spectrum (two epochs) for source 013336.04+303332.9 from T11. The spectrum shows strong Hα emission, as well as Hβ and Hγ absorption. *Left inset*: *Chandra* three-color image of the X-ray source (26" × 22"), indicative of hard X-ray emission. Red is 0.35–1.0 keV (soft band), green is 1.0–2.0 keV (medium band), and blue is 2.0–8.0 keV (hard band). *Middle inset*: LGGS three narrow-band color image (7" × 6") at the location of the X-ray source (X-ray error circle in green). Red is Hα, green is [S II], and blue is [O III]. The narrow band emission at the location of the source is consistent with the background. *Right inset*: *HST* WFPC2 three color imaging at the location of the X-ray source (7" × 6"). The X-ray error circle is in green, with the location of the candidate donor star indicated by the white arrow. Blue is F336W, green is F439W, and red is a combination of F336W and F439W.

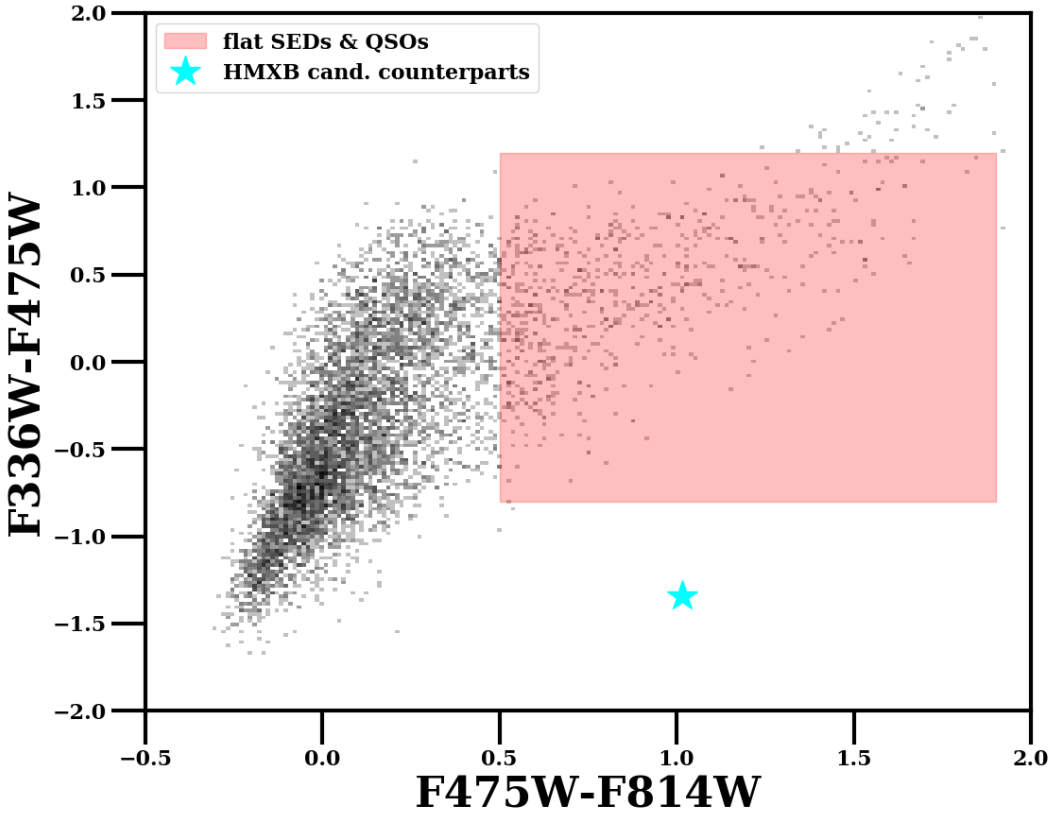

Figure 5.2: Color-color plot from *HST* photometry in F336W, F475W, and F814W. The candidate counterpart to source 013336.04+303332.9 is marked with a cyan star. The region likely to host sources with flat SEDs (i.e. QSOs, AGN) is highlighted in red.

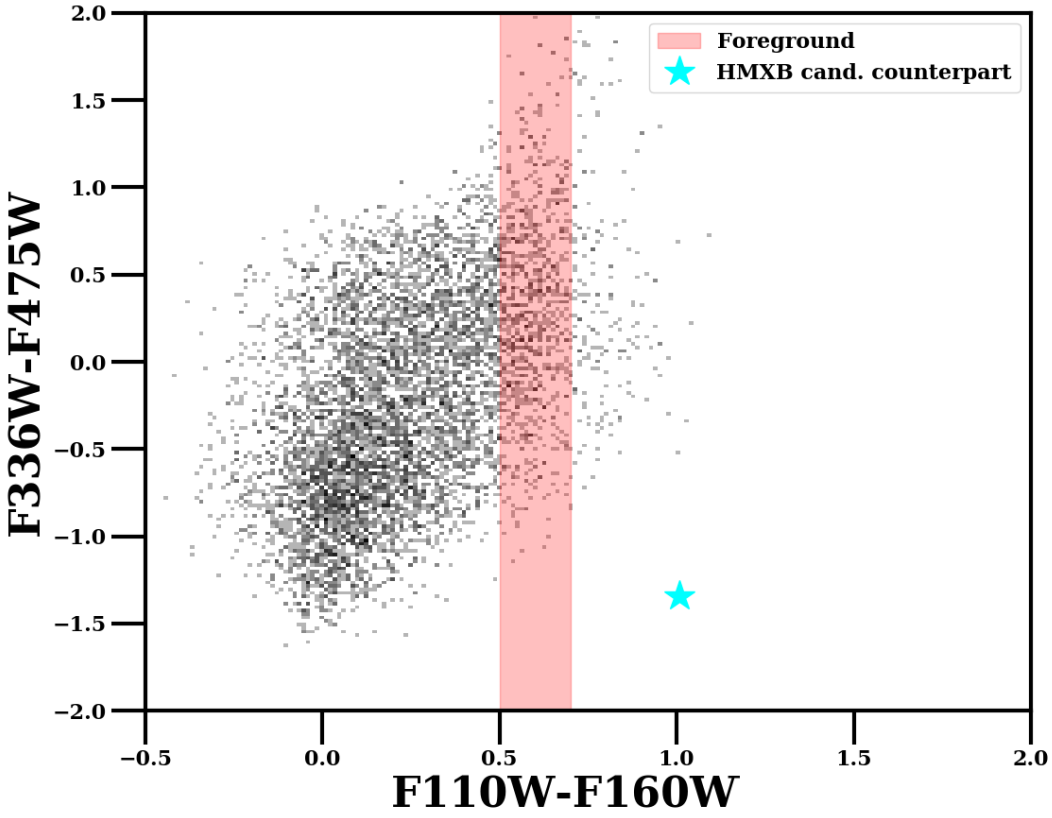

Figure 5.3: Color-color plot from *HST* photometry in F336W, F475W, F110W, and F160W. The candidate counterpart to source 013336.04+303332.9 is marked with a cyan star. The region denoting likely foreground sources is highlighted in red.

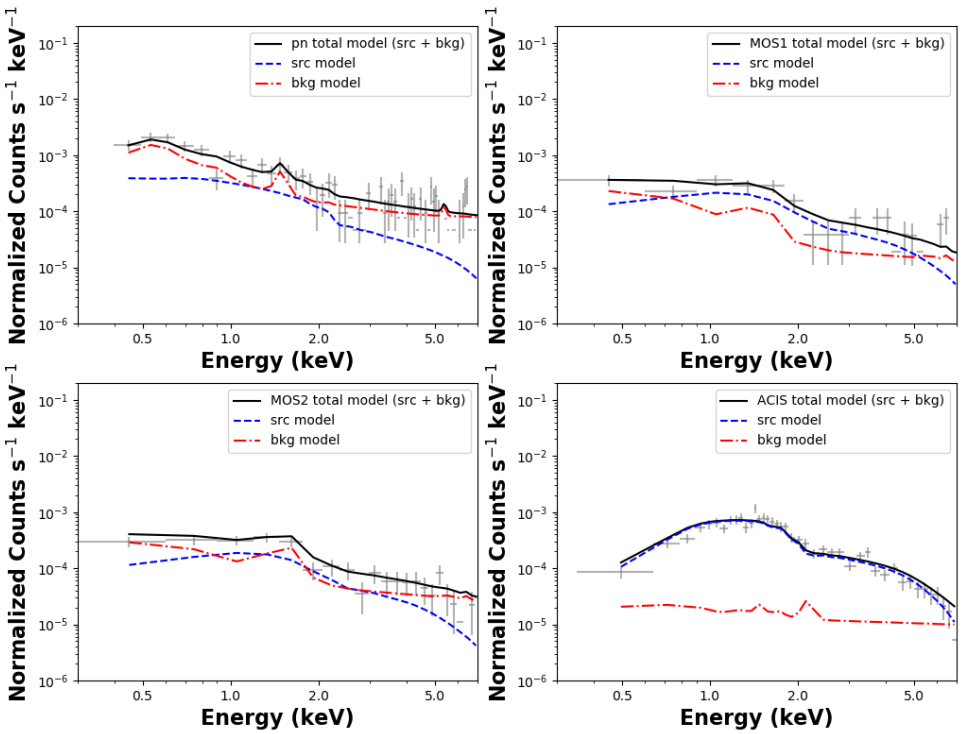

Figure 5.4: *Top-Left*: The source plus background model fit is in black, with the absorbed power-law source model component in blue, and the total background model in red for the PN camera. Source counts and associated errors from the PN camera are in grey. *Top-Right*: Same as the top-right, but for the MOS1 camera. *Bottom-left*: Same as top-right but for the MOS2 camera. *Bottom-right*: Same as top-right but for the ACIS camera on *Chandra*.

is distinct from the main sequence in the optical color-color diagram, as it is redder than expected and also somewhat UV bright. Likewise, it shows a IR excess in the IR color-color diagram. These distinct colors may be explained by the nature of the donor star. An IR excess is expected from the circumstellar disk around a Be star due to continuum free-free emission (Gehrz et al., 1974). Likewise, detection of a UV bright counterpart is expected, as massive donor stars are strong emitters at UV wavelengths, and X-ray radiation from accretion onto the compact object may be absorbed by the accretion disk itself and reprocessed into UV emission as well. Thus, in this case, the near-IR to UV colors support classification as a Be-XRB.

The X-ray spectrum can strengthen the source classification through characterization of the source of the X-ray emission. The X-ray spectrum and best-fit model for this source are shown

in Figure 5.4. The background was fit as described in Section 5.2.5, with the source spectrum modeled as an absorbed power-law (`tbabs*powerlaw`). The model with the absorption component fixed to the Galactic value in the direction of M33 (6×10^{20} cm^{-2}; Stark et al., 1992) provided a better fit, so the only source components allowed to vary in the total fit were the power-law photon index and normalization. The best fit power-law photon index is $1.51^{+0.09}_{-0.09}$, with a normalization $K = 2.11 \times 10^{-6}$ photons/keV/cm^2/s. The power-law photon index is consistent with the source being an XRB, which typically have hard spectra with photon indices between 1.3–2.0 (e.g. Madau & Efstathiou, 1999; Mirabel et al., 2011). Based on the spectral characteristics, the colors from *HST*, and the inferred formation timescale for this source ($\sim$ 20–50 Myr) from Chapter 4, this source is likely a Be-XRB.

5.3.2 Source 013339.46+302140.8: Background AGN?

Source 013339.46+302140.8 was first classified as a candidate HMXB in Chapter 4, with no prior classification in T11. We present further characterization of this source based on its unusual optical spectrum, as well as X-ray spectra from *Chandra* and *XMM-Newton*.

In the absence of six band photometry from *HST* to determine the colors and SED for the optical counterparts to the X-ray source, the optical spectrum from Hectospec provides the best avenue for refining source classification. Figure 5.5 shows the Hectospec spectrum, with insets, from left to right, the non-continuum subtracted narrow-band ground-based image from the LGGS, and the *HST* image with X-ray error circle overlaid for reference. The non-continuum subtracted narrow-band image and the *HST* inset reveal two candidate counterparts to the X-ray source visible on the edge of the X-ray error circle.

The counterpart spectrum shown in Figure 5.5 is dominated by emission features, including Hβ, [O III], Hα, and [S II]. In addition, there are broad, unidentified emission features near $\sim$ 4806 $\mathring{A}$, and $\sim$ 7480 $\mathring{A}$, the latter of which varies in strength between epochs. Such broad emission features may be indicative of a background AGN, however it is unusual for a background AGN to display these broad features coupled with narrow emission lines like Hα, as is seen in this spectrum. If the source is a background AGN, the ratio of the observed wavelengths of the broad emission features can be compared to ratios for commonly observed AGN emission lines to estimate a possible redshift. We find that the broad features seen in this spectrum can be described as AGN

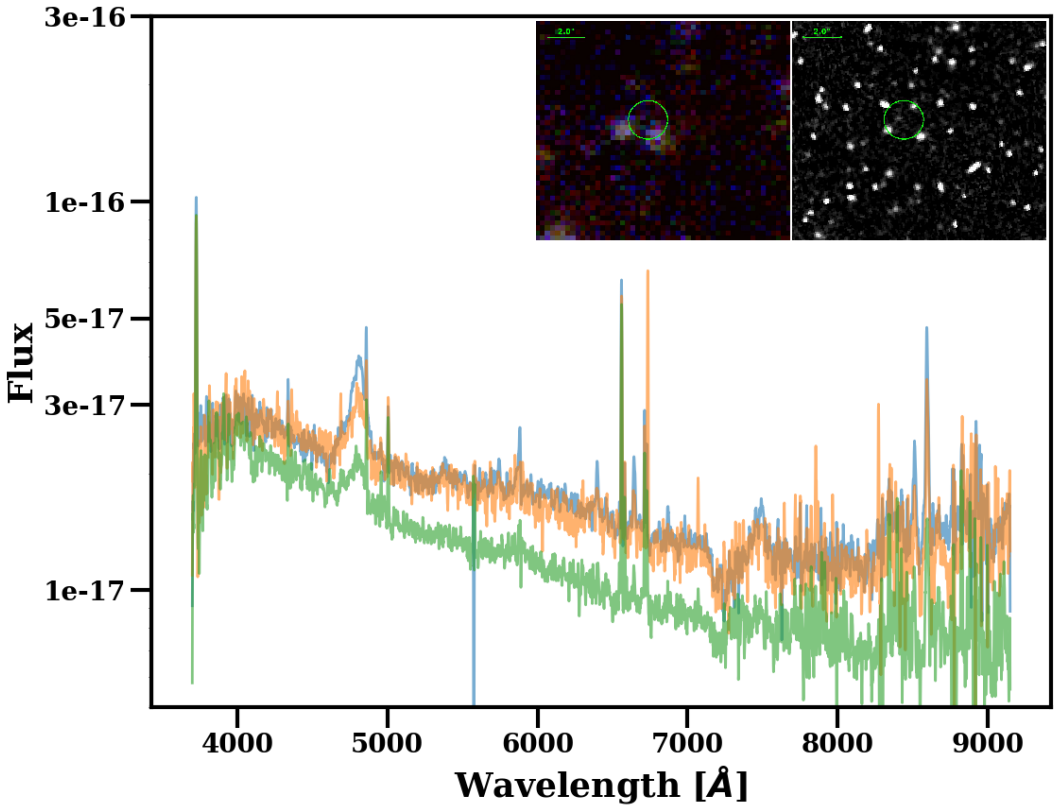

Figure 5.5: Hectospec spectrum (two epochs) for source 013339.46+302140.8 from T11. Emission lines of Hβ (λ 4861), [O III] (λ 5003), Hα, and [S II] ($\lambda\lambda$ 6711,26), as well as several broad emission lines are visible. *Left inset*: LGGS three narrow-band color image (13" $\times$ 11") at the location of the X-ray source (X-ray error circle in green). Red is Hα, green is [S II], and blue is [O III]. The narrow band emission is indicative to two point sources on the edge of the X-ray error circle, visible in [O III]. *Right Inset*: *HST* WFPC2 F439W image (13" $\times$ 11") at the location of the X-ray source. The x-ray error circle is in green, with two bright candidate counterparts on the edge of the error circle.

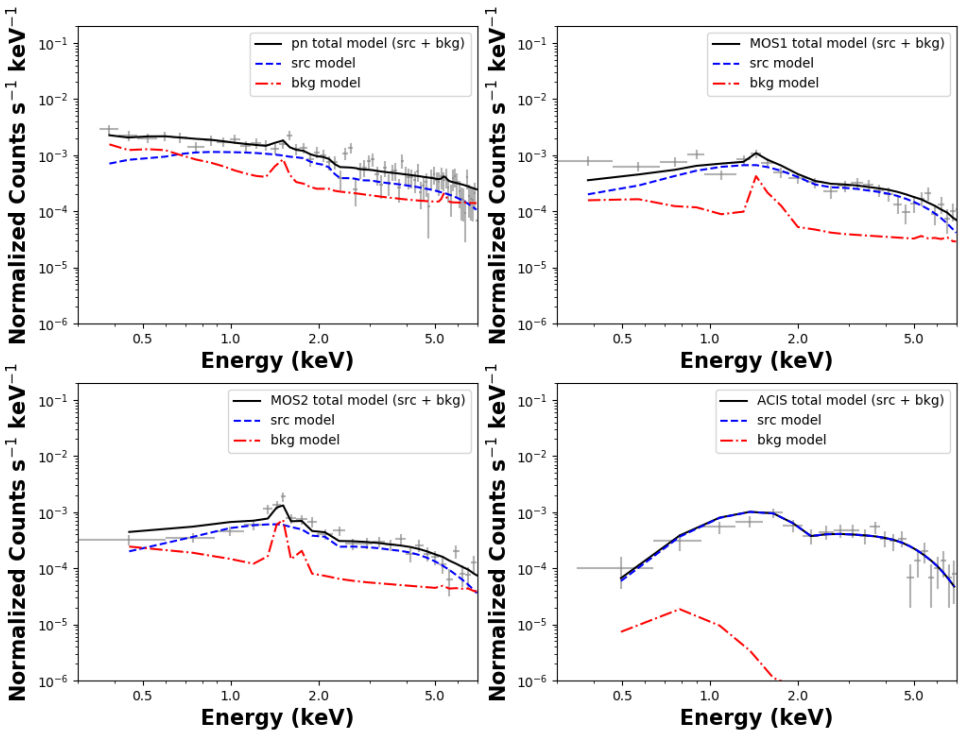

Figure 5.6: *Top-Left*: Total model fit (source plus background) in black, with the absorbed power-law source model component in blue, and the total background model in red for the PN camera. Source counts and associated errors from the PN camera are in grey. *Top-Right*: Same as the top-right, but for the MOS1 camera. *Bottom-left*: Same as top-right but for the MOS2 camera. *Bottom-right*: Same as top-right but for the ACIS camera on *Chandra*.

emission lines Mg II and Hγ at z $\sim$ 0.72.

We also determine the position of the source in the BPT diagram to further check for evidence of a background AGN (Baldwin et al., 1981). To correct for reddening we assume a Milky Way-like extinction curve (Cardelli et al., 1989), and case B recombination at T = 10^4 K and $n_e = 10^4$ cm^{-3} (Baker & Menzel, 1938; Seaton, 1959; Dopita & Sutherland, 2003). After correcting for reddening, we measure the line ratios of [N II] λ6538/Hα λ6563 and [O III] λ5007/Hβ λ4861 and find that the source falls within the star-forming, or H II region of the BPT diagram (Kewley et al., 2001). Thus, the spectral features sensitive to ionization state are not indicative of a background AGN, in contrast to the broad emission features described above. It is possible the emission features are misattributed, and instead originate from a source intrinsic to M33 with heavily broadened and

blueshifted Hβ. It is also possible that the source spectrum is a composite of different sources, one a background AGN, and the other a contaminant intrinsic to M33.

The X-ray spectrum itself may provide further clues, though both HMXBs and background AGN have similarly hard, power-law spectra. The X-ray spectrum and associated best-fit model for this source are shown in Figure 5.6. The background was fit as described in Section 5.2.5, with the source spectrum modeled as an absorbed power-law (`tbabs*powerlaw`). Again, we allowed only the power-law photon index and normalization to vary. The best fit power-law photon index is $0.81^{+0.10}_{-0.06}$ with a normalization $K = 2.85 \times 10^{-5}$ photons/keV/cm^2/s. This photon index is somewhat lower than the range of spectral indices expected of either XRBs or AGN, adding to the ambiguity of the source. With the uncertain origins of the broad and narrow spectral features, and the ambiguity of the X-ray spectrum, this source remains without a secure classification, but may be a background AGN as opposed to an HMXB. Further spectroscopic follow-up that isolates the more likely optical counterpart, as well as the SED from *HST* six band photometry for this counterpart will help further illuminate the nature of the source.

5.3.3 Source 013356.82+303706.7: Candidate Be-XRB

This source was previously classified as an XRB in T11, as well as in Chapter 4, with a candidate donor star counterpart notably redder than the main sequence. Below, we discuss its spectral characteristics, both optical and X-ray, as well as its optical to UV colors in *HST*.

The optical source spectrum is displayed in Figure 5.7 with insets, from left to right, the three-color X-ray image, the ground-based narrow-band imaging, and the *HST* WFPC2 imaging. The two epochs of data from Hectospec show Balmer series absorption lines, as well as strong Hα emission. The peak cross-correlation strength from `FXCOR` returns spectral type B6 III. This stellar type is later than expected for a Be-XRB donor star, which typically have observed spectral types that peak from B0-B2.

The Hα emission may again in this case be due to a surrounding star-forming nebula, or otherwise originate from the equatorial disk of the donor star itself in the case of a Be star. There does not appear to be any considerable enhancement of Hα in the narrow-band ground-based imaging, which points to a stellar origin being more likely for the Hα emission in this case of this source. As can be seen in the *HST* imaging in the right-hand inset, the candidate

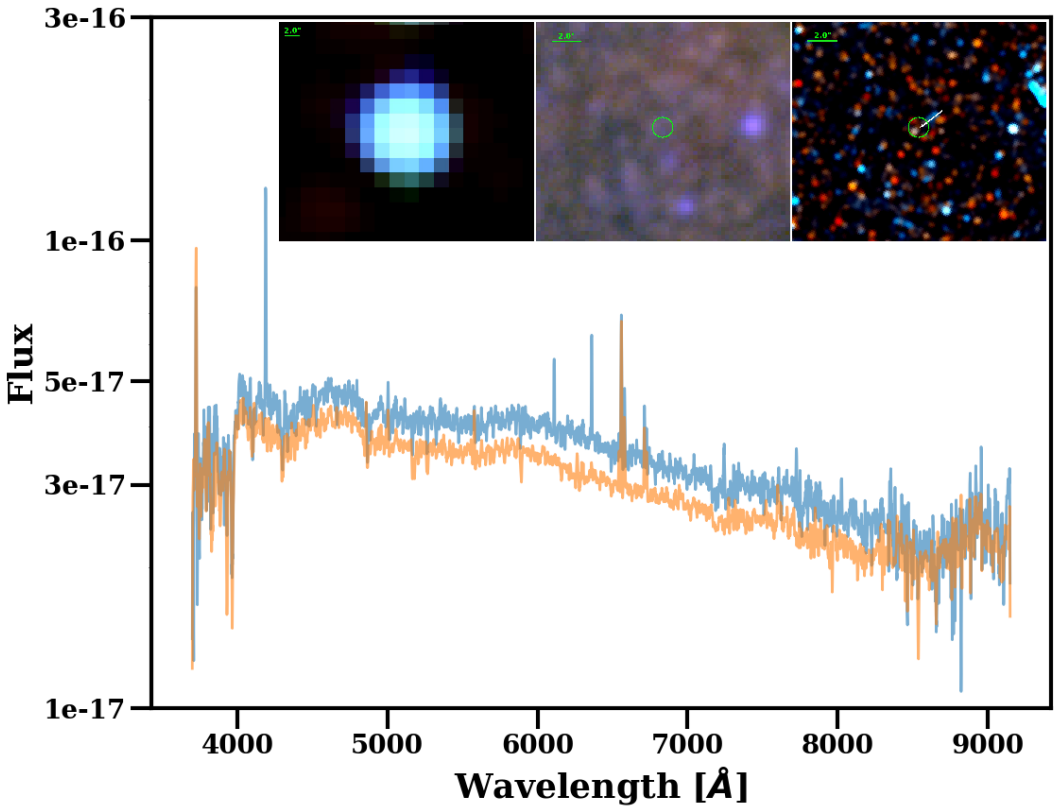

Figure 5.7: Hectospec spectrum (two epochs) for source 013356.82+303706.7 from T11. The spectrum displays weak absorption lines of Hβ and Hγ. as well as Hα emission. *Left inset*: *Chandra* three-color image (26" × 22") of the X-ray source, indicative of hard X-ray emission. Red is 0.35–1.0 keV (soft band), green is 1.0–2.0 keV (medium band), and blue is 2.0–8.0 keV (hard band). *Middle inset*: LGGS three narrow-band color image (13" × 11") at the location of the X-ray source (X-ray error circle in green). Red is Hα, green is [S II], and blue is [O III]. *Right inset*: *HST* WFPC2 three color imaging at the location of the X-ray source (13" × 11"). The X-ray error circle is in green, with the location of the candidate donor star indicated by the white arrow. Red is F814W, green is F555W, and blue is a combination of F555W and F814W.

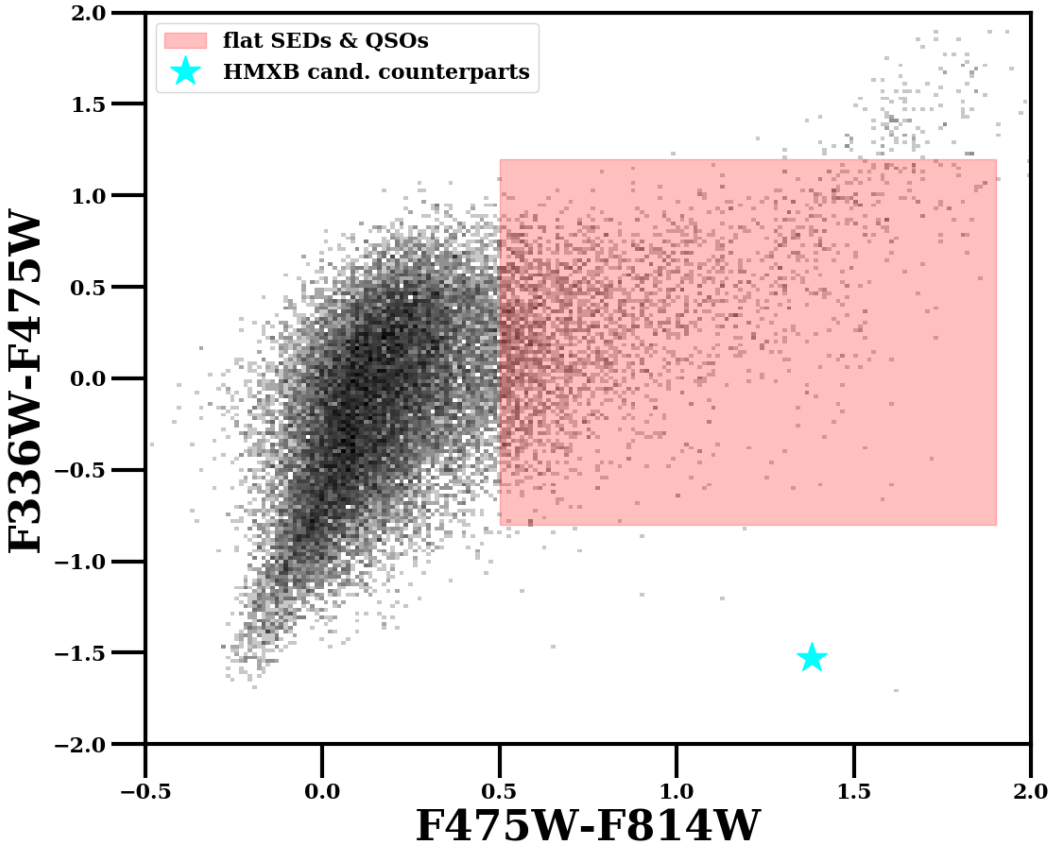

Figure 5.8: Color-color plot from *HST* photometry in F336W, F475W, and F814W. The counterpart to source 013356.82+303706.7 (cyan star) shows up as a distinctly UV bright source, with a red color excess in the bottom-right corner of the plot. The region likely to host sources with flat SEDs (i.e. QSOs, AGN) is highlighted in red.

donor star counterpart, marked with the white arrow, is considerably redder than expected from a young, massive main-sequence star. This is corroborated by the color-color diagram displayed in Figure 5.8, where the candidate donor star (cyan star) shows up as a UV-bright source that is redder than the main sequence. These colors may be indicative of an early-type star (UV bright), with a circumstellar gas disk (red excess), such as is seen in the case of Be stars. The donor star counterpart is not, however, recovered in the IR bands in the *HST* photometry.

As for the sources discussed above, we show the X-ray spectrum and best-fit model in Figure 5.9. As before, we fit the source spectrum with an absorbed power-law model (`tbabs*powerlaw`), where the absorption component is fixed to the Galactic value in the direction of M33 (6×10^{20} cm^{-2}; Stark et al., 1992). With the normalization and spectral index allowed to vary, we find best fit

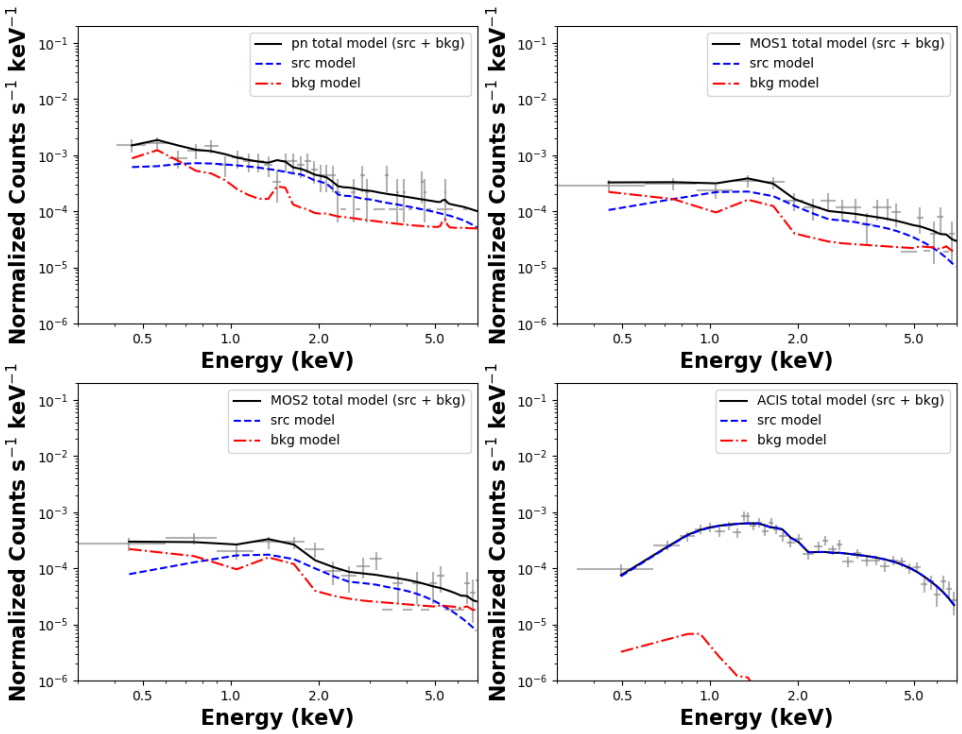

Figure 5.9: *Top-Left*: Total model fit (source plus background) in black, with the absorbed power-law source model component in blue, and the total background model in red for the PN camera. Source counts and associated errors from the PN camera are in grey. *Top-Right*: Same as the top-right, but for the MOS1 camera. *Bottom-left*: Same as top-right but for the MOS2 camera. *Bottom-right*: Same as top-right but for the ACIS camera on *Chandra*.

values of $K = 1.45 \times 10^{-7}$ photons/keV/cm^2/s, and $1.15^{+0.09}_{-0.08}$, respectively. The spectral index is consistent with values expected for hard sources like XRBs.

Based on the X-ray and optical spectrum and donor star photometry, we classify this source as a candidate Be-XRB. There is some uncertainty in the classification given that the donor star spectral type derived from `FXCOR` is later than expected. The age, or formation timescale, measured for this source in Chapter 4 is consistent with this analysis, as it suggests the HMXB formed 10–20 Myr post-starburst. Follow-up spectroscopy, and SED fitting will help determine the donor star spectral type more reliably and provide a more straightforward classification.

5.3.4 Source 013417.08+303426.6: HMXB

Source 013417.08+303426.6 was identified broadly as "stellar" in T11, and as an HMXB candidate in Chapter 4 based on the presence of a bright candidate donor star within the X-ray error circle. Below we describe further source classification on the basis of optical and X-ray spectra, as well as *HST* photometry.

The ground-based optical spectrum, as well as three-color *Chandra* image, ground-based narrow-band imaging, and *HST* photometry is shown in Figure 5.10. The spectrum shows strong emission lines of [O III], Hα, as well as [S II], of which [S II] also shows an underlying broad component. Weak Balmer absorption lines are also visible on the blue end of the spectrum. Cross-correlation with the spectral standard templates with `FXCOR` yields a peak cross-correlation strength for stellar type O9.5 V. The early stellar type is consistent with a massive donor star counterpart to the hard X-ray point source seen in the left inset of Figure 5.10, making this source very likely to be an HMXB. Two bright point sources are visible within the X-ray error circle in the *HST* WFPC2 image in the right inset, and a blend of these sources is visible in the non-continuum subtracted narrow-band imaging in the middle inset.

The *HST* photometry can provide further clues as to the most likely donor star counterpart among the sources within the X-ray error circle. To this end, we show the optical and IR color-color diagrams for the *HST* sources in the vicinity of the X-ray source in Figures 5.11–5.12. Both of the sources visible in the WFPC image are present on the optical color-color diagram as very blue, UV bright sources, making either just as likely to be the donor star. In addition, there is one source within the error circle that falls within the AGN/QSO region of the color-color diagram, though the optical spectrum makes this very unlikely to be the counterpart. On the IR color-color diagram, both stars are relatively unremarkable compared to the main sequence, and neither stands out as a more likely donor counterpart. In this case, it is not possible to determine a unique counterpart within the alignment errors.

We fit the combined *XMM-Newton* and *Chandra* spectrum of the source with two different models using the technique described in Section 5.2.5. For the first model, we use an absorbed power-law (`tbabs*powerlaw`), and for the second we try an absorbed accretion disk model (`tbabs*diskbb`). In both cases, we allow the `tbabs` component (Wilms et al., 2000) to vary as there may be both Galactic absorption in the direction of M33 ($\sim 6 \times 10^{20}$ cm^{-2}; Stark et al., 1992), as well as

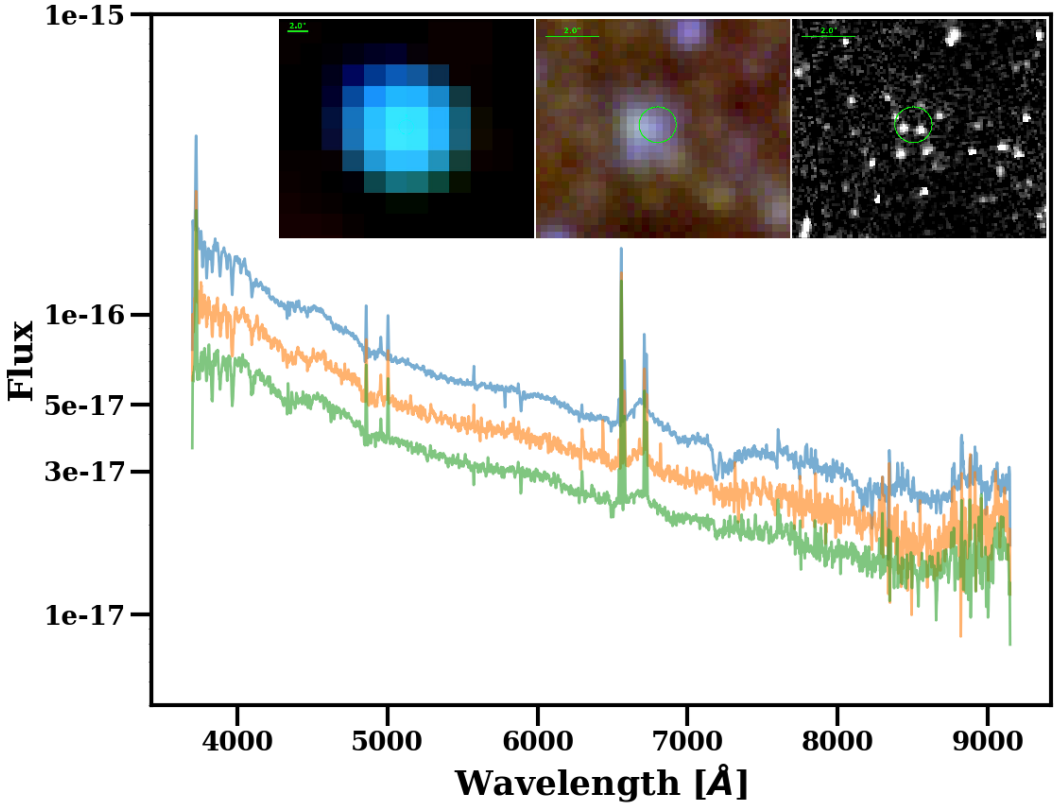

Figure 5.10: Hectospec spectrum (three epochs) for source 013417.08+303426.6 from T11. The spectrum shows strong Hα and [S II] emission lines, as well as emission in [O III] and Balmer absorption lines. *Left inset*: *Chandra* three-color image (26" × 22") of the X-ray source, indicative of hard X-ray emission. Red is 0.35–1.0 keV (soft band), green is 1.0–2.0 keV (medium band), and blue is 2.0–8.0 keV (hard band). *Middle inset*: LGGS three narrow-band color image (10" × 8") at the location of the X-ray source (X-ray error circle in green). Red is Hα, green is [S II], and blue is [O III]. The narrow band imaging shows emission in [S II] and [O III] at the location of the source. *Right inset*: *HST* WFPC2 F439W imaging at the location of the X-ray source (10" × 8"). The X-ray error circle is in green, with two bright candidate counterparts visible within the X-ray error circle.

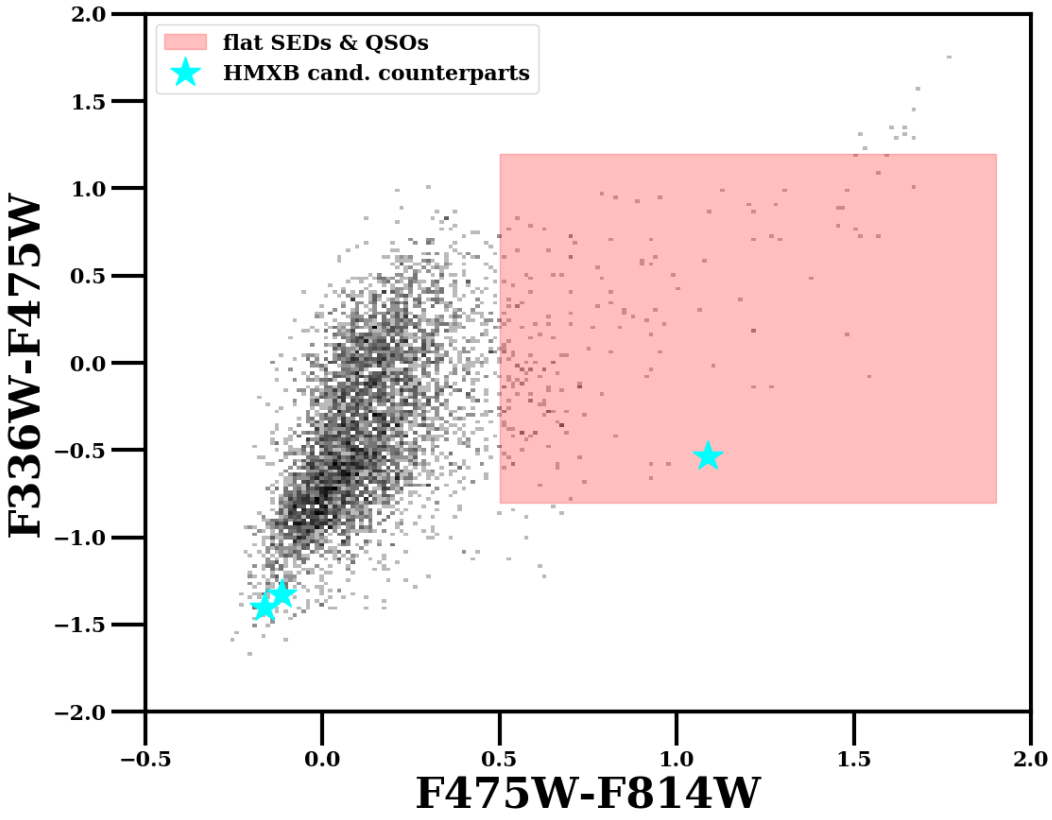

Figure 5.11: Color-color plot from *HST* photometry in F336W, F475W, and F814W. The candidate counterparts within the X-ray error circle of source 013417.08+303426.6 are marked with cyan stars. The region likely to host sources with flat SEDs (i.e. QSOs, AGN) is highlighted in red.

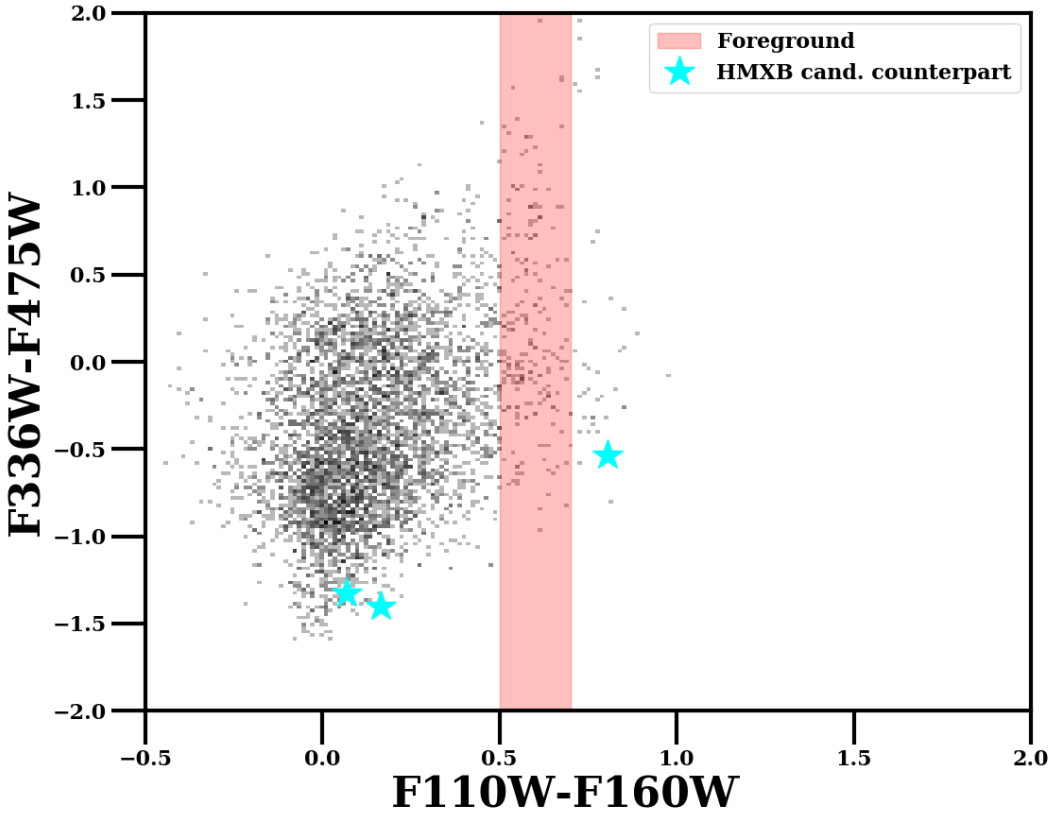

Figure 5.12: Color-color plot from *HST* photometry in F336W, F475W, F110W, and F160W. The candidate counterparts within the X-ray error circle of source 013417.08+303426.6 are marked with cyan stars. The region denoting likely foreground sources is highlighted in red.

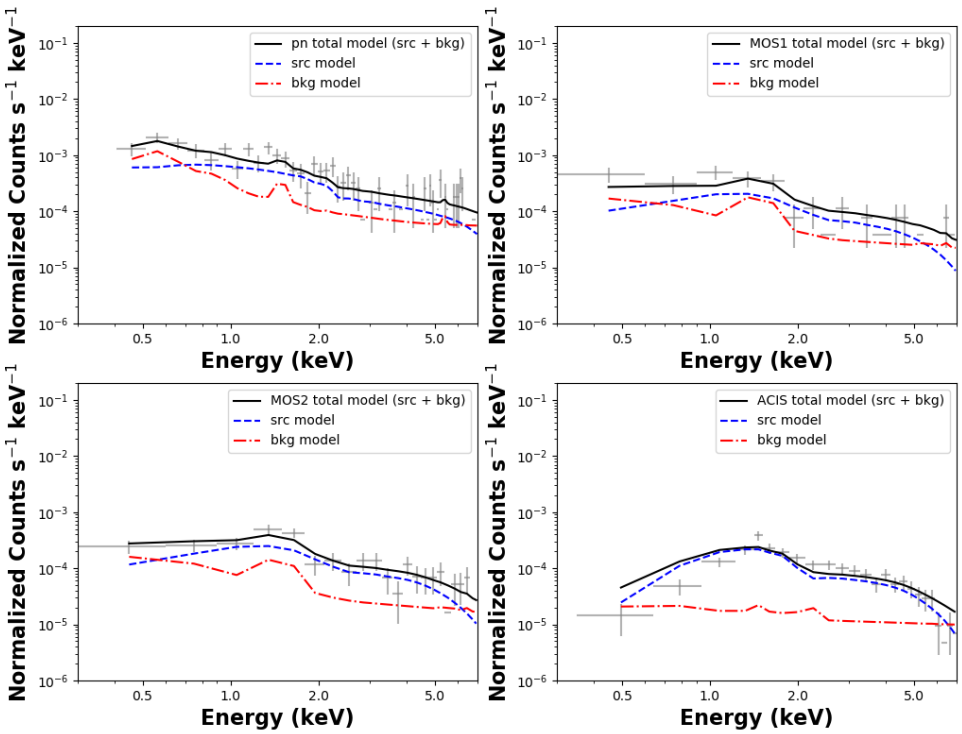

Figure 5.13: *Top-Left*: Total model (source plus background) fit in black, with the absorbed disk blackbody source model in blue, and the total background model in red for the PN camera. Source counts and associated errors from the PN camera are in grey. *Top-Right*: Same as the top-right, but for the MOS1 camera. *Bottom-left*: Same as top-right but for the MOS2 camera. *Bottom-right*: Same as top-right but for the ACIS camera on *Chandra*.

absorption intrinsic to the source. In the case of the power-law model we find that leaving the absorption parameter free gives a bad fit, so for this model we freeze the parameter to the Galactic value. The only free source parameters are thus an overall multiplicative constant, a normalization, and the power-law photon index (power-law model), or accretion disk temperature (disk blackbody model). The multiplicative constants for the background model components were also allowed to vary in the overall fit.

We find that both models produce similar fits to the data (reduced $\chi^2 \sim 2.1$), though the disk black body model allows for a better constraint on the absorption. The absorbed disk blackbody model is shown in Figure 5.13 for all four cameras (PN, MOS1, MOS2, and ACIS), with the total model fit in black, and the individual source and background components in blue and red,

respectively. The disk blackbody model returns an accretion disk temperature of $2.16^{+0.34}_{-0.42}$ keV. The normalization (K) of the disk blackbody model is related to the inner disk radius, with $K = (R_{in}/D_{10})^2 cos\theta$, where R_{in} is the inner disk radius, D_{10} is the distance to the source in units of 10 kpc, and θ is the angle of the disk. The normalization from the fit yields $R_{in}\cos\theta^{1/2} \sim 7$ km. The best-fit for the absorbed power-law model returns a photon index of $1.11^{+0.11}_{-0.12}$. Both are compatible with the source being an HMXB.

Based on the above spectra and optical counterpart colors, the source is a very likely HMXB. Though the nature of the compact object remains uncertain, the donor star is most likely a late-type O star, or early B star. The formation timescale, or age, measured for the source from Chapter 4 is ~ 20 Myr, which corresponds to a progenitor mass of ~ 11 $M_\odot$ for the compact object, roughly consistent with the inferred donor star type, assuming similar mass binary components.

5.3.5 Source 013432.60+304704.1: Colliding Wind Binary

The X-ray source 013432.60+304704.1 was observed as part of the ChASeM33 survey (T11), but was not given a source classification as part of that catalog. The source resides in NGC 604, the giant H II region in M33, and though this region itself has been studied in detail (Tüllmann et al., 2008), the point source itself has not been studied in depth. In Chapter 4, we first catalogued the source as a very young (< 5 Myr) candidate HMXB. Below we describe an updated classification for this source on the basis of its multiwavelength properties.

As part of the ChASeM33 survey, follow-up spectroscopy was taken of the counterpart(s) to source 013432.60+304704.1. The optical spectrum is shown in Figure 5.14, with insets depicting, from left to right, the three-color *Chandra* image, the ground-based narrow-band imaging from the LGGS, and the *HST* WFPC2 image of the counterparts with X-ray error circle overlaid. Given the presence of broad C III λ4650 and C IV λ5806 emission lines in the spectrum, the counterpart to the X-ray source appears to be a WC4 star. However, the *HST* data discussed in Chapter 4, reveal the presence of three bright potential counterparts within the X-ray error circle (~ 0.7" radius). All three potential counterparts to the X-ray source fall within the Hectospec fiber (1.5" diameter) that produced the spectrum in Figure 5.14, thus the total WC-like spectrum is a composite of all three sources.

Analysis of the massive star population in the vicinity of the X-ray source is needed to further

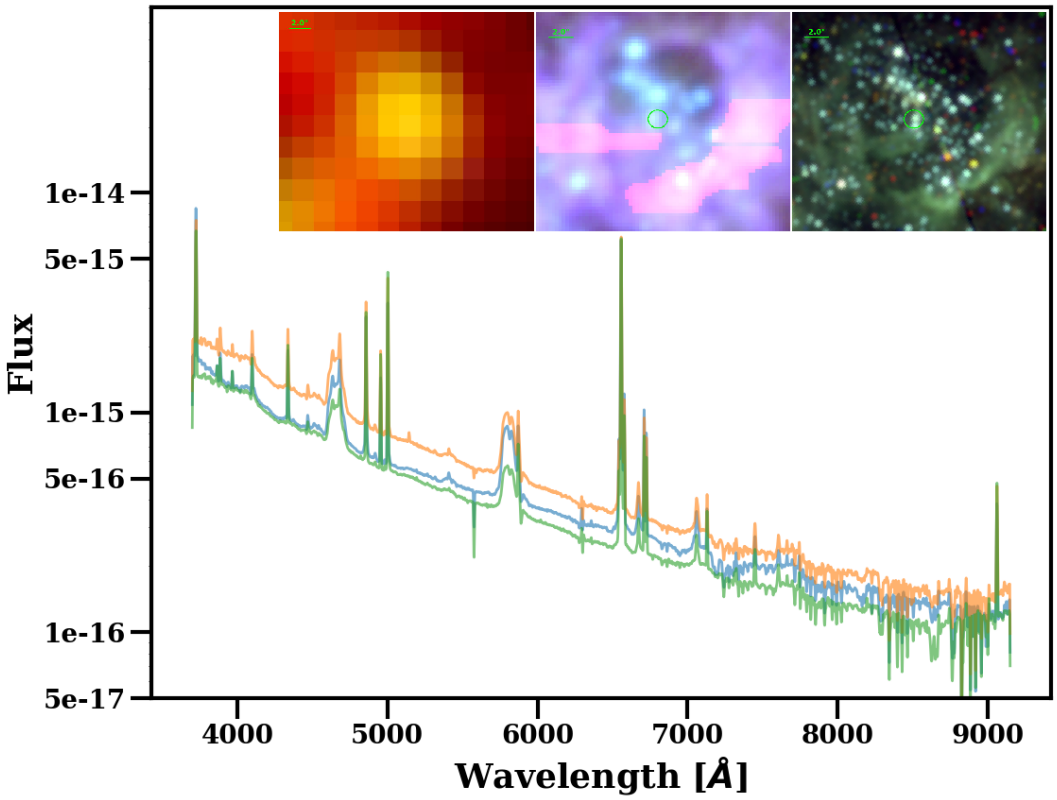

Figure 5.14: Hectospec spectrum of the optical counterparts associated with the X-ray point source in NGC 604 in M33. The broad C III λ4650 and C IV λ5806 lines are indicative of a WC star. The Hectospec fiber contains three distinct point sources, and it is unclear which of the brightest point sources dominates this spectrum. *Left inset*: *Chandra* three-color image (26" × 22") of the X-ray source, indicative of X-ray emission in the soft and medium bands. Red is 0.35–1.0 keV (soft band), green is 1.0–2.0 keV (medium band), and blue is 2.0–8.0 keV (hard band). *Middle inset*: LGGS three narrow-band color image (20" × 20") at the location of the X-ray source (X-ray error circle in green). Red is Hα, green is [S II], and blue is [O III]. *Right inset*: *HST* WFPC2 three color imaging at the location of the X-ray source (20" × 20"). The X-ray error circle is in green, with several bright candidate counterparts visible within the X-ray error circle. Red is F814W, green is F555W, and blue is a combination of F555W and F814W.

probe the nature of the source. Several of the optical sources in this region of NGC 604 have been previously classified as massive stars. One of the bright counterparts in the X-ray error circle was identified as a WN10 type star by Drissen et al. (2008) (star N604-WR12 in their catalog). Furthermore, Bruhweiler et al. (2003) published *HST* STIS spectroscopy of stars in the vicinity of the X-ray source, with classifications of type O5 III and B0 Ib (stars 690A and 690B, respectively in their catalog). The presence of so many massive stars in close proximity to this X-ray point source suggests two possibilities for the source of X-ray emission, which we enumerate below.

One possibility is this source belongs to a rarely observed subclass of HMXBs: WR-XRBs, or compact objects accreting from the strong, fast winds of a WR star. Compact object masses of $\sim$ 20–30 $M_{\odot}$, indicative of black holes have been determined for several WR-XRBs from radial velocity variations measured from the WR spectra (Silverman & Filippenko, 2008; Crowther et al., 2010), and X-ray spectra show that these are hard sources (Maccarone et al., 2014). The Hectospec spectrum for source 013432.60+304704.1 suggests the presence of a WR star within the X-ray error circle, however, the *Chandra* colors denote a relatively soft source. It should be noted, however, the contamination of soft thermal emission from the surrounding nebula may complicate analysis of the point source using the present observations.

Another possibility is that the source contains no compact object at all, but is instead X-ray emission from a massive star or pair of massive stars. The first O star observed as a source of X-ray emission was by Seward et al. (1979); Harnden et al. (1979) with *Einstein*. In the Galaxy and MCs X-ray emitting stars have now been observed to fall largely into three categories: X-ray emission from shocks in stellar winds, X-ray emission from wind-blown bubbles around hot stars, and X-ray emission from wind-wind collisions in massive binaries, so-called colliding wind binaries. Compared to HMXBs, these sources are relatively soft X-ray sources, and are typically relatively faint ($L_x < 10^{35}$ erg s^{-1}). No colliding wind binaries have been observed beyond the MCs to-date, however, the brightest colliding wind binaries in the MCs ($L_x \sim 10^{35}$ erg s^{-1}; Guerrero & Chu, 2008) are similar in luminosity to source 013432.60+304704.1 discussed here.

The X-ray spectrum provides a way to discriminate between the two above possibilities, as WR-XRBs and colliding wind binaries should be hard and soft sources, respectively. However, because the source is located in NGC 604 there is a large chance of confusion and contamination from the surrounding nebula, which may itself be a source of soft X-ray emission due to the presence of

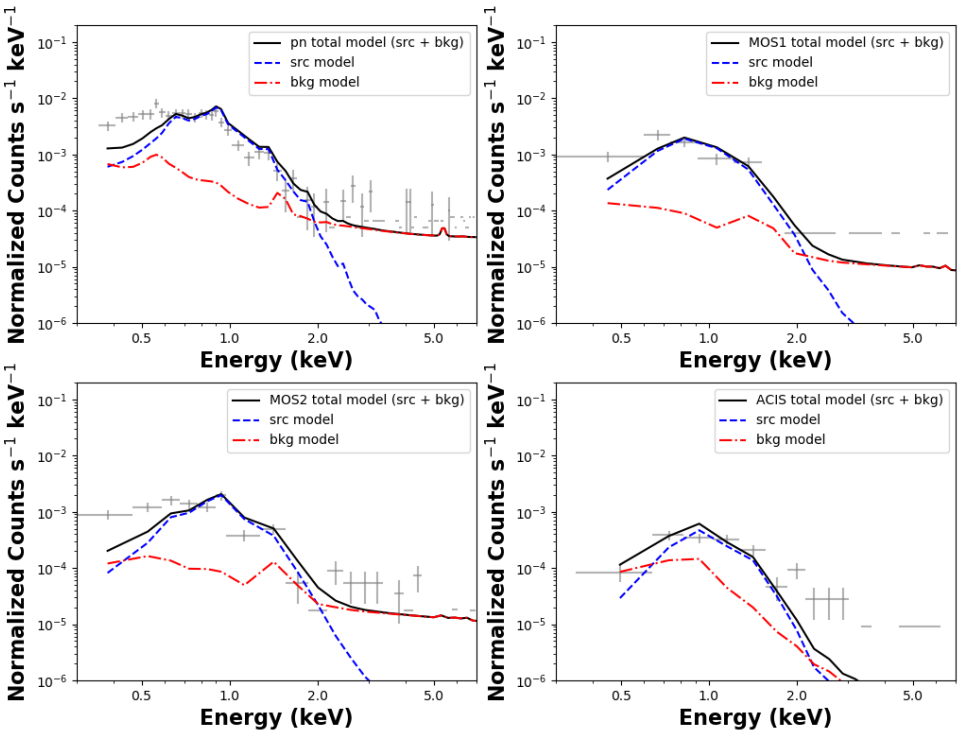

Figure 5.15: *Top-Left*: Total model (source plus background) fit in black, with the two component thermal plasma model in blue, and the total background model in red for the PN camera. Source counts and associated errors from the PN camera are in grey. *Top-Right*: Same as the top-right, but for the MOS1 camera. *Bottom-left*: Same as top-right but for the MOS2 camera. *Bottom-right*: Same as top-right but for the ACIS camera on *Chandra*.

copious amounts of hot gas, ionized by the many surrounding OB stars which create a structured network of cavities and wind-blown bubbles. Based on its X-ray colors, the source is slightly harder than the surrounding soft X-ray emission in NGC 604, marking itself as a distinct point source as can be seen in the left inset in Figure 5.14.

We compare the X-ray spectrum of the point source 013432.60+304704.1 to the spectrum of the surrounding region in NGC 604 as modeled in Tüllmann et al. (2008). Their model for this region of NGC 604 is a two-component thermal plasma model with photoelectric absorption (`phabs*(apec + apec)`). We fit the spectra extracted for the point source using the model parameters for this region of NGC 604 as described Tüllmann et al. (2008). We fix the hydrogen column density, metal abundances, and plasma temperatures to the best-fit model results from Tüllmann et al. (2008), allowing only the normalizations and constants to vary. We find that this model is insufficient to describe the data, as shown in Figure 5.15, with a null hypothesis probability of 100%. The poor model fit strengthens the likelihood that source 013432.60+304704.1 is a point source with emission distinct from the surrounding region in NGC 604, but its soft colors are inconsistent with the spectra of observed WR-XRBs.

Based on the X-ray and optical spectra, as well as the X-ray colors, the source is most likely an X-ray emitting massive star in NGC 604. Its luminosity as measured in T11 ($L_x \sim 10^{35}$) is consistent with the source being a colliding wind binary, though a higher resolution X-ray spectrum with more on-axis counts is necessary to further characterize the nature of the X-ray emission. Follow-up optical spectroscopy with Gemini North is forthcoming, which will be helpful in distinguishing which of the stars within the X-ray error circle are most likely the source of X-ray emission. If confirmed as a colliding wind binary, this source would be the first colliding wind binary observed at a distance greater than the MCs.

5.4 Synopsis

We have explored the nature of several of the HMXB candidates first discussed in Chapter 4 on the basis of their X-ray and optical colors, and spectra in order to confirm or refine the source classification. The multiwavelength data supports classification as HMXBs for three out of the five sources discussed here. One of the sources is a possible background AGN given the presence of broad emission lines in its spectrum, and another source appears too soft to be an XRB, and

instead has spectral characteristics suggestive of a colliding wind binary.

Six band photometry from *HST*, providing UV to near-IR colors, provides a way to differentiate the counterparts to X-ray sources, especially for fainter sources where spectroscopy is difficult. However, the photometry itself is only useful given precise alignment and small enough X-ray error circles, without which issues of stellar crowding make it difficult to determine reliable counterparts. Similarly, optical spectroscopy can be used to classify sources that are photometrically ambiguous, but requires proper localization of the counterpart of interest, as well as careful treatment of the sky background. Here we have used Hectospec spectra from a fiber-fed spectrograph to classify the optical counterparts to X-ray sources, and are able to strengthen source classifications as HMXBs on the basis of donor star counterpart spectral class in three out of five cases. Future work will build on this sample by obtaining spectra of the counterparts for a large number of sources using a multi-slit spectrograph, with which source localization and sky characterization will be improved.

X-ray spectroscopy from *Chandra* and *XMM-Newton* can broadly delineate hard from soft sources, and in the case of sources with many on-axis counts detailed models can provide strong constraints on the source of emission, such as accretion disk temperature. The sources discussed here have enough counts to fit simple models simultaneously to the *Chandra* and *XMM-Newton* data. For four of the sources, this allows us to determine power-law photon indices indicative of hard sources, but without high enough fidelity to delineate between different types of accreting compact objects. Beyond obtaining higher-resolution spectra with more on-axis counts to improve classifications, data from *NuSTAR* will greatly build upon this work by furnishing characterization of accretion states on the basis of very hard X-rays.

The techniques demonstrated and discussed in this chapter lay the groundwork for further studies with *NuSTAR* and *HST*. The characterization of sources on the basis of available multiwavelength data narrows the scope for selection of a sample worthy of detailed follow-up observations. Furthermore, these results serve a pilot study in multiwavelength characterization of HMXBs that can be refined and expanded to more studies of resolved X-ray populations in the Local Volume.

Summary & Future Work

Summary & Future Work

In this thesis, I have focused on the utility of X-ray observations for identifying and characterizing extragalactic massive star populations. In particular, I have focused on the nearby spiral galaxy, M33, which hosts a rich population of SNRs and HMXBs and has extensive multiwavelength coverage. Below, I will briefly summarize the results and conclusions of this thesis, and talk about future work to be carried out.

In Chapter 2, I presented work on the analysis of the X-ray source population of M33 as seen with a deep *XMM-Newton* survey. This survey laid the groundwork for the remainder of the thesis, with the superior soft sensitivity of *XMM-Newton* allowing for the characterization of many new soft sources, including new candidate SNRs, on the basis of custom hardness ratios. Furthermore, the expansive coverage of the survey allowed for matching to previous catalogs in M33 in overlapping regions to search for sources that exhibit long-term variability. In particular, I found ~ 30 new possible transient sources, and ~ 75 sources that showed evidence of long term variability between surveys, some of which were revisited as candidate HMXBs in Chapter 4. Finally, the depth and coverage of this survey allowed for analysis of the radial profile of the M33 X-ray source density, as well as the XLF, which is indicative of a large population of HMXBs.

In Chapter 3, I presented a catalog of SNR candidates in M33, identified on the basis of the deep *XMM-Newton* catalog described in Chapter 2, as well as previous data sets, both X-ray and optical. With this data, I detected at 3σ confidence $\approx 50\%$ of the SNR candidates in M33 from previous X-ray and optical surveys, resulting in > 100 SNRs in M33 verified by both optical and X-ray detections. Using both *XMM-Newton* and *Chandra* I demonstrated the power of detailed X-ray spectral fits for characterizing SNRs, and discussed less expensive methods for typing SNR progenitors, such as custom HRs and X-ray morphology. With this large sample of SNRs, I also constructed an SNR XLF both in the inner (solar metallicity) and outer (LMC-like metallicity) regions of M33, and demonstrated that metallicity, differing SFHs on short timescales, and small scale environmental effects appear to cause differences between X-ray luminosity distributions. Finally, I analyzed the X-ray detectability of M33 SNRs, and found that X-ray detected SNRs were in general smaller in diameter, present at small galactocentric radii, and had higher measured [S II]/Hα values than SNRs non-detected in X-rays, suggesting that X-ray non-detected SNRs are

possibly larger and/or fainter, and may have exploded into regions of lower density and metallicity.

In Chapter 4, I explored the binary nature of M33's massive star population from the perspective of HMXBs. Using a combination of archival *Chandra* and *HST* imaging and precise astrometric alignment, I identified 55 candidate HMXBs in M33. I then used *HST* data to model the CMDs in the vicinity of each candidate HMXB, thereby measuring the distribution of SFHs, or formation timescales for HMXBs in M33. I found preferred formation timescales of < 5 Myr and ~ 40 Myr, indicative of a possible population of relatively massive black holes accreting from the winds of supergiant companions at very early times (e.g. M33 X-7), and a population of Be-XRBs present at later times, respectively. Both populations are predicted by binary population synthesis models, and their inferred presence in M33 based on this work lends credence to the binary evolution scenarios that predict such populations on these timescales.

Finally, in Chapter 5, I presented ongoing work to further characterize candidate HMXBs in M33 on the basis of X-ray and optical spectra, as well as six band *HST* photometry, where available. Of the five sources considered, two are likely Be-XRBs, one is validated as an HMXB on the basis of donor star spectrum, one is reclassified as a possible background AGN, and one is reclassified as a likely colliding wind binary. The combination of X-ray and ground-based optical spectra with colors from both *Chandra* and *HST* are highly complementary and invaluable in sussing out the nature of the X-ray emission from the point sources considered here. Future work will build on the techniques described in Chapter 5 to extend the multiwavelength characterization of X-ray source populations to fainter limits, yielding larger catalogs from which clean samples of HMXBs can be studied.

This work has demonstrated the wealth of information to be gained from studying massive stars and their end products in X-rays. As discussed throughout this thesis, there is still work to be done in putting together a comprehensive picture of massive star evolution as it relates to host galaxy environment, and factors such as metallicity and SFH. Fortunately, upcoming projects in M33, and more broadly the Local Volume, will continue chipping away at these broad questions towards a unified view of massive star and binary evolution in LG environments. Below, I will briefly introduce some of these projects.

In Chapter 3, I concluded that HRs or colors alone are too coarse as methods for detailed SNR progenitor typing, and that current limits on telescope collecting area and resolving power do not

allow for distinguishing SN progenitor type for a large sample of SNRs in M33 on the basis of quantitative morphology. An alternate method for understanding SNR progenitor characteristics is via "SFH-typing," inferring progenitor masses on the basis of the surrounding stellar population (e.g. Jennings et al., 2012, 2014; Williams et al., 2018; Díaz-Rodríguez et al., 2018). The MCs are a promising environment in which to test and calibrate various SNR progenitor typing methods, owing to their rich SNR population (> 70 sources), resolved SFH maps (Harris & Zaritsky, 2004, 2009b), and pre-existing archival *Chandra* imaging for a large number of SNRs. In future work, I will seek to unify our understanding of SNR progenitor characteristics by comparing quantitative X-ray morphologies and the lifetimes of SNR progenitors inferred from SFHs for ~ 50 MC SNRs. These results can then be compared to progenitor classifications from abundance ratio analysis to test the techniques more rigorously than ever before. This calibration of methods locally will allow for the application of the morphology and SFH-typing techniques to SNRs without detailed abundance measurements, thus furnishing a large sample of SNRs with progenitor classifications that will probe the connections between metallicity and SFH of host galaxy and their combined effects on the resultant populations of SNe and subsequently SNRs. Such work will further allow us to look for trends in measured SFHs within progenitor subclasses to improve upon constraints on preferred timescales for CC and Type Ia progenitors (e.g., Maoz & Badenes, 2010). Such measurements can be directly compared to predictions from models of stellar evolution and even for expected progenitor ages that include the effects of binaries (e.g., Zapartas et al., 2017).

The sample of candidate HMXBs with measured ages described in Chapter 4 will also be expanded upon with future work. Namely, I will extend the preliminary work discussed in Chapter 5 to a larger number of sources, securing HMXB classifications for many more sources. With incoming data from the M33 Legacy Survey (PI: Dalcanton), SFHs can not only be measured for a larger number of HMXB candidates, but also characterized in a more homogenous way than for the archival data discussed in Chapter 4. Furthermore, the *HST* legacy data will allow for full SED fitting to determine donor star spectral class, and for the first time characterize the distribution of donor star types for a population of HMXBs beyond the MCs. The donor star information will be complemented by forthcoming *NuSTAR* data in M33, and the rich *Chandra* and *XMM-Newton* archival data already present for M33, which will provide further details about the population of compact objects present, including information about accretion state. All together, this work

will yield the first large sample of well-characterized HMXBs in a large spiral galaxy outside the Milky Way. Such a population is of great interest in understanding the potential local analogue precursors to gravitational wave sources.

In the era of multi-messenger astronomy, understanding the utility and power of observational touchstones in massive star evolution, such as SNRs and HMXBs, will be of great importance. The future work discussed above, coupled with proposed missions such as *Lynx* will make great strides towards understanding some of the outstanding questions in massive star evolution investigated here.

References

Abbott, D. C. 1982, ApJ, 263, 723

Alp, D., Larsson, J., Fransson, C., et al. 2018, ArXiv e-prints, arXiv:1805.04526

Antoniou, V., & Zezas, A. 2016, MNRAS, 459, 528

Antoniou, V., Zezas, A., Hatzidimitriou, D., & Kalogera, V. 2010, ApJ, 716, L140

Arnaud, K. A. 1996, in Astronomical Society of the Pacific Conference Series, Vol. 101, Astronomical Data Analysis Software and Systems V, ed. G. H. Jacoby & J. Barnes, 17

Badenes, C., Bravo, E., Borkowski, K. J., & Domínguez, I. 2003, ApJ, 593, 358

Badenes, C., Hughes, J. P., Bravo, E., & Langer, N. 2007, ApJ, 662, 472

Badenes, C., Maoz, D., & Draine, B. T. 2010, MNRAS, 407, 1301

Baker, J. G., & Menzel, D. H. 1938, ApJ, 88, 52

Baldwin, J. A., Phillips, M. M., & Terlevich, R. 1981, PASP, 93, 5

Belczynski, K., Bulik, T., Mandel, I., et al. 2013, ApJ, 764, 96

Belczynski, K., Kalogera, V., & Bulik, T. 2002, ApJ, 572, 407

Belczynski, K., & Taam, R. E. 2008, ApJ, 685, 400

Belczynski, K., Taam, R. E., Kalogera, V., Rasio, F. A., & Bulik, T. 2007, ApJ, 662, 504

Belczynski, K., & Ziolkowski, J. 2009, ApJ, 707, 870

Berghea, C. T., Dudik, R. P., Tincher, J., & Winter, L. M. 2013, ApJ, 776, 100

Binder, B., Williams, B. F., Kong, A. K. H., et al. 2016, MNRAS, 457, 1636

Binder, B., Williams, B. F., Eracleous, M., et al. 2012, ApJ, 758, 15

Bjorkman, J. E., & Cassinelli, J. P. 1993, ApJ, 409, 429

Blair, W. P., Kirshner, R. P., & Chevalier, R. A. 1981, ApJ, 247, 879

Blair, W. P., Morse, J. A., Raymond, J. C., et al. 2000, ApJ, 537, 667

Borkowski, K. J., Lyerly, W. J., & Reynolds, S. P. 2001, ApJ, 548, 820

Borkowski, K. J., Williams, B. J., Reynolds, S. P., et al. 2006, ApJ, 642, L141

Braun, R., & Walterbos, R. A. M. 1993, A&AS, 98, 327

Broos, P. S., Feigelson, E. D., Townsley, L. K., et al. 2007, ApJS, 169, 353

Broos, P. S., Townsley, L. K., Feigelson, E. D., et al. 2010, ApJ, 714, 1582

—. 2011, ApJS, 194, 2

Bruhweiler, F. C., Miskey, C. L., & Smith Neubig, M. 2003, AJ, 125, 3082

Bulik, T., Belczynski, K., & Prestwich, A. 2011, ApJ, 730, 140

Cappelluti, N., Brusa, M., Hasinger, G., et al. 2009, A&A, 497, 635

Cardelli, J. A., Clayton, G. C., & Mathis, J. S. 1989, ApJ, 345, 245

Casares, J., Negueruela, I., Ribó, M., et al. 2014, Nature, 505, 378

Chevalier, R. A. 1982, ApJ, 258, 790

—. 2005, ApJ, 619, 839

Chu, Y.-H., & Kennicutt, Jr., R. C. 1988, AJ, 96, 1874

Coe, M. J., Edge, W. R. T., Galache, J. L., & McBride, V. A. 2005, MNRAS, 356, 502

Coe, M. J., & Kirk, J. 2015, MNRAS, 452, 969

Conti, P. S., Garmany, C. D., De Loore, C., & Vanbeveren, D. 1983, ApJ, 274, 302

Corbet, R. H. D. 1984, A&A, 141, 91

—. 1986, MNRAS, 220, 1047

Crowther, P. A. 2007, ARA&A, 45, 177

Crowther, P. A., Barnard, R., Carpano, S., et al. 2010, MNRAS, 403, L41

Cutri, R. M., Skrutskie, M. F., van Dyk, S., et al. 2003, 2MASS All Sky Catalog of point sources.

Dalcanton, J. J., Williams, B. F., Seth, A. C., et al. 2009, ApJS, 183, 67

Dalcanton, J. J., Williams, B. F., Lang, D., et al. 2012, ApJS, 200, 18

de Mink, S. E., Langer, N., Izzard, R. G., Sana, H., & de Koter, A. 2013, ApJ, 764, 166

Díaz-Rodríguez, M., Murphy, J. W., Rubin, D. A., et al. 2018, ArXiv e-prints, arXiv:1802.07870

Dodorico, S., Dopita, M. A., & Benvenuti, P. 1980, A&AS, 40, 67

Dolphin, A. E. 2000, PASP, 112, 1383

—. 2002, MNRAS, 332, 91

—. 2012, ApJ, 751, 60

—. 2013, ApJ, 775, 76

Dominik, M., Belczynski, K., Fryer, C., et al. 2012, ApJ, 759, 52

Dopita, M. A., & Sutherland, R. S. 2003, Astrophysics of the diffuse universe

Dopita, M. A., Tuohy, I. R., & Mathewson, D. S. 1981, ApJ, 248, L105

Dray, L. M. 2006, MNRAS, 370, 2079

Drissen, L., Crowther, P. A., Úbeda, L., & Martin, P. 2008, MNRAS, 389, 1033

Dubus, G., Charles, P. A., & Long, K. S. 2004, A&A, 425, 95

Dubus, G., & Rutledge, R. E. 2002, MNRAS, 336, 901

Dwarkadas, V. V. 2005, ApJ, 630, 892

Ekström, S., Georgy, C., Eggenberger, P., et al. 2012, A&A, 537, A146

Eldridge, J. J., Langer, N., & Tout, C. A. 2011, MNRAS, 414, 3501

Eldridge, J. J., & Tout, C. A. 2004, MNRAS, 353, 87

Filipović, M. D., Payne, J. L., Reid, W., et al. 2005, MNRAS, 364, 217

Filippenko, A. V. 1997, ARA&A, 35, 309

Foley, R. J., Smith, N., Ganeshalingam, M., et al. 2007, ApJ, 657, L105

Foreman-Mackey, D., Hogg, D. W., Lang, D., & Goodman, J. 2013, PASP, 125, 306

Foschini, L., Rodriguez, J., Fuchs, Y., et al. 2004, A&A, 416, 529

Fragos, T., Lehmer, B. D., Naoz, S., Zezas, A., & Basu-Zych, A. 2013, ApJ, 776, L31

Freedman, W. L., Madore, B. F., Gibson, B. K., et al. 2001, The Astrophysical Journal, 553, 47

Fryer, C. L. 1999, ApJ, 522, 413

Fryer, C. L., Belczynski, K., Wiktorowicz, G., et al. 2012, ApJ, 749, 91

Gaetz, T. J., Blair, W. P., Hughes, J. P., et al. 2007, ApJ, 663, 234

Gal-Yam, A., Leonard, D. C., Fox, D. B., et al. 2007, ApJ, 656, 372

Garofali, K., Williams, B. F., Hillis, T., et al. 2018, MNRAS, 479, 3526

Garofali, K., Williams, B. F., Plucinsky, P. P., et al. 2017, MNRAS, 472, 308

Gehrz, R. D., Hackwell, J. A., & Jones, T. W. 1974, ApJ, 191, 675

Georgy, C., Ekström, S., Meynet, G., et al. 2012, A&A, 542, A29

Ghavamian, P., Blair, W. P., Sankrit, R., Raymond, J. C., & Hughes, J. P. 2007, ApJ, 664, 304

Gilfanov, M., Grimm, H.-J., & Sunyaev, R. 2004, MNRAS, 347, L57

Girardi, L., Bertelli, G., Bressan, A., et al. 2002, A&A, 391, 195

Gogarten, S. M., Dalcanton, J. J., Williams, B. F., et al. 2009, ApJ, 691, 115

Gordon, K. D., Fouesneau, M., Arab, H., et al. 2016, ApJ, 826, 104

Gordon, S. M., Duric, N., Kirshner, R. P., Goss, W. M., & Viallefond, F. 1999, ApJS, 120, 247

Gordon, S. M., Kirshner, R. P., Long, K. S., et al. 1998, ApJS, 117, 89

Green, D. A. 2014, Bulletin of the Astronomical Society of India, 42, 47

Grimm, H.-J., Gilfanov, M., & Sunyaev, R. 2003, MNRAS, 339, 793

Grimm, H.-J., McDowell, J., Zezas, A., Kim, D.-W., & Fabbiano, G. 2005, ApJS, 161, 271

—. 2007, ApJS, 173, 70

Guerrero, M. A., & Chu, Y.-H. 2008, ApJS, 177, 216

Haberl, F., & Pietsch, W. 2001, A&A, 373, 438

Haberl, F., & Sturm, R. 2016, A&A, 586, A81

Haberl, F., Sturm, R., Ballet, J., et al. 2012, A&A, 545, A128

Hainich, R., Oskinova, L. M., Shenar, T., et al. 2017, ArXiv e-prints, arXiv:1707.01912

Harnden, Jr., F. R., Branduardi, G., Elvis, M., et al. 1979, ApJ, 234, L51

Harris, J., & Zaritsky, D. 2004, AJ, 127, 1531

—. 2009a, AJ, 138, 1243

—. 2009b, AJ, 138, 1243

Heger, A., Fryer, C. L., Woosley, S. E., Langer, N., & Hartmann, D. H. 2003, ApJ, 591, 288

Heger, A., Langer, N., & Woosley, S. E. 2000, ApJ, 528, 368

Heinz, S., Sell, P., Fender, R. P., et al. 2013, ApJ, 779, 171

Hernández-García, L., Masegosa, J., González-Martín, O., et al. 2017, A&A, 602, A65

Holtzman, J. A., Burrows, C. J., Casertano, S., et al. 1995a, PASP, 107, 1065

Holtzman, J. A., Hester, J. J., Casertano, S., et al. 1995b, PASP, 107, 156

Hughes, J. P., Hayashi, I., & Koyama, K. 1998, ApJ, 505, 732

Hughes, J. P., Hayashi, I., Helfand, D., et al. 1995, ApJ, 444, L81

Humphreys, R. M., & Davidson, K. 1979, ApJ, 232, 409

Janka, H.-T. 2012, Annual Review of Nuclear and Particle Science, 62, 407

Jansen, F., Lumb, D., Altieri, B., et al. 2001, A&A, 365, L1

Jennings, Z. G., Williams, B. F., Murphy, J. W., et al. 2012, ApJ, 761, 26

—. 2014, ApJ, 795, 170

Jerkstrand, A., Fransson, C., Maguire, K., et al. 2012, A&A, 546, A28

Justham, S., & Schawinski, K. 2012, MNRAS, 423, 1641

Kelly, P. L., Diego, J. M., Rodney, S., et al. 2018, Nature Astronomy, 2, 334

Kewley, L. J., Dopita, M. A., Sutherland, R. S., Heisler, C. A., & Trevena, J. 2001, ApJ, 556, 121

Khan, R., Stanek, K. Z., Kochanek, C. S., & Sonneborn, G. 2015, ApJS, 219, 42

Kilpatrick, C. D., Foley, R. J., Abramson, L. E., et al. 2017, MNRAS, 465, 4650

Kroupa, P. 2001, MNRAS, 322, 231

Kudritzki, R. P., Pauldrach, A., & Puls, J. 1987, A&A, 173, 293

Kudritzki, R.-P., & Puls, J. 2000, ARA&A, 38, 613

Lada, C. J., & Lada, E. A. 2003, ARA&A, 41, 57

Langer, N., Hamann, W.-R., Lennon, M., et al. 1994, A&A, 290, 819

Laycock, S. G. T., Christodoulou, D. M., Williams, B. F., Binder, B., & Prestwich, A. 2017, ApJ, 836, 51

Lazzarini, M., Hornschemeier, A. E., Williams, B. F., et al. 2018, ArXiv e-prints, arXiv:1806.03305

Lee, J. H., & Lee, M. G. 2014a, ApJ, 786, 130

—. 2014b, ApJ, 793, 134

Lee, J.-J., Park, S., Hughes, J. P., Slane, P. O., & Burrows, D. N. 2011, ApJ, 731, L8

Leitherer, C., Ekström, S., Meynet, G., et al. 2014, ApJS, 212, 14

Leonidaki, I., Boumis, P., & Zezas, A. 2013, MNRAS, 429, 189

Leonidaki, I., Zezas, A., & Boumis, P. 2010, ApJ, 725, 842

Levesque, E. M., Leitherer, C., Ekstrom, S., Meynet, G., & Schaerer, D. 2012, ApJ, 751, 67

Linden, T., Kalogera, V., Sepinsky, J. F., et al. 2010, ApJ, 725, 1984

Linden, T., Sepinsky, J. F., Kalogera, V., & Belczynski, K. 2009, ApJ, 699, 1573

Lipunov, V. M., Postnov, K. A., & Prokhorov, M. E. 1997, MNRAS, 288, 245

Liu, J.-F., Bregman, J. N., Bai, Y., Justham, S., & Crowther, P. 2013, Nature, 503, 500

Liu, Q. Z., van Paradijs, J., & van den Heuvel, E. P. J. 2000, A&AS, 147, 25

—. 2006, A&A, 455, 1165

Long, K. S., Blair, W. P., Kirshner, R. P., & Winkler, P. F. 1990, ApJS, 72, 61

Long, K. S., Blair, W. P., Milisavljevic, D., Raymond, J. C., & Winkler, P. F. 2018, ApJ, 855, 140

Long, K. S., Charles, P. A., Blair, W. P., & Gordon, S. M. 1996, ApJ, 466, 750

Long, K. S., Charles, P. A., & Dubus, G. 2002, ApJ, 569, 204

Long, K. S., Dodorico, S., Charles, P. A., & Dopita, M. A. 1981, ApJ, 246, L61

Long, K. S., & Helfand, D. J. 1979, ApJ, 234, L77

Long, K. S., Kuntz, K. D., Blair, W. P., et al. 2014, ApJS, 212, 21

Long, K. S., Blair, W. P., Winkler, P. F., et al. 2010, ApJS, 187, 495

Lopez, L. A., Castro, D., Slane, P. O., Ramirez-Ruiz, E., & Badenes, C. 2014, ApJ, 788, 5

Lopez, L. A., Ramirez-Ruiz, E., Badenes, C., et al. 2009, ApJ, 706, L106

Lopez, L. A., Ramirez-Ruiz, E., Huppenkothen, D., Badenes, C., & Pooley, D. A. 2011, ApJ, 732, 114

Lutovinov, A. A., & Tsygankov, S. S. 2009, Astronomy Letters, 35, 433

Maccarone, T. J., Lehmer, B. D., Leyder, J. C., et al. 2014, MNRAS, 439, 3064

Madau, P., & Efstathiou, G. 1999, ApJ, 517, L9

Madau, P., & Fragos, T. 2017, ApJ, 840, 39

Maeder, A., & Meynet, G. 2000, A&A, 361, 159

Maggi, P., Haberl, F., Kavanagh, P. J., et al. 2014, A&A, 561, A76

—. 2016, A&A, 585, A162

Magnier, E. A., Prins, S., van Paradijs, J., et al. 1995, A&AS, 114, 215

Magrini, L., Vílchez, J. M., Mampaso, A., Corradi, R. L. M., & Leisy, P. 2007, A&A, 470, 865

Mandel, I. 2016, MNRAS, 456, 578

Mannucci, F., Della Valle, M., Panagia, N., et al. 2005, A&A, 433, 807

Maoz, D., & Badenes, C. 2010, MNRAS, 407, 1314

Marigo, P., Girardi, L., Bressan, A., et al. 2008, A&A, 482, 883

Markert, T. H., & Rallis, A. D. 1983, ApJ, 275, 571

Massey, P. 2003, ARA&A, 41, 15

Massey, P., Neugent, K. F., & Smart, B. M. 2016, AJ, 152, 62

Massey, P., Olsen, K. A. G., Hodge, P. W., et al. 2006, AJ, 131, 2478

Mathewson, D. S., & Clarke, J. N. 1973, ApJ, 180, 725

Mathewson, D. S., Ford, V. L., Dopita, M. A., et al. 1983, ApJS, 51, 345

Mathewson, D. S., & Healey, J. R. 1963, Nature, 199, 681

Maund, J. R., & Smartt, S. J. 2005, MNRAS, 360, 288

McSwain, M. V., & Gies, D. R. 2005, ApJS, 161, 118

Merritt, D., Ferrarese, L., & Joseph, C. L. 2001, Science, 293, 1116

Meynet, G., Maeder, A., Schaller, G., Schaerer, D., & Charbonnel, C. 1994, A&AS, 103, 97

Milne, D. K. 1979, Australian Journal of Physics, 32, 83

Mineo, S., Gilfanov, M., & Sunyaev, R. 2012, MNRAS, 419, 2095

Mirabel, I. F., Dijkstra, M., Laurent, P., Loeb, A., & Pritchard, J. R. 2011, A&A, 528, A149

Mirabel, I. F., & Rodrigues, I. 2003, Science, 300, 1119

Misanovic, Z., Pietsch, W., Haberl, F., et al. 2006, A&A, 448, 1247

Monet, D. G., Levine, S. E., Canzian, B., et al. 2003, AJ, 125, 984

Moran, E. C., Eracleous, M., Leighly, K. M., et al. 2005, AJ, 129, 2108

Mudd, D., & Stanek, K. Z. 2015, MNRAS, 450, 3811

Murphy, J. W., Khan, R., Williams, B., et al. 2018, ArXiv e-prints, arXiv:1803.00024

Negueruela, I. 1998, A&A, 338, 505

Negueruela, I., & Coe, M. J. 2002, A&A, 385, 517

Negueruela, I., Smith, D. M., Reig, P., Chaty, S., & Torrejón, J. M. 2006, in ESA Special Publication, Vol. 604, The X-ray Universe 2005, ed. A. Wilson, 165

Neugent, K. F., & Massey, P. 2011, ApJ, 733, 123

—. 2014, ApJ, 789, 10

Nurgaliev, D., McDonald, M., Benson, B. A., et al. 2013, ApJ, 779, 112

Orosz, J. A., McClintock, J. E., Narayan, R., et al. 2007, Nature, 449, 872

Pannuti, T. G., Rho, J., Heinke, C. O., & Moffitt, W. P. 2014, AJ, 147, 55

Pannuti, T. G., Schlegel, E. M., & Lacey, C. K. 2007, AJ, 133, 1361

Paolillo, M., Schreier, E. J., Giacconi, R., Koekemoer, A. M., & Grogin, N. A. 2004, ApJ, 611, 93

Park, T., Kashyap, V. L., Siemiginowska, A., et al. 2006, ApJ, 652, 610

Pauldrach, A., Puls, J., & Kudritzki, R. P. 1986, A&A, 164, 86

Payne, J. L., White, G. L., Filipović, M. D., & Pannuti, T. G. 2007, MNRAS, 376, 1793

Pfahl, E., Rappaport, S., Podsiadlowski, P., & Spruit, H. 2002, ApJ, 574, 364

Pietsch, W., Haberl, F., Sasaki, M., et al. 2006, ApJ, 646, 420

Pietsch, W., Haberl, F., & Vogler, A. 2003, A&A, 402, 457

Pietsch, W., Misanovic, Z., Haberl, F., et al. 2004a, A&A, 426, 11

—. 2004b, A&A, 426, 11

Pietsch, W., Mochejska, B. J., Misanovic, Z., et al. 2004c, A&A, 413, 879

Pietsch, W., Haberl, F., Gaetz, T. J., et al. 2009, ApJ, 694, 449

Plucinsky, P. P., Williams, B., Long, K. S., et al. 2008, ApJS, 174, 366

Plucinsky, P. P., Beardmore, A. P., DePasquale, J. M., et al. 2012, in Proc. SPIE, Vol. 8443, Space Telescopes and Instrumentation 2012: Ultraviolet to Gamma Ray, 844312

Podsiadlowski, P., Hsu, J. J. L., Joss, P. C., & Ross, R. R. 1993, Nature, 364, 509

Podsiadlowski, P., Joss, P. C., & Hsu, J. J. L. 1992, ApJ, 391, 246

Podsiadlowski, P., Langer, N., Poelarends, A. J. T., et al. 2004, ApJ, 612, 1044

Porter, J. M., & Rivinius, T. 2003, PASP, 115, 1153

Poutanen, J., Fabrika, S., Valeev, A. F., Sholukhova, O., & Greiner, J. 2013, MNRAS, 432, 506

Prestwich, A. H., Kilgard, R., Crowther, P. A., et al. 2007, ApJ, 669, L21

Rappaport, S., & van den Heuvel, E. P. J. 1982, in IAU Symposium, Vol. 98, Be Stars, ed. M. Jaschek & H.-G. Groth, 327–344

Raymond, J. C. 1984, ARA&A, 22, 75

Repetto, S., & Nelemans, G. 2015, MNRAS, 453, 3341

Rest, A., Suntzeff, N. B., Olsen, K., et al. 2005, Nature, 438, 1132

Reynolds, S. P. 2008, ARA&A, 46, 89

Ribó, M., Munar-Adrover, P., Paredes, J. M., et al. 2017, ApJ, 835, L33

Rizzi, L., Tully, R. B., Makarov, D., et al. 2007, ApJ, 661, 815

Roper, Q., McEntaffer, R. L., DeRoo, C., et al. 2015, ApJ, 803, 106

Sabbadin, F. 1979, A&A, 80, 212

Salpeter, E. E. 1955, ApJ, 121, 161

Sana, H., de Mink, S. E., de Koter, A., et al. 2012, Science, 337, 444

Sarbadhicary, S. K., Badenes, C., Chomiuk, L., Caprioli, D., & Huizenga, D. 2017, MNRAS, 464, 2326

Sasaki, M., Pietsch, W., Haberl, F., et al. 2012, A&A, 544, A144

Schulman, E., & Bregman, J. N. 1995, ApJ, 441, 568

Seaton, M. J. 1959, MNRAS, 119, 90

Sepinsky, J., Kalogera, V., & Belczynski, K. 2005, ApJ, 621, L37

Seward, F. D., Forman, W. R., Giacconi, R., et al. 1979, ApJ, 234, L55

Shtykovskiy, P., & Gilfanov, M. 2005, A&A, 431, 597

Shu, X. W., Wang, T. G., Jiang, N., et al. 2017, ApJ, 837, 3

Silverman, J. M., & Filippenko, A. V. 2008, ApJ, 678, L17

Smartt, S. J. 2009, ARA&A, 47, 63

—. 2015, PASA, 32, e016

Smartt, S. J., Eldridge, J. J., Crockett, R. M., & Maund, J. R. 2009, MNRAS, 395, 1409

Smartt, S. J., Maund, J. R., Hendry, M. A., et al. 2004, Science, 303, 499

Smith, C., Leiton, R., & Pizarro, S. 2000, in Astronomical Society of the Pacific Conference Series, Vol. 221, Stars, Gas and Dust in Galaxies: Exploring the Links, ed. D. Alloin, K. Olsen, & G. Galaz, 83

Smith, N. 2014, ARA&A, 52, 487

Stark, A. A., Gammie, C. F., Wilson, R. W., et al. 1992, ApJS, 79, 77

Strüder, L., Briel, U., Dennerl, K., et al. 2001, A&A, 365, L18

Sturm, R., Haberl, F., Pietsch, W., et al. 2013, A&A, 558, A3

Sukhbold, T., Ertl, T., Woosley, S. E., Brown, J. M., & Janka, H.-T. 2016, ApJ, 821, 38

Sukhbold, T., Woosley, S., & Heger, A. 2017, ArXiv e-prints, arXiv:1710.03243

Tauris, T. M., Kramer, M., Freire, P. C. C., et al. 2017, ApJ, 846, 170

Trudolyubov, S. P. 2013, MNRAS, 435, 3326

Tüllmann, R., Gaetz, T. J., Plucinsky, P. P., et al. 2008, ApJ, 685, 919

—. 2011, ApJS, 193, 31

Tuohy, I. R., Dopita, M. A., Mathewson, D. S., Long, K. S., & Helfand, D. J. 1982, ApJ, 261, 473

Turner, M. J. L., Abbey, A., Arnaud, M., et al. 2001, A&A, 365, L27

Valsecchi, F., Glebbeek, E., Farr, W. M., et al. 2010, Nature, 468, 77

van Bever, J., & Vanbeveren, D. 1997, A&A, 322, 116

Van Bever, J., & Vanbeveren, D. 2000, A&A, 358, 462

van den Heuvel, E. P. J., Portegies Zwart, S. F., & de Mink, S. E. 2017, MNRAS, 471, 4256

van der Klis, M. 2004, ArXiv Astrophysics e-prints, astro-ph/0410551

Van Dyk, S. D., Li, W., & Filippenko, A. V. 2003, PASP, 115, 1

van Kerkwijk, M. H., Geballe, T. R., King, D. L., van der Klis, M., & van Paradijs, J. 1996, A&A, 314, 521

Vink, J. 2012, A&A Rev., 20, 49

Vink, J., Laming, J. M., Gu, M. F., Rasmussen, A., & Kaastra, J. S. 2003, ApJ, 587, L31

Vink, J. S., de Koter, A., & Lamers, H. J. G. L. M. 2001, A&A, 369, 574

Walter, R., Lutovinov, A. A., Bozzo, E., & Tsygankov, S. S. 2015, A&A Rev., 23, 2

Wik, D. R., Lehmer, B. D., Hornschemeier, A. E., et al. 2014, ApJ, 797, 79

Williams, B. F., Dalcanton, J. J., Dolphin, A. E., Holtzman, J., & Sarajedini, A. 2009, ApJ, 695, L15

Williams, B. F., Dalcanton, J. J., Stilp, A., et al. 2013a, ApJ, 765, 120

—. 2013b, ApJ, 765, 120

Williams, B. F., Hillis, T. J., Murphy, J. W., et al. 2018, ArXiv e-prints, arXiv:1803.08112

Williams, B. F., Gaetz, T. J., Haberl, F., et al. 2008, ApJ, 680, 1120

Williams, B. F., Hatzidimitriou, D., Green, J., et al. 2014a, MNRAS, 443, 2499

Williams, B. F., Lang, D., Dalcanton, J. J., et al. 2014b, ApJS, 215, 9

Williams, B. F., Wold, B., Haberl, F., et al. 2015, ApJS, 218, 9

Wilms, J., Allen, A., & McCray, R. 2000, ApJ, 542, 914

Woltjer, L. 1972, ARA&A, 10, 129

Woosley, S. E., Heger, A., & Weaver, T. A. 2002, Reviews of Modern Physics, 74, 1015

Woosley, S. E., Pinto, P. A., & Ensman, L. 1988, ApJ, 324, 466

Woosley, S. E., & Weaver, T. A. 1995, ApJS, 101, 181

Yamaguchi, H., Badenes, C., Petre, R., et al. 2014, ApJ, 785, L27

Yokogawa, J., Imanishi, K., Tsujimoto, M., Koyama, K., & Nishiuchi, M. 2003, PASJ, 55, 161

Yukita, M., Ptak, A., Hornschemeier, A. E., et al. 2017, ApJ, 838, 47

Zapartas, E., de Mink, S. E., Izzard, R. G., et al. 2017, A&A, 601, A29

Zaritsky, D., Elston, R., & Hill, J. M. 1989, AJ, 97, 97

Vita

Kristen Garofali was born in Detroit, Michigan in 1990 to Cynthia and Charles. She graduated from Troy High School in Troy, Michigan in 2008. Kristen earned dual BS degrees in Astrophysics and Physics from Michigan State University in 2012 before coming to the University of Washington to pursue her PhD. She completed her doctorate in 2018 and will next be heading to the University of Arkansas for a postdoctoral research position.